

# **HIGH SPEED BRUSHLESS DC PMSM: OPTIMAL DESIGN AND CONTROL CONTRIBUTIONS**

Teză destinată obținerii  
titlului științific de doctor inginer  
la  
Universitatea "Politehnica" din Timișoara  
în domeniul INGINERIE ELECTRICĂ  
de către

**Ing. Vlad-Nicolae Grădinaru**

Conducător științific:	prof.univ.dr.ing. Ion Boldea
Referenți științifici:	prof.univ.dr. Mircea Rădulescu
	prof.univ.dr.ing. Iulian Birou
	conf.univ.dr.ing. Lucian Tutelea

Ziua susținerii tezei: 27.09.2012

Seriile Teze de doctorat ale UPT sunt:

- |                        |   |
|------------------------|---|
| 1. Automatică          | 7. Inginerie Electronică și Telecomunicații |
| 2. Chimie              | 8. Inginerie Industrială                    |
| 3. Energetică          | 9. Inginerie Mecanică                       |
| 4. Ingineria Chimică   | 10. Știința Calculatoarelor                 |
| 5. Inginerie Civilă    | 11. Știința și Ingineria Materialelor       |
| 6. Inginerie Electrică |   |

Universitatea „Politehnica” din Timișoara a inițiat seriile de mai sus în scopul diseminării expertizei, cunoștințelor și rezultatelor cercetărilor întreprinse în cadrul școlii doctorale a universității. Seriile conțin, potrivit H.B.Ex.S Nr. 14 / 14.07.2006, tezele de doctorat susținute în universitate începând cu 1 octombrie 2006.

Copyright © Editura Politehnica – Timișoara, 2012

Această publicație este supusă prevederilor legii dreptului de autor. Multiplicarea acestei publicații, în mod integral sau în parte, traducerea, tipărirea, reutilizarea ilustrațiilor, expunerea, radiodifuzarea, reproducerea pe microfilme sau în orice altă formă este permisă numai cu respectarea prevederilor Legii române a dreptului de autor în vigoare și permisiunea pentru utilizare obținută în scris din partea Universității „Politehnica” din Timișoara. Toate încălcările acestor drepturi vor fi penalizate potrivit Legii române a drepturilor de autor.

România, 300159 Timișoara, Bd. Republicii 9,  
tel. 0256 403823, fax. 0256 403221  
e-mail: editura@edipol.upt.ro

## **PREFACE**

This thesis represents an approach to optimal design and control of brushless DC permanent magnet motors fed with trapezoidal currents for refrigerator compressors. The thesis contains an overview of the existent brushless DC drives, hybrid analytical/Finite Element Method (FEM) and optimal design of a 6/4 brushless DC motor, FEM validation of the topologies obtained through optimal design, analysis of the best methods to reduce the cogging torque without affecting too much the medium torque, introduces an accurate dynamic model of the brushless DC motor and proposes a new sensorless control for brushless DC drives and a new Pulse Amplitude Modulation (PAM) converter topology to reduce the cost and size of the inverter.

## Acknowledgements

I wish to express my gratitude to my supervisor Prof. Ion Boldea from University "Politehnica" Timișoara, Faculty of Electrical and Power Engineering. His guidance, support and encouragements made this work possible. I wish to thank all of those who contributed to my engineering education and also to my colleagues from Intelligent Motion Control Laboratory at Faculty of Electrical and Power Engineering, Timișoara. Assoc.Prof. Lucian Tutelea, Ph.D.Eng. Sorin Agarliță and Ph.D.Eng. Ana Moldovan deserve my special gratitude.

I would like to thank to my former colleagues from BeeSpeed Automatizari for their understanding and support, especially to Ph.D.Eng. Sever Scridon. Also, many thanks to my colleagues from Continental Automotive Romania, Timișoara.

A special thank for Mr. Irineu Setter and to Mr. Cristofaro Pompermaier for their help and support during my period of six months spent at Embraco S.A. in Joinville, Brazil.

Most of all, I want to thank my family and my girlfriend, Anca, for their understanding, encouragement and support.

Timișoara, July 2012

Vlad-Nicolae Grădinaru

Grădinaru, Vlad-Nicolae

### **High speed brushless DC PMSM: optimal design and control contributions**

Teze de doctorat ale UPT, Seria 6, Editura Politehnica, 2012, 268 pagini, 185 figuri, 15 tabele.

Keywords: high speed, brushless DC motor, hybrid analytical/FEM design, optimal design, cogging torque, dynamic modeling, sensorless control, starting method, PAM converter, low cost, high efficiency

### **Abstract**

The present thesis investigates the optimal design with embedded FEM of a 6/4 brushless DC motor fed with trapezoidal currents for refrigerator compressors. Validation of the optimal topologies is done through FEM and cogging torque reduction techniques are employed in order to minimize as possible torque pulsations.

A dynamic model is built taking into account phase commutation phenomenon and using back EMF waveforms from FEM to be more realistic. Sensorless control based on active power combined with I-f method for low speeds is developed and verified through simulations and experiments with satisfying results.

A new PAM converter is introduced in the DC link to reduce the size and cost of the inverter and simulated with satisfying results.

## Table of Contents

<b>Preface</b> .....	<b>3</b>
<b>Acknowledgements</b> .....	<b>4</b>
<b>Table of Contents</b> .....	<b>5</b>
<b>Motivation</b> .....	<b>9</b>
<b>Objectives of the thesis</b> .....	<b>10</b>
<b>Outline of the thesis</b> .....	<b>11</b>
<b>Chapter 1 Permanent magnet motor drives</b> .....	<b>12</b>
Abstract.....	12
1.1 Introduction.....	12
1.2 Permanent magnet motor drives.....	13
1.2.1 Synchronous motor drives.....	14
1.2.2 Permanent magnet DC brushless motor drives .....	15
1.3 Classification of permanent magnet electric motors .....	16
1.4 Permanent magnet materials and circuits.....	18
1.5 Control techniques overview for PM motors with rectangular currents.....	23
1.5.1 Brushless DC operating principle .....	23
1.5.2 Control techniques for trapezoidal PM motors .....	26
1.6 Applications .....	30
1.7 Conclusions .....	35
References .....	35
<b>Chapter 2 Hybrid FEM/Analytical Optimization Design of a Surface Permanent Magnet Synchronous Machine</b> .....	<b>38</b>
Abstract.....	38
2.1 Introduction.....	38
2.2 Design theme.....	40
2.2.1 Motivation .....	40
2.2.2 Choosing the right motor.....	41
2.2.3 Number of magnet poles .....	43
2.2.4 Motor air gap.....	44
2.2.5 Rotor.....	44
2.2.6 Stator and windings.....	45
2.2.7 Current shape.....	48
2.2.8 Materials selection.....	50
2.2.8.1 Iron core laminations .....	50
2.2.8.2 The permanent magnets.....	52
2.2.9 Preliminary design data.....	53
2.2.10 Electric and magnetic loadings .....	54

## 6 Table of Contents

---

2.2.11	Choosing a few dimensioning factors.....	55
2.2.12	A few technological constraints.....	55
2.3	Analytical model .....	56
2.3.1	Geometrical dimensioning .....	56
2.3.2	Number of turns/coil and electrical parameters.....	62
2.3.3	Machine losses.....	66
2.3.4	Active materials weights and costs.....	70
2.3.5	Thermal verification.....	71
2.4	Optimization .....	72
2.4.1	An overview of the optimization techniques.....	72
2.4.1.1	Mathematical formulation of optimization problem ....	74
2.4.1.2	Nonlinear programming methods .....	75
2.4.1.2.1	Direct search methods .....	75
2.4.1.2.2	Stochastic methods .....	76
2.4.1.2.3	Gradient methods .....	76
2.4.1.3	Constrained optimization techniques.....	76
2.4.2	Optimization problem definition.....	78
2.4.2.1	Choosing the optimization variables .....	78
2.4.2.2	Choosing the objective function .....	79
2.4.3	Hybrid analytical/FEM modified Hooke-Jeeves optimization algorithm .....	81
2.4.3.1	Algorithm description .....	82
2.4.3.2	Optimization results .....	87
2.4.4	Hybrid analytical/FEM artificial bee colony (ABC) optimization algorithm .....	91
2.4.4.1	Algorithm description .....	92
2.4.4.2	Optimization results .....	94
2.5	Conclusion .....	99
	References .....	100
<b>Chapter 3 Finite element validation and torque pulsations reduction techniques .....</b>		<b>105</b>
	Abstract.....	105
3.1	Introduction.....	105
3.2	Theoretical background .....	107
3.2.1	Vector fields and operators .....	107
3.2.2	Maxwell's equations.....	110
3.2.3	Finite element method (FEM) .....	113
3.2.4	Boundary conditions .....	116
3.2.4.1	Dirichlet boundary conditions .....	116
3.2.4.2	Neumann boundary conditions.....	117
3.3	Finite element analysis .....	118
3.3.1	Finite element software .....	118

---

3.3.2 Finite element model of the 6/4 BLDC .....	119
3.3.3 Field distribution .....	121
3.3.4 No-load flux linkages and back EMFs .....	134
3.3.5 Forces in an electromagnetic field .....	138
3.3.6 Torques in an electromagnetic field .....	142
3.3.7 Cogging torque .....	145
3.3.8 Torque pulsations reduction techniques .....	150
3.3.8.1 Skewing .....	151
3.3.8.2 Magnet width variation .....	157
3.3.8.3 Magnet shifting .....	161
3.3.8.4 Tooth notches .....	166
3.3.9 Rotor eccentricity .....	175
3.4 Conclusion .....	177
References .....	178
<b>Chapter 4 Dynamic model of BLDC .....</b>	<b>181</b>
Abstract .....	181
4.1 Introduction .....	181
4.2 BLDC motor .....	182
4.3 Inverter .....	185
4.3.1 Half-wave mode (unipolar excitation) .....	186
4.4 Controllers .....	188
4.5 Dynamic model implementation .....	189
4.5.1 BLDC Motor block .....	190
4.5.2 Voltage source inverter block .....	191
4.5.3 Hall sensor feedback .....	194
4.5.4 Current and speed controllers .....	195
4.6 Simulation results and discussions .....	196
4.7 Conclusion .....	202
References .....	203
<b>Chapter 5 Sensorless control of BLDC with instantaneous active power observer and I-f starting method, with experiments .....</b>	<b>205</b>
Abstract .....	205
5.1 Introduction .....	205
5.2 Instantaneous active power observer .....	207
5.3 I-f starting method .....	209
5.4 Transition strategies .....	210
5.4.1 I-f to sensorless smooth transition .....	210
5.4.2 Sensorless to I-f transition .....	211
5.5 Simulation results .....	212
5.6 Experimental results .....	217

---

5.6.1 Constant speed operation.....	218
5.6.2 Dynamics.....	225
5.6.3 I-f to sensorless transition.....	229
5.6.4 Sensorless to I-f transition .....	231
5.7 Conclusion .....	233
References .....	233
<b>Chapter 6 Pulse Amplitude Modulation (PAM) converter control of BLDC motor with and without Hall sensors – digital simulations .</b>	<b>237</b>
Abstract.....	237
6.1 Introduction.....	237
6.2 Overview of the proposed drive .....	238
6.2.1 Inverter .....	239
6.2.2 Rectifier .....	239
6.2.3 Buck-boost converter.....	240
6.3 Control theory.....	241
6.3.1 Speed and current control (PAM control).....	241
6.3.2 PWM control with Hall sensors.....	242
6.3.3 PWM control with back-EMF sensing technique .....	243
6.4 Simulation results and discussions .....	243
6.5 Conclusion .....	251
References .....	251
<b>Chapter 7 The experimental test bench.....</b>	<b>254</b>
Abstract.....	254
7.1 Brushless DC motor .....	254
7.2 Test bench equipment .....	255
7.2.1 Inverter .....	256
7.2.2 Measurement board.....	257
7.2.3 Hall signal sensors.....	258
7.2.4 dSpace DS1103 platform.....	259
7.3 Software implementation.....	260
7.4 Conclusion .....	262
References .....	262
<b>Chapter 8 Conclusion and Contributions .....</b>	<b>263</b>
8.1 Conclusion .....	263
8.2 Original contributions .....	264
8.3 Future work .....	265
<b>Author’s papers related to the Ph.D. thesis.....</b>	<b>266</b>
<b>Author’s CV .....</b>	<b>267</b>



## Motivation

In the last two decades home appliances markets were booming. With the rise of the demand of refrigerating systems, the energy consumption became more and more problematic. Considering the cost of electric energy production and its impact on the environment, the manufacturers had to consider more efficient solutions while keeping the costs at a minimum level. While the refrigerators became more and more intelligent, with settings for energy saving, the attention shifted to the compressor.

Induction motors, used on large scale in this type of applications, although robust, could not meet the new, ever-growing demands of energy consumption so alternatives were sought. The brushless DC motors with permanent magnets were fitted for the new challenges as they provide high torque per volume ratio and high efficiency. Also, they are easy to control and can operate at various speeds, depending on the refrigerator settings.

Once the problem of energy saving criteria was met, the manufacturers met another challenge – the price. Somehow, they needed to merge intelligent home appliances with an affordable price for the customers. An affordable price at the end of the market chain meant reduced fabrication costs. This is why thorough design of the drive right from the start is mandatory and optimal design developed on already existing tools is more than useful. Control is also problematic in this field, because Hall sensors, although cheap, may not be reliable in harsh environments, sensorless control becoming in such a case a viable option.

This thesis aims right at the most stringent points on the market, its theme being more actual than ever. Optimization design methods that verify as much variables and parameters as it can without compromising the fast response time are analyzed, while converter topologies that minimize the size and costs are verified while easy-to-implement sensorless technique is presented.

## Objectives of the thesis

The major objectives of the thesis are:

- To offer an overview of the existing brushless DC drives and their control;
- Implementation of two hybrid analytical/FEM optimal design methods for a 6/4 brushless DC motor for low cost and high efficiency refrigerator compressor application;
- Analysis of cogging torque reduction techniques and finding the optimal combination between them that reduces greatly the torque pulsations, while not reducing that much the value of the total torque;
- FEM validation of the topologies obtained from optimal design in order to find the best configuration from all points of view, like radial forces, flux linkage and field distribution;
- To develop a dynamic model of the drive, taking into account the commutation phenomenon and using FEM extracted back EMF waveform to be as real as it can be and use it for sensorless control development;
- To develop, analyze and test through digital simulations and experiments the validity of a sensorless control based on active power combined with I-f starting method for low speeds;
- To present and analyze a PAM converter topology in order to reduce as much as possible the size and cost of the inverter, while also reducing the commutation losses.

## Outline of the thesis

The thesis is organized in 8 chapters following the above presented objectives:

**First** chapter offers a comprehensive overview of the existing brushless DC permanent magnet topologies, control strategies and application areas. From all of that, the reason of choosing this particular type of motor is drawn

**Second** chapter is focused on optimal design of the motor. The choice of the 6/4 brushless DC with surface permanent magnets topology is presented in detail and analytical design as a starting point for optimal cases is implemented. Two optimal design techniques with embedded FEM are analyzed and used further. In the end, the two topologies obtained are compared in terms of efficiency, manufacturing costs and optimization time.

In the **third** chapter the topologies from the previous chapter are validated through FEM in order to check field distribution, linkage flux, back EMF waveform and radial forces that affect the rotor. Also eccentricity was studied with promising results. Since in surface permanent magnet motors cogging torque is a serious issue, several torque pulsations reduction techniques were studied carefully. In the end, the most suitable combination of techniques was chosen, as it reduces the cogging torque but there is only a small reduction of the total torque.

**Fourth** chapter is dedicated entirely to the development and simulation of a dynamic model of the brushless DC drive, considering the commutation phenomenon and using the back EMF shapes obtained from finite element analysis. Hall sensor delay due to improper mounting is corrected and a complex model is obtained. Speed and current controllers were designed and used efficiently in simulations, needing no correction for experiments, thus proving robust.

**Fifth** chapter is focused on development of a sensorless control strategy that implies calculation of active power from measured phase currents and voltages, subtracting the copper losses and load power (load torque is proportional to speed) and with motor inertia and friction coefficient known, the speed is estimated and, by integration, the angle. Simulations and experiments validate the robustness and functionality of the observer. For low speeds, I-f strategy is employed with seamless transition to sensorless mode.

**Sixth** chapter presents a new PAM converter topology in DC link used for reduction of cost, size and commutation losses in the inverter. Simulation results with Hall sensors and back EMF detection show promising results.

**Seventh** chapter is dedicated to the experimental test bench presentation, with every element described in detail.

Last but not least, chapter **eight** summarizes conclusions drawn throughout the thesis and present original contributions from author's point of view. Future work is also presented, as some subjects treated in the thesis need further development and intense study.

# Chapter 1

## Permanent magnet motor drives

### Abstract

The introductory chapter of the thesis is aimed at offering a motivation for the research in the field of permanent magnet machines and their use in home appliances. As we advance on the chapter, the overview shifts from a general perspective of permanent magnet drives to essential details as motor topology, materials and control.

The scope of the chapter is to present a general view of the permanent magnet motors field, with its advantages and drawbacks, with its evolution throughout time and future perspectives and last, but not least, the vast range of applications, from automotive industry to medical instruments and home appliances. Specifics of permanent magnet motors design, control and use in refrigerator compressors are subjects of the following chapters.

### 1.1 Introduction

Permanent magnet motors, today widely used in a large number of applications, are an alternative to electromagnetic excitation motors. The later ones dominated the 20<sup>th</sup> century as they are robust and not at all pretentious when it comes about control. However, limitations in efficiency, ability to work in a wide range of speeds and high maintenance could not be overcome.

The introduction of permanent magnets brought the following advantages over electromagnetic excitation [1]:

- Higher output power/torque density per volume;
- Improved dynamic performance due to higher magnetic flux density in the air gap;
- Increase in efficiency due to absence of excitation losses;
- Higher output power/torque density per volume;
- Simplification of construction and maintenance;
- Overall price reduction for some types of machines.

As impressive as they are, these advantages come at a price. The magnets require mounting precision on or in the rotor and their price are quite high. Another drawback of the magnets is related to demagnetization at high temperatures, thus the design of the motor, including cooling capabilities, should take this into account. Last, but not least, since the field produced by the magnets is rather constant, additional effort should be put in the field weakening region.

The history of the permanent magnet motors is strongly linked to developments in magnetic materials and breakthroughs in the field of power electronics. Although used for the first time in the 4<sup>th</sup> decade of the 19<sup>th</sup> century, the PM motors were not so popular due to the poor quality of the magnetic materials. However, a small portion of the electric machines market, for small and fractional horsepower PM DC commutator motors, was conquered roughly 100 years later with the introduction of AlNiCo. Ferrite based magnets are still used in some applications, like toys or household equipments and they might be revived by the recent increase in the price of rare earth magnets.

Induction motors dominated the last century due to simple construction and maintenance, low price and robustness. High power applications, like industrial ones, still benefit from these advantages of induction machines, but for low and even medium power applications, synchronous machines conquered more and more ground.

The use of PM brushless motors has become a more attractive option than induction motors. Rare earth magnets cover the weak spots in induction machines, namely they offer better steady-state performance, power density, dynamic performance and quality [1]. That and the possibility of cost effective control over a wide range of speeds helped the ascension of PM motors.

Developments in power electronics, semiconductors, microprocessors and even drives that use PM machines were a part of their ascension, as one cannot progress without another.

The PM brushless motor electromechanical drive has become a more viable option than its induction or reluctance counterpart in motor sizes up to 10 – 15 kW. This opened the way for their usage in numerous applications, from aerospace, automotive, home appliances and medical instruments, to toys and machine tools. A detailed vision of this variety and how magnetic materials and control evolved will be presented next.

## 1.2 Permanent magnet motor drives

A drive is defined to be an entity that contains the motor, the converter that interfaces the motor and the power supply and the control (sensors and controller unit). In what follows, a characterization of permanent magnet motor drives is presented. Depending on speed and/or position control and speed variation, permanent magnet motor drives are of three types [1]:

**Constant speed drives**, where the motor runs at a constant speed and where its variation is not a constraint. The main advantage is the absence of any sensor and of any solid state converter between the supply and motor. However, the induction machine is used the same way, so they are applicable only if the situation demands performances associated to permanent magnet motors.

**Variable speed drives (VSD)** are the most common application in industry. Permanent magnet motors have the advantage of operating on a wide speed range without losing much of their efficiency. This is the main reason they are preferred to induction machine VSDs, especially in low and mid power range. The basic requirement

in VSDs is to operate properly from very low to medium or high speeds. This assumes the presence of a solid state converter (rectifier -> dc-link (or converter) -> inverter) between power supply and motor and at least a primitive type of speed or position sensing for speed control.

**Servo systems** are built for applications where control's accuracy is the key. This is why speed and/or position must be sensed accurately and during transients, the prescribed quantities must be followed rapidly. This is useful in precision tools or sensitive applications (automotive, avionics), where fast response is essential.

Although permanent magnet motor drives can be divided into three categories, DC commutator, stepping and brushless motor drives, only the later one is studied in this chapter.

Brushless motor drives can be of two types, depending on their current waveform: sinusoidal or rectangular motors (Fig. 1.1).

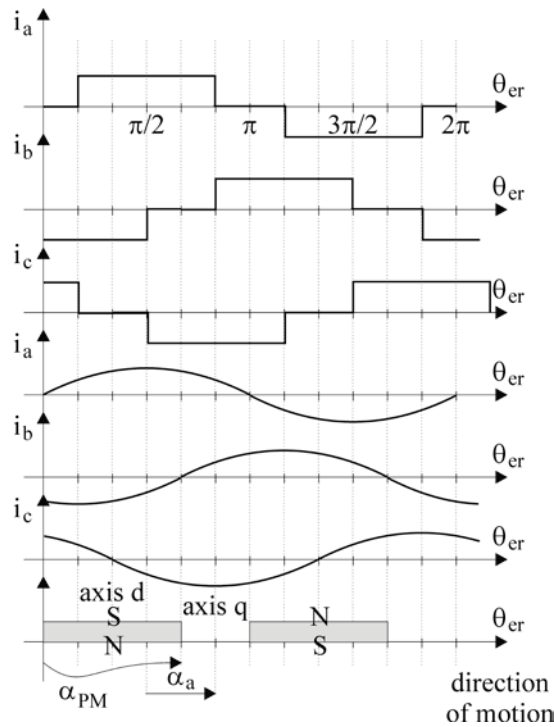


Fig. 1.1 Rectangular or sinusoidal current control [2]

### 1.2.1 Synchronous motor drives

Sinusoidal excited motors, known as synchronous motors or AC permanent magnet motors are fed with three phase sinusoidal waveforms (Fig. 1.1, the three bottom currents) and operate on the principle of a rotating magnetic field. All phase windings conduct current at a time [1].

The PM synchronous motor operates as a synchronous reluctance motor if the magnets are left out or demagnetized. This provides a measure of fault-tolerance in the event of partial or total demagnetization through abnormal operating conditions. In fig. 1.2, the typical topology for synchronous motors is shown.

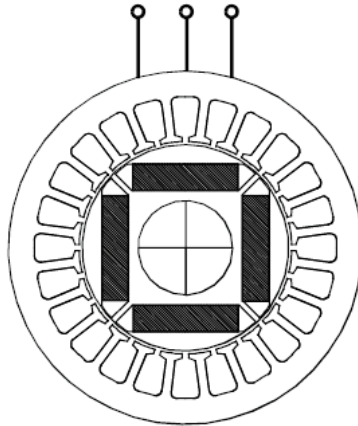


Fig. 1.2 Brushless PM AC (synchronous) motor with interior magnets [3]

In larger sizes, the brushless synchronous machine is sometimes built with a brushless exciter on the same shaft, feeding a rotating rectifier which passes DC to a field winding on the main rotor. This motor has full field control and it is capable of a high specific torque and high speeds [3].

In terms of sensorless control, the most popular and used techniques are scalar (V/f) control, vector control or direct torque and flux control (DTFC).

### 1.2.2 Permanent magnet DC brushless motor drives

Square wave motors are also fed with three phase waveforms shifted by  $120^\circ$  one from another, but these waveforms are not sinusoidal, but rather rectangular (trapezoidal). This particular type of current shape is due to precise synchronization between armature current (MMF) and rotor instantaneous position and speed. This time, only two out of three phase windings conduct current in the same time. This electronic commutation is equivalent to the mechanical commutation in DC motors, which explains the name of brushless DC motors [2].

In any drive that contains a brushless DC motor, the following elements are mandatory: solid state converter (rectifier (line-side converter), DC link and inverter), position sensor (typically Hall sensors but, where precision is required, an encoder or resolver is used), gate signal generator (to assure that proper switches are on and to avoid short circuit on any phase due to transition between upper and lower legs), current measurement (typically DC current through a shunt) and a controller that controls all the operations. In fig. 1.3, the basic topology for a brushless DC motor is shown [3].

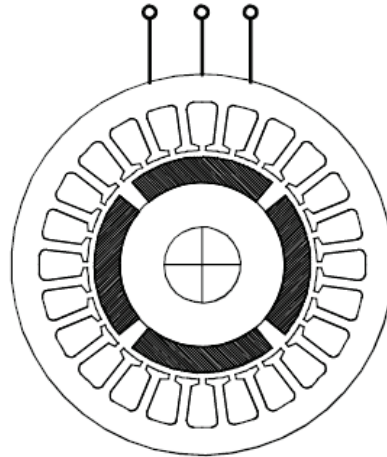


Fig. 1.3 Brushless PM DC (or AC) motor with surface magnets [3]

In terms of sensorless control, the most popular ones are back-EMF sensing technique, back-EMF integration technique, flux-linkage technique and freewheeling diode conduction technique.

Next, essential parts of any motor topology are presented and how they influence the final product is detailed.

### 1.3 Classification of permanent magnet electric motors

The most important component of a drive is the motor. The purpose of a drive is to deliver mechanical torque from electric energy and this is what a motor does. The other elements are used to ensure proper output torque by optimal control of the motor. As presented above, permanent magnet motors can be brushless AC (synchronous) machines (BLAC), brushless DC machines (BLDC) and special brushless machines.

**Brushless AC machines** are designed to have sinusoidal back-EMF waveform through windings placement and through sinusoidal currents feeding. One of the main advantages of this type of motors is the smooth shape of the output torque, which makes them suitable for use in servo systems. However, to obtain a very accurate position, speed and/or position sensors are used namely encoders or resolvers. Permanent magnets can be placed either on the surface, as in fig. 1.3, or mounted inside the rotor, as in fig. 1.2. In the later case, the placement of the magnets introduces saliency and a reluctance torque component.

**Brushless DC motors** are derived directly from the classical DC machine, the mechanical commutation provided by the slip rings being replaced with electronic commutation. If brushless AC motors are designed to provide a sinusoidal back-EMF, brushless DC motors provide trapezoidal back-EMF waveform, while they are fed with rectangular (slightly trapezoidal) current waveform. The current polarity is switched with the rotor position. The information is provided mainly by a combination of 3 Hall



sensors, which leads to a six-step operation scheme. However, this type of commutation introduces torque pulsations, which are undesirable in highly accurate systems. Even with this type of drawback, the advantage of low cost of the entire systems and reduced losses in the inverter makes them suitable for applications where efficiency and price are serious constraints.

**Special brushless motors** are not derived from classical AC or DC machines. This category covers a huge range of different designs [3].

Brushless AC and DC motors design are similar, because they have polyphase (usually three-phase) stator and magnets placed on/in the rotor in the same configurations. The essential differences are in control and shape of the excitation voltage, as presented above.

The following constructions of PM AC and DC brushless motors have been developed [1]:

- Motors with conventional slotted stators (fig. 1.4.a);
- Motors with slotless (surface-wound) stators (fig. 1.4.b);

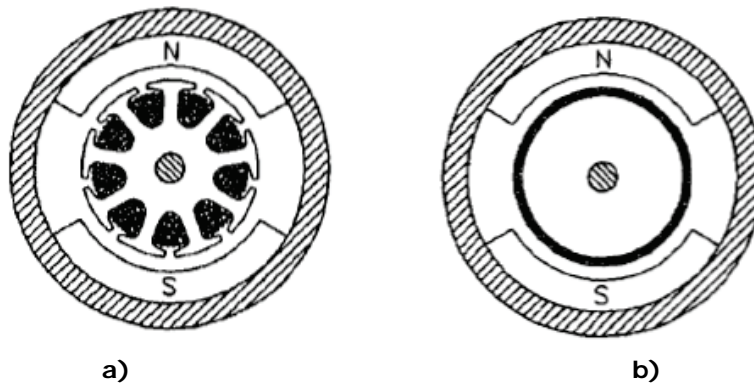


Fig. 1.4 Construction of PM AC and DC brushless motors with: a) slotted stator and b) slotless rotor [1]

- Cylindrical type (fig. 1.5):
  - Surface magnet rotor (uniform thickness PMs, bread loaf PMs)
  - Inset magnet rotor
  - Interior magnet rotor (single/double layer PMs)
  - Rotor with buried magnets symmetrically distributed
  - Rotor with buried magnets asymmetrically distributed
- Disk type [4]:
  - Single-sided
  - Double-sided
    - with internal rotor
    - with internal stator
  - Multi-stack

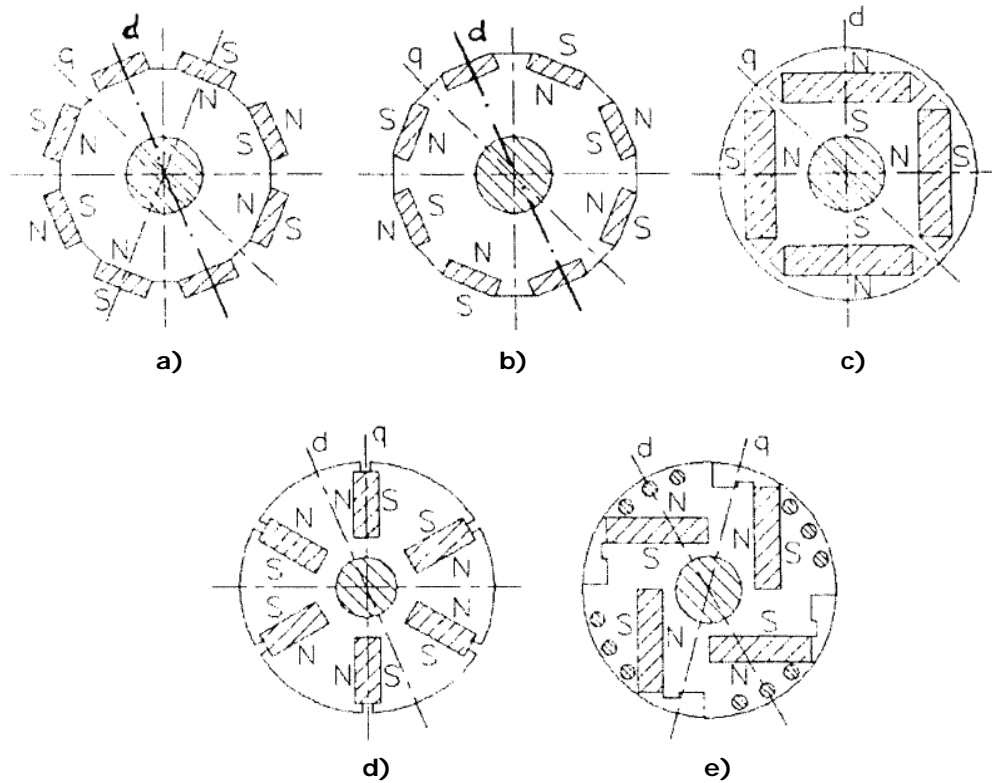


Fig.1.5 Rotor configurations for PM AC and DC motors: **a)** surface magnet; **b)** inset magnet; **c)** interior magnet; **d)** rotor with buried magnets symmetrically distributed and **e)** rotor with buried magnets asymmetrically distributed [1]

## 1.4 Permanent magnet materials and circuits

The shift of focus from induction machines towards permanent magnet machines is linked to the evolution of the permanent magnet materials and power electronics. The discovery of magnetic materials with high values of maximum energy product  $(BH)_{\max}$  made possible the reduction in size and increase in efficiency of magnets. In the following paragraphs, the main three classes of permanent magnets used today in motors are presented. But first, it is necessary to make an introduction about magnet characteristics.

Permanent magnets provide the motor with life-long excitation. Their cost is a fraction of the initial cost, which is why the choice of the adequate magnet is a design issue. The primary determinants of magnet cost are the torque per unit volume of the motor, the operating temperature range and the severity of the operational duty [3].

The first and most important thing that defines a magnet is the B-H (hysteresis) loop, which contains the demagnetization curve (fig. 1.6).

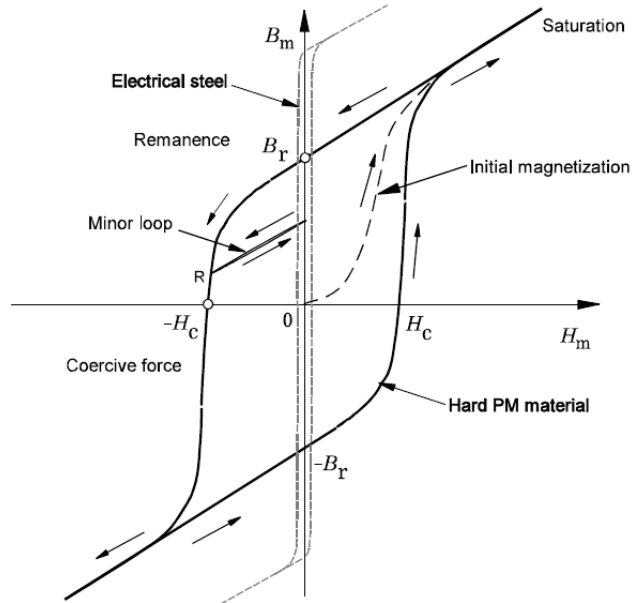


Fig.1.6 B-H loop a hard PM material with electrical steel shown for comparison [3]

Since the way an electrical machine with permanent magnets works requires a magnetic field strength to be applied through the coils will reduce the magnet's flux density, the second quadrant from the figure above is considered to be the most important. The demagnetization curve is essential because the magnets need not have an external excitation once they are magnetized, but magnetic field is generated in the coils, thus the operation of the machine and the magnets lies in the demagnetization domain [6].

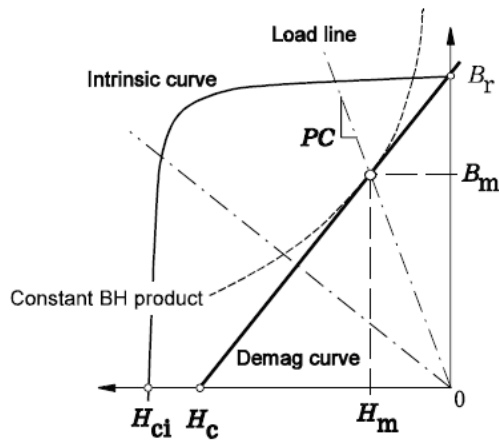


Fig.1.7 Second quadrant demagnetization characteristic showing intrinsic curve [3]

In the absence of externally applied ampere-turns, the magnet operates at the intersection of the demagnetization curve and the load line, whose slope is the product of  $\mu_0$  and the permeance coefficient (PC) of the external circuit. Since  $B_m$  and  $H_m$  both vary according to the external circuit permeance, it is natural to ask what it is about the magnet that is permanent. The relationship between  $B_m$  and  $H_m$  can be written:

$$B_m = \mu_0 \cdot H_m + J \quad (1.1)$$

The first term is the flux density that would exist if the magnet were removed and the magnetizing force remained at the value  $H_m$ . Therefore the second term can be regarded as the contribution of the magnet to the flux density within its own volume; accordingly,  $J$  is called the magnetization. If the demagnetization curve is straight, and if its relative slope  $\mu_{rec}=1$ , then  $J$  is constant. This is shown in figure above for negative values of  $H_m$  up to the coercivity  $-H_c$ . In most hard magnets  $\mu_{rec}$  is slightly higher than 1 and there is a slight decrease of  $J$  as the negative magnetizing force increases, but this is reversible down to the knee of the B-H loop. Evidently, the magnet can recover or recoil back to its original flux density as long as the magnetization is constant. The coercive force required to demagnetize the magnet permanently is called the intrinsic coercivity and this is shown as  $H_{ci}$  [5].

Besides magnetic remanent flux density and coercive force, another aspect of great concern is the demagnetization temperature. Exposure to high temperatures for long periods can produce metallurgical changes which may impair the ability of the material to be magnetized and may even render it nonmagnetic. There is also a temperature, called the Curie temperature, at which all magnetization is reduced to zero. After a magnet has been raised above the Curie temperature it can be re-magnetized to its prior condition provided that no metallurgical changes have taken place [5].

There are three types of magnetic materials used in permanent magnet motors, namely AlNiCo, ferrites and rare-earth.

**AlNiCo**, a short name for mixture of aluminum, nickel, cobalt and iron, was the first magnetic material to be used in PM d.c. commutator motors of disk type, from a few watts to 150 kW, between mid 40s and late 60s. The main advantages of AlNiCo are its high remanent flux density and low temperature coefficients, as seen in figure 1.8 and Table 1.1. These advantages allow a high air gap magnetic flux density at high magnetic temperature. The main drawback is the low coercive force and the demagnetization curve is extremely non-linear, making it not only easy to magnetize, but most importantly, easy to demagnetize.

**Ferrites**, especially barium and strontium ones were developed during the 50s to overcome the drawback of AlNiCos for fractional horsepower motors. Economically, ferrites are better than AlNiCo up to 7.5 kW. The main advantage for ferrites is the higher coercive force, but they have lower remanent flux density. Other advantages are their low cost and very high electric resistance (no eddy-current losses in the PMs). Since these magnets are feasible for low powers, their main applications are linked to automobile industry and electric toys.

**Rare-earth** permanent magnets were developed mainly in the last three decades, achieving higher energy density. Combined with the evolution of the power electronics, they made permanent magnet motors the most popular choice in terms of applications, being able to keep the pace with growing demands in terms of efficiency and price. The rare-earth elements are in general not rare at all, but their natural minerals are widely mixed compounds. To produce one particular rare-earth metal, several others, for which no commercial application exists, have to be refined. This limits the availability of these metals [1].

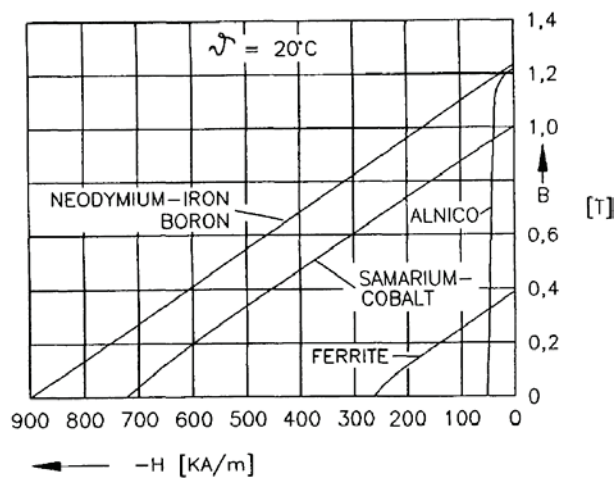


Fig.1.8 Demagnetization curves for different permanent magnet materials [1]

This type of magnets can be divided in two known generations. The first one was  $\text{SmCo}_5$ , which was developed during the early 70s. The second one is NdFeB (Neodymium – Iron - Boron), first developed in 1983 by Sumitomo Special Metals.

Samarium-cobalt alloy ( $\text{SmCo}_5$ ) has the advantage of high remanent flux density, high coercive force, high energy product, linear demagnetization curve and low temperature coefficient. It is well suited to build motors with low volume, high power density and class of insulation F or H [1]. However, the main drawback is the price of the components, making them suitable only for applications where the price is not an important issue.

On the other hand, NdFeB magnets have better magnetic properties than its predecessor, but only at room temperature. The demagnetization curves, especially the coercive force, are strongly temperature dependent. However, latest grades of NdFeB magnets have better thermal stability and higher remanent magnetic flux density. Another major drawback is the magnet's susceptibility to corrosion, but even this issue has been diminished lately, by introduction of metallic or resin coating to improve resistance to corrosion. Despite all that, NdFeB magnets have great potential for considerably improving the performance-to-cost ratio for many applications [1].

Below, a table with the most relevant information about every type of magnet described previously is shown.

**Table 1.1 Typical characteristics for magnets [1]**

Characteristic	Magnet type				Unit
	<i>AlNiCo</i>	<i>Ferrites</i>	<i>SmCo<sub>5</sub></i>	<i>NdFeB</i>	
Maximum energy product $(BH)_{max}$	39.8	30	170	295	$\text{kJ/m}^3$
Remanence	1210	395	925	1240	mT
Reverse temperature coefficients for $B_r$	0.02	-0.2	-0.042	-0.1	$\%/^{\circ}\text{K}$
Reverse temperature coefficients for $H_{cJ}$	-	0.3	-0.25	-0.6	$\%/^{\circ}\text{K}$
Coercivity $H_{cB}$	51.3	265	2000	920	kA/m
Coercivity $H_{cJ}$	51.7	275	1900	1900	kA/m
Density	7.4	4.85	8.3	7.6	$\text{g/cm}^3$
Maximum service temperature	550	250	250	160	$^{\circ}\text{C}$
Curie temperature	890	400	800	310	$^{\circ}\text{C}$

Until now, we could see why permanent magnet motors became so popular due to evolution of magnets. However, magnets alone cannot improve the overall efficiency, if other losses are not also reduced. For that, electrical steels with reduced losses have been developed. In figure 1.9, one can see d.c. B-H curve for two electrical steels and variation of losses versus frequency and flux density.

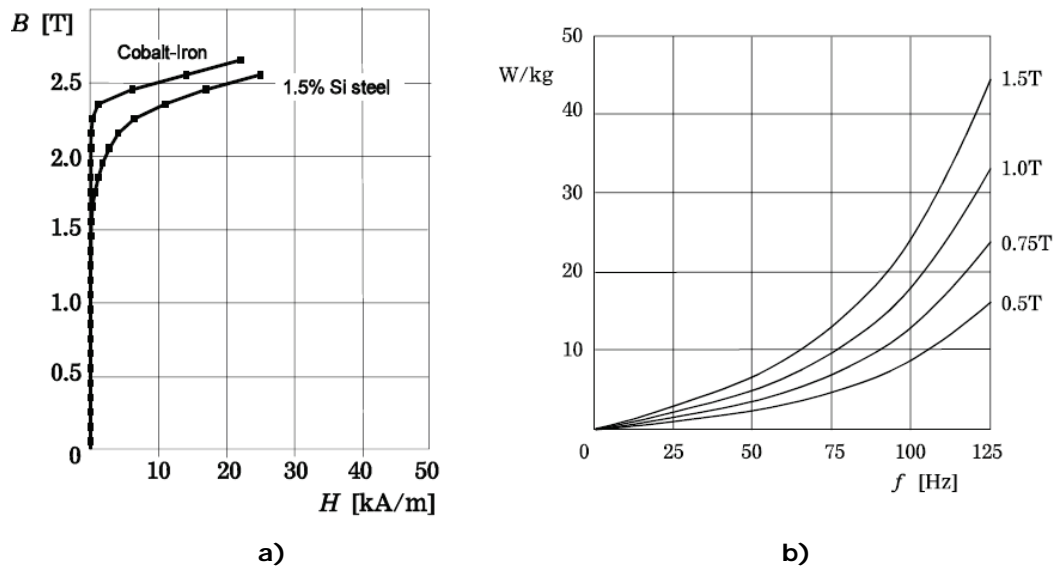


Fig.1.9 Electrical steels: a) d.c. B-H curve and b) typical form of variation of losses versus frequency and flux density [3]

The lower curve in the above figure is typical electrical motor steel having 1.5% silicon to increase the resistivity to limit eddy current losses. The saturation flux density of such steels is typically about 2.1 [T]. The upper curve is for a Cobalt-Iron alloy with a saturation flux density of about 2.3 [T]. This material is much more expensive than normal electrical steel, and is only used in special applications. The maximum permeability of electrical steels is of the order of  $5000 \mu_0$ , and usually occurs between 1 and 1.5 [T] [5].

Under a.c. conditions, a power loss appears, as can be seen in fig.1.9 b), which rises with the increase of frequency and flux density. This type of loss, as it occurs in steel, is generally known as iron losses and it is attributed to hysteresis, eddy currents or “anomalous loss”.

The hysteresis component is associated with the changing magnitude and direction of the domains, while the eddy current loss is generated by induced currents. Eddy currents can be inhibited by laminating the steel, so that the eddy currents become resistance limited and the loss is then inversely proportional to the resistivity. If the eddy currents are resistance-limited the loss is also proportional to  $1/t^2$ , where  $t$  is the lamination thickness. At higher frequencies the resistance limitation condition is lost, and the losses increase rapidly with frequency. For this reason, very thin laminations, as thin as 0.1 [mm], may be used at very high frequencies (such as 400 [Hz] in aircraft generators or 3000 [Hz] in certain specialty machines) [5].

The “anomalous loss” is associated with domain wall movement and it is not often accounted for in empirical expression of the iron loss.

## **1.5 Control techniques overview for PM motors with rectangular currents**

### **1.5.1 Brushless DC operating principle**

Up until now, the main details of PM machines were discussed. One can see how due to the evolution of materials and from market demands, the PM machines became more and more used in various applications. The purpose of this sub-chapter is to present how this kind of motors operate, with an emphasis on brushless dc motors.

Generally, the magnets are placed on the moving part, the rotor. However, depending on the application, the magnets are mounted on the rotor (surface PM), embedded (inset PMs) or inside the rotor (interior PMs). Furthermore, the shape of the magnets and the way PMs are magnetized determines the flux density waveform in the air gap. Here, only PM motors with surface magnets will be considered.

In sinusoidal surface magnet motors, the stator has a three-phase sinusoidal winding, which creates a synchronously rotating air gap flux. All phase windings conduct current at a time.

A trapezoidal surface permanent magnet (SPM) machine is a non-salient pole, surface mounted PM machine similar to a sinusoidal SPM machine except its three phase stator winding (normally Y-connected) has concentrated full-pitch distribution instead of sinusoidal winding distribution. As the machine rotates, most of the time the

flux linkage in a phase winding varies linearly, except when the magnet gap passes through the phase axis. An electronic inverter is required in the front end to establish a six-step current wave at the center of each half-cycle to develop torque. Since converter use is mandatory, it is often defined as an electronic motor. With the help of an inverter and an absolute position sensor mounted on the shaft, both sinusoidal and trapezoidal SPM machines can be controlled to have brushless dc motor performance [8].

A three-phase brushless dc motor is generally designed so that the flat top of the phase back-EMF waveform is just  $120^\circ$  wide. Then each phase is supplied with a current waveform consisting of blocks of constant current  $120^\circ$  wide. During each  $120^\circ$  period, the electromagnetic power conversion is  $e_a i_a = T_e \omega_m$ , where  $T_e$  is the electromagnetic torque. If the EMF and current waveforms are sufficiently flat during this period, and the speed is essentially constant,  $T_e$  is also constant [3, 9].

With three phases on all the time, sinusoidal PM motors develop rather smooth continuous torque. On the other hand, trapezoidal PM motors are driven with only two phases on at a time, leading to torque development in 6 blocks of  $60^\circ$  per electrical revolution, hence the term six-step drive.

In the figure below, one can notice the Y-connection of the motor to a three phase inverter, while in the next figure, back-EMF, current and torques for this configuration are shown.

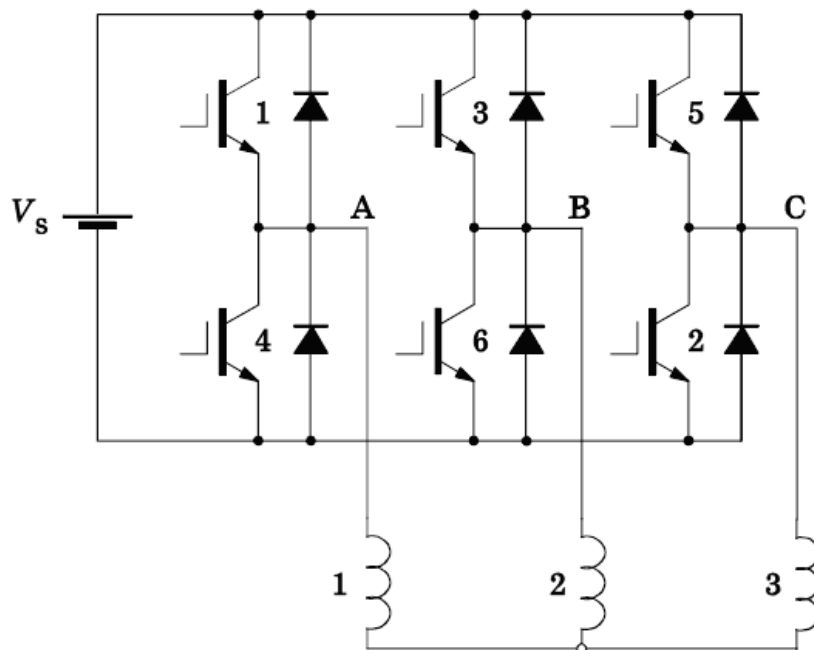


Fig. 1.10 Drive circuit for Y-connected brushless dc motor [3]



1.5 Control techniques overview for PM motors with rectangular currents 25

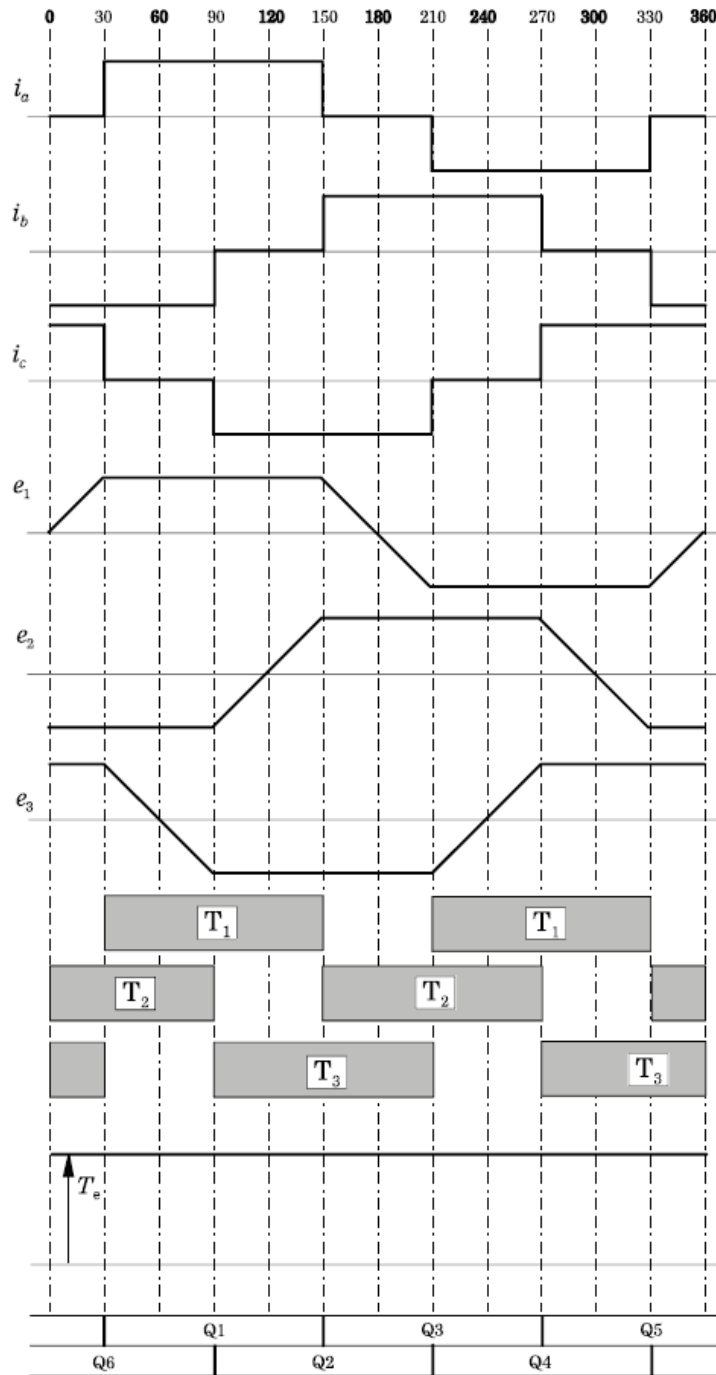


Fig.1.11 Ideal waveforms of phase currents, back-EMFs and torques and total torque in Y-connected brushless dc motor [3]

### 1.5.2 Control techniques for trapezoidal PM motors

The operation of a brushless permanent-magnet machine requires rotor-position information, which is used to control the frequency and phase angle of the machine's winding currents. An absolute position sensor is placed on the stator side at the edge of the rotor poles so as to generate 120° angle phase-shifted square waves. Sensor control is widely used due to its robustness and reliability, and for trapezoidal brushless dc machines, for its ease of implementation. Torque is produced in six blocks, and the maximum number of combinations for two phases on at one time is six, so we only need to determine when to commute from one combination of phases to another, thus only commutation points are needed. Sensors or sensorless methods developed for trapezoidal brushless dc motors focus on this.

Sinusoidal brushless PM motors need accurate position or speed sensors, like encoders or resolvers, which increase the total cost of the drive. Trapezoidal PM motors need only a combination of three Hall-effect sensors [10, 11] to determine the exact moment to switch phases. Their low cost and ease of implementation made them a popular choice for applications where cost is a serious issue. In the figures below, the typical placement of the sensors (fig.1.12) and commutation sequences for both motor rotation directions (fig.1.13) are shown.

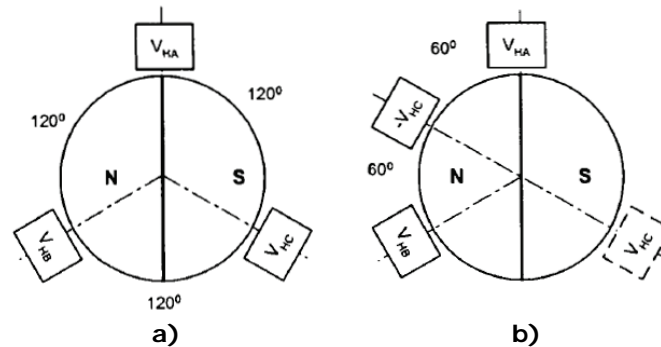


Fig.1.12 Hall sensor spacing for: a) 120° electrical and b) 60° electrical [1]

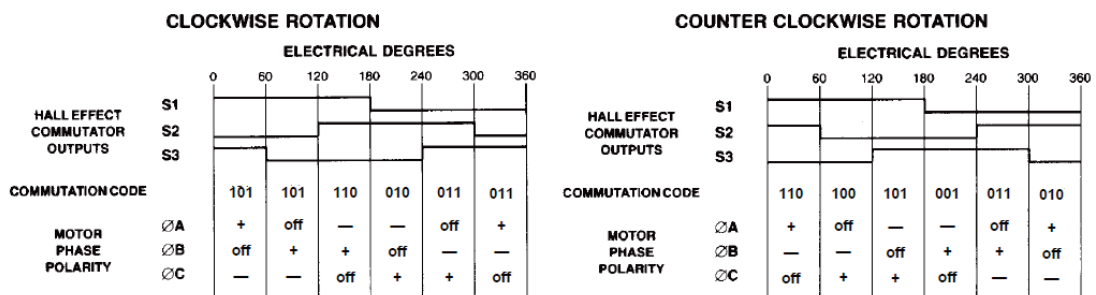


Fig. 1.13 Commutation sequences for clockwise and counter clockwise rotation directions for a brushless dc motor [36]

Simple control logic, robust and reliable motor start, and maximum motor torque are the main benefits of Hall sensor based systems. The additional wiring for the sensors, potential malfunction due to contamination, and general failures of the sensors themselves are the primary disadvantages. Besides these disadvantages, economical reasons for low power motors or compact applications led to researches in the field of sensorless control. After all, alternate ways to determine commutation points needed to be discovered.

Sensorless techniques for estimating rotor position from measurements of voltage and currents have been the subject of intensive research (fig.1.13). However, the key point was to develop robust sensorless strategies, not expensive than sensors and reliable in terms of information accuracy. The sensorless techniques can be classified in three categories: back-EMF, inductance and flux linkage.

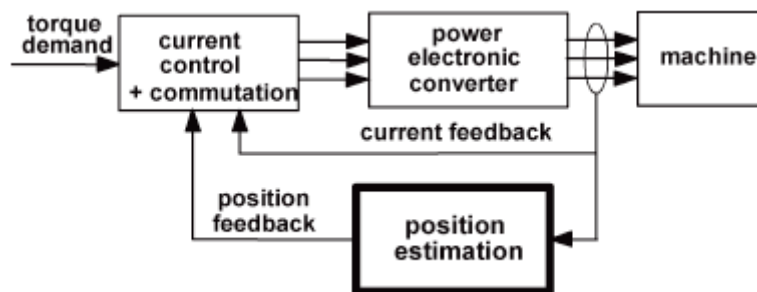


Fig.1.13 Position estimation from measurements of voltage and current in the machine supply [12]

The most popular sensorless technique, due to its ease of implementation and low cost regards back-EMF detection.

**Back-EMF zero crossing** can be implemented because in brushless PM machines, movements of the magnets relative to the armature windings cause a back-EMF to be induced [12 – 18]. Since the instantaneous magnitude of the EMF is a function of rotor position relative to the winding, information about position is contained in the EMF waveform. Switching instants of the converter can be obtained by knowing the zero-crossing of the back-EMF and a speed-dependent period of delay. The zero-crossing values of the back-EMF in each phase are an attractive feature to use for sensing, because they are independent of speed and because they occur at rotor positions where the phase winding is not excited. However, the EMF zero crossings do not correspond to those rotor positions where commutation between phases should take place. Therefore, the signals must be phase shifted by  $90^\circ$  electrical before they can be used for commutation. In practice, however, it is difficult to extract the information about EMF, because the machine windings are carrying rapidly changing currents and experience substantial induced voltages from phase switching. A further obstacle is that the back-EMF is proportional to rotor speed. When the machine is to operate from standstill, position sensing is possible only when a threshold speed is attained, so it is usual practice to make the initial acceleration under open-loop control

using a ramped-frequency signal, the parameters of which must be chosen to match drive and load parameters. Acceleration from rest at an arbitrary start position for the rotor is particularly problematic, as it is possible for the motor to run initially in the reverse direction, and so, some schemes involve auxiliary sensors or high-frequency excitation tests to establish the rotor position and define the appropriate initial winding excitation pattern [12]. For the starting problem, some solutions were suggested depending on the application. The most popular starting techniques are open-loop starting or “align and go” technique.

**Sensing from the third harmonic of back-EMF** was introduced in [19] to reduce the phase-shifting problem that appears in back-EMF zero crossing. This method is not as sensitive to phase delay as the first method, as the frequency to be filtered is three times as high. An additional star connection of three identical resistors is connected between the phase ends and a separate star point  $n$ . Assuming that the resistances and inductances of the three machine windings are identical and that the phase back-EMF are trapezoidal, it can be shown that the voltage between the two star points is equal to the mean of the three EMFs [12]. The summed terminal voltages contain only the third and multiples of the third harmonic due to the fact that only zero sequence current components can flow through the motor neutral. This voltage is dominated by the third harmonic, which does not necessitate much filtering. To obtain switching instants, the filtered voltage signal which provides the third harmonic voltage component is integrated to find the third harmonic flux linkage. The third harmonic flux linkage lags the third harmonic of the phase back-EMF voltages by  $30^\circ$ . Thus, the zero crossings of the third harmonic of the flux linkage correspond to the commutation instants of the BLDC motor [13].

Compared to the previous method, this technique has the following advantages: a reduced filtering requirement, because the integration (low-pass filtering) function is performed on a signal, which has a frequency three times that of the fundamental signal, which improves the dynamic performance and operation at high speeds is possible in principle, because  $v_{ns}$  can be recovered even if current continues to flow in the third (unexcited) phase [12].

**Freewheeling diode conduction** uses indirect sensing of the zero-crossing of the phase back-EMF to obtain the switching instants of the BLDC motor and relies on the fact that always one phase is open-circuited [20]. For a short period after opening the phase, there remains phase current flowing, via a freewheeling diode. This open phase current becomes zero in the middle of the commutation interval, which corresponds to the point where back-EMF of the open phase crosses zero. The biggest downfall of the method is the requirement of six additional isolated power supplies for the comparator circuitry for each freewheeling diode. The main advantage of this technique is that it works at lower speeds (45 [rpm] achieved), outperforming previously presented methods [13].

**Back-EMF integration** technique is based on extracting information by integrating the back-EMF of the unexcited phase [21, 22]. The integration is based on the absolute value of the open phase’s back-EMF. Integration of the back-EMF starts when the open phase’s back-EMF crosses zero. A threshold is set to stop the

integration which corresponds to a commutation instant. As the back-EMF is assumed to vary linearly from positive to negative (trapezoidal back-EMF assumed), and this linear slope is assumed speed insensitive, the threshold voltage is kept constant throughout the speed range. If desired, current advance can be implemented by changing the threshold. Once the integrated value reaches the threshold voltage, a reset signal is asserted to zero the integrator output. To prevent the integrator from starting to integrate again, the reset signal is kept on long enough to ensure that the integrator does not start until the residual current in the open phase has passed a zero crossing. This type of control algorithm has been implemented commercially. The integration approach is less sensitive to switching noise, automatically adjusts to speed changes, but the low speed operation is poor [13].

**Inductance variation sensing** is an alternative method of position sensing involves monitoring rates of change of winding current. Since the rate of current change depends on the inductance of the winding, and this inductance is a function of rotor position and winding current, then rotor position can be deduced from winding current and its rate of change [23, 24]. This scheme has the advantage of working at zero speed, where previous techniques do not work. On the other hands, it is a complicated method because in a machine with surface PMs, there is no inherent saliency, so any variation of winding inductance with rotor position arises only from magnetic saturation, the rate of change of current in the PM machine is dominated by the back-EMF and the variation of incremental inductance with rotor position undergoes two cycles per single electrical cycle of the PM machine, causing an ambiguity in sensed position. The first application of inductance method addresses the problem of starting, including identification of rotor position before full excitation is applied to the machine. Initial position identification is particularly important in applications such as traction, where any reverse motion caused by incorrect excitation is unacceptable. Exploratory voltage signals have been applied to the phase windings of a salient PM machine that was stationary. The resulting current amplitudes depended on the incremental inductance, and therefore the rotor position. However, the sensed position spanned a range of 180° electrical and there remained the problem of resolving the orientation of the rotor over the full 360° electrical range. The universally adopted solution to the issue of rotor orientation ambiguity is to consider the effect of magnetic saturation on the incremental inductance [12].

**Flux-linkage variation** method has been known for many years, but its successful implementation has become possible in the last decade with the emergence of devices with sufficient real-time processing power. The fundamental idea of flux-linkage position sensing is deceptively simple:

$$V_{ph} = R_{ph} \cdot i_{ph} + \frac{d\Psi}{dt} \quad \rightarrow \quad \Psi = \int (V_{ph} - R_{ph} \cdot i_{ph}) \cdot dt \quad (1.2)$$

This way, by subtracting the resistive voltage drop from the phase voltage and integrating, then a continuous estimate of the flux linkage can be produced. In most electrical machines, it is not practicable to measure the phase voltages directly,

because of isolation issues, and instead, the applied phase voltage is estimated from knowledge of the solid-state converter dc supply voltage and demands being input to the voltage controller. Flux estimation can be realized with a mechanical model and without a mechanical model.

Flux estimation with a mechanical model is based on the fact that flux linkages with each phase arise from the permanent magnet itself and the currents flowing in the machine windings. Flux linkage and current can be used to calculate torque, and the torque data are input to a mechanical model. Estimates of rotor speed and position are produced. To close the estimation loop, the estimated values of position and phase flux linkages are used to estimate the phase currents, which are compared to the measured currents to generate an estimation error. This error is fed back into the initial flux-linkage estimator, where it counteracts the tendency to drift caused by offsets in the measurements.

Flux estimation without a mechanical model is needed because closed-loop observers that include a model of the mechanical dynamics are prone to errors caused by incorrect specification or variability of the mechanical parameters. To overcome this drawback, analog integrators are used for flux-linkage calculation. Integrator drift was counteracted by calculation of an offset signal, which insures that the average flux linkage with each phase is zero when the machine operates at steady-state speed and torque. This approach is an effective low-cost solution, but does not allow the machine to self-start and is unable to deal with fast changes in speed or torque [12]. Below, the sensorless techniques are summarized in Table 1.2.

**Table 1.2 Sensorless techniques summary with functional speed range**

Sensorless technique	Starting method	Speed range [rpm]
Back-EMF zero crossing	<ul style="list-style-type: none"> <li>- Open-loop;</li> <li>- Known initial position;</li> <li>- Machine interrogation and signal processing;</li> <li>- Computationally complex methods;</li> </ul>	1000 – 6000
Back-EMF 3 <sup>rd</sup> harmonic		100 – 6000
Back-EMF integration		1000 – 3600
Freewheeling diode conduction		45 – 2300
Inductance variation	None	0 – high speeds
Flux-linkage variation	<ul style="list-style-type: none"> <li>- Hall sensors;</li> <li>- Open-loop;</li> </ul>	100 – high speeds

## 1.6 Applications

The brushless dc (BLDC) motors started to be used more and more frequently in a large variety of applications, either to replace other types of motors, less efficient, or to work in a hybrid configuration, alongside mechanical or hydraulic parts. For engineers, the usage of BLDC motors translates into an increase of torque per volume and higher efficiency, while for the consumers it means lower costs per consumed energy and more environmental friendly devices.

From the variety of categories where BLDC motors are used, in this subchapter a few dominant examples will be presented, as automotive parts [1, 25], recreational electronic devices [1, 26], aerospace tools and home appliances [27 – 34].

The field of **automotive** applications spans a broad range from active steering, power steering, electromechanical brakes, clutch and shift actuators, suspension, damping and stabilization actuators, heating, ventilation and air conditioning (HVAC) up to starter-generators and traction, including x-by-wire (e.g. steer-by-wire, brake-by-wire) [25].

**Table 1.3 Electric drives automotive applications [25]**

	$T_{peak}$ [Nm]	$n_{base}$ [rpm]	$n_{max}$ [rpm]	Motor technology
Active steering	< 1	3000	6000	DC, IM, PMSM
Power steering	3 ... 10	500	2000	DC, IM, PMSM
Clutch/shift	< 2	3000	6000	DC, PMSM
Braking	1 ... 3	1000	3000	DC, PMSM
HVAC	< 2.5	15000	17000	DC, PMSM
Starter/generator	< 300	250	6000	IM, PMSM
Traction	40 ... 180	3000	9000	IM, PMSM

Induction motors, switched reluctance motors and PM brushless motors are candidates as propulsion motors for electrical vehicles. Simulations indicate that a 15% longer driving range is possible for an electric vehicle with PM brushless motor drive systems compared with induction types [1].

The usage of PM motors in automotive industry increased with the trend to introduce a lot of decentralized electric drive systems in the vehicles. The main motivation aspects are enhancement of the vehicle performance and driving comfort, rise of the safety on the road, improvement of the fuel economy and reduction of the emissions. The advances in electric motor technology for automotive applications are resulting from advances in permanent magnet materials, power electronics and motor control [25].

**Variable speed fans** (fig.1.14.a)) were introduced because instruments require some sort of forced air cooling, in addition to the traditional line voltage operated ac motor fans [26]. Running the fan from a low voltage dc source, usually 12 or 24 [V] makes it easy to control the fan speed electronically, in response to the actual temperature inside the instrument. A variable speed drive with temperature sensor can suppress the noise since under most conditions the fan noise is far less than that at full speed condition (between 25 and 40 [dB]) which is needed only when operating an instrument at its maximum ambient temperature. The rated power of fan brushless motors is in the range from 0.6 to 180 [W] and maximum speed can vary from 2000 to 6000 [rpm].

The data storage capacity of a **hard disk drive** (HDD) (fig.1.14.b)) is determined by the aerial recording density and number of disks. The aerial density is

now at the level of 51 [Gbit/cm<sup>2</sup>]. Mass of the rotor, moment of inertia and vibration increase with the number of disks. The need for large storage capacity and increased data access performance of modern disk drive technology over the past two decades has meant the continuous development of small spindle motors. Disk drive spindle motors are BLDC motors with outer rotor designs. The outer rotor design is used to increase the inertia and thus reduce torque pulsations during operation. The operation of these motors is identical to inner rotor BLDC motors, using power electronics and rotor position feedback. Special design features of spindle motors are their high starting torque (10 to 20 times the running torque), limited current supply (less than 2 [A]), reduced vibration and noise (below 30[dB(A)]), physical constraints on volume and shape, contamination and scaling problems [1, 27].

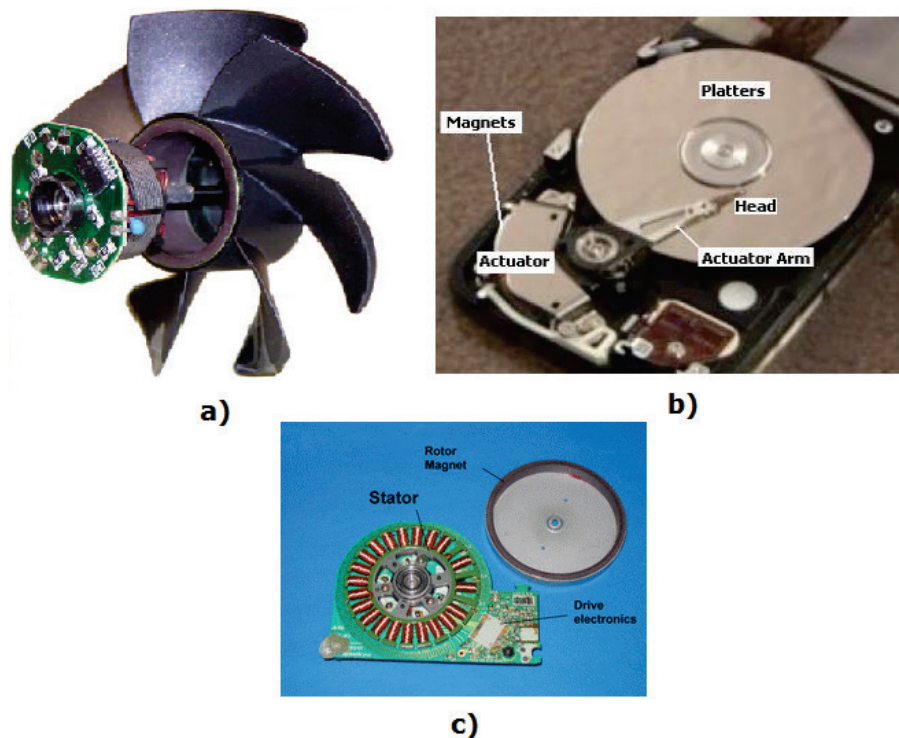


Fig.1.14 BLDC motor configurations for: a) variable-speed fans [26], b) hard disk drives [1] and c) CD player [1]

**CD players and CD-ROMs** (fig.1.14.c)) are other applications of spindle motors. Information on a compact disk (CD) is recorded at a constant linear velocity. Miniature PM motors are used for spindle rotation, drawer/tray opening/closing, pickup position (coarse tracking) and disk changing (disk changers only). The most common causes of CD motor failures are open or shorted windings, dry/worn bearings and partial short caused by dirt or carbon buildup on commutator (in the case of dc commutator motors) [1].



**Space mission tools** are used in space stations and space shuttles for rechargeable hand tools, due to limitations in power availability. PM brushless motors are the best motors for space mission tools. The high technology power ratchet tool and pistol grip driven by PM brushless motors were used in a servicing mission in 1993 to conduct planned maintenance on the Hubble Space Telescope [1].

The applications presented above are just a small part of the variety of BLDC drives used nowadays. The criteria of choosing these applications were their actuality and their coverage of the area of interest for people today – transportation, computers, entertainment and space conquest. However, the most developing industry regards home appliances. In a short period of time, the requirements for energy consumption become more and more drastic, to balance the increasing demand of household appliances.

For some years now, refined sensing and controls have been raising the IQ of household appliances. The challenge is to improve the control technology while adhering to cost constraints. Because of consumer and marketplace pressures, domestic appliances are among the price-sensitive electromechanical systems mass-manufactured today. Even fractions of dollars of added cost when multiplied by millions of units makes a huge difference to the bottom line of manufacturers [28].

A smart appliance is one that incorporates novel sensing and control algorithms so as either to automate some manual function, to economize on energy use, or to introduce something completely new. The incentives to smarten up domestic appliances are several: energy efficiency, environmental protection and the availability of enabling technology. Together, these factors have bred a distinct evolution in the control technology of household appliances, which have moved from open-loop electromechanical controls, to electronic controls plus simple sensing, and to closed-loop systems in which sensors are integrated with controls.

Refrigerators have been a ripe area for the introduction of new sensors and controls. The key opportunities for smarter controls have been in the areas of improved compartment temperature and better defrost control. The units keep food cool by means of a refrigeration cycle, in which a fluid material (the refrigerant) passes cyclically through some components (the main ones are the compressor, condenser, throttle and evaporator) or actuators. Temperature control must ensure the same temperature in the freezer (approximately  $-15^{\circ}\text{C}$ ) and in the fresh food compartment (around  $5^{\circ}\text{C}$ ), especially with the doors opening and closing, which rise the overall temperature by several degrees.

To cope with all that, one solution was to replace the induction motors inside compressors with low power, low cost, high efficiency PM BLDC motors. Besides the obvious advantages of PM motors, other aspect has been considered: working at high speeds.

However, some challenges appear when rotating at high speeds, and these challenges are taken into account from the design phase [30 – 33, 35]. Usually, speed limits are thermal (the higher the speed, the higher the temperature for the magnet, the higher the risk of demagnetization), elastic (there is a certain stress limit to impose to the rotor) and rotordynamical (resonant and self-excited vibrations). The limit that is

common to all machines is the thermal limit. The air gap flux density of PM machines is determined predominantly by the quality of utilized PMs and does not depend on the size of the machine, making them suitable for low volume applications. The maximum tangential speed of the rotor can be determined at which wither the maximum permissible stress is reached in one of the cylinders or the contact at the boundary surface(s) is lost. The working speed must be sufficiently remote from the resonant speeds and below the threshold of instability.

High-speed centrifugal turbo-compressors, compared to the conventional compressors, have numerous qualities such as simple structure, light weight, small size, and high efficiency. In order to achieve high power levels, high-speed permanent magnet machine designs typically use magnets with high energy products, such as NdFeB, SmCo<sub>5</sub>.

The technical issues related to integrating a brushless motor drive into a compressor are considerable due to the harsh environment that the electronic components would be exposed to inside the compressor. The motor can survive this environment more easily, which is why a semi-integrated configuration with the PM motor inside the compressor housing and the electronics on the outside was chosen.

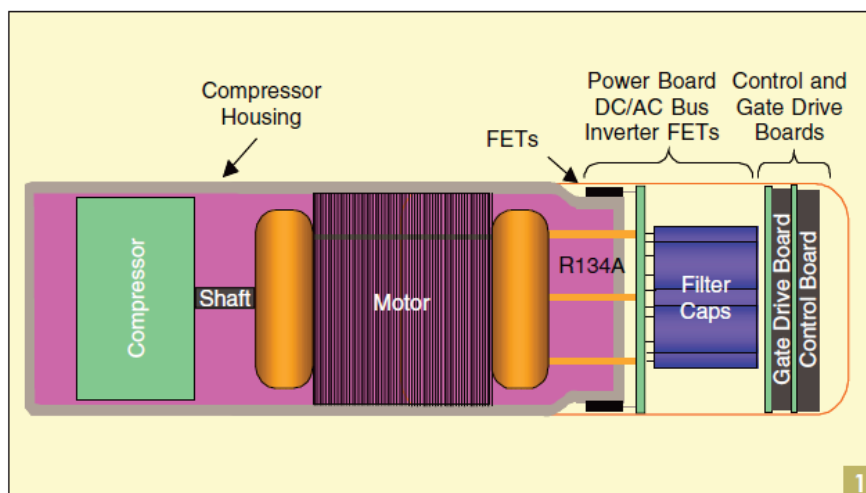


Fig. 1.15 Semi-integrated packaging configuration for the compressor drive [34]

The advantage of electrically driven HVAC compressors (fig.1.15) include: efficient operation as the compressor speed is independent of engine speed unlike conventional belt driven units; improved packaging as the location is not restricted to the accessory drive side of the engine; elimination of the rotating seals reduces the leakage of the refrigerant into atmosphere.

A significant cost incurs for any electrical connections between the inside and outside of the compressor housing due to the requirement of a hermetic seal. For this reason, a sensorless approach is sought that minimizes these connections beyond the

three motor phase leads. Key issues involved in the controller design include compressor starting, tuning of the sensorless controller and speed control loop, minimizing dc bus ripple current, and designing the layout of various components in order to have low electromagnetic interference [34].

Design issues for a high speed BLDC motor for a high speed compressor will be treated in the following chapter, while sensor and sensorless control issues will be treated later on.

## 1.7 Conclusions

This chapter's mission was to introduce the reader in the field of brushless PM motors. While not new, the original approach of BLDC motors starting with a general view and ending with a close-up on household appliances is meant to accustom the reader with the structure of this work.

The advantages of PM motors over other categories, especially over induction motors, are highlighted to emphasize their popularity and the wide spread of their use in the latest drives.

A brief history of magnetic materials gives us the reason why this type of motors started to gain interest only in the later decades, overcoming induction motors in low to medium power range. However, only the evolution of magnets could not help that much, without the developments of power electronic devices and control techniques.

Since the fields mentioned above reached their peaks and only small steps are taken, the area of interest shifted to commutation techniques, in order to eliminate the usage of position sensors and development of reliable, robust and easy-to-implement sensorless methods.

## References

- [1] Jacek F. Gieras, "Permanent Magnet Motor Technology – Design and Applications", book, 3<sup>rd</sup> edition, CRC Press, Taylor & Francis Group LLC, Boca Raton, Florida, 2010
- [2] Ion Boldea and Syed A. Nassar, "Electric Drives", book, 2<sup>nd</sup> edition, CRC Press, Taylor & Francis Group LLC, Boca Raton, Florida, 2005
- [3] T.J.E. Miller, "SPEED's electric motors – An outline of some of the theory in the SPEED software for electric machine design with problems and solutions", book, University of Glasgow, 2002
- [4] Sunil Kumar Challa, "Comparative study of axial flux permanent magnet brushless DC motor operating with the winding connected in single-phase and two-phase system", Master thesis, Louisiana State University, August 2006
- [5] T.J.E. Miller, "SPEED Summer School in Electric Machine Design", classbook, University of Glasgow, 2006
- [6] Ramu Krishnan, "Permanent Magnet Synchronous and Brushless DC Motor Drives", book, CRC Press, Taylor & Francis Group LLC, Boca Raton, Florida, 2010

- [7] Ion Boldea and Lucian Tutelea, "Electric Machines – Steady State, Transients and Design with MATLAB®", book, CRC Press, Taylor & Francis Group LLC, Boca Raton, Florida, 2010
- [8] Bimal K. Bose, "Modern Power Electronics and AC Drives", book, Prentice Hall PTR, Prentice Hall Inc., Upper Saddle River, New Jersey, 2002
- [9] Ali Emadi et al., "A Novel, Low-Cost, High-Performance Single-Phase Adjustable-Speed Motor Using PM Brush-Less DC Machine", Final Project Report, Illinois Institute of Technology, March 2003
- [10] Bilal Akin and Manish Bhardwaj, "Trapezoidal Control of BLDC Motors Using Hall Effect Sensors", Application Note, Texas Instruments, Ver. 1.0, February 2010
- [11] N. Samoylenko, Q. Han and J. Jatskevich, "Dynamic Performance of Brushless DC Motors with Unbalanced Hall Sensors", *IEEE Trans. on En. Conversion*, vol.23, no.3, pp. 752–763, September 2008
- [12] Paul P. Acarnley and John F. Watson, "Review of Position-Sensorless Operation of Brushless Permanent-Magnet Machines", *IEEE Trans. on Ind. Electronics*, vol.53, no.2, pp.352–362, April 2006
- [13] J.P. Johnson, M. Ehsani and Y. Güzelgünler, "Review of Sensorless Methods for Brushless DC", *Conf. Rec. of the 1999 IEEE 34<sup>th</sup> IAS Annual Meeting*, vol.1, pp. 143–150, October 1999
- [14] J. Shao, D. Nolan and T. Hopkins, "A novel direct back EMF detection for sensorless brushless DC (BLDC) motor drive", *17<sup>th</sup> Annual IEEE APEC 2002*, vol.1, pp. 33–37, March 2002
- [15] J. Shao, D. Nolan and T. Hopkins, "Improved direct back EMF detection for sensorless brushless DC (BLDC) motor drive", *18<sup>th</sup> Annual IEEE APEC 2003*, vol.1, pp. 300–305, February 2003
- [16] Yen-Shin Lai and Yong-Kai Lin, "Back-EMF Detection Technique of Brushless DC Motor Drives for Wide Range Control", *32<sup>nd</sup> Annual Conf. on IEEE Ind. Electronics (IECON) 2006*, pp.1006–1011, November 2006
- [17] Yen-Shin Lai and Yong-Kai Lin, "Novel Back-EMF Detection Technique of Brushless DC Motor Drives for Wide Range Control Without Using Current and Position Sensors", *IEEE Trans. on Power Electronics*, vol.23, no.2, pp.934–940, March 2008
- [18] Heidi Barriage, "Advances in Sensorless Control of BLDC Motors", *E-Drive Magazine*, April 2005
- [19] Julio C. Moreira, "Indirect sensing for rotor flux position of permanent magnet AC motors operating over a wide speed range", *IEEE Trans. on Ind. Appl.*, vol.32, no.6, pp.1394–1401, November/December 1996
- [20] Satoshi Ogasawara and Hirofumi Akagi, "An approach to position sensorless drive for brushless dc motors", *IEEE Trans. on Ind. Appl.*, vol.27, no.5, pp.928–933, September/October 1991
- [21] R.C. Becerra, T.M. Jahns and M. Ehsani, "Four-Quadrant sensorless brushless ECM drive", *6<sup>th</sup> Annual IEEE APEC 1991*, pp.202–209, March 1991
- [22] T.M. Jahns, R.C. Becerra and M. Ehsani, "Integrated current regulation for a brushless ECM drive", *IEEE Trans. on Power Electronics*, vol.6, no.1, pp.118–126, January 1991

- [23] Ashok B. Kulkarni and Mehrdad Ehsani, "A novel position sensor elimination technique for the interior permanent-magnet synchronous motor drive", *IEEE Trans. on Ind. Appl.*, vol.28, no.1, pp.144–150, January/February 1992
- [24] Toshihiko Noguchi and Satoshi Kohno, "Mechanical-sensorless permanent-magnet motor drive using relative phase information of harmonic currents caused by frequency-modulated three-phase PWM carriers", *IEEE Trans. on Ind. Appl.*, vol.39, no.4, pp.1085–1092, July/August 2003
- [25] Dorin Iles-Klumpner, "Automotive permanent magnet brushless actuation technologies", PhD Thesis, Ed. UPT, Timișoara, May 2005
- [26] Vincent Ko, "Variable speed DC fan control using the MC9RS08KA2", Designer Reference Manual, Rev.0, Freescale Semiconductor Inc., Hong Kong, May 2006
- [27] Gunhee Jang and M.G. Kim, "A bipolar-starting and unipolar-running method to drive a hard disk drive spindle motor at high speed with large starting torque", *IEEE Trans. on Magn.*, vol.41, no.2, pp.750–755, February 2005
- [28] Vivek V. Badami and Nicolas W. Chbat, "Home appliances get smart", *IEEE Spectrum*, pp.36–43, August 1998
- [29] T.P. Bohn et al., "A low cost 500 Watt motor and drive for HVAC applications: UW-Madison's design for the future energy challenge", *Proc. of 35<sup>th</sup> Annual IEEE Power Electronics Specialists Conference (PESC) 2004*, vol.1, pp.376–382, June 2004
- [30] A. Borisavljevic, H. Polinder and J.A. Ferreira, "On the speed limits of permanent-magnet machines", *IEEE Trans. on Ind. Electronics*, vol.57, no.1, pp. 220–227, January 2010
- [31] N. Bianchi, S. Bolognani and F. Luise, "Potentials and limits of high-speed PM motors", *IEEE Trans. on Ind. Appl.*, vol.40, no.6, pp. 1570–1578, November/December 2004
- [32] N. Bianchi, S. Bolognani and F. Luise, "Analysis and design of a PM brushless motor for high-speed operations", *IEEE Trans. on En. Conv.*, vol.20, no.3, pp. 629–637, September 2005
- [33] Z.Q. Zhu, K. Ng and D. Howe, "Design and analysis of high-speed brushless permanent-magnet motors", *Proc. of 8<sup>th</sup> Intl. Conf. on Electrical Machines and Drives (EMD) 1997*, pp. 381–385, September 1997
- [34] Malakondaiah Naidu et al., "Keeping cool while saving space and money. A semi-integrated, sensorless PM brushless drive for a 42-V automotive HVAC compressor", *IEEE Ind. Appl. Magazine*, pp.20–28, July/August 2005
- [35] Seok-Myeong Jang et al., "Development of high-speed brushless DC motor for turbo-compressor", *Proc. of the 8<sup>th</sup> Intl. Conf. on Electrical Machines and Systems (ICEMS) 2005*, vol.2, pp.877–882, September 2005
- [36] -, "Introduction to Hurst brushless DC motors", datasheet

## Chapter 2

# Hybrid FEM/Analytical Optimization Design of a Surface Permanent Magnet Synchronous Machine

### Abstract

This chapter is focused on optimization design of a synchronous machine with surface permanent magnet rotor for compressor load application. An overview of the existing optimization techniques compared to the pure analytical design is presented. One step further, the analytical part of the optimization design is intertwined with finite element analysis (FEA), to obtain accurate values of the cogging and average torque, which will be used as components of the penalty function.

After the theoretical walkthrough, optimal design of a brushless DC (BLDC) motor with surface permanent magnets, used in home appliances, will be performed with two different techniques. A comparison of the resulting dimensions, motor performances and total computation time is presented at the end of the chapter.

### 2.1 Introduction

Electric and electronic devices are a part of everyday life of each individual. They long surpassed the period where they were identified as comfort enhancers and nowadays these devices become utilities. Every household in the world has at least one piece of home appliance, thus pushing the manufacturers to compete in winning the largest share of the market and offer new and improved products. However, this is not an easy task. Due to the invasion of electronic equipments and gadgets that make everyone's life easier, in order to win clients is important to keep the price as low as possible.

From client's point of view, the devices must be affordable, efficient and to consume less electric energy. Of course, the client is very exigent and he wants the best, but the manufacturers must meet him in the middle. This is the reason why the key concepts of the industry are low cost and high efficiency. Since the most expensive part in a home appliance is related to the drive, electric motor and especially electronic control, the job for the research engineers is to develop cheaper and efficient drives.

Usually, the electric power of the home appliances varies from watts to a few kilowatts. In this field, induction motors and reluctance synchronous machines were used extensively in the past. However, the PM excited motors started to replace these

conventional electrically excited machines because of their obvious superiority. The advantages brought by magnet excitation as compared to electromagnetic excitation are higher power and torque density, better dynamic performance, simplification of construction and maintenance, low noise and elimination of copper losses in the rotor, due to the absence of excitation windings, which leads to a serious increase in the efficiency [1, 2]. But as it turned out, all these advantages came with a price, not only metaphorically speaking, and that was the cost of the magnets. Adding other disadvantages, like demagnetization at high temperatures and increased effort to integrate the magnets in/on the rotor, this solution brought with itself other issues to be solved.

The electromagnetic interaction between the stator field, as a product of currents circulating in the windings, and the rotor field excited by permanent magnets produces the desired output torque. Byproducts of this interaction are the iron losses in the stator frame and in the rotor and copper losses in the stator windings. Together with the inherent mechanical losses, these components affect the overall efficiency of the motor. Since the power electronics have higher efficiency than the motor itself, the important part in designing a drive for home appliances should focus on the motor.

In terms of costs, the most expensive parts of the drive are the power electronics and the control. Since there is almost no flexibility in optimizing the price of these components, the motor cost is the only one that can be reduced through careful designing, proper material choice and by employing the right topology for the application.

The base of the design is the analytical model of the motor. An extensive analytical model is given in [3 - 6], considering the prediction of the instantaneous magnetic field distribution in the air gap region of BLDC, taking into account the shape of the current waveform and the influence of stator slot openings, the effect of the armature reaction field produced by the 3-phase stator windings, the stator slotting effect and the effect of the load changes on the magnetic field distribution. Furthermore, the complexity of the model increases if all phenomena are to be considered, like operational speed [7, 8], stator lamination [9], slotting effect [10, 11] or geometrical asymmetries due to faulty construction [12].

Although design is based on analytical model, finding the optimal configuration is not an easy task. Depending on technical constraints, type of application and knowledge of the field, an experienced designer can find the right topology after several runs, which takes time, even with the aid of modern fast computer processors.

With clear objectives and strictly defined constraints, optimization algorithms can be introduced to reduce the search time of the best solution. Optimization methods try to find the maximum or minimum of a function, where there may exist restrictions or constraints on the independent variables. Finding the maximum or minimum of a function which is also the global maximum or minimum of a function has considerable difficulty and is the complex part of any optimization method. In engineering, it is generally considered practical to search only for local solutions [1].

A new idea of optimization combines analytical model with finite element analysis (FEA), to replace complex analytical equations of back EMF, inductances, flux

linkages or torque ripples [15] or to calculate the average torque and cogging torque [16] as penalties for the objective function. The ascending trend of optimization in motor design is visible in different types of algorithms used over time, like modified Hooke-Jeeves [16 – 20], genetic algorithms (GA) [20 – 24], simulated annealing [20], population based incremental learning (PBIL) [25 – 27], evolution strategies [28, 29] or particle swarm optimization (PSO) [30 – 32].

In this chapter, a trapezoidal-driven PMSM, known as brushless DC (BLDC) motor will be designed for a compressor application. The requirements, constraints, reason for choosing a certain topology and design steps will be addressed in the following subchapter. Two hybrid analytical/FEM optimization techniques are experimented, and a comparison between them based on computational effort, precision of the optimization results and ease of implementation is realized. In the final part of the chapter, optimization results are presented, both numerically and graphical.

## **2.2 Design theme**

### **2.2.1 Motivation**

One of the major points of interest these days is to find ways to reduce energy consumption and to reduce gas emissions into the atmosphere, in order to stabilize the greenhouse gas at a level that would prevent dangerous anthropogenic interference with the climate system, as stated by the Kyoto Protocol.

The use of green energy is the subject of many studies and projects and it is now in a period of transition from the status of idea to certain implementation. That is why most of the developed countries in the world are updating their legislation to impose levels of energy use in each field, from industry to buildings and transportation. Of course, the transition will take years, but the point is to find a compromise between the increasing influence of technological devices in our life and the impact of these technologies on the natural environment.

As part of the Kyoto protocol, European Union (EU) has started since the early years of this century to modify its legislation with mid and long term goals on energy saving. Spanning over several fields that use intensively energy, from automotive to buildings, household appliances and transportation, EU pinned clear targets for energy saving all over member countries up to 2020. Since the actuality of this topic is at its peak, motor design is realized for a brushless DC motor used in compressors for refrigeration units and will take into account both the economical impact on manufacturer and client and technological efficiency requirements.

Used in transportation and preservation of perishable goods, refrigeration systems are one of the biggest consumers of electrical energy. For the countries members of EU, application of the eco-design requirements for household refrigerating appliances could amount to annual electricity savings of 6 TWh by 2020, compared to the situation if no measures were taken, as stated in paragraph 5 of the Commission Delegated Regulation (EU) no. 1060/2010.



The second player and the most affected one by these efficiency requirements is the manufacturer. As it turns out, the manufacturers encourage energy savings and also are willing to be implicated in consumer's education regarding the responsible use of any home appliance, as can be seen from CECED's report on energy consumption of domestic appliances in European households [33].

An extensive market study all over European countries regarding "cold appliances", namely refrigerators and freezers, covering current legislation, targets, economical aspects and environmental impact [34 – 37] concluded, among others, that consumers are more concerned about energy savings, mostly for financial reasons, than other aspects regarding domestic appliances.

As the premises are set, the need for energy efficient domestic appliances is a topic for present and future times. One of the largest energy consuming devices in every household is the refrigerator, which makes it prone to improvements in terms of efficiency. While other components of it remain unchanged, like the refrigerant or the way it circulates, the compressor can be improved even more. This is the reason why motor design for compressors is so important and optimization algorithm, as a part of designing process, is mandatory, in order to obtain the best results in terms of efficiency and cost.

### 2.2.2 Choosing the right motor

There are three classical types of compressor that are used in refrigeration systems, namely reciprocating, rotary screw and rotary centrifugal. At the beginning of this century, LG introduced the linear compressor, based on linear motion, and it's now a serious competitor for the classical types that use rotational motion.

The design is realized for a reciprocating compressor for low power. Although induction, PM synchronous, reluctance synchronous and switched reluctance motors are competitors for this type of application, the best option is the PM synchronous motor (PMSM) due to its high torque density and highest efficiency.

Because one of the constraints is the size occupied by the motor, further minimized by the introduction of the power electronics, the choice of the topology and materials should be done such as the motor is able to provide the required torque. The link between the motor size and output torque is the classical output equation, which relates the torque per rotor volume (TRV – eq.2.1), measured in [Nm/m<sup>3</sup>], to the electric loading  $A$  (eq.2.2) and magnetic loading  $B_{mg}$  (eq.2.3) [38], as presented below:

$$TRV = \frac{T}{\frac{\pi D_{in}^2 L_{stk}}{4}} = \frac{\pi}{\sqrt{2}} k_w l AB_{mg} \quad (2.1)$$

$$A = \frac{2mN_{ph} I_{ph}}{\pi D_{in}} \quad (2.2)$$

$$B_{mg} = \frac{2p\Phi_g}{\alpha_i \pi D_{in} L_{stk}} \quad (2.3)$$

In the above equations  $k_{w1}$  is the stator winding factor and usually has a value of 0.9,  $m$  is the number of phases (1 or 3),  $N_{ph}$  is the number of turns in series per phase,  $I_{ph}$  is the RMS value of the phase current,  $D_{in}$  is the rotor diameter of the motor (including the air gap),  $\alpha_i$  is the effective pole arc coefficient,  $L_{stk}$  is the stator stack length and  $2p$  is the number of pole pairs.

On the other hand, the output power is related to the speed of the motor in the same manner as the torque is related to electric and magnetic loadings, and it is expressed as output (mechanical) power per rotor volume [W/m<sup>3</sup>]:

$$PRV = \frac{P}{\frac{\pi D_{in}^2 L_{stk}}{4}} = \frac{n}{4} AB_{mg} \quad (2.4)$$

As can be observed from the expression above, the mechanical power depends on peak value of the air gap magnetic flux, on armature line current density and  $n_s$ , which is the synchronous speed. One can see that the higher the speed, the higher the output power. Common factors of both equations are the electric and magnetic loadings which can be also raised to improve the output torque and power. High magnetic flux density can be achieved by using magnetic materials with high saturation magnetic flux density, while high line current density can be achieved by using intensive cooling systems, like liquid cooling systems [1]. However, one should consider the extra costs added by high performance magnets and cooling systems.

Another measure to increase both torque and power is to reduce the size of the rotor volume, but at some point the rotor will be too fragile to sustain a high speed or the pressure on the shaft, while the magnet volume increase will increase the total costs, which will make the motor not feasible for the purpose of design.

As stated in eq. (2.4), the developed power is proportional to the speed and the volume of the rotor. Increase in the speed while maintaining the value of the output power will affect the motor dimensions, reducing its volume and mass, which is ideal for the purpose of this design. The improving performance-cost relationship of PM materials is getting to the point where the increased power density of the PM motor can be large enough to offset the cost of the magnets.

Along with dimensional advantages, the increase in speed introduces also some limitations and drawbacks. An extensive study on the subject is realized in [7], covering the main issues in high speed PM motor design. The most important one is the development of the centrifugal forces which will try to remove the magnets from the shaft, mainly because PM material exhibits poor mechanical characteristics. This issue can be solved wither by integrating the magnets in the rotor (interior-type permanent magnets) or to use a non-magnetic retaining sleeve to cancel the effect of the forces on the magnets. The usage of glue is preferred, because no other locking option is

feasible; if a perfect locking of the PM is realized (hard to do in mass production, almost impossible), the centrifugal forces won't have much impact on PMs. The limitations are introduced by maximum winding temperature rise and irreversible PM demagnetization, thus the value of the maximum stator current should be limited. Apart from centrifugal forces, the fringing effects and acoustic noise should be considered during the design. Since the frequency will also increase, the iron losses will be higher than copper losses, while the usage of the retaining sleeve will introduce more rotor losses.

Since the advantages of high speed were presented, the proper motor speed has to be chosen. The compressor is a variable speed drive, making the most from the usage of the PM synchronous motor, meaning that it will work in a variable range of speeds, proportional to the amount of refrigerant that needs to circulate in the refrigeration system to keep a constant temperature. During normal functioning regime, the compressor's motor will rotate in the range of 6000 – 12000 [rpm]. To be sure that the motor won't break at maximum normal speed, it should be designed to support about 125% of this speed, around 15000 [rpm].

### 2.2.3 Number of magnet poles

One of the reasons for the introduction of PMSMs is the high efficiency and the possibility to work at variable speed, by introduction of power electronics, such as the system losses are smaller than losses in line start 50Hz constant speed standard devices. However, the presence of power electronics is adding extra costs to the total price of the compressor. To make the system cost effective, we need to use power electronic devices that switch at hundreds of Hertz, like thyristors or silicon controlled rectifiers (SCRs), with smaller prices. The relation between the rotational speed  $\omega$ , in [rad/s], the number of poles  $p$  and the frequency  $f$ , in [Hz], is given below.

$$\omega = \frac{2\pi f}{p} \quad (2.5)$$

The synchronous speed  $n_s$  is expressed in [rpm], while the rotational speed  $\omega$  is expressed in [rad/s]. The relation between the two of them is:

$$\omega = n \cdot \frac{\pi}{30} = 15000 \cdot \frac{\pi}{30} = 500 \cdot \pi \left[ \frac{rad}{s} \right] \quad (2.6)$$

Combining equations (2.5) and (2.6), we obtain the relationship between switching frequency of the converter and the number of the rotor pole pairs of the motor:

$$f = \frac{500 \cdot \pi \cdot p}{2 \cdot \pi} = 250 \cdot p [Hz] \quad (2.7)$$

From equation (2.7) it can be seen that only motors with 2 or 4 rotor poles ( $2p$ ) must be considered. Since the large starting torque is a serious issue, capable of reducing drastically the life span of the compressor, the single phase configurations are left aside and only three phase configurations are taken into account.

Increasing the number of magnet poles increases the force generated by the motor, as can be seen from equation (2.8). Increasing the number of poles in a fixed area implies decreasing the magnet width to accommodate the additional magnets.

$$F_{\max} = p \cdot B_{mg} \cdot L_{stk} \cdot I_{ph} \quad (2.8)$$

This increases the relative amount of magnet leakage flux, which in turn decreases the air gap flux density. Thus the increase in force does not increase indefinitely. Sooner or later the force will actually decrease with an increase in magnet poles. This implies that there is some optimum number of magnet poles [39]. In the end, the number of poles must be chosen such as the leakage flux, core loss and drive frequency requirements do not have a significant negative effect on motor performance.

#### 2.2.4 Motor air gap

Now that we have settled to a topology with 2 or 4 rotor poles and we know that the number of stator poles should be a multiple of the phase number, let's focus on motor configuration. A PM motor is composed from stator, the static part, air gap, where the electromagnetic interaction takes place, and rotor, the moving part.

For starters, the choice of the air gap is simpler and defines the geometry of the entire motor. The air gap can be radial or axial.

The advantage of the axial air gap is that it can provide smaller rotor inertia. However, it presents a huge drawback, as it requires more PM weight to produce the same amount of torque as in radial air gap, due to the fact that it is doubled in size, which leads to an increase in total costs. Another important disadvantage of the axial air gap is the difficulty of manufacturing the rotor core from rolled laminations on a large scale. Since the radial air gap is not as disadvantageous as axial air gap, the cylindrical stator and rotor configuration with radial air gap is preferred.

#### 2.2.5 Rotor

Now that the shape of the motor is known we have to choose the rotor. What interests us is the placement of the rotor, outer or inner one, and magnet type, interior or surface. If the rotor with surface magnets is to be placed on the outer side, it means that the stator will be smaller in size and the copper losses will be less than if the stator will be placed on the outer side. Other advantages for this type of rotor are small weight and small inertia, but the main drawback is the increase of the magnets weight and also a more complex configuration of the motor, yielding increased magnet and manufacturing costs. As a good compromise between costs and efficiency is the goal of

this design, the evident advantage of a higher efficiency is not enough to compensate the extra costs. This way, only internal rotor configuration is chosen, meaning implicitly that the stator will be placed on the outer side.

Since the rotor type is chosen, the next thing is to establish what kind of magnet placement will be used. Different types of magnets can be divided into two categories, based on which the choice of placement will be made. Rotors can be either salient-pole type, where the stator phase inductance varies with position, or non-salient pole type, where the value of the phase inductance is constant.

Surface or external PM rotors with radial or parallel magnetization are definitely non-salient, breadloaf PM rotors can be considered as non-salient, due to the fact that phase inductance varies weakly with position, while interior, spoke and inset PM rotors are salient [2, 38].

The final decision regarding the rotor type, salient or non-salient, will be taken after the windings type and current shape are chosen. However, the competitors are surface and interior PMs, one from each category, as can be seen in Fig. 2.1.

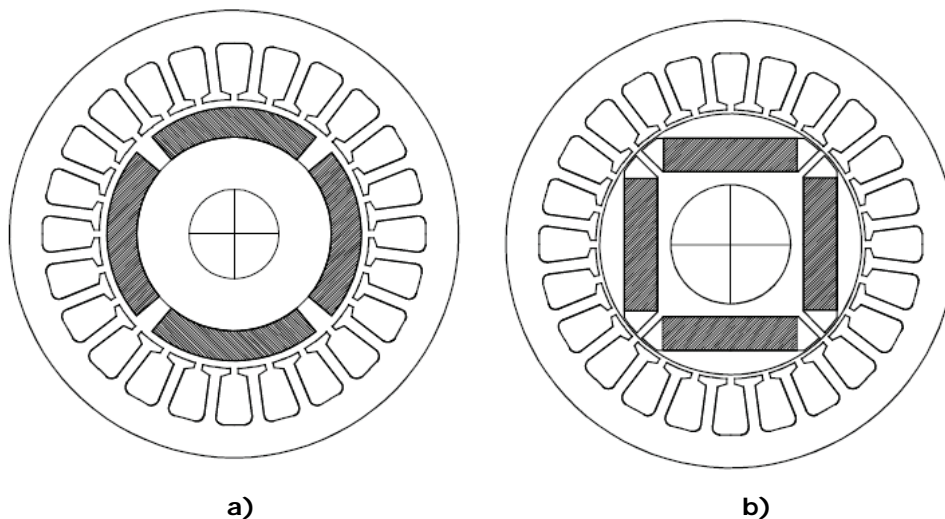


Fig.2.1 PM synchronous motor topologies: a) non-salient – surface PM rotor, b) salient – interior PM rotor [38]

### 2.2.6 Stator and windings

Output torque is produced by the energy conversion during the interaction of rotor field excited by permanent magnets and currents carried by the stator windings. Until now, air gap and rotor construction were treated, leaving only the stator to be analyzed. Regarding the fixed part of the motor, from the point of view of topology selection, a designer should think about stator core, slot and teeth shape and last but not least, the windings.

In terms of losses and heating, the stator is the most vulnerable part. There are two types of stator core configurations, namely slotted and slotless [8, 17, 19, 39], as presented below in Fig.2.2.

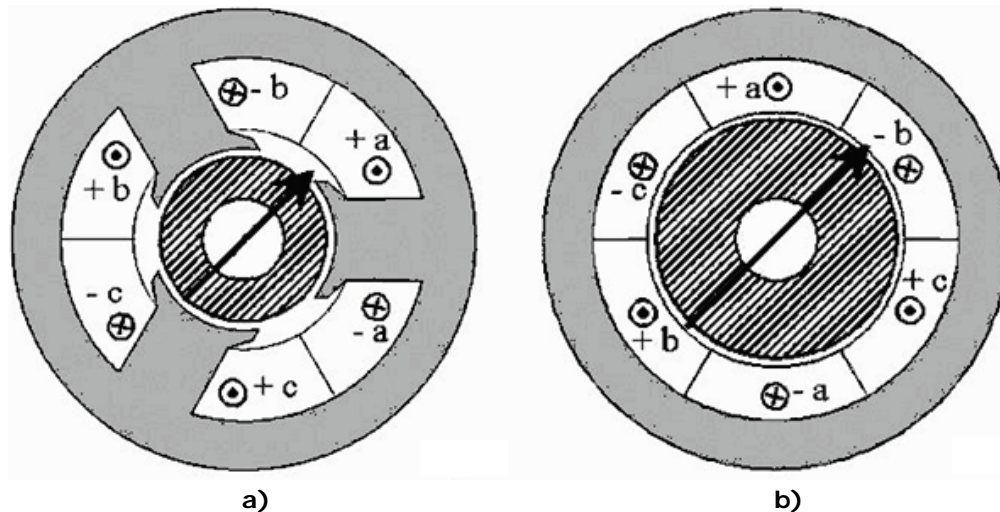


Fig. 2.2 PM stator configurations: a) slotted, b) slotless [8]

Slotless configuration means that slots are eliminated and the windings are distributed inside the stator back iron. The obvious advantages of this topology are the reduction of iron losses, both in the stator and rotor, and the absence of the cogging torque, due to the absence of slot openings. The absence of the stator teeth makes the air gap to grow substantially, equal to the distance between rotor surface and stator back iron. Therefore, to obtain the same torque-per-volume, an increase in the PM weight is mandatory, the length of the magnet growing substantially [39]. Also, the number of windings must be increased to compensate the decrease in the air gap flux density. However, even if there is enough room to do that, the rather poor thermal conductivity between windings and stator back iron limits the increase of the electrical loading. Another limitation occurs at high speeds, where mechanical boundaries of the rotor configuration can be reached by the large centrifugal forces.

As opposite to the slotless configuration, the slotted stator has none of the disadvantages, but instead has larger iron losses and cogging torque is a serious issue, especially if the rotor has surface permanent magnets. Despite that, the slotted stator is common in most PMSM applications. Due to the fact that drawbacks of slotted stator are not so numerous, its design allows more flexibility. The only design constraint is that the number of slots must be an integer multiple of the number of phases, such as to be sure that no slots are left empty, both sides of each coil have slots to pass through and no phase windings share the same slot [39]. All in all, this translates in a parameter  $q$  known as slots/pole/phase and it is expressed as:

$$q = \frac{N_s}{2p \cdot m} \quad (2.9)$$

In general it is better that  $q \neq 1$ , larger integer values being related to integral slot motors, while fractional values are related to fractional slot motors. The proper value is chosen by the designer after considers which type of windings wants to use in the construction of the motor.

Integral slot or integral pitch motor uses overlapping windings, which can be either distributed or concentrated windings, and generally results in a more sinusoidal distribution of the magneto-motive force (MMF) and back-EMF waveform.

Fractional slot or fractional pitch motor uses non-overlapping, concentrated windings, which can be either single-layer, with alternate teeth wound, or double-layer, with all teeth wound [19, 40], as presented in Fig. 2.3.

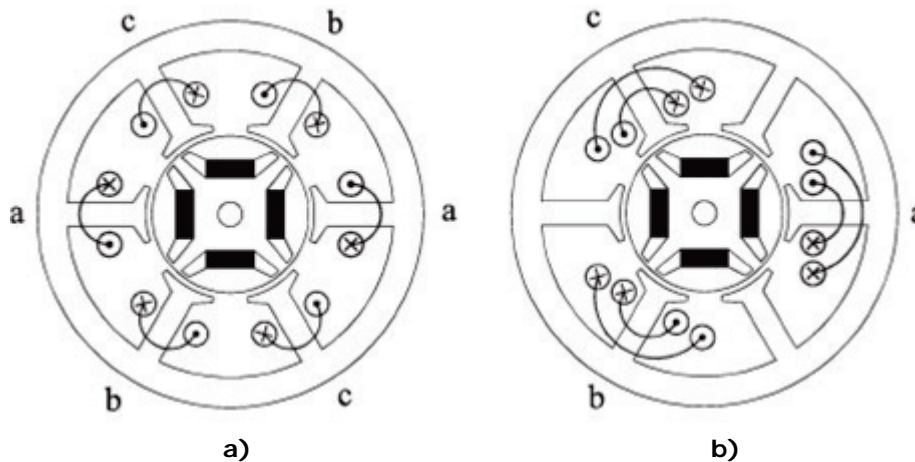


Fig. 2.3 Fractional slot motor with: a) single-layer and b) double-layer windings [40]

The latter motor type has gaining interests in the last years, based on the advantages provided by the non-overlapping windings, like high power density, high efficiency, short end turns, high slot fill factor, lower cogging torque, flux weakening capability and fault tolerance. On the other hand, distributed windings are especially used when low pulsations, vibrations and noise, are seek upon, but at the cost of notable additional copper weight and losses and frame additional axial length, to accommodate large end connections.

Fractional slot three phase motors with tooth wound coils (double-layer) are characterized by  $q \leq 0.5$ . The use of tooth wound coils has numerous advantages for machines with radial air gap, like reduction of copper volume used for end connections, minimization of Joule losses, reduction of the manufacturing costs and improved output characteristics.

Based on eq. (2.9) and knowing that  $m=3$  phases and  $2p$  is either 2 or 4, only three configurations are viable: 3/2, 3/4 and 6/4 motors. Furthermore, tooth wound coils are obtained when a coil throw  $y_q$  (expressed in number of slots) is equal to 1. The expression of the coil throw can be approximated as in eq. (2.10), which results in a number of slots equal to the number of pole pairs, as in eq. (2.11) [40].

$$y \approx \frac{Q}{2p} \quad (2.10)$$

$$Q \approx 2p \quad (2.11)$$

We can see that all the configurations mentioned above satisfy this condition and combined with the fact that the machines with a number of slots/pole/phase in the range between 1/3 to 1/2 exhibits higher performances, only configurations with 3-slots 2-poles (3/2) and 6-slots 4-poles (6/4) will be considered. Comparisons between these two configurations were done in [17 – 19] and, as finite element analysis shows, the 3/2 configuration exhibits large radial forces, which is undesirable because will lead to vibrations and noise. Finally, the six stator slot and four rotor poles topology, though a little bit costly than its competitor, doesn't have the drawback of large radial forces, thus it will be considered the best competitor.

However, one issue is still unknown and that is the permanent magnets placement relative to the rotor. Interior-type magnets and surface-type magnets are considered, but the choice of the current control will be essential for the final motor configuration.

### 2.2.7 Current shape

The chosen PMSM configuration can produce either sinusoidal or trapezoidal back-EMF waveform by proper design. As input, the motor can accommodate sinusoidal or rectangular (in reality, slightly trapezoidal) current control. The reason to choose one over another is related to the functioning regime of the motor, power electronics in terms of costs and losses and the complexity of motor control.

For compressor application, the motor needs to deliver full torque up to the highest speed, so no flux weakening is required. For sinusoidal control, this means pure  $i_q$  control ( $i_d=0$ ), while for trapezoidal control the back-EMF is in phase with the current, thus no advance angle is required, as can be seen in Fig. 2.4.

From the point of view of power electronics, sinusoidal current needs three switches working at a time (all three phases active), while trapezoidal current needs only two switches (two phases active). However, whenever commutation occurs, for a shorter period of time (between  $10^\circ$  and  $30^\circ$ ), all three phases are on. Two phases on mean that the inverter losses are less than for three phases on, which leads to an increase in the overall efficiency. On the other hand, trapezoidal current control, with sensors or sensorless, is easier and cheaper to implement.



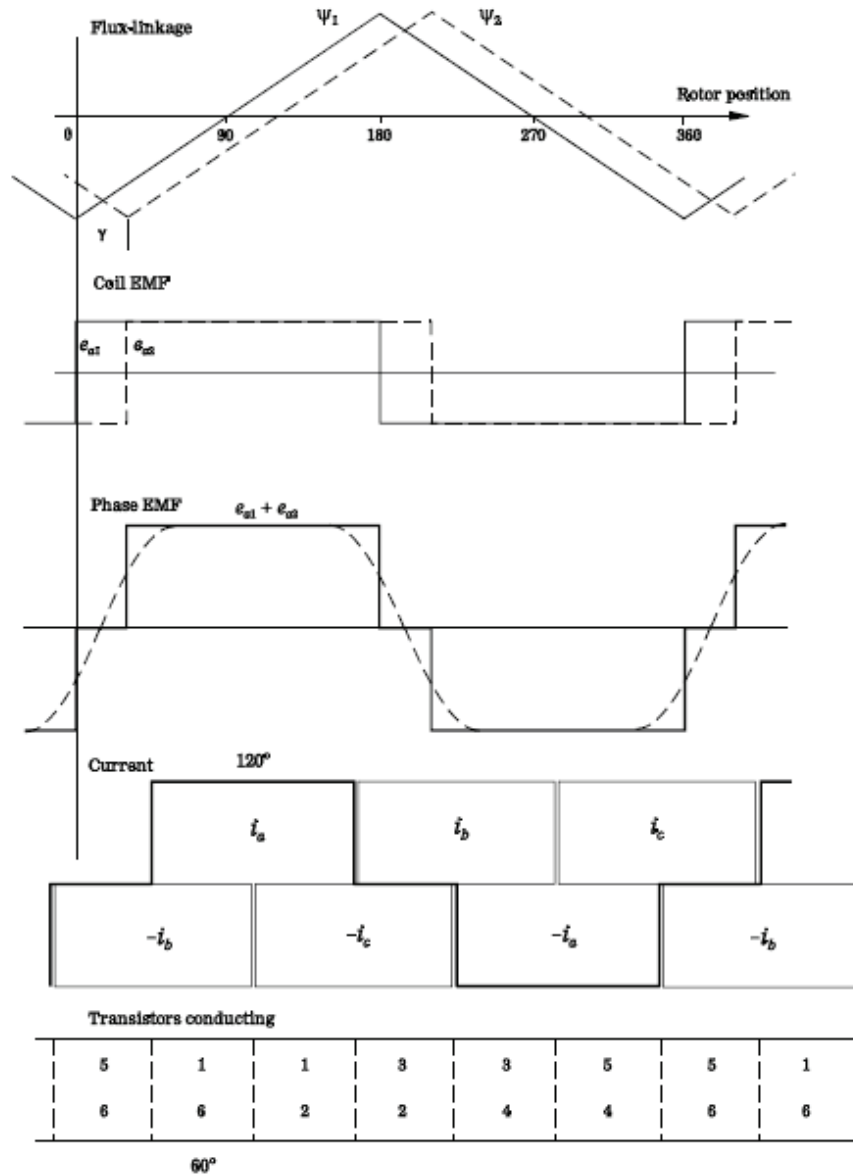


Fig. 2.4 Flux linkage, back-EMF and current waveforms for trapezoidal current controlled PMSM [39]

The commutation angle of the switches is dependent on machine time constant and implicitly on phase inductance  $L_s$  and phase resistance  $R_s$ . To reduce the motor time constant, a smaller phase inductance is required and this goal is achieved by using surface permanent magnets on the rotor. Another advantage of the surface magnets is the non-saliency, thus the inductance is invariant with the position.

For sinusoidal current control the usage of interior permanent magnets is recommended, to cut down the permanent magnets cost. Though the cogging torque is reduced and the extra retaining sleeve is not necessary, the rotor structure with interior permanent magnets should be designed carefully to avoid it break down at high speeds, when large eccentricity radial forces occur.

After weighing the advantages and disadvantages, not an easy task for a designer with the multitude of possible topologies, the three-phase PMSM with 6 stator slots, double-layer concentrated winding and 4 rotor poles, surface permanent magnets, with trapezoidal currents through the windings seems the best option for the design requirements.

### 2.2.8 Materials selection

Since the topology of the motor is chosen, the next step is to present the materials for the active parts, the iron core laminations and the permanent magnets, as they need to be highly efficient but at a low cost.

#### 2.2.8.1 Iron core laminations

The material for the stator and rotor cores was chosen to be laminated non-oriented silicon SURA® NO18 (European denomination – 0.178 [mm] thickness) electric steel [41].

For the BLDC rotor a massive one-piece iron core could have been chosen, but in terms of costs and ease of manufacturing, the inner parts from the stamping process of the stator laminations can be used. Table 2.1 presents the main material properties of the iron core laminations.

**Table 2.1 Material properties for iron core laminations**

Parameter	Symbol	Value	Unit
Composition	$U$	99.95	% Fe
Initial relative permeability at $B=0.02$ [T]	$\mu_{ri}$	1076	-
Maximum relative permeability	$\mu_{rmax}$	4173	-
Saturation induction	$B_{sat}$	1.8	T
Mass density	$\rho_{Fe}$	7650	kg/m <sup>3</sup>

The DC magnetization curve is shown in Fig. 2.5. The variation of the specific total losses versus frequency at 1.5 [T] (peak value) and versus peak flux density at 50 Hz is presented in Fig. 2.6 and 2.7 respectively.

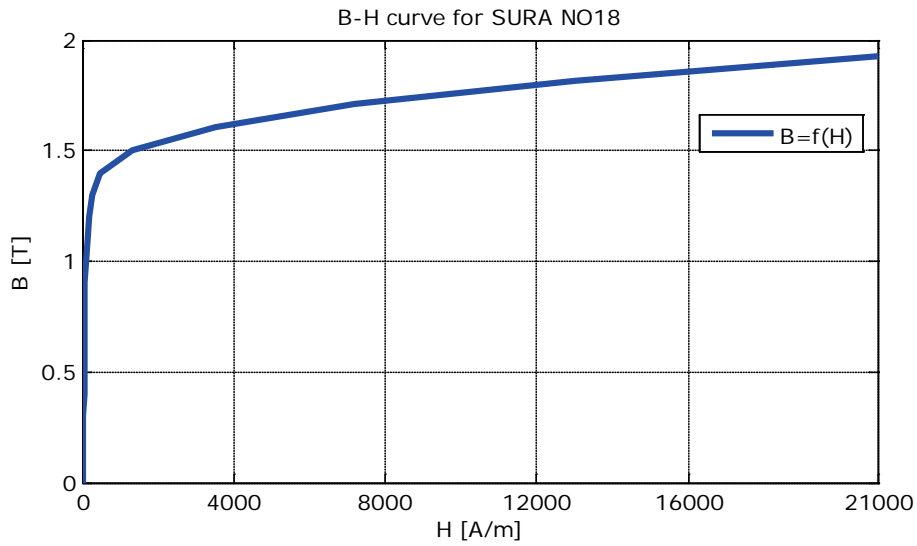


Fig. 2.5 DC magnetization curve

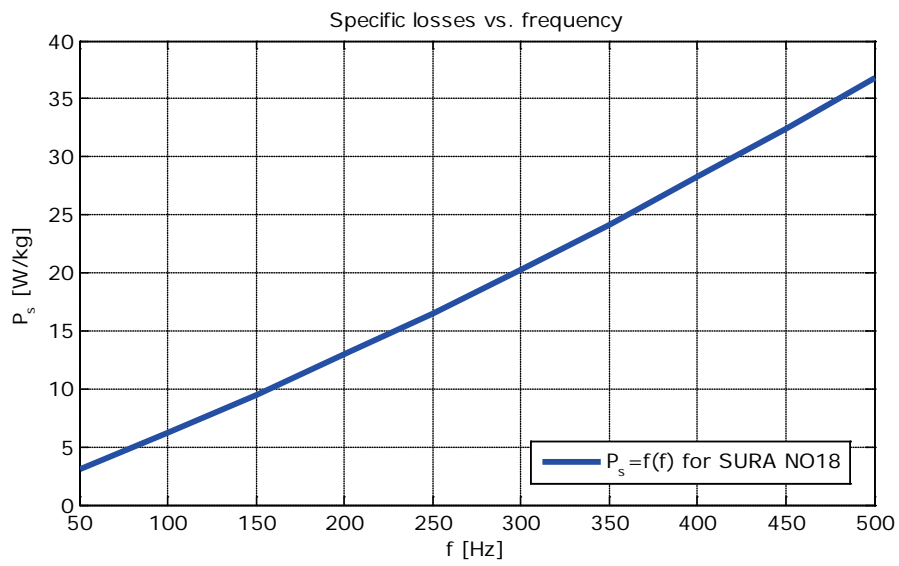


Fig. 2.6 Specific total losses versus frequency @ 1.5 [T] (peak value)

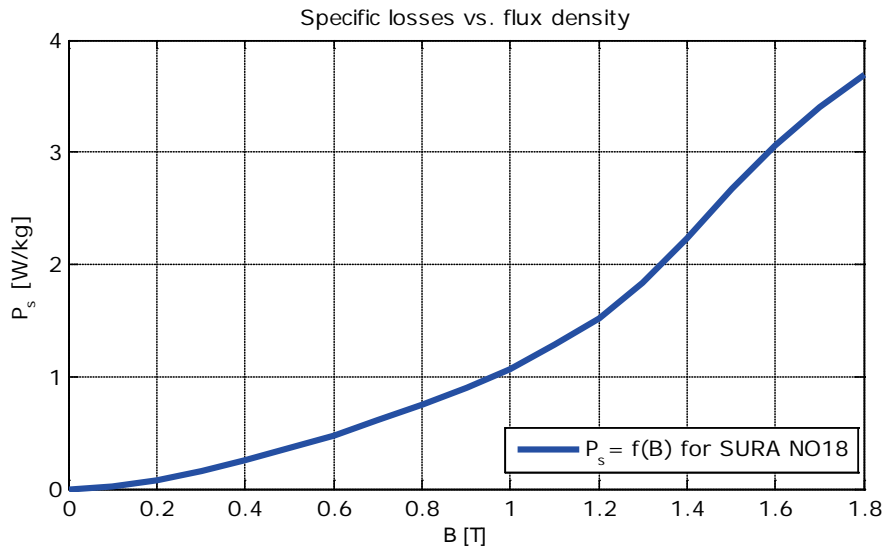


Fig. 2.7 Specific total losses versus peak flux density @ 50 Hz

### 2.2.8.2 The permanent magnets

To accomplish the task of high performance application, a magnet with high energy properties is required. However, the price of the magnets must be considered, so a Neodymium-Iron-Boron (NdFeB) magnet is the perfect choice. Table 2.2 shows the main material properties of magnetic material [42].

**Table 2.2 Material properties for permanent magnet**

Parameter	Symbol	Value	Unit
Remanent induction	$B_r$	1.12	T
Intrinsic coercivity	$H_{cJ}$	860000	A/m
Recoil permeability	$\mu_r$	1.31	-
Maximal energy product	$BH_{max}$	240	$\text{kJ/m}^3$
Magnetizing force	$H_{magn}$	2500000	A/m
Temperature coefficient of the remanent induction	$a_{Br}$	-0.085	$1/^\circ\text{C}$
Temperature coefficient of the intrinsic coercivity	$a_{HcJ}$	-0.55	$1/^\circ\text{C}$
Curie temperature	$T_{Curie}$	330	$^\circ\text{C}$
Mass density	$\rho_{PM}$	7700	$\text{kg/m}^3$

Whenever a permanent magnet is chosen, the demagnetization curve at  $20^\circ\text{C}$  is important. The demagnetization curve for the magnet Vacodym 677 AP 215/223 from Vacuumschmelze GmbH, used further in the motor design, is shown in Fig. 2.8.

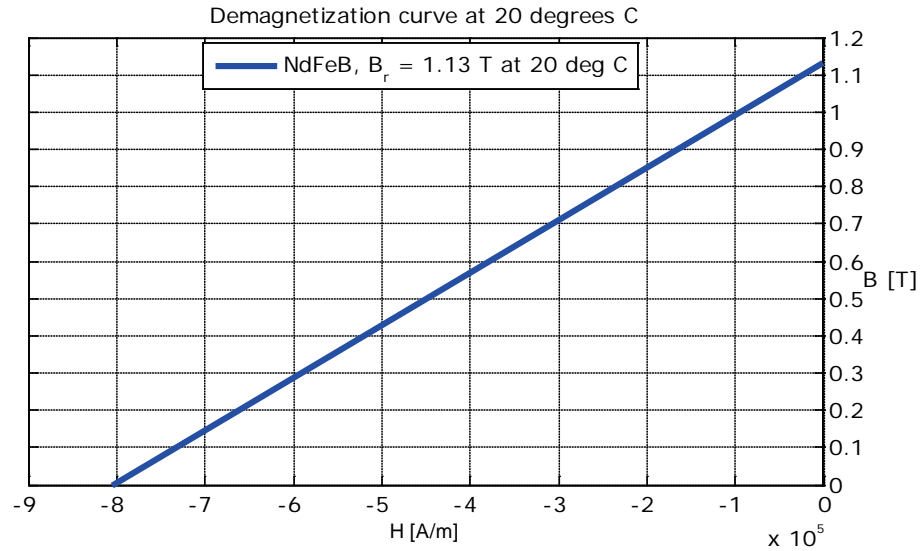


Fig. 2.8 Demagnetization curve for Vacodym 677 AP 215/223 magnet @ 20°C

### 2.2.9 Preliminary design data

General specifications of a variable speed surface PM synchronous machine, used for compressor applications:

- Base power:  $P_b = 150$  [W]
- Base speed:  $n_b = 15000$  [rpm]
- Nominal frequency:  $f = 500$  [Hz]
- Maximum speed:  $n_{max} = 15000$  [rpm]
- Power at maximum speed:  $P_{max} = 150$  [W]
- DC voltage:  $V_{DC} = 310$  [V]
- Number of phases:  $m = 3$
- Number of poles:  $2p = 4$
- Efficiency @  $P_b$  and  $n_b$ :  $\eta > 92$  [%]
- Connection of phases: Star (Y)
- Number of slots / pole / phase:  $q = 0.5$
- Supply: 3-phase PWM inverter, rectangular current control

Other specifications can be added to help the designer to calculate more accurately the geometrical dimensions of the motor and to establish how much material can be used to obtain the required performances. These specifications may be related to cogging torque, average torque, duty cycle, motor-cooling system, material insulation class or protection degree against alien bodies [17].

Flux weakening ( $n_{max}/n_b > 1.5$ ) is not very feasible with surface PMSM, (unless its synchronous inductance  $L_s$  is large in p.u., such as for tooth-wound stator windings) and thus  $n_{max} = n_b$ .

### 2.2.10 Electric and magnetic loadings

The first stage in general design of electric machines is about choosing the electric and magnetic loadings. As can be seen from equations (2.1) and (2.4), torque-per-rotor volume (TRV) and power-per-rotor volume (PRV) are dependent on electric and magnetic loadings. For surface PM synchronous machines, the loadings are described as follows [1, 17, 38, 39]:

- Specific electric loading  $A_m$  [A/m] represents the total effective value of the ampere turns in stator slots per stator periphery length.  $A_m$  relates to thermal loading and torque density. Large values of  $A_m$  lead to large torque density, and consequently to smaller machine size, which may end up in machine over heating and lower efficiency.
- When high torque density is target in the design, the specific tangential force,  $f_{tp}$ , concept may be preferred. It is measured in [N/cm<sup>2</sup>] and varies from 0.1 [N/cm<sup>2</sup>] in micro-motors to 10 [N/cm<sup>2</sup>] in larger torque density.  $A_m$  and  $f_{tp}$  are complementary concepts.
- PM air-gap flux density:  $B_{ag}$  [T], varies from 0.2 [T] in micro-motors to 1 [T] in large torque density design. Together  $B_{ag}$ ,  $A_m$  and  $f_{tp}$  determine the volume of the machine for given base torque ( $T_b$ ).
- Stator tooth flux density:  $B_{st}$  [T] determine the magnetic saturation degree in the machine; it varies from 1.2 [T] to 1.8 [T] in general, for silicon laminated stator cores. As the machine magnetic air-gap (which includes the surface PM thickness) is large the teeth magnetic saturation influence is rather small and thus  $B_{st}$  may be chosen rather large; in contrast, if  $B_{st}$  is large (and the fundamental frequency  $f_n$  is large) the core losses would be large. Smaller values of  $B_{st}$  lead to wider teeth and thus thinner slots, that is larger design current densities and consequently, larger copper losses. To prevent this, deeper slots are adapted, but then the machine external diameter (and volume) is increased. Moreover the copper losses may not decrease notably by deepening the slot as the average diameter (and length) of end connection of coils increase. So the design should start with moderate to large values for  $B_{st}$  and then reduce or increase them according to obtained performance in comparison to the design theme.
- The stator yoke flux density  $B_{st}$  [T] is again chosen as a compromise between magnetic saturation level and core losses limitations. Small values of  $B_{sy}$  may lead to a larger machine size and weight, especially if the number of poles is small ( $2p=2,4$ ).
- Current density  $J_s$  [A/mm<sup>2</sup>] determines the copper losses and the copper volume. Small values of  $J_s$  (2 – 3.5 [A/mm<sup>2</sup>]) corroborated thin and deep slots may lead to high leakage inductance, and machine volume (and weight). On the other hand, high  $J_s$  values (> 8 [A/mm<sup>2</sup>]) in general not only imply forced cooling but also lead to lower efficiency, while reducing the machine volume.
- Rotor yoke flux density  $B_{ry}$  [T] is imported in machine with a large number of poles (and large diameter) when the PMs are not any more placed directly on the shaft.

### 2.2.11 Choosing a few dimensioning factors

- Machine shape factor  $\lambda_c$ : the ratio between the axial (stack) length of the machine  $L_{stk}$  and the stator bore diameter  $D_{is}$  ( $\lambda_c = L_{stk} / D_{is}$ , usual between 0.3 and 3).
- PM pole span factor  $\gamma_{PM}$ : ratio between PM width and pole pitch. This factor influences the PM total weight, the emf space harmonics content, and, to some extent, the cogging torque.
- Stator winding current path count  $a_1$ , is always a divisor of number of poles for two layers winding and of the number of pole pairs for single layers windings. To avoid circulation current between current paths, due to inherent machine symmetry imperfection,  $a_1 = 1$  whenever possible.
- Elementary conductors in parallel: for large currents (or fundamental frequency) the coil turns are made of multiple elementary conductors in parallel with same degree of transposition to reduce skin effects.
- Coil span  $x_s$  is the distance between forward and return sides of coil; it may be measured not only in [mm] but also in number of slot pitches: between  $2q$  and  $3q$  for phase distributed windings, but below 0.5 for tooth wounded windings.
- Slot opening:  $s_o$ . Its minimum value is limited by the possibility to introduce the coils, turn by turn, in the slot and by the increase of slot leakage inductance and PM flux fringing its maximum value is limited by the PM flux reduction, cogging torque increase and torque ripple.
- Tooth top height  $h_{s4}$  is limited down by technological (and magnetic saturation) constraints and upper by the increase slot leakage inductance. (in high speed PMSM, with  $f_n > 1$  [kHz],  $h_{s4}$  may be increased, to increase machine inductances  $L_s$  and thus decrease current ripple).

### 2.2.12 A few technological constraints

- The laminated core filling factor,  $k_{stk} = 0.8 - 0.95$  is the ratio of laminations height to total laminated core length (laminations insulation coating means  $k_{stk} < 1$ ).
- Slot copper filling factor,  $k_{sf} = 0.33 - 0.7$ ; lower values corresponds to semiclosed slots with coils introduced turn by turn in the slot while larger values corresponds to open slot and pre-made coils made of rectangular cross section conductors.
- Minimum air-gap  $g_{min}$  from mechanical considerations in super high speed machines  $g_{min}$  is increased to reduce PM eddy currents losses due to stator mmf space harmonic; a resin coating of PMs is also added for mechanical rigidity;
- Overload demagnetization safety factor  $k_{sPM}$ : the max overload stator mmf that avoids PM demagnetization in worst load scenario, is limited by this factor;
- Slot geometry type: if more than one slot shape is used, design expression for chosen shape should be provided and the computer code calls for the specific geometrical and specific magnetic permeance expression on a menu basis.
- Difference between PM length,  $l_{PM}$ , and stator stack length,  $L_{stk}$ , in order to avoid axial forces on the bearings.

## 2.3 Analytical model

As stated earlier, the sizing of an electric motor should start with torque-per-rotor volume (TRV) and power-per-rotor volume (PRV) relations, expressed in equations (2.1) and (2.4). Since both the output torque and power depend on rotor volume, first the designer must calculate the geometrical dimensions, and then the electrical and magnetic loadings based on the selected materials. Afterwards, the windings parameters, inductance and resistance are calculated, and then follow electrical parameters, phase voltage and current, all losses, efficiency and thermal verifications.

Different algorithms for electrical machine sizing are presented in [1, 17, 38]. For this particular application, the dimensioning is developed step by step in this paragraph.

### 2.3.1 Geometrical dimensioning

First step of geometrical dimensioning is to calculate the internal stator diameter, because both output torque and power depend on rotor volume, which is expressed in eq. (2.12). The inner diameter in the volume formula is equal to the outer rotor diameter  $D_{ro}$ , where magnetic flux is produced from the magnets, plus the air gap height  $g$ , where all the flux density is concentrated. The sum of them is equal to the interior stator diameter, as in eq. (2.13).

$$V_{rot} = \frac{\pi D_{in}^2 L_{stk}}{4} \quad (2.12)$$

$$D_{in} = D_{si} = D_{ro} + 2g \quad (2.13)$$

The minimal air gap height  $g$ , taking into account manufacturing constraints, is 0.5 [mm]. For geometrical dimensioning the minimal value of the air gap is chosen. The stator bore diameter can be calculated related to base electromagnetic torque  $T_{eb}$ , machine shape factor  $\lambda_c$  and tangential specific force  $f_{tp}$ . The relation between mechanical power and shaft torque is expressed in (2.14), while the stator bore diameter is calculated in (2.15).

$$T_{eb} = \frac{P_b}{\omega_b} = \frac{P_n}{\omega_n} = \frac{P_n}{2\pi \frac{n_n}{60}} = \frac{150}{2\pi \frac{15000}{60}} = \frac{3}{10 \cdot \pi} = 0.0955 [Nm] \quad (2.14)$$

$$D_{si} = 100 \cdot \sqrt[3]{\frac{4p}{10\pi^2} \cdot \frac{T_{eb}}{\lambda_c f_{tp}}} = 100 \cdot \sqrt[3]{\frac{8 \cdot 0.0955}{10\pi^2 \cdot 2.66 \cdot 0.85}} = 100 \cdot 0.1506 \approx 15 [mm] \quad (2.15)$$



Since we are limited in terms of outer diameter to  $D_{so}=32$  [mm], in order to produce torque we need a longer stack length, thus machine shape factor is chosen to be almost 3, namely  $\lambda_c = 2.66$ . Also, the motor is quite small in volume so we need larger specific electric loading, so the specific tangential force is chosen to be  $f_{tp}=0.85$  [N/cm<sup>2</sup>]. From that we can further derive the pole pitch  $\tau_{PM}$ , the stack length  $L_{stk}$  and rotor length  $L_{rot}$ , taking into account that the latter is just a little bit longer than the former.

$$\tau_{PM} = \pi \frac{D_{Si}}{2p} = \pi \frac{15}{4} = 11.78[\text{mm}] \quad (2.16)$$

$$L_{stk} = \lambda_c D_{Si} = 2.666 \cdot 15 \approx 40[\text{mm}] \quad (2.17)$$

$$L_{rot} = 1.05 \cdot L_{stk} = 1.05 \cdot 40 = 42[\text{mm}] \quad (2.18)$$

Based on eq. (2.13), and with stator bore diameter value calculated in (2.15), we can find the value of the outer rotor diameter:

$$D_{ro} = D_{Si} - 2g = 15 - 2 \cdot 0.5 = 15 - 1 = 14[\text{mm}] \quad (2.19)$$

Now that we have established the rotor length and the rotor outer diameter, we can calculate the other two geometrical dimensions of the rotor, namely the inner rotor diameter  $D_{ri}$  and the magnet height  $h_{PM}$ , represented in Fig. 2.9.

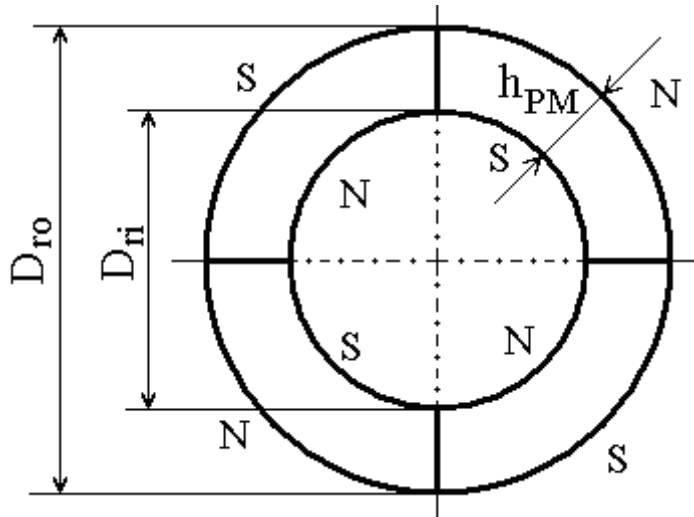


Fig. 2.9 Rotor geometrical dimensions [18]

The relation that defines the minimal height criteria for the magnets is:

$$h_{PM} \geq 4g \quad (2.20)$$

We have chosen the magnet height  $h_{PM}$  to be 2.5[mm]. This way the rotor inner diameter value is:

$$D_{ri} = D_{ro} - 2h_{PM} = 14 - 2 \cdot 2.5 = 14 - 5 = 9[\text{mm}] \quad (2.21)$$

Now that the rotor geometrical dimensions are calculated, including the magnet height, the next step is to determine the magnetic loading provided by the permanent magnets. Their effect is quantified in the magnetic flux density  $B_{gPM}$  and magnet flux per pole  $\Phi_{PM}$ . Below, their expressions are given.

$$\Phi_{PM} = B_{ag} \tau_{PM} L_{stk} \quad (2.22)$$

$$B_{ag} = k_{av} \cdot B_{mg} \quad (2.23)$$

$$B_{mg} = \frac{B_r}{1 + k_{fring}} \cdot \frac{h_{PM}}{h_{PM} + g} \quad (2.24)$$

The unknown term in eq. (2.22) is  $B_{ag}$ , which can be found through eq. (2.23). From eq. (2.23), one can observe that the average flux density value in the air gap is a part of the total flux density  $B_{mg}$ . Ideally, for rectangular distribution, the flux density shape is rectangular and the factor  $k_{av}$  is equal to 1. For sinusoidal distribution, the same factor is about 0.636 ( $2/\pi$ ), thus the average flux density value in the air gap is about 64% from the total flux density. Although in the ideal case, for brushless DC motors, we can consider that the average value is equal to the total flux density, due to the fringing effect, the  $B_{ag}$  shape is somewhat rounded at the corners, making  $k_{av}$  to be sensibly smaller than 1, around 0.95.

Going backwards, the total flux density will be calculated choosing following values for the fringing coefficient in the equation  $k_{fring} = 0.15$  (varies in the range (0.1 – 0.2)).

After the value of the total flux density is found, the value of the average air gap flux density is calculated with a factor of 0.85, to be closer to reality, and then the PM flux is calculated by choosing  $\lambda_{PM}$  to be equal with 0.9.

$$B_{mg} = \frac{1.12}{1 + 0.15} \cdot \frac{2.5}{2.5 + 0.5} = 0.82[T] \quad (2.25)$$

$$B_{ag} = 0.85 \cdot 0.82 = 0.7[T] \quad (2.26)$$

$$\Phi_{PM} = 0.7 \cdot 11.78 \cdot 10^{-3} \cdot 40 \cdot 10^{-3} = 3.3 \cdot 10^{-4}[Wb] \quad (2.27)$$

With rotor and air gap magnetic parameters calculated it is time for stator sizing. The main stator geometrical parameters are given in Fig. 2.10.

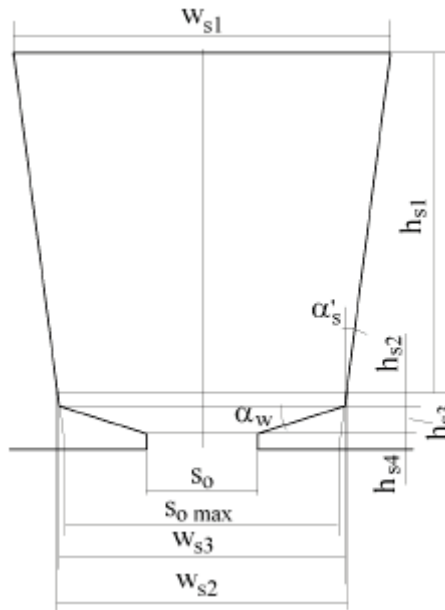


Fig.2.10 Stator geometrical parameters [17]

First we calculate the stator pole pitch and the stator teeth width.

$$\tau_{SS} = \pi \frac{D_{Si}}{N_s} = \pi \cdot \frac{15}{6} = 7.85[mm] \quad (2.28)$$

$$w_{sp} = \tau_{SS} \frac{B_{ag}}{B_{St}} = 7.85 \cdot \frac{0.82}{1.7} \approx 3.5[mm] \quad (2.29)$$

Next step is to calculate the slot geometrical angle  $\alpha_s$  and the angle of tooth slice  $\alpha_{st}$ .

$$\alpha_s = \frac{2\pi}{N_s} = \frac{2\pi}{6} = \frac{\pi}{3} = 60^\circ \quad (2.30)$$

$$\alpha'_s = \frac{\pi}{N_s} = \frac{\pi}{6} = 30^\circ \quad (2.31)$$

$$\alpha_{sO} = 2 \arcsin\left(\frac{s_O}{D_{Si}}\right) \quad (2.32)$$

$$\alpha_{st} = \alpha_s - \alpha_{sO} \quad (2.33)$$

The slot opening must be determined in order to establish how much room we need to insert the windings. A compromise must be found between minimum slot opening (optimal value), where insertion of the coils is still possible and the maximum value, where cogging torque is drastically reduced.

Below we have the expression for the slot opening angle, the minimum value being:

$$\alpha_{st \min} = 2 \arcsin\left(\frac{w_{sp}}{D_{Si}}\right) \quad (2.34)$$

The expression for the maximum value of the slot opening for open slots is:

$$s_{O \max} = D_{Si} \sin\left(\alpha'_s - \frac{\alpha_{st \min}}{2}\right) \quad (2.35)$$

Again, if we go backwards with the calculus, we will obtain the following values for the parameters above.

$$\alpha_{st \min} = 2 \cdot \arcsin\left(\frac{3.5}{15}\right) = 0.471[\text{rad}] \approx 27^\circ \quad (2.36)$$

$$s_{O \max} = 15 \cdot \sin(30^\circ - 13.5^\circ) = 4.26[\text{mm}] \quad (2.37)$$

For our application, a slot opening of 1.2 [mm] is chosen. For this value, we will calculate the value of the slot opening angle and the angle of tooth slice.

$$\alpha_{sO} = 2 \cdot \arcsin\left(\frac{1.2}{15}\right) = 0.1602 = 9^\circ \quad (2.38)$$

$$\alpha_{st} = \alpha_s - \alpha_{sO} = 60^\circ - 9^\circ = 51^\circ \quad (2.39)$$

The main slot geometrical parameters are calculated with the following equations.

$$h_{s2} = \frac{\frac{s_{o\max} - s_o}{2} + h_{s3} \tan(\alpha'_s)}{\frac{1}{\tan(\alpha'_w)} - \tan(\alpha'_s)} = \frac{1.531 + 0.1732}{2.4706 - 0.5774} = \frac{1.7042}{1.8932} = 0.9[mm] \quad (2.40)$$

$$w_{s2} = s_{o\max} + 2(h_{s3} + h_{s2}) \tan(\alpha'_s) = 4.26 + 1.24 = 5.5[mm] \quad (2.41)$$

To obtain the value of the slot area, we need to know its height  $h_{s1}$  and its top width  $w_{s1}$ , as the bottom width of the slot (insulation included)  $w_{s2}$  has been calculated earlier. These three parameters combined give the slot area  $A_{slot}$ . Also, from the slot area we can easily obtain the winding area, known as copper area  $A_{co}$ , through the slot filling factor  $k_{sf}$ . The relations between the two areas are given below, with  $k_{sf}$  value chosen to be 0.4.

$$A_{slot} = w_s \cdot h_s = \frac{aN_{ph}I_{ph}}{k_{sf}J_{co}} \quad (2.42)$$

The slot width is derived from the trapeze area, knowing that  $w_{s1}$  is the top base and  $w_{s2}$  is the bottom base.

$$w_s = \frac{w_{s1} + w_{s2}}{2} \quad (2.43)$$

$$\tau_{PM} = w_s + w_{sp} = \frac{w_{s1} + w_{s2}}{2} + w_{sp} \quad .44)$$

Including the values of  $w_{sp}$  and  $\tau_{PM}$  in the equation above, we obtain the value of  $w_{s1}$ .

$$w_{s1} = 2 \cdot \left( \tau_{PM} - w_{sp} - \frac{w_{s2}}{2} \right) = 2 \cdot \left( 11.78 - 3.5 - \frac{5.5}{2} \right) = 11.06[mm] \quad (2.45)$$

Knowing the dependence between slot width  $w_s$  and slot height (depth)  $h_{s1}$ , we can find the value of the latter.

$$w_{s1} = w_{s2} + 2h_{s1} \tan(\alpha'_s) \quad (2.46)$$

$$h_{s1} = \frac{w_{s1} - w_{s2}}{2 \cdot \tan(\alpha'_s)} = \frac{11.06 - 5.5}{2 \cdot 0.577} = 4.8[mm] \quad (2.47)$$

Combining equations (2.40) and (2.47) we obtain the full slot (tooth) height  $h_s$ .

$$h_s = h_{s1} + h_{s2} + h_{s3} = 4.8 + 0.9 + 0.3 = 6[mm] \quad (2.48)$$

Including (2.46) and (2.48) in (2.42), we obtain the values of the slot area and copper area:

$$A_{slot} = w_s \cdot h_s = \frac{11.06 + 5.5}{2} \cdot 6 = 49.68[mm^2] \quad (2.49)$$

$$A_{co} = 0.4 \cdot 49.68 = 19.87[mm^2] \quad (2.50)$$

With the value of the slot area we can now obtain the value of Ampere-turns.

$$N_{ph} I_{ph} = \frac{A_{slot} \cdot k_{sf} \cdot J_{co}}{a} = \frac{49.68 \cdot 0.4 \cdot 13.5}{2} \approx 134[Aturns] \quad (2.51)$$

Next we can obtain the values of the stator and rotor yoke height, taking into account that the flux density in the stator yoke is  $B_{ys}=1.05[T]$ , while in the rotor yoke is  $B_{ry}=1.2[T]$ .

$$h_{sy} = \frac{B_{ag}}{B_{sy}} \cdot \frac{\tau_{PM}}{\pi} = \frac{0.7 \cdot 11.78}{1.05 \cdot \pi} = 2.5[mm] \quad (2.52)$$

$$h_{ry} = \frac{B_{ag}}{B_{ry}} \cdot \frac{\tau_{PM}}{\pi} = \frac{0.7 \cdot 11.78}{1.2 \cdot \pi} = 2.19[mm] \quad (2.53)$$

Now that we have also the value of the stator yoke height, the value of outer stator diameter  $D_{so}$ , equivalent with motor diameter, is:

$$D_{so} = D_{sj} + 2(h_s + h_{sy}) = 15 + 17 = 32[mm] \quad (2.54)$$

### 2.3.2 Number of turns/coil and electrical parameters

The parameter that links geometrical dimensioning and electrical parameters, through electrical loading, is the number of turns per coil  $N_{ph}$ . To find its value and

implicitly the value of the rated current in the windings, we must start the calculation with the voltage expression for rectangular current control, two phases on at a time.

$$\frac{V_{DC}}{2} = R_S I_{ph} + L_S \frac{dI_{ph}}{dt} + E_{ph} \quad (2.55)$$

Each term of this equation is reduced to an expression dependant only on the number of turns per coil,  $N_{ph}$ . First, the expression for phase back-EMF is derived.

$$E_{ph} = -\frac{d\lambda_{PM}(\theta_m)}{dt} = -\frac{d\lambda_{PM}(\theta_m)}{d\theta_m} \cdot \frac{d\theta_m}{dt} = -\frac{d\lambda_{PM}(\theta_m)}{d\theta_m} \cdot \omega_m \quad (2.56)$$

$$E_{ph} = \frac{2p}{\pi} \cdot \lambda_{PMmax} \cdot \omega_m = \frac{2}{\pi} \cdot \Phi_{PM} \cdot N_{ph} \cdot 2 \cdot \pi \cdot f \quad (2.57)$$

Replacing each known term in eq. (2.55), we obtain the relation between phase back-EMF and  $N_{ph}$ :

$$E_{ph} = 4 \cdot 3.3 \cdot 10^{-4} \cdot 500 \cdot N_{ph} = 0.66 \cdot N_{ph}[V] \quad (2.58)$$

The expression for phase resistance is:

$$R_S = \rho_{co} \cdot \frac{L_{turn} \cdot N_{ph}^2}{a \cdot \frac{N_{ph} \cdot I_{ph}}{a \cdot J_{co}}} \quad (2.59)$$

The turn length  $L_{turn}$  equation is:

$$L_{turn} = 2 \cdot \left( L_{stk} + \frac{\pi}{2} \cdot (D_{sj} + h_s) \cdot \sin(\alpha_s) \right) = 2 \cdot \left( 40 + \frac{\pi}{2} \cdot 18.06 \right) = 137[mm] \quad (2.60)$$

Now that the turn length is calculated and knowing that copper resistivity value is  $\rho_{co}=2.3 \cdot 10^{-8}$  [ $\Omega m$ ] at 105°C (working temperature), the phase resistance is:

$$R_S = 2.3 \cdot 10^{-8} \cdot 2 \cdot 13.5 \cdot 10^6 \cdot \frac{0.137}{2 \cdot 220} \cdot N_{ph}^2 = 1.9 \cdot 10^{-4} \cdot N_{ph}^2 \quad (2.61)$$

The last unknown term in equation (2.55) is the phase inductance  $L_S$ , which comprises the main inductance  $L_m$ , the leakage inductance  $L_{sj}$  and the coupling (mutual) inductance  $L_{12}$ .

The phase main inductance is calculated first, the mutual inductance is related to the main inductance and finally, the leakage inductance is calculated using geometrical slot and end connection permeances.

$$L_s = L_m + L_{12} + L_{sl} = L_m + \frac{L_m}{2} + L_{sl} = \frac{3}{2} L_m + L_{sl} \quad (2.62)$$

$$L_m = \frac{\mu_0 N_{ph}^2 \tau_{PM} L_{stk}}{2(g + h_{PM})} = \frac{4 \cdot \pi \cdot 10^{-7} \cdot 0.01178 \cdot 0.04}{2 \cdot (0.5 + 2.5)} = 9.948 \cdot 10^{-8} \cdot N_{ph}^2 \quad (2.63)$$

$$L_{sl} = 2\mu_0 N_{ph}^2 \lambda_s L_{stk} \frac{\lambda_s}{p \cdot a \cdot q} \quad (2.64)$$

To be able to calculate the leakage inductance, the stator permeance  $\lambda_s$  must be determined.

$$\lambda_s = \lambda_{ss} + \lambda_{s0} \quad (2.65)$$

$$\lambda_{ss} = \frac{h_{s1}}{3 \cdot w_{s2}} k_t + \frac{2 \cdot h_{s2}}{w_{s2} + s_0} + \frac{h_{s3}}{s_0} \quad (2.66)$$

$$\lambda_{s0} = \frac{p \cdot q \cdot D_{end}}{16 \cdot L_{stk}} \ln \left( \frac{D_{end}^2 \cdot \pi}{2 \cdot h_s (w_{s1} + w_{s2})} \right) \quad (2.67)$$

First thing is to calculate slot permeance  $\lambda_s$  by finding  $k_t$ .

$$k_t = \frac{4 \cdot \left( \frac{w_{s1}}{w_{s2}} \right)^2 - \left( \frac{w_{s1}}{w_{s2}} \right)^4 \cdot \left[ 3 - 4 \ln \left( \frac{w_{s1}}{w_{s2}} \right) \right] - 1}{4 \cdot \left[ \left( \frac{w_{s1}}{w_{s2}} \right)^2 - 1 \right]^2 \cdot \left( \frac{w_{s1}}{w_{s2}} - 1 \right)} \quad (2.68)$$

If we calculate the widths ratio we obtain a value of 2.01. Introducing this value in eq. (2.68), and afterwards its result into (2.67), we obtain the value of the slot permeance.



$$k_t = \frac{4 \cdot 2.01^2 - 2.01^4 \cdot [3 - 4 \ln(2.01)] - 1}{4 \cdot [2.01^2 - 1]^2 \cdot 1.01} = 0.342 \quad (2.69)$$

$$\lambda_{SS} = \frac{4.8}{3 \cdot 5.5} \cdot 0.342 + \frac{2 \cdot 0.9}{5.5 + 1.2} + \frac{0.3}{1.2} = 0.6181 \quad (2.70)$$

To calculate the end connection permeance, we need to determine the value of the end connection diameter  $D_{end}$ .

$$D_{end} = (D_{sl} + h_s) \sin(\alpha_s) = (15 + 6) \cdot 0.866 = 18.186 [mm] \quad (2.71)$$

$$\lambda_{s0} = \frac{2 \cdot 0.5 \cdot 18.186}{16 \cdot 40} \ln \left( \frac{18.186^2 \cdot \pi}{2 \cdot 6 \cdot (11.06 + 5.5)} \right) = 0.047 \quad (2.72)$$

Combining the results from equations (2.70) and (2.72) and introducing them in (2.64), we obtain the leakage inductance.

$$L_{sl} = 2 \cdot 4 \cdot \pi \cdot 10^{-7} \cdot \frac{0.6181 + 0.047}{2 \cdot 2 \cdot 0.5} \cdot 0.04 \cdot N_{ph}^2 = 3.343 \cdot 10^{-8} \cdot N_{ph}^2 \quad (2.73)$$

The phase inductance expression dependant on number of turns per coil can be now completed, by introducing equations (2.63) and (2.73) in (2.62).

$$L_s = \left( \frac{3}{2} \cdot 9.948 + 3.343 \right) \cdot 10^{-8} \cdot N_{ph}^2 = 14.963 \cdot 10^{-8} \cdot N_{ph}^2 \quad (2.74)$$

With the phase inductance expression, we now have all the dependences on  $N_{ph}$  and thus its value can be determined from equation (2.53), knowing that the value of  $V_{DC}$  is 150 [V].

$$\frac{149.56}{2} = 1.9 \cdot 10^{-4} \cdot N_{ph}^2 \cdot I_{ph} + 0.05 \cdot 14.963 \cdot 10^{-4} \cdot N_{ph}^2 \cdot I_{ph} + 0.66 \cdot N_{ph} \quad (2.75)$$

To eliminate the unknown parameter phase current, we can introduce the value of the Ampere-turns in the equation above, such that the only unknown term remains the number of turns per coil.

$$75 = (1.9 \cdot 134 + 0.748 \cdot 134) \cdot 10^{-4} \cdot N_{ph} + 0.66 \cdot N_{ph} \quad (2.76)$$

$$N_{ph} = \frac{75}{0.6955} \approx 108[\text{turns / coil}]$$

Now that the number of turns per coil is found, the electrical parameters of the machine, expressed before as function of  $N_{ph}$ , are calculated:

$$R_s = 1.9 \cdot 10^{-4} \cdot N_{ph}^2 = 1.9 \cdot 10^{-4} \cdot 108^2 = 2.21[\Omega] \quad (2.77)$$

$$L_s = 14.963 \cdot 10^{-8} \cdot N_{ph}^2 = 14.963 \cdot 10^{-8} \cdot 108^2 = 1.75[mH] \quad (2.78)$$

$$E_{ph} = 0.66 \cdot N_{ph} = 0.66 \cdot 108 = 71.28[V] \quad (2.79)$$

$$I_{ph} = \frac{N_{ph} I_{ph}}{N_{ph}} = \frac{134}{108} = 1.24[A] \quad (2.80)$$

### 2.3.3 Machine losses

With geometrical dimensions and electrical parameters of the machine calculated and having knowledge of the magnetic loading values, the efficiency needs to be found. The overall efficiency is derived from power balance after an accurate estimation of machine losses, which comprises mechanical, copper and iron losses.

$$P_{loss} = P_{Co} + P_{Fe} + P_{mech} \quad (2.81)$$

Usually, the mechanical losses are function of the angular speed, as expressed in equation (2.82). For the base angular speed of 1570[rad/s], we choose the mechanical losses to be around 0.67% of the base power.

$$P_{mech} = f(\omega_m) \quad (2.82)$$

$$P_{mech} = 0.67\% \cdot P_b = 0.0067 \cdot 150 = 1[W] \quad (2.83)$$

The copper losses occur in the windings whenever the current passes through the conductors. For 120° square wave current in the three phase armature winding, the value of these losses is:

$$P_{Co} = 2 \cdot R_s \cdot I_{ph}^2 = 2 \cdot 2.21 \cdot 1.24^2 = 6.8[W] \quad (2.84)$$

While the finding of copper and mechanical losses seems an easy task, the

calculation of iron losses requires an increased complexity in the formulas. With available core-loss data from iron core laminations datasheet, the iron losses can be divided in hysteresis and eddy current losses, both in the stator teeth and stator yoke [17].

$$P_{Fet} = P_{ht} + P_{et} \quad (2.85)$$

$$P_{Fey} = P_{hy} + P_{ey} \quad (2.86)$$

$$P_{ht} = \frac{1}{\gamma_{Fe}} \cdot k_h \cdot f_b^{fhe} \cdot B_{st}^{Bhe} \quad (2.87)$$

$$P_{et} = \frac{\pi^2}{6 \cdot \rho_{Fe} \cdot \gamma_{Fe}} \cdot f_b^{fee} \cdot B_{st}^{Bee} \quad (2.88)$$

$$P_{hy} = \frac{1}{\gamma_{Fe}} \cdot k_h \cdot f_b^{fhe} \cdot B_{ys}^{Bhe} \quad (2.87)$$

$$P_{ey} = \frac{\pi^2}{6 \cdot \rho_{Fe} \cdot \gamma_{Fe}} \cdot f_b^{fee} \cdot B_{ys}^{Bee} \quad (2.88)$$

In the above expressions, the following values are chosen for the unknown terms:

- The iron density:  $\gamma_{Fe} = 7.8 \cdot 10^3$  [kg/m<sup>3</sup>];
- The electrical iron resistivity @ 20°C:  $\rho_{Fe} = 61.9 \cdot 10^{-9}$  [ $\Omega$ m]
- Multiplier constant for hysteresis losses:  $k_h = 1$ ;
- Operating frequency:  $f = 500$  [Hz];
- Stator teeth flux density:  $B_{st} = 1.5$  [T];
- Lamination thickness:  $d = 0.18$  [mm];
- Frequency exponent for hysteresis losses:  $fhe = 1.1$ ;
- Frequency exponent for eddy current losses:  $fee = 2$ ;
- Flux density exponent for hysteresis losses:  $Bhe = 1.8$ ;
- Flux density exponent for eddy current losses:  $Bee = 2$ ;
- Lamination thickness exponent:  $de = 2$ .

Replacing these values in eq. (2.85) – (2.88), we obtain:

$$p_{ht} = \frac{1}{7.8 \cdot 10^3} \cdot 1 \cdot 500^{1.1} \cdot 1.5^{1.8} = 0.248 \left[ \frac{W}{kg} \right] \quad (2.89)$$

$$p_{et} = \frac{\pi^2}{6 \cdot 61.9 \cdot 10^{-9} \cdot 7.8 \cdot 10^3} \cdot 500^2 \cdot 1.5^2 \cdot (0.18 \cdot 10^{-3})^2 = 62.091 \left[ \frac{W}{kg} \right] \quad (2.90)$$

To find the total iron losses in the stator teeth, we need to calculate the teeth weight, considering the stack factor  $k_{st} = 0.6$ :

$$\begin{aligned} m_{st} &= \frac{N_s}{2} \cdot w_s \cdot h_s \cdot L_{stk} \cdot k_{stk} \cdot \gamma_{Fe} = 6 \cdot 8.28 \cdot 6 \cdot 40 \cdot 0.7 \cdot 7.8 \cdot 10^{-6} \\ &= 0.0651 [kg] \end{aligned} \quad (2.92)$$

$$P_{Fet} = (p_{ht} + p_{et}) \cdot m_{st} = (0.248 + 62.091) \cdot 0.0651 = 4.058 [W] \quad (2.91)$$

In a similar manner, the iron losses in the stator yoke are calculated.

$$p_{hy} = \frac{1}{7.8 \cdot 10^3} \cdot 1 \cdot 500^{1.1} \cdot 1.05^{1.8} = 0.130 \left[ \frac{W}{kg} \right] \quad (2.93)$$

$$p_{ey} = \frac{\pi^2}{6 \cdot 61.9 \cdot 10^{-9} \cdot 7.8 \cdot 10^3} \cdot 500^2 \cdot 1.05^2 \cdot (0.18 \cdot 10^{-3})^2 = 30.425 \left[ \frac{W}{kg} \right] \quad (2.94)$$

$$\begin{aligned} m_{sy} &= \frac{\pi}{4} \cdot \left( D_{so}^2 - (D_{so} - 2 \cdot h_{sy})^2 \right) \cdot L_{stk} \cdot k_{stk} \cdot \gamma_{Fe} \\ &= \frac{\pi}{4} \cdot (32^2 - 27^2) \cdot 40 \cdot 0.7 \cdot 7.8 \cdot 10^{-6} = 0.0506 [kg] \end{aligned} \quad (2.95)$$

$$P_{Fey} = (p_{hy} + p_{ey}) \cdot m_{sy} = (0.13 + 30.425) \cdot 0.0506 = 1.546 [W] \quad (2.96)$$

The total iron losses are found by summing the stator teeth and yoke losses.

$$P_{Fe} = P_{Fet} + P_{Fey} = 4.058 + 1.546 = 5.604 [W] \quad (2.97)$$

The total machine losses and the motor efficiency are:

$$P_{loss} = P_{mech} + P_{Co} + P_{Fe} = 1 + 6.8 + 5.604 = 13.404 [W] \quad (2.98)$$

$$\eta_n = \frac{P_b}{P_b + P_{loss}} = \frac{150}{150 + 13.404} = 0.918 \quad (2.99)$$

Finally, the geometrical dimensions are listed in Table 2.3 and the electrical parameters of the motor, including the efficiency, are listed in Table 2.4.

**Table 2.3 Geometrical dimensions and materials for designed BLDC**

Parameter	Value	Unit
<b>Topology</b>		
Number of phases $m$	3	-
Number of stator slots $N_s$	6	-
Number of rotor poles $2p$	4	-
<b>Stator geometrical dimensions</b>		
Stator outer diameter $D_{so}$	32	mm
Stator inner diameter $D_{si}$	15	mm
Stator tooth width $w_{sp}$	3.5	mm
Stator tooth height $h_s$	6	mm
Stator slot depth $h_{s1}$	4.8	mm
Stator wedge place height $h_{s3}$	0.9	mm
Stator tooth pole tip height $h_{s4}$	0.3	mm
Stator slot top width $w_{s1}$	11.06	mm
Stator slot bottom width $w_{s2}$	5.5	mm
Stator slot width $w_s$	8.28	mm
Stator slot opening $s_o$	1.2	mm
Stator yoke height $h_{sy}$	2.5	mm
Stator slot area $A_{slot}$	49.68	mm <sup>2</sup>
Stator coil area $A_{co}$	19.87	mm <sup>2</sup>
Stator pole pitch $\tau_{ss}$	7.85	mm
Stack length $L_{stk}$	40	mm
Air gap height $g$	0.5	mm
<b>Rotor geometrical dimensions</b>		
Rotor outer diameter $D_{ro}$	14	mm
Rotor inner diameter $D_{ri}$	9	mm
Permanent magnet height $h_{PM}$	2.5	mm
Rotor length $L_{rot}$	42	mm
Rotor pole pitch $\tau_{PM}$	11.78	mm
Rotor yoke height $h_{ry}$	2.19	mm
<b>Windings</b>		
Number of turns per phase $N_{ph}$	108	-
Number of slots/pole/phase $q$	0.5	-
Number of parallel current paths $a$	2	-
Slot filling factor $k_{sf}$	0.4	-

<b>Materials</b>	
Iron core	SURA® NO18
Permanent magnet	Vacodym 677 AP 215/223

Table 2.4 BLDC's electrical parameters

Parameter	Value	Unit
Base voltage $V_b$	75	V
Phase back-EMF voltage $E_{ph}$	71.28	V
Phase current $I_{ph}$	1.24	A
Output power $P_b$	150	W
Phase resistance $R_s$	2.21	$\Omega$
Phase inductance $L_s$	1.75	mH
Rated copper losses $P_{co}$	6.8	W
Rated mechanical losses $P_{mech}$	1	W
Rated iron losses $P_{Fe}$	5.6	W
Rated efficiency $\eta$	91.8	%

### 2.3.4 Active materials weights and costs

The objective of the design is to build a motor with high efficiency and low costs. Since the functioning regime of the compressor and its costs can only be estimated, based on geometrical dimensions we can calculate the initial cost of the motor. This task is achieved by computing the weights of the active materials, such as windings, stator and rotor iron cores and permanent magnet and multiplying them by their market price in US dollars.

First thing is to compute the weight of the stator components, namely iron core (teeth and yoke) and windings.

Having knowledge of the stator yoke and teeth weights, stator iron core weight can be calculated by summing equations (2.92) and (2.95).

$$m_{sFe} = m_{st} + m_{sy} = 0.065 + 0.051 = 0.116[\text{kg}] \quad (2.100)$$

The windings weight is:

$$\begin{aligned} m_{Co} &= \frac{N_s \cdot I_{turn}}{2 \cdot a} \cdot A_{slot} \cdot k_{sf} \cdot \gamma_{Co} = \frac{6 \cdot 0.137}{4} \cdot 49.68 \cdot 10^{-6} \cdot 0.4 \cdot 8.93 \cdot 10^3 \\ &= 0.037[\text{kg}] \end{aligned} \quad (2.101)$$

The next step is to calculate the rotor weight. The rotor is composed from rotor yoke and permanent magnet. Consequently, the permanent magnet weight is:

$$m_{PM} = \pi \cdot h_{PM} \cdot (D_{ro} - h_{PM}) \cdot L_{rot} \cdot \gamma_{PM} \quad (2.102)$$

In the above equation, the mass density of the magnet is given in Table 2.2 and its value is 7700 kg/m<sup>3</sup>.

$$m_{PM} = \pi \cdot 2.5 \cdot 11.5 \cdot 42 \cdot 10^{-9} \cdot 7.7 \cdot 10^3 = 0.029[\text{kg}] \quad (2.103)$$

The rotor yoke weight is:

$$m_{ry} = \pi \cdot D_{ri}^2 \cdot L_{rot} \cdot \gamma_{Fe} = \pi \cdot 81 \cdot 42 \cdot 10^{-9} \cdot 7800 = 0.021[\text{kg}] \quad (2.104)$$

The total weight of the active materials is:

$$m_{tot} = m_{sFe} + m_{Co} + m_{PM} + m_{ry} = 0.116 + 0.037 + 0.029 + 0.021 = 0.203[\text{kg}] \quad (2.105)$$

With the weights of each material calculated we can obtain the total cost of the active materials, knowing that the cost of iron is  $C_{Fe}=5$  [USD/kg], the cost of copper is  $C_{Co}=10$  [USD/kg] and the cost of PMs is  $C_{PM}=20$  [USD/kg].

$$\begin{aligned} C_{mot} &= (m_{sFe} + m_{ry}) \cdot C_{Fe} + m_{Co} \cdot C_{Co} + m_{PM} \cdot C_{PM} \\ &= 0.137 \cdot 5 + 0.037 \cdot 10 + 0.029 \cdot 20 = 1.632[\text{USD}] \end{aligned} \quad (2.106)$$

### 2.3.5 Thermal verification

One issue that concerns the functioning of the motor and consequently its design is the thermal solicitation of the windings. Compressor motor works in a closed environment with high temperatures, which may further affect the normal functioning regime. Although not very complex, thermal models are presented as a necessary part of the motor design [17, 38].

From that, we can calculate the over temperature of the windings, we know if it is in the temperature class range and we can derive from there what type of cooling is needed.

To determine winding over temperature, we have to know the frame area  $A_{frame}$ . To calculate it, we have to determine first the value of the frame length  $l_{frame}$ . Also, the cooling surface increase due to fins must be considered, which leads to  $k_f=3$ .

$$L_{frame} = L_{stk} + D_{end} = 40 + 18.186 = 58.186[\text{mm}] \quad (2.107)$$

$$\begin{aligned}
 A_{frame} &= \pi \cdot D_{so} \cdot L_{frame} \cdot kf + \frac{\pi}{2} \cdot D_{so}^2 \\
 &= \pi \cdot 32 \cdot 58.186 \cdot 0.3 + \frac{\pi}{2} \cdot 32^2 = 0.0192 \left[ m^2 \right]
 \end{aligned}
 \tag{2.108}$$

Depending on the type of cooling, a factor  $\alpha_t$  (in  $W/m \cdot ^\circ C$ ) is added. Its value may vary from 14 for unventilated frames to 100 for water-cooled frame jackets. Considering the temperature of the cooling fluid inside the compressor to be  $T_{amb}=50^\circ C$ , the value of the winding over temperature is:

$$T_w = \frac{P_{Co} + P_{Fe}}{\alpha_t \cdot A_{frame}} + T_{amb} = \frac{6.8 + 5.6}{14.2 \cdot 0.0192} + 50 = 45.6 + 50 = 95.6 \left[ ^\circ C \right] \tag{2.109}$$

Temperature class is chosen to be F, which means that the winding temperature should not exceed in the worst case  $155^\circ C$ . As can be observed from eq. (2.109), this is not the case. However, if the over temperature would be greater than the class range, the design must be redone from the start, increasing the stack length or reducing the specific tangential force.

## 2.4 Optimization

### 2.4.1 An overview of the optimization techniques

As stated before, analytical design of an electric motor must be repeated until an optimum is found. To do so in a very accurate manner and in few steps, a designer must be very experienced in this field. The more complex is the analytical model, the more time for design is needed. Luckily, these days' computers offer high data processing capabilities, so computation time is strongly reduced. However, achieving the goal of an optimum solution still relies on the experience of the designer, so alternative faster methods were searched. This way the use of optimization methods, borrowed from mathematical field, emerged as a good solution.

In the optimization of electrical machines the objective function and constraints can be computed using either the classical (circuital) approach or a numerical field computation approach, such as the FEM. In numerical field computation problems the standard prerequisites of local optimization (convexity, differentiability and accuracy of the objective function) are usually not guaranteed [1].

Stochastic methods of optimization, such as simulated annealing [21], genetic algorithm [20 – 24] and evolution strategies [14 – 16, 25 – 32] have become more popular over the last few years for optimization of electrical machines due to their high probability to find global minima and their simplicity. However, they have the disadvantage of being not very efficient, due to large computation time of the numeric field computations.



Other methods, like direct search or gradient are used in the last years for electric motor design with very good results to replace stochastic methods [17, 20]. Their advantage is the reduced computation time compared to genetic algorithms, while the optimal solution is found with same precision. In Table 2.5, a summary of the optimization methods used today for electric machine optimal design and their advantages/disadvantages are presented.

**Table 2.5 Optimization methods**

No.	Optimization methods	Types	Functionality
1.	Deterministic	<ul style="list-style-type: none"> <li>• Steepest-descent</li> <li>• Conjugate gradient</li> <li>• quasi-Newton</li> </ul>	<i>Not ideal</i> (discretization errors, numerical inaccuracy)
2.	Non-iterative	<ul style="list-style-type: none"> <li>• Artificial neural network</li> </ul>	<i>Working</i>
3.	Stochastic	<ul style="list-style-type: none"> <li>• Simulated annealing</li> <li>• Genetic algorithm</li> <li>• Evolution strategies</li> <li>• Population-based incremental learning (PBIL)</li> </ul>	<i>Successful</i>

Optimization of a process can be applied to the whole entity, like for the entire drive (motor, electronics and control), or can be employed for each part of the process, with separate objective functions and performance criteria. However the case may be, the first to be optimized is the motor. The criterion can be to minimize the manufacturing and exploitation costs, to obtain a better efficiency, to develop a certain amount of torque, to reduce torque pulsations or any combination of the aforementioned objectives.

For example, to improve the efficiency, the losses must be reduced. Of course, through detailed and experienced eye, a very good efficiency can be obtained via analytical design. However, optimization process can improve even further this objective, minimizing copper, iron, or mechanical losses. This thing is not very easy to achieve because, in terms of copper losses, any change in the number of turns per phase let's say can affect the design either in terms of material costs, either in terms of output torque. So, a balance must be found between the two extreme cases [17].

In terms of keeping the costs at lowest values, as possible as it can, one must think of all the costs involved in mass production of the motor. Since we are talking in terms of millions of units per year, especially when it comes to home appliances industry, each dollar saved through optimal design translates into millions of dollars saved at the end of the year. But when it comes to costs, nothing is simple. To cut down expenses, the designer must consider and weight each and every possible cost

involved in mass production and that is not an easy task. One must take a look at the big picture and see what is included in the total amount, from the step where the motor is designed until the product comes out the factory and is delivered to the client:

**1. Designing costs** (research materials, designer's wages, powerful computer, design software etc.);

**2. Material used to build the electric machine:**

**a) Active material** – stator coils, magnetic soft material cores, permanent magnets;

**b) Passive material** – bearings, shaft, ventilation system, winding terminal, connection box;

**3. Costs related to manufacturing** (adaptation of the production line, raw material storage, special tools, writing the specifications, teaching the workers, acquisition of new components for the production line, etc.);

**4. Indirect manufacturing costs** (electrical energy, water consumption, wages, taxes etc.);

**5. Costs for marketing the product**

As can be seen, the total amount to produce a drive involves several departments, from managers to financial department and engineers. As it is beyond the scope of this work to take into account every economical aspect involved in the production of an electric drive, the design will consider for the objective function only the costs that can be derived directly from the motor geometrical parameters. Though it is only a small portion of the total amount, it can offer an insight of whether the chosen motor topology serves the final purpose and it can fit the price range, while being better than any competitor's motor, or is not worth trying to develop an entire drive based on it.

The aim of the optimal design presented in this chapter is to find the compromise between two rather opposite criteria, the initial cost of the motor and the efficiency. Since the cheapest version doesn't necessarily means that is the most efficient one and vice versa, the optimum between those two must be found.

#### 2.4.1.1 Mathematical formulation of optimization problem

The optimization of an electrical machine can be formulated as a general constrained optimization problem with more than one objective, as can be seen in Fig. 2.11. Finding the extremum of vector optimization problems is defined as [1]:

$$\text{Extr } F(x) = \text{Extr} [f_1(x), f_2(x), \dots, f_k(x)] \quad (2.110)$$

where  $F: R^n \rightarrow R^k$ ;  $g_j, h_j: R^n \rightarrow R$ ;  $x \in R^n, x = (x_1, x_2, \dots, x_n)$  subject to specified equality and inequality constraints:

$$\begin{aligned} g_i(\mathbf{x}) &\leq 0, & i = 1, 2, \dots, m \\ h_j(\mathbf{x}) &= 0, & j = 1, 2, \dots, p \end{aligned} \quad (2.111)$$

And specified limits for the independent variables:

$$x_{min} \leq x \leq x_{max} \quad (2.112)$$

In the equation above,  $F(\mathbf{x})$  is the vector objective function with the objectives  $f_i(\mathbf{x})$  to be minimized,  $\mathbf{x}$  is the vector of design variables used in the optimization,  $g_i$  are the inequality constraints,  $h_j$  are the equality constraints, and  $\mathbf{x}_{min}$  and  $\mathbf{x}_{max}$  are vectors of lower and upper bounds for the design variables [1,17].

In vector optimization problems there is a conflict between the individual objective functions  $f_i(\mathbf{x})$  since there exists no solution vector  $\mathbf{x}$  for which all objectives gain their individual minimum. Vector optimization problems can be transformed from multi-objective optimization into single objective optimization using the method of objective weighting. The estimation of the weighting factors and the optimization starting point are subjective choices and their influence can rarely be estimated in advance. A more practical method of optimization is to minimize only one objective function while restricting the others with appropriate constraints. Most constraints will be upper or lower bound inequality constraints, which mean constraint optimization procedures are required.

### 2.4.1.2 Nonlinear programming methods

In nonlinear programming both the objective and constraint functions may be nonlinear. There is no general agreement to the best optimization method or approach. This type of programming was divided into direct search methods, stochastic methods and gradient methods.

#### 2.4.1.2.1 Direct search methods

These methods are minimization techniques that rely solely on values of the objective function, plus information gained from earlier iterations. Also, there are three distinct classes of direct search, tabulation, sequential and linear methods.

**Tabulation** methods assume that the minimum lies within a known region.

**Sequential** methods investigate the objective function by evaluating the function at the vertices of some geometric configuration in the space of independent variables. The **simplex** method evaluates the objective function of  $n$  independent variables at  $(n+1)$  mutually equidistant points, forming the vertices of a regular simplex [13].

**Linear** methods use a set of direction vectors to direct the exploration. Currently, there are many linear methods available, like: the alternating variable search method, Rosenbrock's method, Davies, Swann and Campey method, Powell's method and last, but not least, Hooke and Jeeves method [16 – 20].

The main drawback of numerical methods is the algorithm convergence to a

local optimum which could be far away from the global optimum. The optimization algorithm could fail in a local minimum, even if the objective function is a unimodal function due to constraints. The probability to find the global minimum is increasing by starting the optimization algorithm from several initial points, chosen by the designer or in a random fashion.

#### 2.4.1.2.2 Stochastic methods

There are several widely used stochastic methods and they will be presented below.

**Simulated annealing** (SA) method generates a sequence of states based on an analogy from thermodynamics where a system is slowly cooled in order to achieve its lowest energy state [21].

**Multiple-restart stochastic hill-climbing** (MRSH) initially generates a random list of solution vectors of the independent variables, using binary vectors.

**Genetic algorithm** (GA) is rooted in the mechanisms of evolution and natural genetics. A GA combines the principle of survival of the fittest with a randomized information exchange. GAs generate a sequence of populations by using a selection mechanism, and use crossover as the search mechanism to guide the search towards the optimal solution [20 – 24].

**Population-based incremental learning** (PBIL) is a combination of evolutionary optimization and hill-climbing. PBIL is an abstraction of the GA that maintains the statistics of the GA, but abstracts away the crossover operation and redefines the role of population [25 – 27].

#### 2.4.1.2.3 Gradient methods

The core of this type of methods is to select the direction  $\mathbf{s}_i$ , of the  $n$  dimensional direction vector, using values of the partial derivatives of the objective function  $F$  with respect to the independent variables, as well as values of  $F$  itself, together with the information gained from earlier iterations.

The most used gradient methods are steepest descent method, Newton's method and quasi-Newton method.

#### 2.4.1.3 Constrained optimization techniques

Constrained optimization problems are generally transformed to unconstrained ones and are then optimized using one of the nonlinear programming methods described above. Some of the techniques used on constrained problems are feasible direction method, penalty function, sequential unconstrained minimization technique and augmented Lagrangian function or multiplier penalty function.

Penalty function transforms the optimization problem to include the constraints which enable  $F$  to be maintained while controlling constraint violation by penalizing them. Exact penalty function is similar to the classical penalty function except that the

absolute values of the constraints are used.

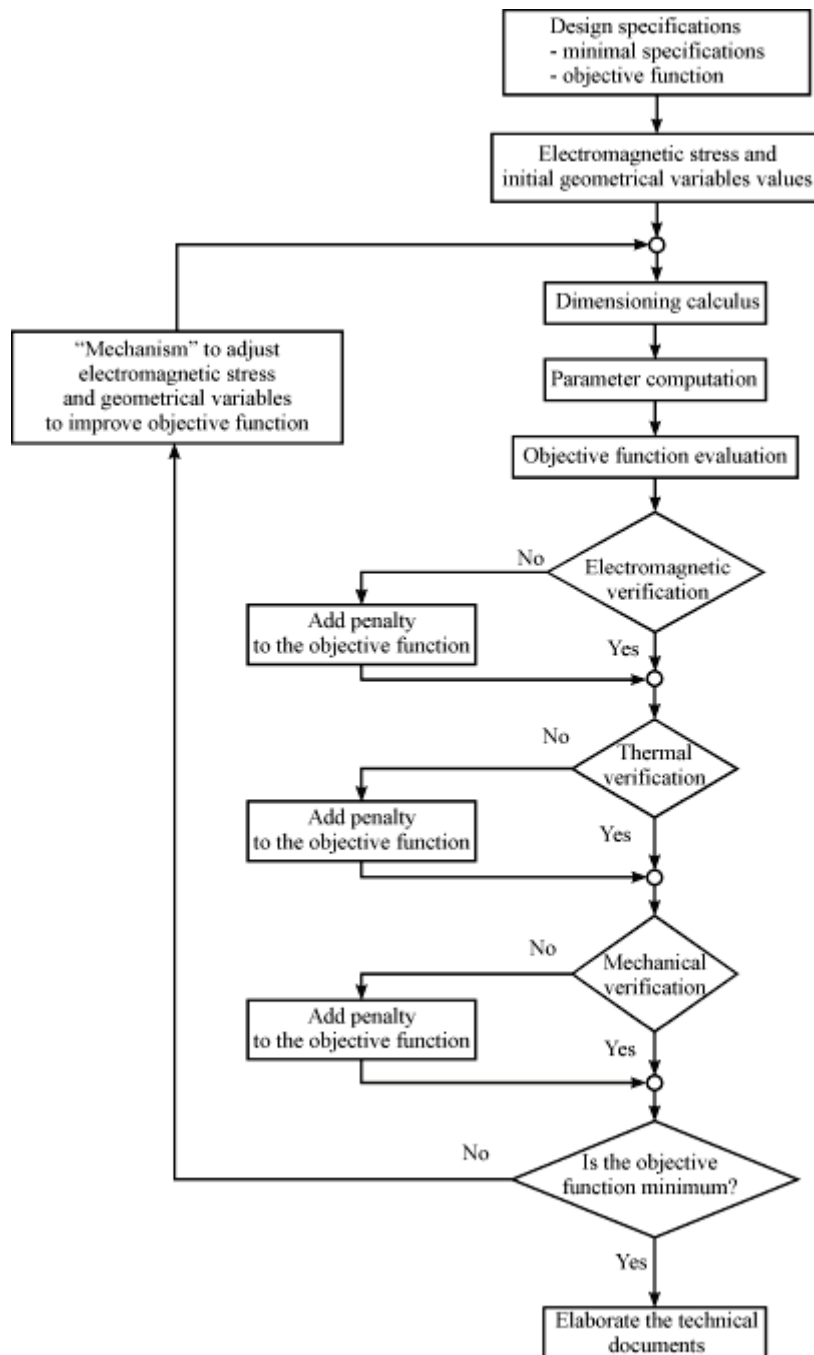


Fig. 2.11 Optimal design flow chart [17]

### 2.4.2 Optimization problem definition

Whilst the dimensioning calculus and verification are done by computer, the pillars of the design, selection of electric and magnetic loadings and initial geometric parameters, are chosen by the designer for the analytical design. To overcome the human bias, optimal design is working in a certain range of values to find the global optimum. Since the analytical approach was discussed earlier in this chapter, now it is time to develop the usage of two different optimization techniques in electrical machine design.

As in the classical design approach, the first step is to establish the boundaries of the geometrical parameters and the electric and magnetic stresses, either by designer or randomly, within a certain domain. What need to be specified from the beginning are the minimal performance criteria and the objective function. The calculus of the machine dimensions is done as in the previous case, followed by electromagnetic, thermal and mechanical verifications. The novelty is that penalties are used for every criterion that is not fulfilled. If the penalties are judiciously chosen, the requirements will be fulfilled in the end.

How the minimum objective function is achieved and how the new stresses are chosen before each calculus cycle is solely dependent on the optimization method used for motor design. If the optimization method is chosen carefully, and with the aid of the computer, this can greatly reduce the calculation time and give better results than for analytical design technique, because it can logically follow the best way to achieve the original requirements.

Besides the design and technological specifications and limitations, other essential parts for optimization are the choice of the variables to be optimized and the definition of the objective function, including the penalties.

#### 2.4.2.1 Choosing the optimization variables

Based on what kind of application the motor will be used and the particularities and constraints imposed by this, the optimization variables are carefully chosen and grouped in a vector. For both optimization algorithms presented in this chapter, the variables vector is:

$$\bar{X} = (D_{Si}, D_{So}, h_{s4}, h_{s3}, h_{sy}, w_{sp}, L_{stk}, s_o, h_{PM}, g)^T \quad (2.113)$$

In this case, the variables in the vector have the following meanings:  $D_{Si}$  – internal stator diameter,  $D_{out}$  – outer stator diameter,  $h_{s4}$  – stator tooth pole tip height,  $h_{s3}$  – stator wedge place height,  $h_{sy}$  – stator yoke width,  $w_{sp}$  – stator tooth width,  $L_{stk}$  – stator core stack length,  $s_o$  – stator slot opening width,  $h_{PM}$  – permanent magnet height and  $g$  – air gap height.

Since the optimization process of these variables must find an optimal solution in a given interval, the lower and upper bounds of each variable are give in Table 2.6.

**Table 2.6 Minimum and maximum values of the optimized variables**

Variable	Symbol	Minimum	Maximum	Units
Inner stator diameter	$D_{si}$	10	30	mm
Outer stator (motor) diameter	$D_{so}$	15	60	mm
Stator tooth pole tip height	$h_{s4}$	0.2	1.5	mm
Stator wedge place height	$h_{s3}$	0.5	2	mm
Stator yoke width	$h_{sy}$	1	5	mm
Stator tooth width	$w_{sp}$	1.8	6	mm
Stator core stack length	$L_{stk}$	10	80	mm
Stator slot opening width	$s_o$	0.6	5	mm
Permanent magnet height	$h_{PM}$	0.5	5	mm
Air gap height	$g$	0.3	1	mm

The designed brushless DC motor is meant to be used in a compressor for refrigeration systems, where the space is a major constraint. Thus, the challenge is to optimize the geometry of the motor to fit in that space, to provide the requested torque and to be cost effective. From this point of view, one of the variables that must be optimized is the outer diameter of the motor.

The air gap also must be considered, because it affects mainly the PM flux circulation. A very large air gap will require a stronger magnet to produce the same amount of flux which will increase the production costs. On the other hand, a very small air gap is not acceptable due to manufacturing irregularities that may affect the placement of the rotor that may lead to direct contact between the rotor and the stator.

The amount of magnetic flux necessary to obtain a certain output torque is given by the permanent magnet height. However, the magnet influences also the cogging torque, the total price (it is the most expensive part in the motor) and the motor efficiency, thus an optimum height must be found as a compromise between these elements.

Other variables to be optimized are related to the stator tooth shape, core length and pole span, in order to be easy to manufacture, proper for winding insertion and to occupy the given space in the compressor.

#### 2.4.2.2 Choosing the objective function

While the optimization "objects" were presented in the previous sub-section, the objective of the process is presented here. As stated from the beginning, the goal of this design is to develop an electric motor that can be highly efficient and low cost at the same time. These two objectives are somehow opposed, as one knows that is hard to find something cheap and good. However, there is a threshold where the final price

of the motor is affordable and its efficiency is high enough to satisfy both the manufacturer and the client. This is why the objective function is the total cost of the motor. At the end of the analytical design, an initial cost was calculated taking into account the cost of active materials. However, the manufacturer should be also concerned on how much electric energy the motor will consume in the final product and how much this will cost the customer. This is expressed by adding another term based on the motor efficiency, number of functioning hours per year ( $hpy$ ) and the number of years ( $ny$ ) in which the compressor is supposed to work. Thus, the formula expressed in eq. (2.106) becomes:

$$C_{mot} = (m_{sFe} + m_{ry}) \cdot C_{Fe} + m_{Co} \cdot C_{Co} + m_{PM} \cdot C_{PM} + \frac{P_b \cdot \left( \frac{1}{\eta_n} - 1 \right)}{hpy \cdot ny} \cdot C_{en} \quad (2.114)$$

A concerning issue regarding the motor design is the thermal verification of the calculated topology, as the windings and magnet over temperature shortens the life of the motor and can cause serious damage to the whole mechanism. This is why the exceeding over temperature should be an integrating part of the penalty function.

$$C_{pt} = \max(0, T_w - T_{wad}) \cdot k_t \cdot C_{mot} + \max(0, T_r - T_{rad}) \cdot k_t \cdot C_{mot} \quad (2.115)$$

In the equation above, the first term is the over-temperature penalty function for windings and the second one is the over-temperature penalty function for permanent magnets, where  $T_w$  and  $T_r$  are windings and rotor calculated temperatures,  $T_{wad}$  and  $T_{rad}$  are windings and rotor maximum admissible temperatures,  $k_t$  is a proportional factor and  $C_{mot}$  is the initial cost of the motor, as stated in eq. (2.114).

The efficiency criterion is of highly importance in the final cost of the motor, thus it should also be included in the penalty function. If the design is not capable of achieving a minimum efficiency, then the final cost of the motor should be adjusted accordingly, replacing the term regarding the electrical energy losses costs in the eq. (2.114) with the one below:

$$C_{pe} = \frac{P_b \cdot \left( \frac{1}{\eta_n} - \frac{1}{\eta_{min}} \right)}{hpy \cdot ny} \cdot C_{en} \quad (2.116)$$

On a similar manner, a penalty function might be added if the average torque is not achieved via the motor design. Compared to other penalties, this function is not only adding cost if the objective is not fulfilled, but reduces the initial cost value if the average torque is higher than the analytical value by at least 10%.

$$C_{ptrq} = \left( \max(0, T_{avmin} - T_{av}) - \max(0, T_{av} - T_{avmax}) \right) \cdot k_{tav} \cdot C_{mot} \quad (2.117)$$



In the equation above,  $T_{av}$  is the calculated average torque,  $T_{avmin}$  is the minimum admissible value of the average torque, which is 90% of the analytical average torque,  $T_{avmax}$  is the value of the average torque above which the initial cost can be reduced (110% of the analytical average torque),  $C_{mot}$  is the initial cost of the motor and  $k_{tav}$  is the average torque coefficient.

For surface permanent magnet machines, the cogging torque is a drawback that can cause noise and vibration, thus its limitation in the preliminary design is important. Though its complete elimination is not possible due to motor geometry, a minimum value can be imposed. The penalty function for cogging torque is expressed as:

$$C_{pcg} = \max(0, T_{cg} - T_{cgmin}) \cdot k_{tcg} \cdot C_{mot} \quad (2.118)$$

In the equation above,  $T_{cg}$  is the calculated cogging torque,  $T_{cgmin}$  is the minimum admissible value of the cogging torque and  $k_{tcg}$  is the cogging torque penalty coefficient.

Summing up all the penalty function components, the penalty function is:

$$C_p = C_{pt} + C_{pe} + C_{ptrq} + C_{pcg} \quad (2.119)$$

With the penalty function and initial costs defined, the objective function is expressed as:

$$f(\bar{X}) = C_{mot}(\bar{X}) + C_p(\bar{X}) \quad (2.120)$$

The task of the optimization algorithm is to find the minimum of this function, adjusting the motor geometry until the best configuration, in terms of cost and efficiency is achieved.

### 2.4.3 Hybrid analytical/FEM modified Hooke-Jeeves optimization algorithm

The Hooke-Jeeves optimization algorithm is a grid search algorithm using two kinds of moves: exploratory moves and pattern moves. A modified version of Hooke-Jeeves algorithm was applied for constrained system optimization using external penalty functions in [17 – 20] with very good results, even in comparison to classical optimization methods like genetic algorithm [17, 20].

In this section, the algorithm description is presented and then optimization results for machine design are shown.

### 2.4.3.1 Algorithm description

For our application, the optimal design was further modified by addition of another step, becoming a hybrid analytical/FEM algorithm [16]. While efficiency and temperature can be calculated analytically, the torque components are quite complex to be found through classical ways. The best way, although more time consuming, is to call finite element software and obtain the cogging and average torque values.

Along with this addition, the optimization algorithm contains the following steps [16 – 20]:

1. Choose the variables to be optimized and the constant geometrical dimensions and grouping them in a vector, as in equation (2.113).
2. Implement the geometrical constraints previously mentioned, find the technological limitations and use them to bound the optimization range between minimum and maximum limits:

$$\bar{X}_{min} \leq \bar{X} \leq \bar{X}_{max} \quad (2.121)$$

Equality and inequality constraints are expressed in equation (2.111).

3. The next step is to choose the objective scalar function. In order to meet the objective, the constraints should be introduced in the objective function via a penalty function. The final form of the objective function is the one expressed in (2.120).

The members of the final form are the objective scalar function  $C_{mot}$  and the penalty function  $C_p$ . The objective scalar function is defined as:

$$C_{mot}(\bar{X}), C_{mot} : \mathfrak{R}^n \rightarrow \mathfrak{R} \quad (2.122)$$

The penalty function is defined as:

$$C_p = \sum_{i=1}^{p+q} C_{pi} \left( g_i(\bar{X}) \right), C_p : \mathfrak{R}^{p+q} \rightarrow \mathfrak{R}_+ \quad (2.123)$$

The value of the function  $C_{pi}$  is 0 for  $1 \leq i \leq p$  and  $g_i(\bar{X}) = 0$  and for  $p+1 \leq i$  and  $g_i(\bar{X}) \leq 0$  and is monotonic positive in all other cases.

4. The next step is to choose the initial values of the optimized variable vector,  $\bar{X}_0$ , the initial step vector  $\bar{dX}_0$ , minimum step vector  $\bar{dX}_{min}$  and the step actualization ratio  $r$ , with  $0 < r < 1$ .

Any experienced designer can start from fixed values in the optimization range, thus reducing the overall computation time. However, to overcome any human error that may occur in the process and to improve the chances of finding the optimal value of the objective function, the initial values of the variables can be chosen randomly and the algorithm must run several times.

In our case, the initial values were chosen randomly between the boundaries and the modified Hooke-Jeeves algorithm ran 5 times, each time starting with another random set of values.

5. After finishing the initial phase of the design, where the objectives are defined, the optimization variables are established, the constraints implemented as penalty function and the objective function accurately defined, the next step is to compute all necessary geometric values and the motor's performance from the analytical model.

6. This step is the one where the algorithm becomes hybrid. FEM is called to evaluate the parameters of the penalty function, the cogging torque and the average torque respectively.

For cogging torque it is easy to calculate the peak-to-peak value, because its extreme values occur whenever the magnets edges pass one tooth edge or another. The expression of the minimum and maximum cogging torque values angles are:

$$\alpha_{cgmin} = \frac{\alpha_{sp}}{2} \quad (2.124)$$

$$\alpha_{cgmax} = \frac{2\pi}{N_s} - \frac{\alpha_{sp}}{2} \quad (2.125)$$

As a result, the machine built in FEM will be rotated, without current in the windings, only to these two points and the cogging torque values will be obtained via the Maxwell stress tensor. A more detailed explanation of how finite element is used to compute torque values, at zero current and at full current, will be presented in the next chapter.

The average value of the torque is found through the following expression:

$$T_{avg} = \frac{6}{\pi} \int_0^{\pi/6} Trq(\theta) d\theta \quad (2.126)$$

Calculation of the average value of the torque over one electrical cycle with minimum FEM calls is presented in [53 – 55] and it is based on flux-MMF diagram or “i -  $\psi$ ” loop. This method is completely general for computation of any synchronous machine providing as output the average torque and inductances over one electrical cycle. Fig.2.12 exhibits the current and flux linkage waveforms over phase A with the key points identified. Those key points are on the boundary of the loop, as can be seen in Fig.2.13, and their number gives the number of FEM solutions.

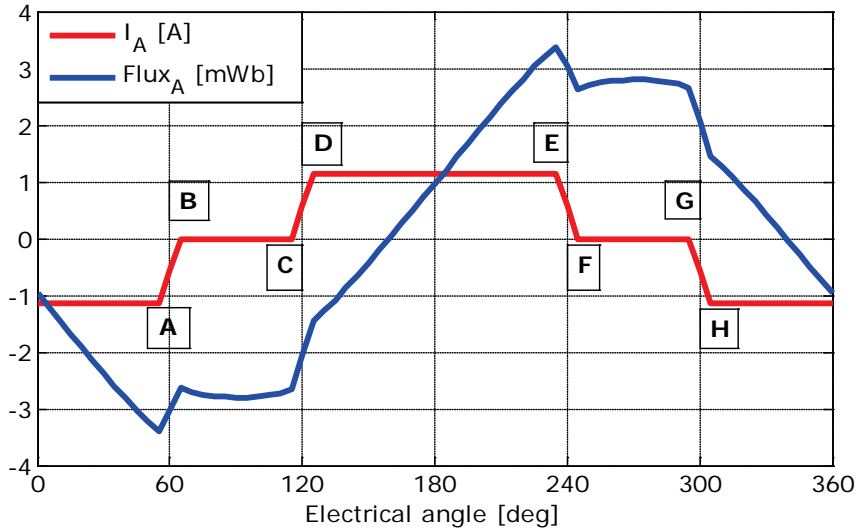


Fig.2.12 Current and flux linkage waveforms

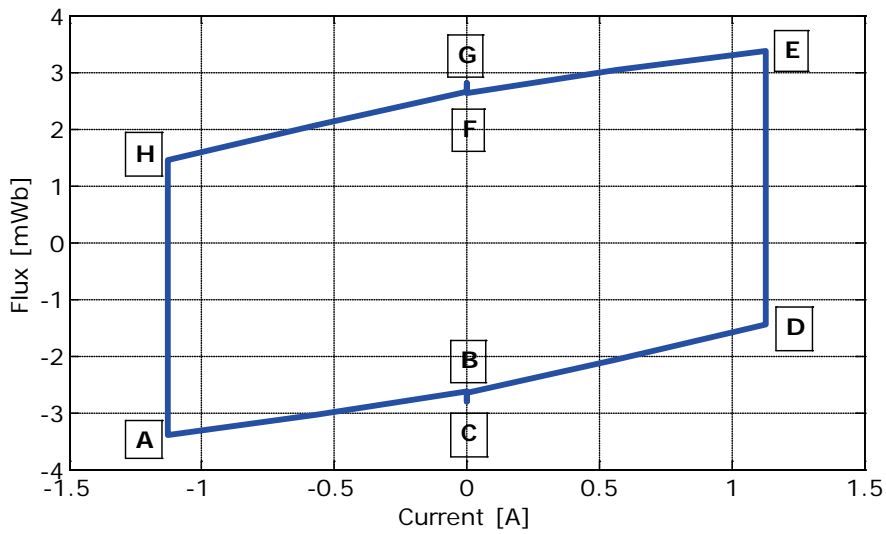


Fig.2.13 "i – ψ" loop for squarewave drive

The area of the flux-MMF diagram is proportional to the average electromagnetic torque and it is expressed as:

$$T_{avg} = mp \frac{W}{2\pi} \quad (2.127)$$

From the regular shape of the “i -  $\psi$ ” loop, the area of W can be estimated as twice the area of the parallelogram BDEF and:

$$W = 2i_{pk}(\psi_E - \psi_D) \quad (2.128)$$

Furthermore, by introducing (2.128) in (2.127), for the 6/4 motor configuration, the value of the average torque is:

$$T_{avg} = \frac{6}{\pi} \cdot i_{pk} \cdot (\psi_E - \psi_D) \quad (2.129)$$

From (2.129), we can see that is enough to analyze the magnetic field in only two points to obtain the value of the flux linkage via FEM. From equations (2.124) and (2.125), the peak-to-peak value of the cogging torque is calculated by acquiring its minimum and maximum values in other two points via FEM. Thus, the usage of FEM limits to only four points of the field, which requires only a small amount of computation time.

7. Make a research movement along each optimized variable in positive and negative direction, local grid search, using the initial step as it is shown for a two dimension vector. Compute the objective function and then compute the objective function gradient:

$$\bar{h} = (h_1, h_2, \dots, h_n) = \left( \frac{\partial f}{\partial x_1}, \frac{\partial f}{\partial x_2}, \dots, \frac{\partial f}{\partial x_n} \right) \quad (2.130)$$

The partial derivative is computed numerically using function evaluation in 3 points along k direction.

$$\frac{\partial f}{\partial x_k} = \begin{cases} \frac{f_k - f_0}{dx_k} & \text{if } f_{-k} \geq f_0 > f_k \\ \frac{f_0 - f_{-k}}{dx_k} & \text{if } f_{-k} < f_0 \leq f_k \\ \frac{f_k - f_{-k}}{2dx_k} & \text{if } f_{-k} < f_0 > f_k \\ 0 & \text{if } f_{-k} > f_0 < f_k \end{cases} \quad (2.131)$$

where  $f_k$  is the objective function evaluation in point  $\bar{X}_k$  obtained from  $\bar{X}_0$  by moving along k direction with  $dx_k$ , respectively  $-dx_k$  for  $f_{-k}$ . The point  $\bar{X}_0$  is placed on the slope in the first and second case from equation above. The  $\bar{X}_0$  is the worst point in case 3, respectively, the better point in case 4. In the last two cases the partial derivative is

not mathematically correct but it provides information to leave the worse point or stay near the good point. The step along gradient is computed:

$$\bar{\Delta} = (\bar{\Delta}_1, \bar{\Delta}_2, \dots, \bar{\Delta}_n) = \left( \frac{h_1 \cdot dx_1}{\bar{h}}, \frac{h_2 \cdot dx_2}{\bar{h}}, \dots, \frac{h_n \cdot dx_n}{\bar{h}} \right) \quad (2.132)$$

8. Make an optimized variable vector movement with step  $\bar{\Delta}$  until the objective function is decreasing.

9. Repeat the research movement (steps 5 and 6) in order to find a new gradient direction and then repeat the gradient movement (step 7), until the research movement is not able to find better points around the current point. This condition is equivalent to  $\|\bar{h}\| = 0$ .

10. Reduce the variation step by ratio  $r$  and repeat the previous steps until the minimum of the variable variation is reached and the gradient norm vanish. When the research movement can't find better points even using the smallest variable variation, then a minimum objective function is reached with the given resolution. Probably this is not the global minimum, thus the algorithm runs several times with random initial values of optimized variables in order to increase the probability to find the global minimum. Optimization algorithm may start with a 1.6 [mm] variation step for all variables and then this is reduced by ratio 2 until it reached the minimum value equal by 0.1 [mm]. The minimum step value is usual chosen around the technological permissible variation. The variation step should be a vector for a large machine because the ratio between the largest dimension and smaller dimensions could be hundreds or thousands.

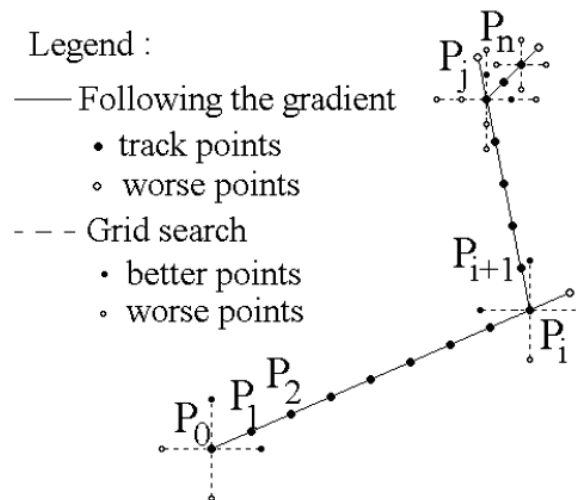


Fig. 2.14 Search and gradient movement considering a 2D optimization problem [17]

### 2.4.3.2 Optimization results

After the algorithm steps were presented and optimal design ran 5 times to be sure that it will find the optimum, it is time to show the results for the best optimization run of the algorithm.

First, in Fig. 2.15, the evolution of the main geometrical dimensions of the machine are shown, the inner and outer stator diameter and the stack length. It can be seen that the only parameter that doesn't vary too much is the outer stator diameter.

In Fig. 2.16 the evolution of stator geometrical variables is shown, respectively for stator tooth wedge place and pole tooth tip heights, tooth width, yoke height and slot opening width. It can be observed that the slot opening remains constants during the whole period, while the optimal values for the others are found very fast, after 25 optimization steps. Finally, the air gap height and permanent magnet height evolution is presented in Fig. 2.17.

As in analytical design, the next step after geometrical dimensions evolution is to show the copper and iron core losses. The losses are presented in Fig. 2.18, while the electrical efficiency variation is shown in Fig. 2.19. It can be seen that the efficiency varies from 90% up to 94% after a short number of steps.

In Fig. 2.20 the PM and total motor weights are presented. As can be seen, the magnet weight doesn't vary too much, mostly because its height doesn't vary in a large range. Also, it can be observed that at the beginning, the motor is bulkier though not efficient, which means that an increase in motor mass is not necessarily an improvement in terms of efficiency. In Fig. 2.21, one can observe the evolution of the motor total costs, reduced at almost half during the optimization process.

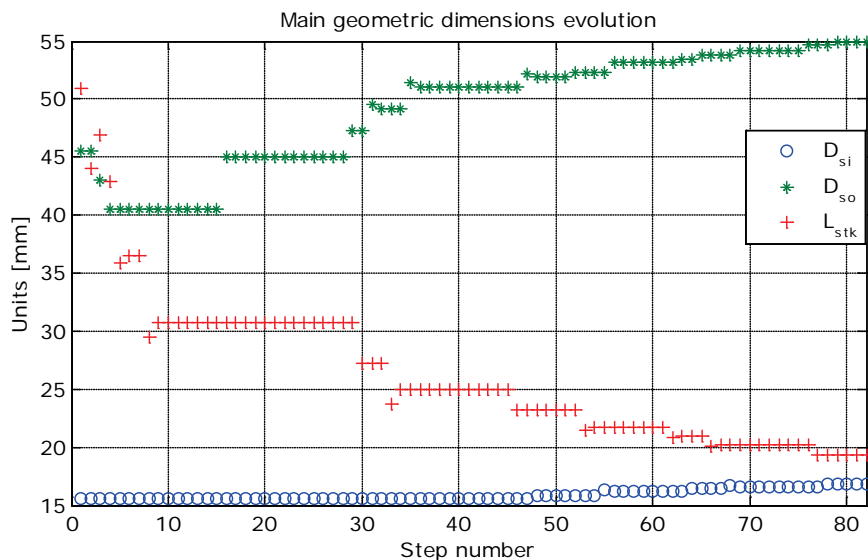


Fig. 2.15 Main geometric dimensions evolution

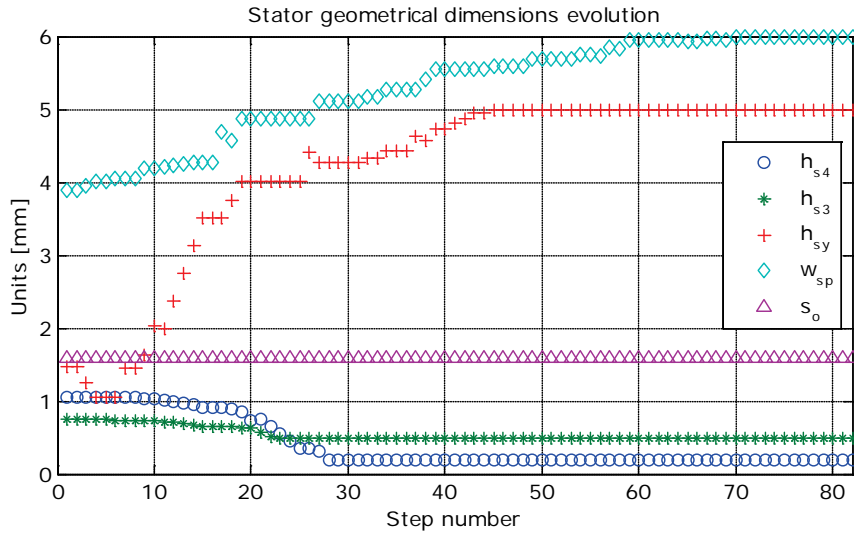


Fig. 2.16 Stator geometrical dimensions evolution

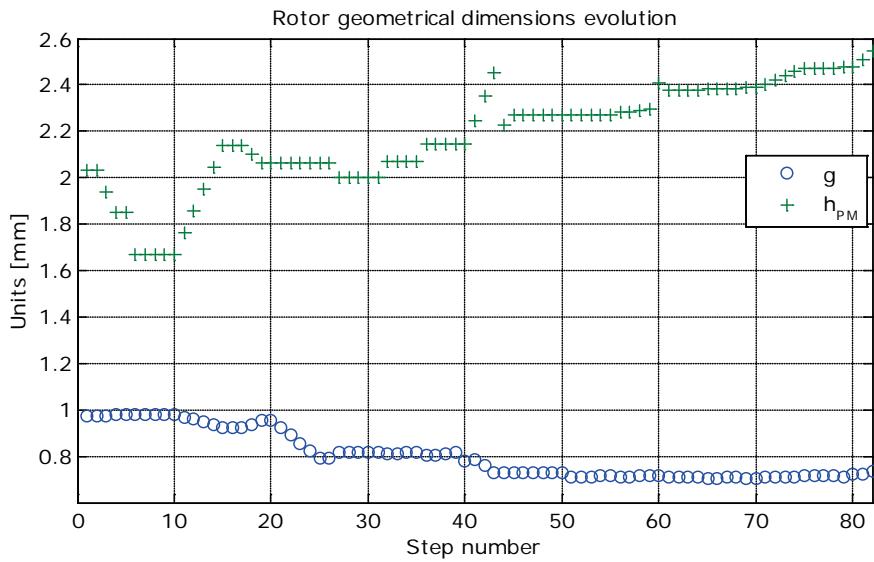


Fig. 2.17 Air gap and permanent magnet heights evolution



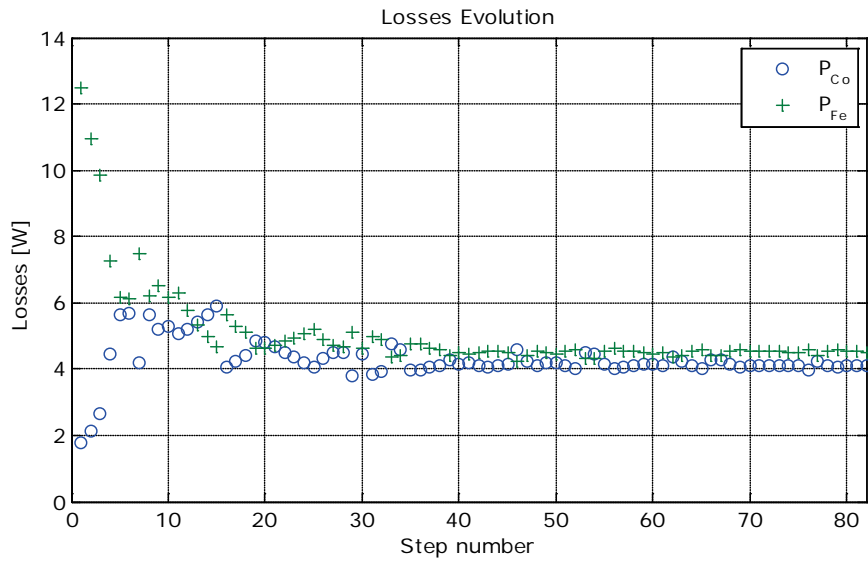


Fig. 2.18 Motor losses evolution

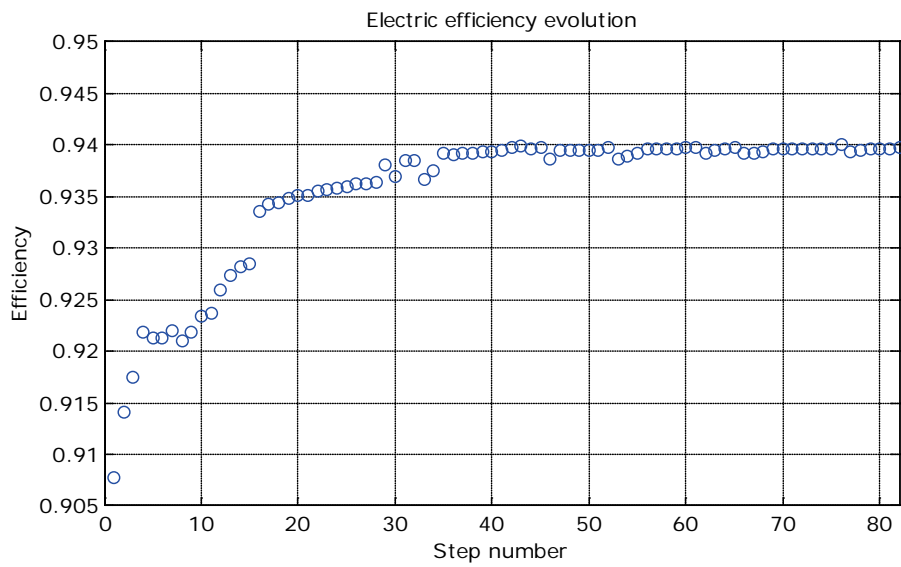


Fig. 2.19 Electric efficiency evolution

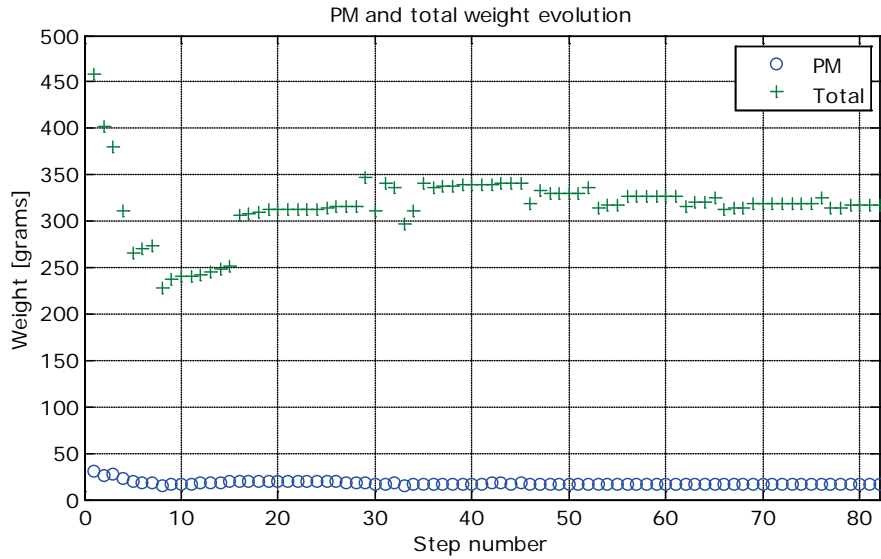


Fig. 2.20 Permanent magnet and motor weight evolution

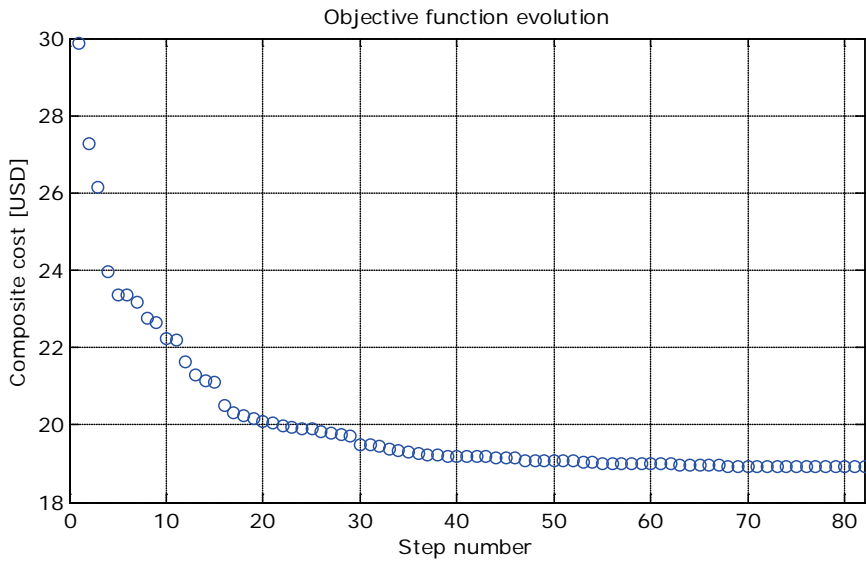


Fig. 2.21 Objective function evolution

In the figures above only the best solution is shown, taking 82 steps to reach the optimum. The optimization process took 1437 seconds to run 5 times. Without FEM and ran only once, the optimization algorithm took only 90 seconds. So, to be sure that the global optimum is found and by introduction of the finite element analysis, the computation time increased by almost 16 times.

#### **2.4.4 Hybrid analytical/FEM artificial bee colony (ABC) optimization algorithm**

Classical optimization methods become more and more inefficient as the problems that need to be solved through this process become more and more complex. To overcome the limitations of classical methods for larger scale combinatorial or highly non-linear problems, new methods emerged. As previously presented, direct search methods are one robust type of optimization, but during the last years, methods inspired from nature gain interest [43 – 52].

Although they are placed in the same optimization class as genetic algorithms, they can provide better computation time and similar results, which makes them competitive with direct search methods.

A special type of this nature inspired algorithms is swarm optimization. Swarm intelligence is based on the ability of different groups of insects, animals or even cells to work organized in order to insure the wealth of the entire community. Developed in thousands of years of adaptation to the surroundings, their evolution and survival are the cornerstones of swarm optimization. For motor design, the goal is to obtain a highly efficient topology with minimum costs. For swarms, the goal is to reach the best food source with minimum of energy or to obtain better offspring by selected mating between the queen and the most fitted males of the species. Since the goals are similar, the swarm's behavior can be imitated and introduced in optimization algorithms.

As there is a variety of swarms, each with their own way to adapt to the surroundings, there is a variety of optimization algorithms based on them. The most popular are particle swarm optimization (PSO), ant colony optimization (ACO) and algorithms based on bees' behavior, like bee colony optimization (BCO), used in transportation [43, 44], or variants of the artificial bee colony (ABC) algorithm [16, 45 - 52].

The latter one was chosen for electrical machine optimization because, when compared to other swarm intelligence algorithms, in ABC algorithm the possible solutions represent food sources (flowers), not individuals (honeybees) [49].

ABC algorithm was introduced in 2006 by Derviş Karaboğa [45], based on foraging behavior of the bees and developed later on [46 – 52]. From his initial report we find the basics of the ABC method, respectively the elements of the optimization and the way to retain the best information.

For starters, the food sources represent random values of the variables vector that will be explored by the employed foragers. They carry with them information about the source, like distance from the hive, direction and profitability. Once they get to the hive, they unload the nectar harvested from the food source and perform a waggle dance (Fig. 2.22) for the unemployed bees, giving them the information about the source.

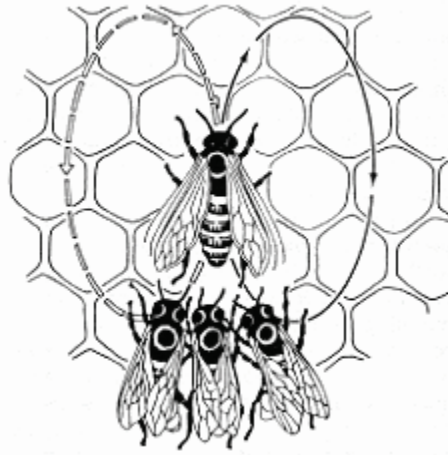


Fig. 2.22 Employed bees performing a waggle dance [47]

There are two types of unemployed bees: scout bees, which look food sources in the proximity of the hive and onlooker bees, which wait for the employed bees to bring them the information about food source and exploiting it afterwards.

The exchange of information among bees is the most important occurrence in the formation of the collective knowledge. While examining the entire hive it is possible to distinguish between some parts that commonly exist in all hives. The most important part of the hive with respect to exchanging information is the dancing area. Communication among bees related to the quality of food sources takes place in the dancing area. Since information about all the current rich sources is available to an onlooker on the dance floor, probably she can watch numerous dances and decides to employ herself at the most profitable source. There is a greater probability of onlookers choosing more profitable sources since more information is circulated about the more profitable sources. Employed foragers share their information with a probability proportional to the profitability of the food source, and the sharing of this information through waggle dancing is longer in duration. Hence, the recruitment is proportional to the profitability of the food source [45].

Since this cycle can go on and on to keep a constant supply of food in the hive, the algorithm process should be limited to a fair amount of time, to obtain the optimal value. In the following, the algorithm steps are presented.

#### 2.4.4.1 Algorithm description

The original ABC algorithm is described in [45 – 47]. Several adaptations were deployed in [48 – 52], but for this application, a hybrid analytical/FEM ABC optimization technique is presented [16].

1. The first step is to initialize the population of solutions  $x_{i,j}$ . This is done by selecting a number of variables vectors from eq. (2.113) equal to the number of food sources. The values of each variable is chosen randomly in each vector, thus a variety of solutions are selected.

The number of food sources is chosen to be 15, half the value of the bees in the colony. The ABC algorithm will run for 200 steps and each food source that can't be improved after 50 evaluations will be abandoned.

2. Since there is a chance that some combinations are not possible, the population of solutions is evaluated and the best food source is memorized.

3. The cycle is initialized. New solutions (food sources)  $V_{i,j}$  are produced in the neighborhood of  $x_{i,j}$  for the employed bees using the equation below, where  $k$  is a solution in the neighborhood of  $i$  and  $\Phi$  is a random number in the range  $[-1,1]$ :

$$v_{i,j} = x_{i,j} + \Phi_{i,j} \cdot (x_{i,j} - x_{k,j}) \quad (2.133)$$

In this case, a randomly selected variable is changed and the new solution is evaluated.

4. A greedy selection between the old solution  $x_i$  and new solution  $V_i$  is applied. If the new solution is better than the old one, then the latter is replaced by the former. Then the probability values  $P_i$  for the solution  $x_i$  are calculated, by means of their fitness values, expressed in the equation below.

$$P_i = \frac{fit_i}{\sum_{i=1}^{SN} fit_i} \quad (2.134)$$

To calculate the fitness values of solutions, the following equation is used:

$$fit_i = \begin{cases} \frac{1}{1 + f_i}, & \text{if } f_i \geq 0 \\ 1 + abs(f_i), & \text{if } f_i < 0 \end{cases} \quad (2.135)$$

At the end of finding the probability values, they are normalized to  $[0, 1]$  interval.

5. This step repeats steps 3 and 4 for onlooker bees. The employed bees come back to the hive and perform the waggle dance. From the solutions  $x_i$  selected depending on  $P_i$ , new solutions (positions)  $V_i$  are produced. After that a greedy selection between the old and new solution is applied.

6. Until now, only the employed and the onlooker bees were introduced in the algorithm. From their selection, some food sources were abandoned as not suitable, so

it is better to replace them by employing the scout bees to search a new randomly source based on the following equation:

$$x_{i,j} = \min_j + \text{rand}(0,1) \cdot (\max_j - \min_j) \quad (2.133)$$

7. The final step is to memorize the best solution achieved so far and to repeat the cycle until the maximum number of cycles, chosen by the user, is achieved. Each time where a new solution is evaluated compared to the old one (steps 3, 5 and 6), the finite element is called, similar to modified Hooke-Jeeves algorithm presented earlier. Equations (2.124) to (2.129) are also valid here and same procedure is applied to find the cogging and average torques.

Next, the results of the optimization algorithm are presented.

#### 2.4.4.2 Optimization results

Compared to previous optimization algorithm, where the solution was found by exploring different paths, the artificial bee colony algorithm searches the global minimum solution. This way, it can be seen in figures below (Fig.2.23 to Fig.2.29) that variation of the variables covers the entire optimization interval.

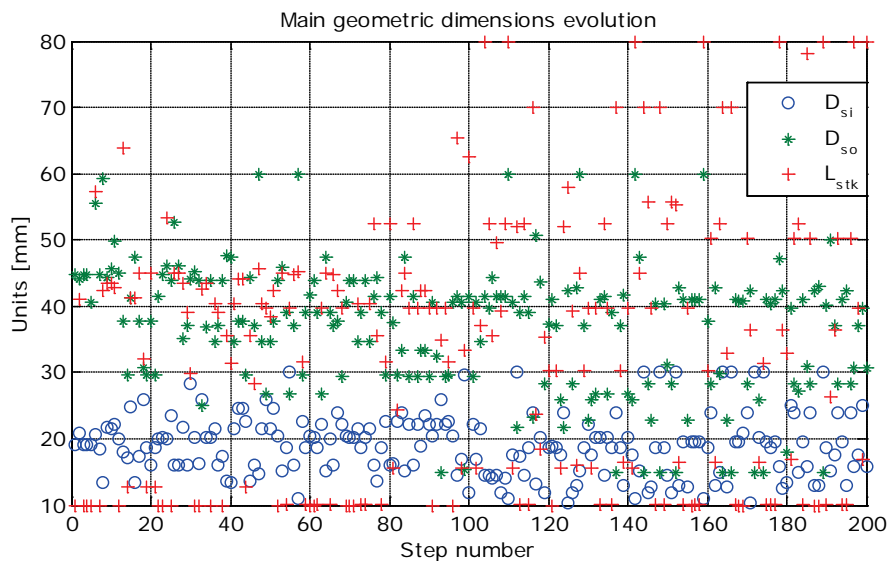


Fig. 2.23 Main geometric dimensions evolution

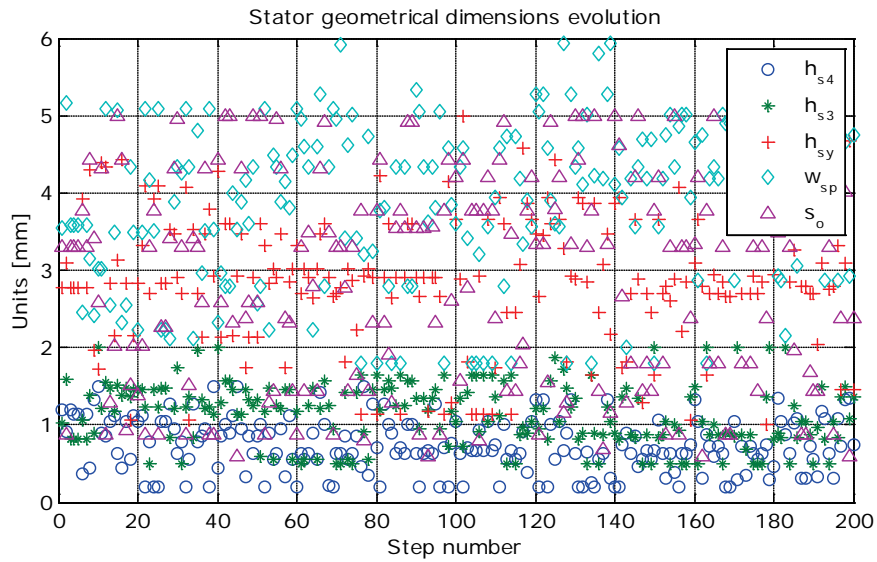


Fig. 2.24 Stator geometrical dimensions evolution

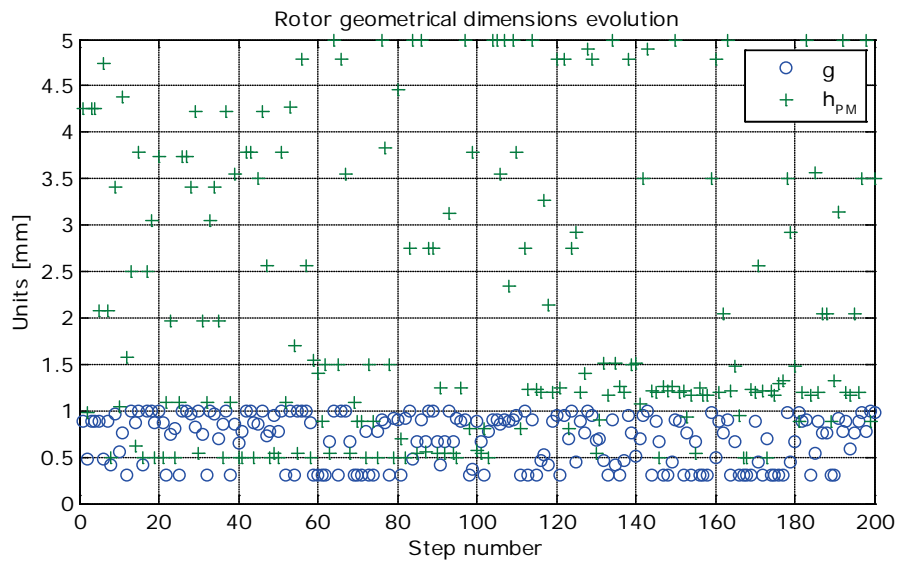


Fig. 2.25 Rotor geometrical dimensions evolution

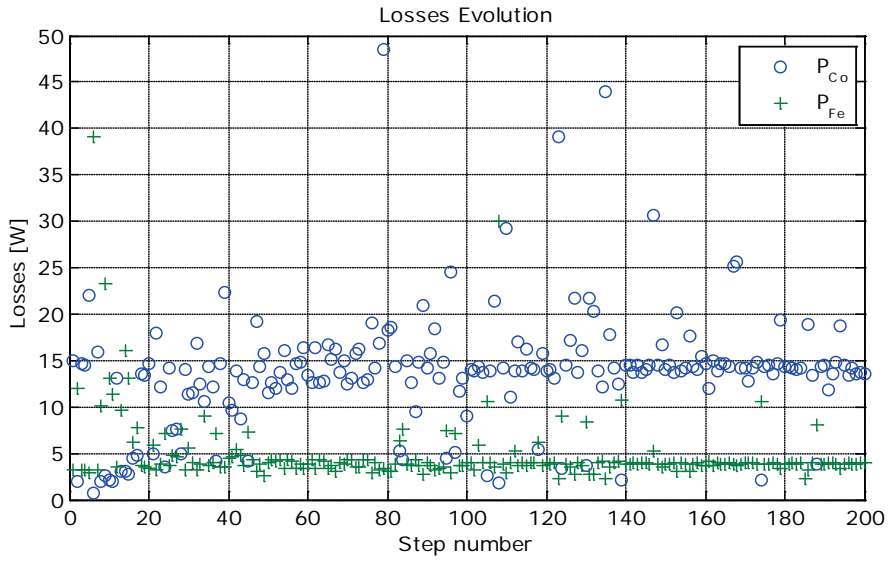


Fig. 2.26 Motor losses evolution

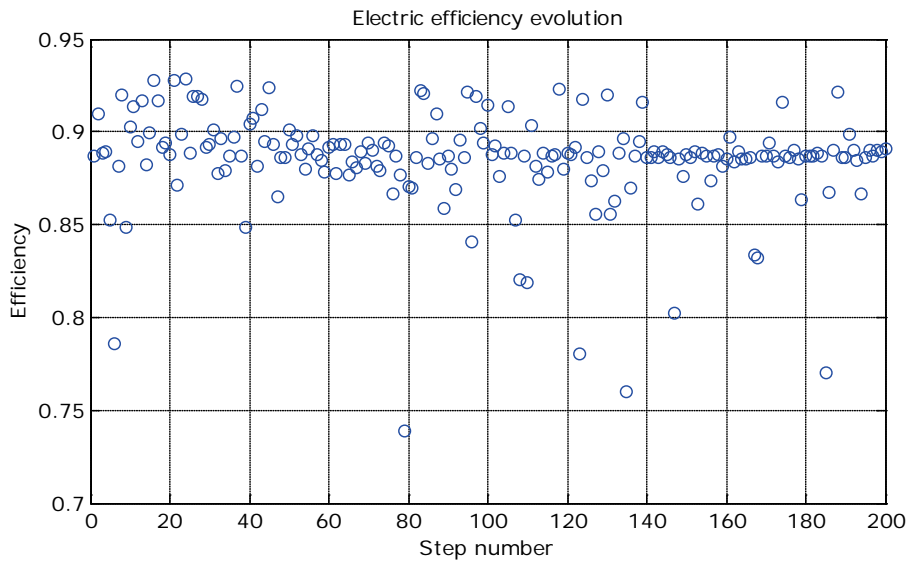


Fig. 2.27 Motor electrical efficiency evolution



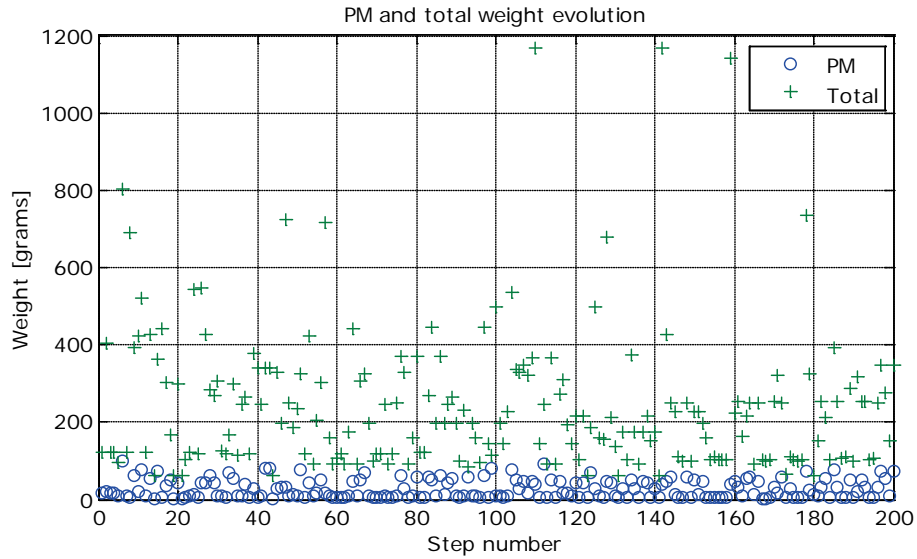


Fig. 2.28 Permanent magnet and motor weight evolution

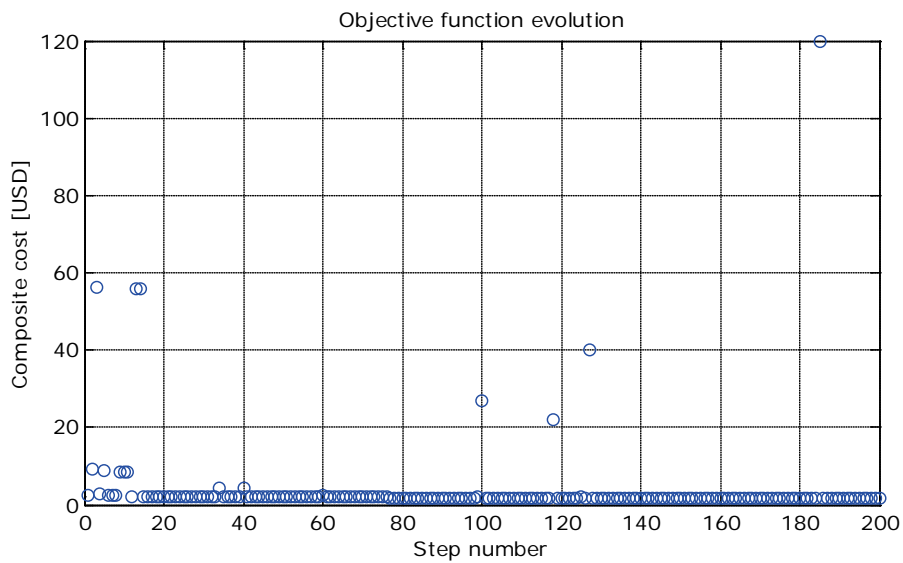


Fig. 2.29 Objective function evolution

The optimization process took 1037 seconds to run 200 cycles. Without FEM and ran only once, the optimization algorithm took only 90 seconds. So, to be sure that the global optimum is found and by introduction of the finite element analysis, the computation time increased by almost 11 times, less than for the previous algorithm.

Since the issue of evolutionary algorithms is the large computation time to obtain best results, new optimization techniques were searched. Direct search methods proved to be better in terms of computation time [20], but they converge rather to local solutions than global ones. To overcome this drawback, but to still keep the advantage of lower computation time, new nature-inspired optimization algorithms were tried. In terms of computation time, ABC algorithm looks better than modified Hooke-Jeeves algorithm by 30%. However, we must see if this is enough. In Table 2.7 a comparison between analytical method, hybrid Hooke-Jeeves optimization and ABC optimization is realized. To be sure which option is the best, machine dimensions, electrical parameters, losses, efficiency, weights and total costs are presented.

Analytical method could yield better results and be less time consuming if the designer is very experienced and senses which way the design goes. However, is highly subjective and no guaranty regarding design time can be offered. On the other hand, with less restrictions, optimization techniques are faster and do not rely on designer's experience.

**Table 2.7 Geometrical dimensions and materials for designed BLDC for analytical and optimization cases**

Parameter	Value			Unit
	Analytical	HJ	ABC	
<b>Topology</b>				
Number of phases $m$	3			-
Number of stator slots $N_s$	6			-
Number of rotor poles $2p$	4			-
<b>Stator geometrical dimensions</b>				
Stator outer diameter $D_{so}$	32	54.6	51.1	mm
Stator inner diameter $D_{si}$	15	16.8	19.8	mm
Stator tooth width $w_{sp}$	3.5	6	5.4	mm
Stator tooth height $h_s$	6	13.9	10.6	mm
Stator slot depth $h_{s1}$	4.8	13.2	9.9	mm
Stator wedge place height $h_{s3}$	0.9	0.5	0.5	mm
Stator tooth pole tip height $h_{s4}$	0.3	0.2	0.2	mm
Stator slot top width $w_{s1}$	11.06	16.9	15.7	mm
Stator slot bottom width $w_{s2}$	5.5	3.4	5.57	mm
Stator slot width $w_s$	8.28	12.31	10.63	mm
Stator slot opening $s_o$	1.2	1.3	1.6	mm
Stator yoke height $h_{sy}$	2.5	5	5	mm
Stator slot area $A_{slot}$	49.68	171.11	112.68	mm <sup>2</sup>
Stator coil area $A_{co}$	19.87	68.44	45.07	mm <sup>2</sup>
Stator pole pitch $\tau_{ss}$	7.85	8.8	10.37	mm
Stack length $L_{stk}$	40	20.2	21	mm
Air gap height $g$	0.5	0.79	0.66	mm

<b>Rotor geometrical dimensions</b>				
Rotor outer diameter $D_{ro}$	14	15.3	18.5	mm
Rotor inner diameter $D_{ri}$	9	10.3	15.6	mm
Permanent magnet height $h_{PM}$	2.5	2.5	1.4	mm
Rotor length $L_{rot}$	42	21.21	22.05	mm
Rotor pole pitch $\tau_{PM}$	11.78	13.2	15.55	mm
Rotor yoke height $h_{ry}$	2.19	2.451	2.89	mm
<b>Windings</b>				
Number of turns per phase $N_{ph}$	108	206	179	-
Number of slots/pole/phase $q$	0.5			-
Number of parallel current paths $a$	2			-
Slot filling factor $k_{sf}$	0.4			-
<b>Materials</b>				
Iron core	SURA® NO18			
Permanent magnet	Vacodym 677 AP 215/223			

**Table 2.8 BLDC's electrical parameters and costs for analytical and optimization cases**

Parameter	Value			Unit
	Analytical	HJ	ABC	
Base voltage $V_b$	75			V
Phase back-EMF voltage $E_{ph}$	71.28	72.8	72.94	V
Phase current $I_{ph}$	1.24	1.13	1.13	A
Output power $P_b$	150			W
Phase resistance $R_s$	2.21	1.59	1.57	$\Omega$
Phase inductance $L_s$	1.75	3.84	2.55	mH
Rated copper losses $P_{co}$	6.8	4.09	4.01	W
Rated mechanical losses $P_{mech}$	1			W
Rated iron losses $P_{Fe}$	5.6	4.48	4.99	W
Rated efficiency $\eta$	91.8	94	93.75	%
Optimization time	-	1437	1037	S
Initial costs	3.68	4.57	4	USD
Penalty costs	20.03	14.35	15	USD
Total costs	23.7	18.92	19	USD

## 2.5 Conclusion

In this chapter, the motor design for a small refrigeration compressor was realized. First, we set the background for design requirements, like laws and regulations, and we establish how necessary such a design is. Next, we look for competitor topologies and, by comparison and analysis of strengths and weaknesses of

each topology, the brushless DC with 6 stator slots and 4 rotor poles is chosen. An analytical design is performed, as it is the backbone of motor design, even in optimal techniques. We verify at the end if the choices made during the design matches the reality, through thermal verification.

Two different optimization strategies are used to further improve the design. A direct search method, modified Hooke-Jeeves algorithm, and a stochastic one, artificial bee colony algorithm, are studied and compared in terms of results and optimization time. Finite element analysis is introduced in the optimization process, in order to obtain accurate values of the cogging and average torques, which leads to a serious increase of the computation time.

As can be seen in Tables 2.8 and 2.9, the results obtained from the two optimization techniques are very similar. The initial cost is lower for the analytical case, but the penalty costs are way larger. For the other two cases, it may be noticed that the initial cost is lower for ABC case, but the total costs are almost equal. The same equality is valid for efficiency, but the computation time is 30% less for ABC case, which makes it feasible for motor design.

## References

- [1] Jacek F. Gieras, "Permanent Magnet Motor Technology – Design and Applications", book, 3<sup>rd</sup> edition, CRC Press, Taylor & Francis Group LLC, Boca Raton, Florida, 2010
- [2] Michael J. Melfi, S. David Rogers, Steve Evon and Bill Martin, "Permanent-magnet motors for energy savings in industrial applications", *IEEE Trans. on Ind. Appl.*, vol.44, no.5, pp.1360-1366, September/October 2008
- [3] Z.Q. Zhu, David Howe, Ekkehard Bolte and Bernd Ackermann, "Instantaneous magnetic field distribution in brushless permanent magnet dc motors, Part I: Open-circuit field", *IEEE Trans. on Magn.*, vol.29, no.1, pp.124-135, January 1993
- [4] Z.Q. Zhu and David Howe, "Instantaneous magnetic field distribution in brushless permanent magnet dc motors, Part II: Armature-reaction field", *IEEE Trans. on Magn.*, vol.29, no.1, pp.136-142, January 1993
- [5] Z.Q. Zhu and David Howe, "Instantaneous magnetic field distribution in brushless permanent magnet dc motors, Part III: Effect of stator slotting", *IEEE Trans. on Magn.*, vol.29, no.1, pp.143-151, January 1993
- [6] Z.Q. Zhu and David Howe, "Instantaneous magnetic field distribution in brushless permanent magnet dc motors, Part IV: Field on load", *IEEE Trans. on Magn.*, vol.29, no.1, pp.152-158, January 1993
- [7] Nicola Bianchi, Silverio Bolognani and Fabio Luise, "Potentials and limits of high speed PM motors", *IEEE Trans. on Ind. Appl.*, vol.40, no.6, pp.1570-1578, November/December 2004
- [8] Nicola Bianchi, Silverio Bolognani and Fabio Luise, "Analysis and design of a PM brushless motor for high-speed operations", *IEEE Trans. on Energy Conv.*, vol.20, no.3, pp.629-637, September 2005

- [9] Yoshiaki Kano and Nobuyuki Matsui, "A design approach for direct-drive permanent-magnet motors", *IEEE Trans. on Ind. Appl.*, vol.44, no.2, pp.543-554, March/April 2008
- [10] Thierry Lubin, Smail Mezani and Abderrezak Rezzoug, "Exact analytical method for magnetic field computation in the air gap of cylindrical electrical machines considering slotting effects", *IEEE Trans. on Magn.*, vol.46, no.4, pp.1092-1099, April 2010
- [11] Thierry Lubin, Smail Mezani and Abderrezak Rezzoug, "2-D exact analytical model for surface-mounted permanent-magnet motors with semi-closed slots", *IEEE Trans. on Magn.*, vol.47, no.2, pp.479-492, February 2011
- [12] L.J. Wu, Z.Q. Zhu, J.T. Chen and Z.P. Xia, "An analytical model of unbalanced magnetic force in fractional-slot surface-mounted permanent magnet machines", *IEEE Trans. on Magn.*, vol.46, no.7, pp.2686-2700, July 2010
- [13] Jérôme Legranger, Guy Friedrich, Stéphane Vivier and Jean Claude Mipo, "Combination of finite-element and analytical models in the optimal multidomain design of machines: Application to an interior permanent-magnet starter generator", *IEEE Trans. on Ind. Appl.*, vol.46, no.1, pp.232-239, January/February 2010
- [14] Kim, Yong Bae, et al., "A back EMF optimization of double layered large-scale BLDC motor by using hybrid optimization method", *IEEE Trans. on Magn.*, vol.47, no.5, pp.998-1001, May 2011
- [15] Ali Sarikhani and Osamma A. Mohammed, "Multiobjective design optimization of coupled PM synchronous motor-drive using physics-based modeling approach", *IEEE Trans. on Magn.*, vol.47, no.5, pp.1266-1269, May 2011
- [16] Vlad Grădinaru, Lucian Tutelea and Ion Boldea, "Hybrid analytical/FEM optimization design of SPMSM for refrigerator compressor loads", in *Proc. of Intl. Aegean Conf. on Electrical Machines and Power Electronics (ACEMP)*, 2011
- [17] Ion Boldea and Lucian Tutelea, "Electric Machines – Steady State, Transients and Design with MATLAB®", book, CRC Press, Taylor & Francis Group LLC, Boca Raton, Florida, 2010
- [18] Lucian Tutelea and Ion Boldea, "Optimal design of residential brushless DC permanent magnet motors with FEM validation", *Proc. of Intl. Aegean Conf. on Electrical Machines and Power Electronics (ACEMP)*, pp.435-439, 2007
- [19] Vlad Grădinaru, Lucian Tutelea, Ion Boldea, "25 kW, 15 krpm, 6/4 PMSM: optimal design and torque pulsation reduction via FEM", in *Proc. of 11<sup>th</sup> Intl. Conf. on Optimization of Electric and Electronic Equipment (OPTIM'08)*, pp.249-256, 2008
- [20] Lucian Tutelea and Ion Boldea, "Induction motor electromagnetic design optimization: Hooke Jeeves method versus genetic algorithms", in *Proc. of 12<sup>th</sup> Intl. Conf. on Optimization of Electric and Electronic Equipment (OPTIM'10)*, pp.485-492, 2010
- [21] Kondapalli Siva Rama Rao and Azrul Hisham Bin Othman, "Design optimization of a BLDC motor by genetic algorithm and simulated annealing", *Intelligent and Advanced Systems*, pp.854-858, November 2007

- [22] S.L. Ho, S.Y. Yang, G.Z. Ni and K.F. Wong, "An efficient multiobjective optimizer based on genetic algorithm and approximation techniques for electromagnetic design", *IEEE Trans. on Magn.*, vol.43, no.4, pp.1605-1608, April 2007
- [23] Gregor Papa, Barbara Koroušič-Seljak, Boris Benedičič and Tomaž Kmecl, "Universal motor efficiency improvement using evolutionary optimization", *IEEE Trans. on Ind. Elec.*, vol.50, no.3, pp.602-611, June 2003
- [24] Xiangjun Meng et al., "Dynamic multilevel optimization of machine design and control parameters based on correlation analysis", *IEEE Trans. on Magn.*, vol.46, no.8, pp.2779-2782, August 2010
- [25] S.Y. Yang et al., "A new implementation of population based incremental learning method for optimizations in electromagnetics", *IEEE Trans. on Magn.*, vol.43, no.4, pp.1601-1604, April 2007
- [26] S.L. Ho and Shiyong Yang, "A population-based incremental learning method for robust optimal solutions", *IEEE Trans. on Magn.*, vol.43, no.4, pp.3189-3192, April 2007
- [27] S.L. Ho, Shiyong Yang and W.N. Fu, "A population-based incremental learning vector algorithm for multiobjective optimal designs", *IEEE Trans. on Magn.*, vol.47, no.5, pp.1306-1309, May 2011
- [28] Christian Magele et al., "Nicheing evolution strategies for simultaneously finding global and Pareto optimal solutions", *IEEE Trans. on Magn.*, vol.46, no.8, pp.2743-2746, August 2010
- [29] Shimpei Sonoda et al., "Application of stepwise multiple regression to design optimization of electric machine", *IEEE Trans. on Magn.*, vol.43, no.4, pp.1609-1612, April 2007
- [30] Yao Duan, R.G. Harley and T.G. Habetler, "A useful multi-objective optimization design method for PM motors considering nonlinear material properties", *Proc. Energy Conversion Congress and Exposition (ECCE)*, pp.187-193, September 2009
- [31] Yao Duan, R.G. Harley and T.G. Habetler, "Method for multi-objective optimized designs of surface mount permanent magnet motors with concentrated or distributed stator windings", *Proc. Intl. Electric Machines and Drives Conf. (IEMDC)*, pp.323-328, May 2009
- [32] Leandro dos Santos Coelho, Leandro Zavarez Barbosa and Luiz Lebenstajn, "Multiobjective particle swarm approach for the design of a brushless DC wheel motor", *IEEE Trans. on Magn.*, vol.46, no.8, pp.2994-2997, August 2010
- [33] Rainer Stamminger and Rene Kemna, "Energy consumption of domestic appliances in European households", CECED Stock Model Report, June 2006
- [34] Stefano Faberi et al., "Preparatory studies for eco-design requirements of EuPs – LOT13: Domestic refrigerators and freezers, Final Report, Tasks 1-2", ISIS Report, December 2007
- [35] Stefano Faberi et al., "Preparatory studies for eco-design requirements of EuPs – LOT13: Domestic refrigerators and freezers, Final Report, Tasks 3-5", ISIS Report, December 2007

- 
- [36] Stefano Faberi et al., "Preparatory studies for eco-design requirements of EuPs – LOT13: Domestic refrigerators and freezers, Final Report, Tasks 6-7", ISIS Report, December 2007
- [37] Stefano Faberi et al., "Preparatory studies for eco-design requirements of EuPs – LOT13: Domestic refrigerators and freezers, Final Report, Appendix", ISIS Report, December 2007
- [38] T.J.E. Miller, "SPEED's electric motors – An outline of some of the theory in the SPEED software for electric machine design with problems and solutions", book, University of Glasgow, 2002
- [39] Duane C. Hanselman, "Brushless Permanent-Magnet Motor Design", book, McGraw-Hill Inc., New York, 1994
- [40] Nicola Bianchi et al., "Design considerations for fractional-slot winding configurations of synchronous machines", *IEEE Trans. on Ind. Appl.*, vol.42, no.4, pp.997-1006, July/August 2006
- [41] Typical data for SURA<sup>®</sup> NO18, Cogent Surahammars Bruks AB, Sweden, 2005
- [42] Typical data for Vacodym 677 AP 215/223, Vaacumschmelze AG, Germany, 2005
- [43] Dušan Teodorović and Mauro Dell'Orco, "Bee colony optimization – a cooperative learning approach to complex transportation problems", in *Proc. of 10<sup>th</sup> EWGT Meeting and 16<sup>th</sup> Mini EURO Conf.*, pp.51-60, 2005
- [44] Dušan Teodorović, Tatjana Davidović and Milica Šelmić, "Bee colony optimization: the applications survey", accepted for publication in *ACM Trans. on Comp., Logic*, 2011
- [45] Derviş Karaboğa, "An idea based on honey bee swarm for numerical optimization", Tech. Rep. TR-06, October 2005
- [46] Derviş Karaboğa and Bahriye Basturk, "A powerful and efficient algorithm for numerical function optimization: artificial bee colony (ABC) algorithm", *J. of Global Optim.*, vol.39, no.3, pp.459-471, November 2007
- [47] Adil Baykasoğlu, Lale Özbakır and Pınar Tapkan, "Artificial Bee Colony algorithm and its application to generalized assignment problem", *Swarm intelligence: Focus on ant and particle swarm optimization*, book, pp.532, Itech Education and Publishing, Vienna, Austria, December 2007
- [48] Leandro dos Santos Coelho and Piergiorgio Alotto, "Gaussian Artificial Bee Colony algorithm approach applied to Loney's solenoid benchmark problem", *IEEE Trans. on Magn.*, vol.47, no.5, pp.1326-1329, May 2011
- [49] Milos Subotic, Milan Tuba and Nadezda Stanarevic, "Parallelization of the Artificial Bee Colony (ABC) algorithm", in *Proc. of 11<sup>th</sup> WSEAS Intl. Conf. on Neural Networks, 11<sup>th</sup> WSEAS Intl. Conf. on Evolutionary Computing and 11<sup>th</sup> WSEAS Intl. Conf. on Fuzzy Systems*, pp.191-196, 2010
- [50] Efrén Mezura-Montes and Omar Cetina-Domínguez, "Exploring promising regions of the search space with the scout bee in the artificial bee colony for constrained optimization", in *Proc. of the Artificial Neural Networks in Eng. Conf. (ANNIE)*, vol.19, pp.253-260, November 2009

- [51] S.N. Omkar et al., "Artificial Bee Colony (ABC) for multi-objective design optimization of composite structures", *J. of Applied Soft Computing*, vol.11, no.1, pp.489-499, January 2011
- [52] Nyree Lemmens et al., "A bee algorithm for multi-agent systems: recruitment and navigation combined", in *Proc. of ALAG 2007, an AALMAS 2007 workshop*, Hawaii, 2007
- [53] D.M. Ionel et al., "Assessment of torque components in brushless permanent-magnet machines through numerical analysis of the electromagnetic field", *IEEE Trans. on Ind. Appl.*, vol.41, no.5, pp.1149-1158, September/October 2005
- [54] T.J.E. Miller et al., "Embedded finite-element solver for computation of brushless permanent-magnet motors", *IEEE Trans. on Ind. Appl.*, vol.44, no.4, pp.1124-1133, July/August 2008
- [55] D.M. Ionel and M. Popescu, "Ultrafast Finite-Element Analysis of Brushless PM Machines Based on Space-Time Transformations", *IEEE Trans. on Ind. Appl.*, vol.47, no.2, pp.744-753, March/April 2011



## Chapter 3

# Finite element validation and torque pulsations reduction techniques

### Abstract

In the previous chapter motor dimensioning was realized through optimal design and a good estimation of the magnetic and electric loadings and parameters was obtained via analytical model. To properly validate the topology and to verify motor characteristics more accurately, usage of FEM is required. For the designed BLDC motor, 2D Finite Element Method (FEM) is enough to provide all the needed information, by numerical calculation of the magnetic field distribution. This way, we can obtain a realistic image of the following motor characteristics: field distribution and flux linkages at no-load and at load, back-EMF at no-load, cogging torque (torque at zero current), load torque variation with rotor angular position, load torque pulsations and the variation of the radial forces with rotor angular position. To observe in detail the differences between the two hybrid optimal strategies used in the previous chapter, namely modified Hooke-Jeeves (HJ) and Artificial Bee Colony (ABC), the above parameters will be obtained for both cases and analyzed in parallel. Hence, after validation via FEM, we will know which strategy offers the best results.

Since cogging torque is a part of the finite element analysis, an in-depth look on this matter is required. One of the major problems in surface-mounted permanent magnet motors and a great component of the total torque pulsations, cogging torque causes are identified and different techniques to minimize it are employed in this chapter.

At the end of the chapter, the issue of eccentricity is analyzed and its possible effects on motor torque are presented. Rotor placement during motor construction, though automated, suffers from small misplacements which can further affect how the motor works. With the eccentricity analysis, its limits for proper motor functioning are found for our case.

### 3.1 Introduction

Today, the usage of permanent magnet motors, either with sinusoidal or trapezoidal currents, extends from hard disks to automotive applications, from home appliances to industrial robots. The scope of this work is to design and control a brushless DC (BLDC) motor for a compressor in refrigeration systems. This might not

sound like a challenging task, but limitations in terms of manufacturing and operational costs and requirements of high efficiency made it much more interesting.

The usage of permanent magnet motors spans over so many areas due to the advantages brought by magnet excitation as compared to electromagnetic excitation. These advantages are higher power and torque density, better dynamic performance, simplification of construction and maintenance, low noise and elimination of copper losses in the rotor, due to the absence of excitation windings, which leads to a serious increase in the efficiency [1, 2]. However, the introduction of permanent magnets brought with itself specific drawbacks such as the cost of the magnets, demagnetization at high temperatures and increased effort to place the magnets on the rotor, especially for high speed operation [3, 4]. Some constructive solutions to reduce the disadvantages will be presented later on this chapter.

Previous chapter was dedicated entirely to set basis for motor design. Demands in terms of energy costs on global markets, high expectations in terms of quality and cost saving from both the manufacturer and the customer and a comparison between different motor topologies lead to a BLDC type with 6 stator slots and 4 rotor poles. Once the motor topology was chosen, a thorough hybrid optimal design was realized. Even though two different strategies were used, the design process was similar, using an analytical model and hybrid optimization algorithm. The outcome of motor design was the optimum geometrical dimensions and estimation of electrical and magnetic parameters based on analytical model.

However, analytical models are not enough to provide an accurate image of the most important motor characteristics, which strongly impacts future system simulation and controllers design. In one way, they tend to simplify some aspects, which in the end will result in a significant difference from reality, while otherwise may tend to be so complex [5 – 8] that the model requires a great deal of computation time or it is prone to errors. To overcome that, finite element analysis (FEA) is used as a tool for some years now to obtain accurate results on magnetic and electric fields of the motor and their interaction, but also to estimate motor parameters [1].

As analytical model for the 6/4 BLDC motor was presented in detail in chapter 2, the first part of this chapter is dedicated to FEM validation of the motor and of the model. Theoretical background, FEM software layout and results for field distribution and flux linkages at no-load and at load, back-EMF at no-load, cogging torque, load torque variation with rotor angular position, load torque pulsations and the variation of the radial forces with rotor angular position and phase inductances are presented.

The second part of this chapter is dedicated for methods to reduce or eliminate the most annoying parasitic element in motor design for surface permanent magnets, the cogging torque. A source of noise and vibrations and, most important, of torque pulsations, cogging torque can be greatly reduced by using some design techniques. Since the objective of motor design is high efficiency and low manufacturing costs, the method that satisfies both criteria will be chosen.

Another aspect to consider on manufacturing side is the dynamic eccentricity that results from improper placement of the rotor. The functional limitations for the eccentricity will be calculated and presented at the end of this chapter.

### 3.2 Theoretical background

As stated before, the FEM analysis of the motor is required to validate the results obtained from the analytical model and to offer more accurate values for other important parameters regarding the electrical and magnetic fields and their interactions. FEM has proved to be particularly flexible, reliable and effective in the analysis and synthesis of power-frequency electromagnetic and electromechanical devices [1]. An in-depth analysis of the theory behind FEM can be found in [1, 9], thus in the following a summary of it will be presented. For starters, the mathematical and physical laws and operators used for electromagnetic fields and the way they are applied in the FEM software are shown. Second, the layout of the used 2D FEM software is briefly described and then, the FEM model is introduced. To sum all up, the laws that govern electromagnetic fields are applied in the real case, to obtain values of the motor parameters, like field, flux linkages, back-EMF, torque and radial forces.

#### 3.2.1 Vector fields and operators

By definition a scalar is a simple physical quantity that is not changed by coordinate system rotations or translations. As opposite, a vector has both length (magnitude) and direction and it changes with system rotation or translation. While the motor runs, the coordinates system rotates and since we have variables that change both direction and magnitude with system's rotation, we have a vector field.

As vectors depend on coordinates system changes, these systems must be introduced. Mathematical operations with vectors may take place in Cartesian coordinates  $(x, y, z)$ , cylindrical coordinates  $(r, \theta, z)$  or spherical coordinates  $(r, \theta, \Phi)$ . There are relations linking the last two systems to the Cartesian one, but for our BLDC application we need only the first two coordinate systems.

In Cartesian coordinates (Fig. 3.1.a), a vector is defined as such:

$$\bar{A} = A_x \cdot \bar{u}_x + A_y \cdot \bar{u}_y + A_z \cdot \bar{u}_z \quad (3.1)$$

where  $\bar{u}_x$ ,  $\bar{u}_y$  and  $\bar{u}_z$  are unitary vectors aligned to orthogonal axes  $x$ ,  $y$  and  $z$ .

For cylindrical coordinates (Fig. 3.1.b), a point P is defined by cylinder radius  $r$ , its angle  $\theta$  with axis  $x$  and the cylinder height  $z$ . The unitary vectors along the coordinate axes are  $\bar{u}_r$ ,  $\bar{u}_\theta$ ,  $\bar{u}_z$ . The transformation matrix between Cartesian and cylindrical coordinates is given as [9]:

$$\begin{pmatrix} A_r \\ A_\theta \\ A_z \end{pmatrix} = \begin{pmatrix} \cos(\theta) & -\sin(\theta) & 0 \\ \sin(\theta) & \cos(\theta) & 0 \\ 0 & 0 & 1 \end{pmatrix} \cdot \begin{pmatrix} A_x \\ A_y \\ A_z \end{pmatrix} \quad (3.2)$$

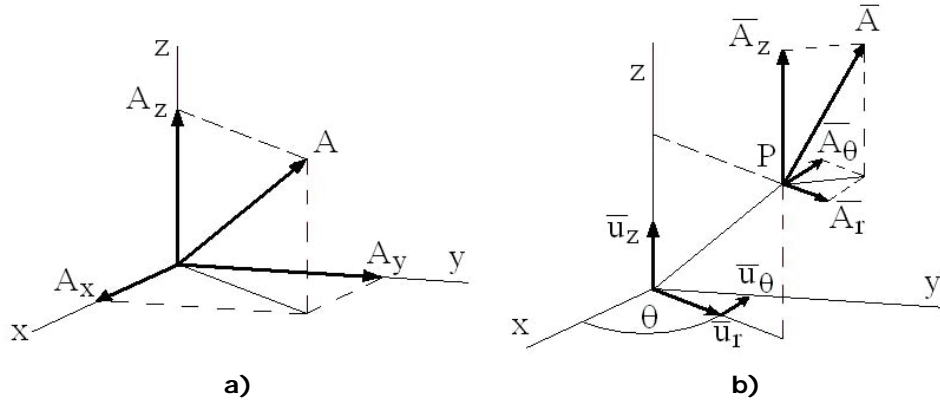


Fig. 3.1 Coordinate systems: a) Cartesian and b) cylindrical [9]

The basic mathematical operations in vector fields are integral and differential operations. The essential integrals of a vector field can be of two types, line and surface. The line integral of a vector field means the integral of the scalar product between the respective vector and the unitary vector which is tangent to that line in every point, as expressed below in Cartesian coordinates [9].

$$L_{12} = \int_c \bar{A} \cdot d\bar{l} = \int_{P1}^{P2} (A_x \cdot dx + A_y \cdot dy + A_z \cdot dz) = \int_{x1}^{x2} A_x \cdot dx + \int_{y1}^{y2} A_y \cdot dy + \int_{z1}^{z2} A_z \cdot dz \quad (3.3)$$

Although a generic expression, the equation above has a physical meaning for the magnetic field, its result being the magneto-motive force (MMF) or the number of ampere-turns required to produce the magnetic field between those two points. However, the result may offer another interesting piece of information. If its value is not dependent on the shape of the line, but rather on the initial and final points, the field can be considered conservative.

The surface integral of a vector field is called the flux of a vector field to a surface  $S$  and is given by the surface integral of the scalar product between the vector and its unitary vector normal to the surface  $S$ , as presented.

$$\Phi = \int_S \bar{A} \cdot \bar{n} \cdot dS = \int_S A_x \cdot dy \cdot dz + \int_S A_y \cdot dx \cdot dz + \int_S A_z \cdot dx \cdot dy \quad (3.4)$$

As its name states, the flux of a vector field through a surface applied to a magnetic field gives us the magnetic flux.

Besides the integral operations with vectors, other important mathematical tools are the one that involves differential operations with scalars and vectors. There are three such differential operations, namely gradient, divergence and curl (rotor). To realize these mathematical relations between scalars and vectors, the “nabla” or “del” operator is introduced. This is a vector operator that has no physical meaning or vector direction by itself [1].

$$\nabla = \bar{u}_x \cdot \frac{\partial}{\partial x} + \bar{u}_y \cdot \frac{\partial}{\partial y} + \bar{u}_z \cdot \frac{\partial}{\partial z} \quad (3.5)$$

The **gradient** of a scalar field is a vector field, whose vectors show in every point in space the direction along which the variation of scalar field is maximum. Its amplitude is equal to the scalar field derivative along that direction [9]. In Cartesian coordinates, the gradient of a scalar field is:

$$\nabla f = \bar{u}_x \cdot \frac{\partial f}{\partial x} + \bar{u}_y \cdot \frac{\partial f}{\partial y} + \bar{u}_z \cdot \frac{\partial f}{\partial z} \quad (3.6)$$

The **divergence** of a field is a scalar associated to every point, which shows the tendency of the field to spring from (when divergence is positive) or to converge to a certain point (when divergence is negative). In Cartesian coordinates, the divergence of a field is:

$$\nabla \cdot \bar{A} = \frac{\partial A_x}{\partial x} + \frac{\partial A_y}{\partial y} + \frac{\partial A_z}{\partial z} \quad (3.7)$$

Divergence of a field is the limit of the ratio between the field flux through a closed surface and the volume closed by that surface when the latter tends to zero:

$$\nabla \cdot \bar{A} = \lim_{V \rightarrow 0} \frac{1}{V} \oint_S \bar{A} \cdot d\bar{S} \quad (3.8)$$

The fields whose divergence is zero in every point are called solenoidal fields.

The **rotor** or **curl** of a vector field is defined as the limit of the ratio between a closed surface integral of a vector product between the respective vector and the normal to the surface unit vector, to the volume enclosed by the surface when the latter tends to zero.

$$\nabla \times \bar{A} = \lim_{V \rightarrow 0} \frac{1}{V} \oint_S \bar{n} \times \bar{A} \cdot dS \quad (3.9)$$

In Cartesian coordinates, the rotor expression is:

$$\nabla \times \bar{A} = \bar{u}_x \cdot \left( \frac{\partial A_z}{\partial y} - \frac{\partial A_y}{\partial z} \right) + \bar{u}_y \cdot \left( \frac{\partial A_x}{\partial z} - \frac{\partial A_z}{\partial x} \right) + \bar{u}_z \cdot \left( \frac{\partial A_y}{\partial x} - \frac{\partial A_x}{\partial y} \right) \quad (3.10)$$

A particular situation occurs when the field is discontinuous relative to the surface. In these cases, the expressions referring to the surface gradient, divergence and rotor are:

$$\nabla_{\Sigma} f = (f_2 - f_1) \cdot \bar{n}_{\Sigma} \quad (3.11)$$

$$\nabla_{\Sigma} \cdot \bar{A} = (\bar{A}_2 - \bar{A}_1) \cdot \bar{n}_{\Sigma} \quad (3.12)$$

$$\nabla_{\Sigma} \times \bar{A} = (\bar{A}_2 - \bar{A}_1) \times \bar{n}_{\Sigma} \quad (3.13)$$

Until now, only first order derivatives of the fields, either scalar or vector, were studied. Second order derivative operator, noted with  $\Delta$ , is called "Laplacian". Fields where the Laplacian is zero in every point are called harmonic fields [9]. This operator applies to scalar fields and vector fields in equal measure.

The Laplacian of a scalar field in Cartesian coordinates is expressed as:

$$\nabla^2 f = \nabla \cdot (\nabla f) = \frac{\partial^2 f}{\partial x^2} + \frac{\partial^2 f}{\partial y^2} + \frac{\partial^2 f}{\partial z^2} \quad (3.14)$$

The Laplacian of a vector field in Cartesian coordinates is expressed as:

$$\nabla^2 \bar{A} = \nabla (\nabla \cdot \bar{A}) - \nabla \times (\nabla \times \bar{A}) = \nabla^2 A_x \bar{u}_x + \nabla^2 A_y \bar{u}_y + \nabla^2 A_z \bar{u}_z \quad (3.15)$$

### 3.2.2 Maxwell's equations

The electromagnetic field, as stated by its name, is a combination of electric and magnetic fields. In depth, it refers to a physical field produced by electric charges in motion, motion that influences their own behavior. This field is governed by a set of four equations that brings together the electric charges, field production and interaction. These mathematical relationships are known as Maxwell's equations, as he is the physicist that united previously unrelated equations regarding electricity and magnetism into classical electromagnetic theory.

The first Maxwell equation refers to the electrostatic field and is derived from earlier Gauss's law (1835), which states that the electric flux through any closed surface is proportional to the enclosed electric charge.

$$\Psi_E = \oint_S \bar{D} \cdot d\bar{S} = \oint_S \bar{D} \cdot d\bar{S} = \oint_S \varepsilon \cdot \bar{E} \cdot d\bar{S} = Q \quad (3.16)$$

In the equation above,  $\Psi_E$  is the electric flux,  $\bar{D}$  is the displacement vector,  $S$  is the surface,  $\varepsilon$  is the electric permittivity,  $\bar{E}$  is the electric field and  $Q$  is the electric charge.

Gauss's theorem, known also as Gauss-Ostrogradsky or divergence theorem, a particular form of Stokes' theorem, states that the outward flux of a vector field through a closed surface is equal to the volume integral of the divergence of the region inside the surface. The most important effect of this theorem is the equivalence of the integral and differential forms of the Gauss's law.

$$\oint_S \bar{D} \cdot d\bar{S} = \int_V \nabla \cdot \bar{D} \cdot dV \Rightarrow Q = \int_V \nabla \cdot (\varepsilon \cdot \bar{E}) \cdot dV \Rightarrow \int_V \rho_V \cdot dV = \varepsilon \cdot \int_V \nabla \cdot \bar{E} \cdot dV \quad (3.17)$$

In the equation above the electric charge  $Q$  enclosed by surface  $S$ , due to a volume charge density  $\rho_V$  is equal to the left term in the last equality.

The **first Maxwell equation** combines the equalities in relations (3.16) and (3.17), resulting the following differential form:

$$\nabla \cdot \bar{E} = \frac{\rho_V}{\varepsilon} \quad (3.18)$$

The **second Maxwell equation** is derived from Gauss's law for magnetism, the counterpart of the law for electrostatic fields, which states that magnetic field is a solenoidal vector field. The most important effect of this law is that there are no magnetic monopoles, only dipoles, which are the magnetic equivalent of the electric charges. Below, the differential form is given in (3.19) and the integral form is given in (3.20).

$$\nabla \cdot \bar{B} = 0 \quad (3.19)$$

$$\oint_S \bar{B} \cdot d\bar{S} = 0 \quad (3.20)$$

While the first two equations set the properties for the electrostatic field and for magnetic field as separate entities, the third equation links the two fields. The basis for

this equation is Faraday's law of induction, which states that the induced electromotive force (EMF) in any closed circuit is equal to the time rate of change of the magnetic flux through the circuit. To simplify, one can say that the EMF generated is proportional to the rate of change of the magnetic flux.

$$e = -N_{ph} \cdot \frac{d\Phi(x, t)}{dt} = -N_{ph} \cdot \left( \frac{\partial\Phi}{\partial t} + \frac{\partial\Phi}{\partial x} \cdot \frac{\partial x}{\partial t} \right) \quad (3.21)$$

In the equation above,  $e$  is the instantaneous EMF induced in a coil with  $N$  turns and  $\Phi$  is the magnetic flux.

The **third Maxwell equation**, also known as Maxwell-Faraday equation since it is derived from the relation (3.21), in a simplified differential form, is expressed as:

$$\nabla \times \bar{E} = -\frac{\partial \bar{B}}{\partial t} \quad (3.22)$$

In its integral form, the relation above is known as Kelvin-Stokes theorem:

$$\oint_{\partial S} \bar{E} \cdot d\mathbf{l} = -\frac{\partial}{\partial t} \iint_S \bar{B} \cdot d\mathbf{S} \quad (3.23)$$

The two equations above represent the effect of the magnetic field on a closed circuit. However, the interaction between the electric and magnetic fields goes both ways, so in the last of the Maxwell's equations the magnetic field produced by the electric current is expressed.

There are two separate laws that have the same outcome, the Biot-Savart law and the Ampère circuital law, although the last one is incomplete, as it ignores the displacement current, as can be seen below, where  $J$  is the total current density.

$$\oint_{\Gamma} \bar{B} \cdot d\mathbf{l} = \mu_0 \cdot \iint_S \bar{J} \cdot d\mathbf{S} \quad (3.24)$$

The displacement current  $J_D$ , introduced by Maxwell to complete the law presented in (3.24), has the following expression:

$$\bar{J}_D = \frac{\partial}{\partial t} \bar{D}(r, t) = \varepsilon_0 \cdot \frac{\partial \bar{E}}{\partial t} + \frac{\partial \bar{P}}{\partial t} \quad (3.25)$$

In the equation above, the unknown parameters are:  $\varepsilon_0$  is the electric constant or the vacuum permittivity and  $P$  is the polarization density. Since only the first term is



present everywhere, even in the vacuum and it doesn't necessary involves actual movement of the electric charge, it is to be considered in the extended formula of the Ampère circuital law. In the integral form, the complete law equation is:

$$\oint_{\Gamma} \bar{B} \cdot d\bar{l} = \iint_S \left( \mu_0 \cdot \bar{J} + \mu_0 \cdot \varepsilon_0 \cdot \frac{\partial \bar{E}}{\partial t} \right) \cdot d\bar{S} \quad (3.26)$$

Its differential form is known as the **fourth Maxwell equation**:

$$\nabla \times \bar{B} = \mu_0 \cdot \bar{J} + \mu_0 \cdot \varepsilon_0 \cdot \frac{\partial \bar{E}}{\partial t} \quad (3.27)$$

Having all the governing equations of the electromagnetic field detailed in relations (3.18), (3.19), (3.22) and (3.27), we can move on to the FEM description and FEM software. After that, all of the Maxwell's equations will be applied to the designed BLDC, to obtain its most important characteristics, which will be used later on in simulation and control.

### 3.2.3 Finite element method (FEM)

The aim of the finite element method is to solve the differential equations that describe the electric and magnetic fields and their interaction. However, this is not an easy task to perform due to the difficulty of solving this for complex geometries, such as electrical motors. With all its implications, like increased computational effort and loss of accuracy in the final result, a simpler solution is chosen. The idea behind finite element is to break the complex geometry in smaller regions, with an inherent increase in problems to solve. Despite that, it is easier to solve more differential equations for simpler geometries, like triangles, plain rectangles, prisms or parallelepipeds and then sum up all the results than to try to solve field variations in complex geometries.

The core of the FEM is the relation between the magnetic vector potential  $\bar{A}$  and the current density vector  $\bar{J}$ :

$$\frac{\partial}{\partial x} \cdot \left( \frac{1}{\mu} \cdot \frac{\partial \bar{A}}{\partial x} \right) + \frac{\partial}{\partial y} \cdot \left( \frac{1}{\mu} \cdot \frac{\partial \bar{A}}{\partial y} \right) = -\bar{J} + j\omega\sigma\bar{A} \quad (3.28)$$

The equation above can be further simplified for 2D FEM problems, taking into account the plane parallel symmetry in rotary electric machines, such as our BLDC, because both the magnetic vector potential and the current density vector have only one non-zero component (along axis  $z$ ). With this property, equation (3.28) becomes:

$$\frac{1}{\mu} \cdot \left( \frac{\partial^2 A_z}{\partial x^2} + \frac{\partial^2 A_z}{\partial y^2} \right) = -J_z \quad (3.29)$$

From the simpler geometries at hand to be used in FEM solvers, the most simple one and hence, the most used to discretize the problem, is the triangle, as presented in Fig. 3.2 below. Each element has at least three vertices called nodes. The number of nodes corresponding to each element depends on the shape of the element and also on the type of function used to model the potential within the element [1].

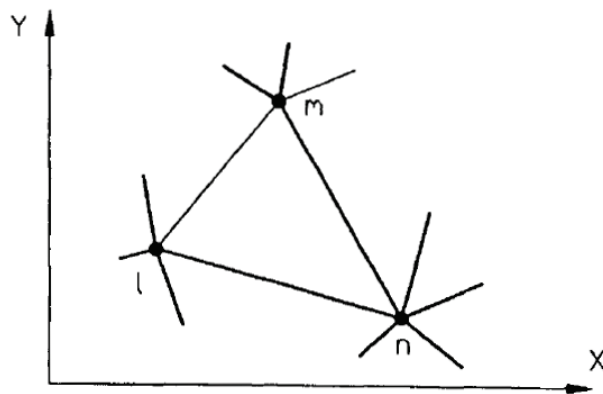


Fig. 3.2 Typical triangular finite element connected to other elements [1]

In what follows, starting from relation (3.29), the algebraic equations for 2D magnetostatic fields are deduced. The minimization of the magnetic vector potential over a set of elements (mesh) will lead to a matrix equation.

Assuming a linear shape function of the magnetic vector potential within an element, its value can be written in the following general form:

$$A(x, y) = a + bx + cy \quad (3.30)$$

For every node of the triangle, the relation above becomes a matrix equation, where the values of the constants  $a$ ,  $b$  and  $c$  can be found by imposing the value of  $A_z$  in the nodes of the discretization mesh [9]:

$$\begin{pmatrix} 1 & x_l & y_l \\ 1 & x_m & y_m \\ 1 & x_n & y_n \end{pmatrix} \cdot \begin{pmatrix} a \\ b \\ c \end{pmatrix} = \begin{pmatrix} A_l \\ A_m \\ A_n \end{pmatrix} \quad (3.31)$$

The energy functional for the surface of the triangle, denoted by  $S$ , can be expressed as:

$$F = \int_S \left( \frac{B^2}{2\mu} - J \cdot A + j\omega\sigma \frac{A}{2} \right) \cdot dS \quad (3.32)$$

The aim is to minimize the energy functional for the entire domain by minimizing its value in every element:

$$\frac{\partial F}{\partial A} = 0 \quad (3.33)$$

The linear interpolation polynomial function is realized by solving first equation (3.31):

$$a = \frac{1}{2S} \begin{vmatrix} A_l & x_l & y_l \\ A_m & x_m & y_m \\ A_n & x_n & y_n \end{vmatrix} \quad b = \frac{1}{2S} \begin{vmatrix} 1 & A_l & x_l \\ 1 & A_m & x_m \\ 1 & A_n & x_n \end{vmatrix} \quad c = \frac{1}{2S} \begin{vmatrix} 1 & x_l & A_l \\ 1 & x_m & A_m \\ 1 & x_n & A_n \end{vmatrix} \quad (3.34)$$

In the equation above, the term  $2S$  is equal to:

$$2S = \begin{vmatrix} 1 & x_l & y_l \\ 1 & x_m & y_m \\ 1 & x_n & y_n \end{vmatrix} \quad (3.35)$$

Including (3.34) and (3.35) in (3.30), the polynomial function becomes:

$$A = \frac{1}{2S} \sum_{k=l,m,n} [d_k + e_k x + f_k y] \cdot A_k \quad (3.36)$$

In order to minimize the energy functional over one element,  $F$  from (3.33) must be replaced with its more detailed form in (3.32). When this operation is realized, the result will be:

$$\int_S \frac{\partial}{\partial A_k} \left( \frac{B^2}{2\mu} - J \cdot A + j\omega\sigma \frac{A^2}{2} \right) \cdot dS = 0 \quad (3.37)$$

In terms of matrices, the equation above can be approximated as below, where  $[S]$  is the global coefficient matrix,  $[A]$  is the matrix of nodal magnetic vector potentials and  $[I]$  is the matrix of the nodal currents:

$$[S] \cdot [A] = [I] \quad (3.38)$$

In detail, the coefficients for matrices  $S$  and  $I$  are denoted as:

$$[S] = \frac{1}{4\mu S} \begin{pmatrix} e_l e_l + f_l f_l & e_l e_m + f_l f_m & e_l e_n + f_l f_n \\ e_m e_l + f_m f_l & e_m e_m + f_m f_m & e_m e_n + f_m f_n \\ e_n e_l + f_n f_l & e_n e_m + f_n f_m & e_n e_n + f_n f_n \end{pmatrix} + j \frac{\omega \sigma S}{12} \begin{pmatrix} 2 & 1 & 1 \\ 1 & 2 & 1 \\ 1 & 1 & 2 \end{pmatrix} \quad (3.39)$$

$$[I] = J \cdot \frac{S}{3} \cdot \begin{pmatrix} 1 \\ 1 \\ 1 \end{pmatrix} \quad (3.40)$$

The matrix equations above are for only one element. In case of a 2D FEM problem, there will be a finite number of elements and thus the whole process to determine these matrices is repeated for each element. In the end, matrix  $[S]$  will have a number of rows and columns equal to the number of elements, while  $[A]$  and  $[I]$  will be column matrices with their row numbers equal to the number of elements.

### 3.2.4 Boundary conditions

While in the electromagnetic fields, the existence of natural boundaries is very rare, in FEM they are used as a convention to simplify the calculus. The introduction of boundaries takes advantage of the symmetries, which leads to a significant reduction of the FEM model. There are three different types of boundary conditions that will be briefly presented, along with the advantages they bring into FEM models.

#### 3.2.4.1 Dirichlet boundary conditions

In this case, the magnetic vector potential, at a particular point, takes a prescribed value:

$$\bar{A} = m \quad (3.41)$$

In 2D FEM problems, flux lines have  $\bar{A}$  of constant value. In real world, some flux lines go beyond the stator yoke and they are known as leakage flux. Since this is not a large quantity, by applying a special Dirichlet boundary condition of  $\bar{A} = 0$  on the outer edge of the stator yoke, the flux lines will be forced to remain inside the electric motor, following its contour, parallel the boundary edge.

### 3.2.4.2 Neumann boundary conditions

These conditions need not to be specified directly in FEM models, as they are natural boundaries. The expression of Neumann boundary conditions is:

$$\frac{\partial \bar{A}}{\partial n} = 0 \quad (3.42)$$

For such a magnetic field, the field lines are normal to the surface while the electrostatic field lines are tangent to the surface [9]. In the figure below, Dirichlet and Neumann boundary conditions are represented.

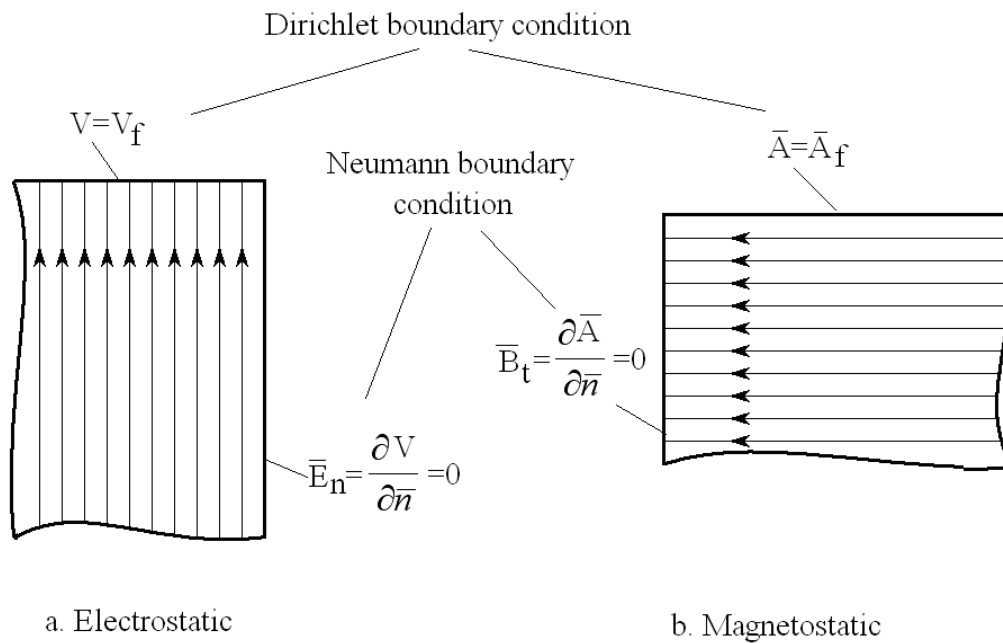


Fig. 3.3 Dirichlet and Neumann boundary conditions [9]

### 3.2.4.3 Robin boundary conditions

This case is a mix of the previous two boundary conditions, prescribing a relationship between the value of the  $A$  and its normal derivative at the boundary.

$$\frac{\partial \bar{A}}{\partial n} + a \cdot \bar{A} = 0 \quad (3.43)$$

Robin boundary conditions allow for defining boundary impedances through which the effect of the fields outside the boundary is considered.

### 3.3 Finite element analysis

In the previous sub-chapter, the theoretical grounds for the finite element analysis (FEA) were set, by describing the governing laws of electromagnetic field and algebraic relations between its components.

The following step is to present the FEM software used to validate the BLDC topology from the previous chapter, together with the geometrical dimensions obtained through hybrid optimal design. The most important characteristics for the motor will be extracted from FEM and compared for the two optimization algorithms, to conclude which one gives the best results.

#### 3.3.1 Finite element software

We already established that FEM is a useful tool to analyze motor geometries and to predict the influence of the motor parameters and their variation on how the motor will work. With the advancement of the computer technology and computational power of the processors, the usage of FEA became more and more frequent.

Although many FEA software packages exist on the market, simpler or more complex, in all prices range, the results in this chapter were obtained with commercial free software, called FEMM (version 4.2).

FEMM (Finite Element Method Magnetics) is a suite of programs for solving low frequency electromagnetic problems on 2D planar and axisymmetric domains. The program currently addresses linear / nonlinear magnetostatic problems, linear / nonlinear time harmonic magnetic problems, linear electrostatic problems and steady state heat flow problems [10].

FEMM software contains three executable parts, namely an interactive shell (femm.exe), a part that divides the domains in elementary triangles (triangle.exe) and the solvers (fkern.exe for magnetostatic problems and belasolv.exe for electrostatic problems).

The **interactive shell** is a Multiple Document Interface pre-processor and a post-processor for the various types of problems solved by FEMM. It contains a CAD-like interface for laying out the geometry of the problem to be solved and for defining material properties and boundary conditions. Autocad DXF files can be imported to facilitate the analysis of existing geometries. Field solutions can be displayed in the form of contour and density plots. The program also allows the user to inspect the field at arbitrary points, as well as evaluate a number of different integrals and plot various quantities of interest along user-defined contours.

**Triangle** breaks down the solution region into a large number of triangles, a vital part of the finite element process.

In case of **solvers**, each solver takes a set of data files that describe problem and solves the relevant partial differential equations to obtain values for the desired field throughout the solution domain [10].

The most important feature of this software is the possibility to import AutoCAD files containing the motor geometry and the LUA scripting language, which are

integrated in the interactive shell. More than a geometry design tool, LUA can both build and analyze geometry and evaluate the post-processing results, simplifying the creation of various sorts of “batch” runs. In addition, all edit boxes in the user interface are parsed by Lua, allowing equations or mathematical expressions to be entered into any edit box in lieu of a numerical value. In any edit box in FEMM, a selected piece of text can be evaluated by LUA via a selection on the right mouse button menu [10].

### 3.3.2 Finite element model of the 6/4 BLDC

In order to obtain the motor characteristics through FEM evaluation, there are some steps to follow. Each of these steps can be implemented directly in FEMM, via its interface or by running a LUA script that contains all the steps. In our case, the latter one was preferred for its flexibility in changing the motor parameters, as three different motor geometries were used (analytical, hybrid Hooke-Jeeves and hybrid ABC designs).

First step is **problem definition** with the following parameters:

- Frequency: 0 [Hz];
- Units: millimeters;
- Type: 2D planar;
- Precision:  $10^{-8}$ , meaning that the RMS of the residual should be less than this value;
- Depth of the problem in the into-the-page (or z axis) direction is set to be equal to the stack length of the motor;
- Minimum angle constraint sent to the mesh generator is set to be 30 degrees.

Second step is **geometry definition**. As stated above, LUA script was used and the geometry was implemented for a general 6/4 BLDC, as detailed in [9]. Parameters were taken for each case from the Table 2.7 in the previous chapter.

Third step is **boundary definition**. For our case, only one boundary was defined, namely the outer edge of the stator yokes. In order to keep the flux lines inside the motor, the edge was set to have Dirichlet boundary conditions.

Fourth step refers to **materials properties definition**. For a BLDC, materials definition is about stator and rotor laminations, magnet, air gap and copper in the windings. A detailed presentation of the materials used for our motor can be found in Chapter 2, respectively the B-H curve for iron and stator cores and permanent magnet characteristics.

Fifth step is **circuit properties definition**, which allows the user to apply constraints on the current flowing in one or more blocks. Circuits can be defined as either series or parallel connected [10].

After the motor is built, materials and circuit properties are defined and boundary condition set, it is time for mesh generation. In FEMM, this can be done manual or automatic. Manual meshing is recommended for the areas where field interactions take place, like in the air gap. However, the user may choose to optimize the number of elements, by choosing larger triangles in areas with small variation of the magnetic vector potential. For our motor, with geometrical dimensions calculated with the analytical method, the number of elements is 20684 and the number of nodes

is 10475, as represented in Fig. 3.4. In case of geometrical dimensions obtained from hybrid Hooke-Jeeves optimization, the FEM analysis was done for a number of 30991 elements and 15645 nodes. For the hybrid ABC optimization motor dimensions, FEM analysis was done for a number of 30750 elements and 15520 nodes. Even if for optimal case the number of elements and nodes is higher with 50%, the numbers are still low, but will not affect negatively the accuracy of results.

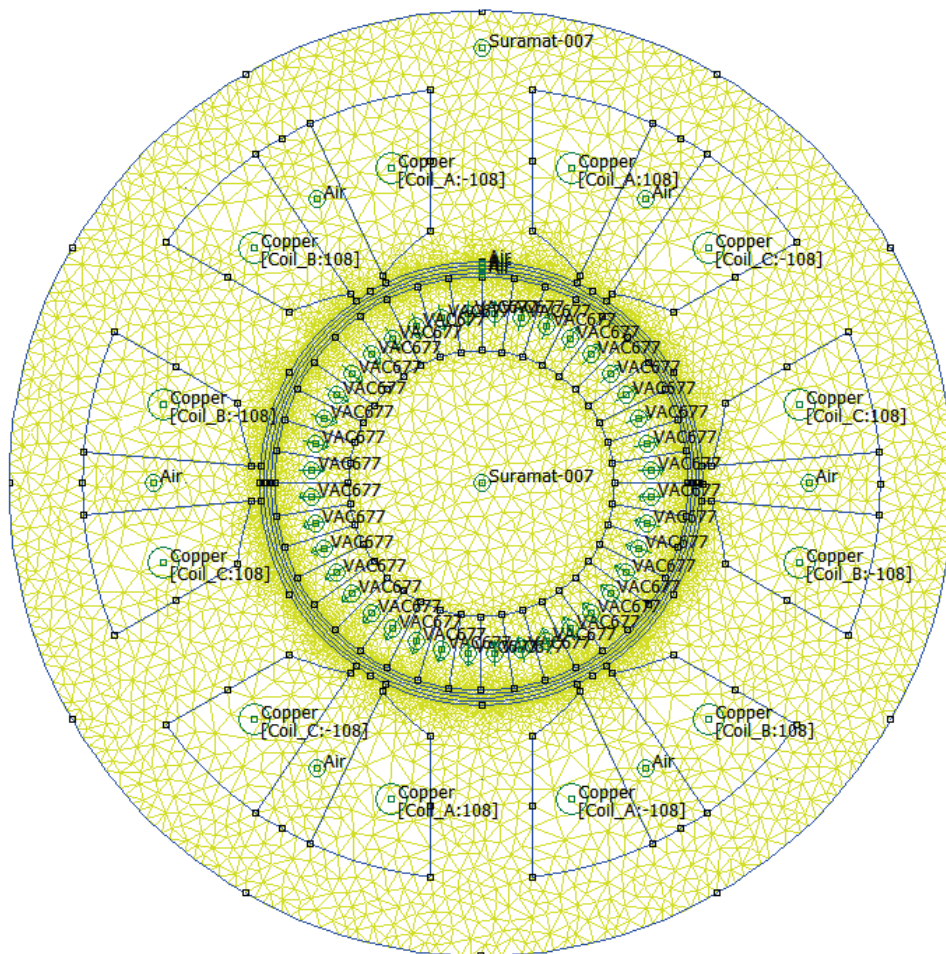


Fig. 3.4 FEM meshing and materials definitions for 6/4 BLDC topology with radial magnetization

Once the meshing is realized, it is time for the analysis to take place as described above, for each element and then to sum all up in the three matrices defined in (3.38) – (3.40). The outcome of this analysis is provided in the post-processor stage of the software, where results are given.



### 3.3.3 Field distribution

The first and most important parameter to be evaluated in FEM analysis is the magnetic field, both at no-load and at load. The information given by the field distribution is the quality of the design.

Both no-load field and load distribution and the air gap flux density were analyzed and calculated for two positions of the rotor, respectively with  $d$  and  $q$  axis aligned with the tooth of phase A.

While at no-load, no armature reaction is present because the current in each phase is null, under load, the base conditions are applied:  $I_n = 1.13$  [A] for both HJ and ABC case.

The no-load field distribution for HJ optimization case is presented in Fig. 3.5 (d-axis) and in Fig. 3.11 (q-axis). Flux density distribution is shown in Fig. 3.7 (d-axis) and in Fig. 3.13 (q-axis). Air gap flux density as a waveform is represented in Fig. 3.9 (d-axis) and Fig. 3.15 (q-axis).

Under load field distribution for HJ optimization case is presented in Fig. 3.6 (d-axis) and in Fig. 3.12 (q-axis). Flux density distribution is shown in Fig. 3.8 (d-axis) and in Fig. 3.14 (q-axis). Air gap flux density as a waveform is represented in Fig. 3.10 (d-axis) and Fig. 3.16 (q-axis).

The no-load field distribution for ABC optimization case is presented in Fig. 3.17 (d-axis) and in Fig. 3.23 (q-axis). Flux density distribution is shown in Fig. 3.19 (d-axis) and in Fig. 3.25 (q-axis). Air gap flux density as a waveform is represented in Fig. 3.21 (d-axis) and Fig. 3.27 (q-axis).

Under load field distribution for ABC optimization case is presented in Fig. 3.18 (d-axis) and in Fig. 3.24 (q-axis). Flux density distribution is shown in Fig. 3.20 (d-axis) and in Fig. 3.26 (q-axis). Air gap flux density as a waveform is represented in Fig. 3.22 (d-axis) and Fig. 3.28 (q-axis).

The flux density has a quite irregular shape due to magnet positioning on the surface of the rotor. If they are inserted in the rotor, the shape of the flux density in the air gap becomes closer to the quasi-rectangular distribution. The ideal waveform for the flux density should be rectangular. However, due to the fringing effect, the corners become more rounded.

The influence of the armature reaction due to current passing through the phases is visible in the figures showing the air gap flux density. Flux density peaks can be observed for shorter periods.

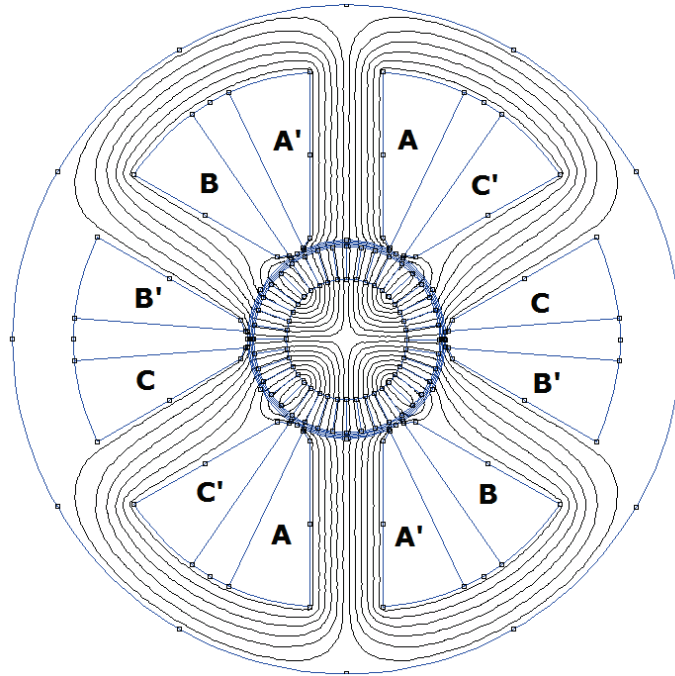


Fig. 3.5 Field distribution at no-load (d-axis aligned with the tooth of phase A) for HJ

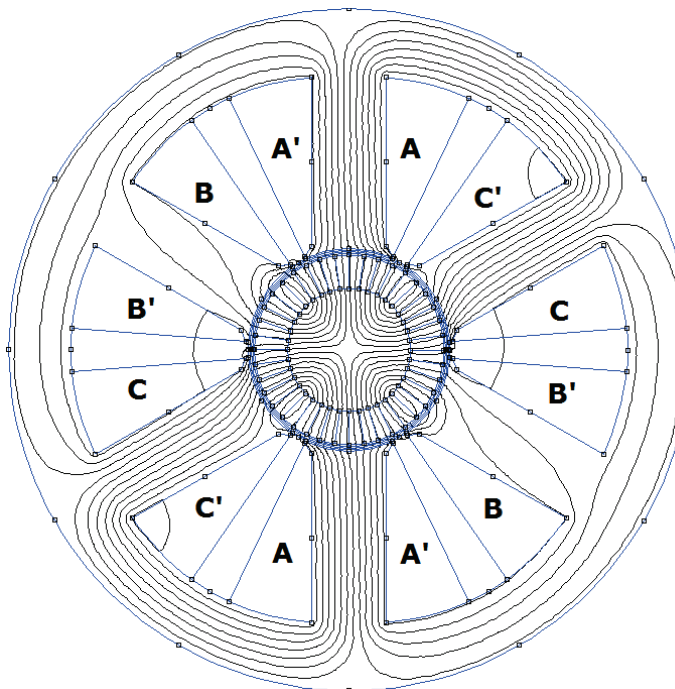


Fig. 3.6 Field distribution under load (d-axis aligned with the tooth of phase A) for HJ

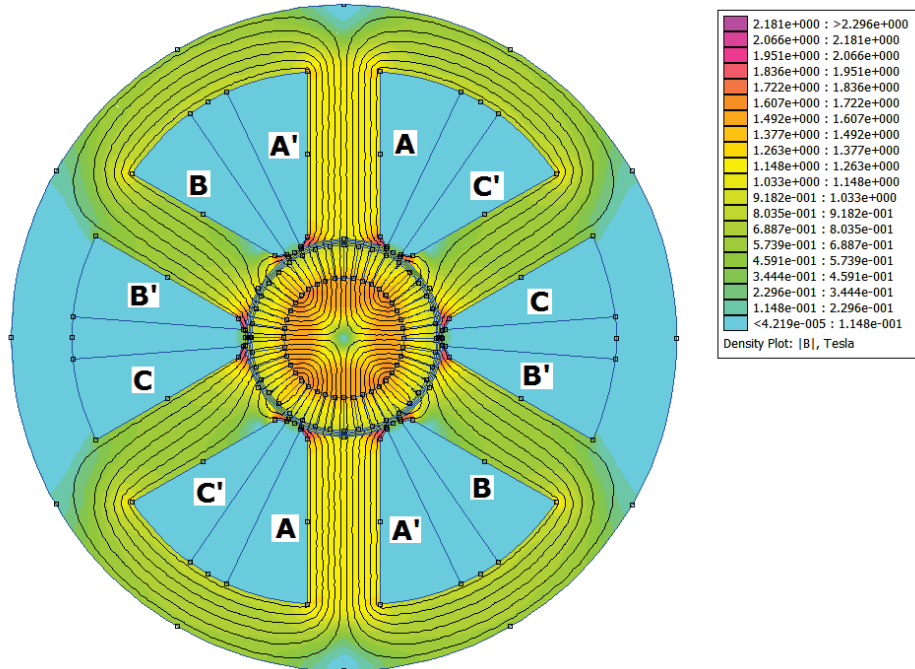


Fig. 3.7 Flux density distribution at no-load (d-axis aligned with the tooth of A) for HJ

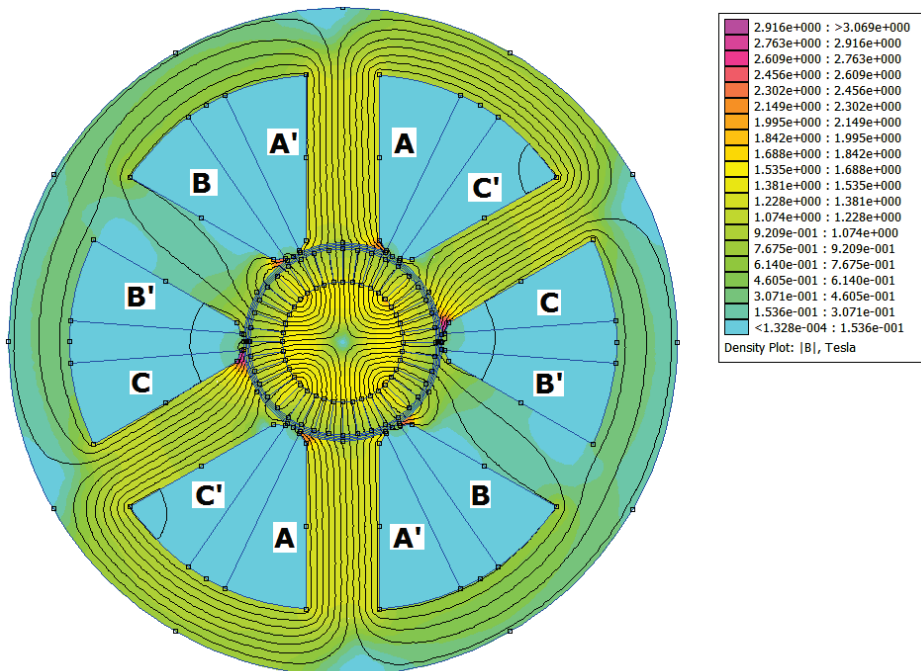


Fig. 3.8 Flux density distribution under load (d-axis aligned with the tooth of A) for HJ

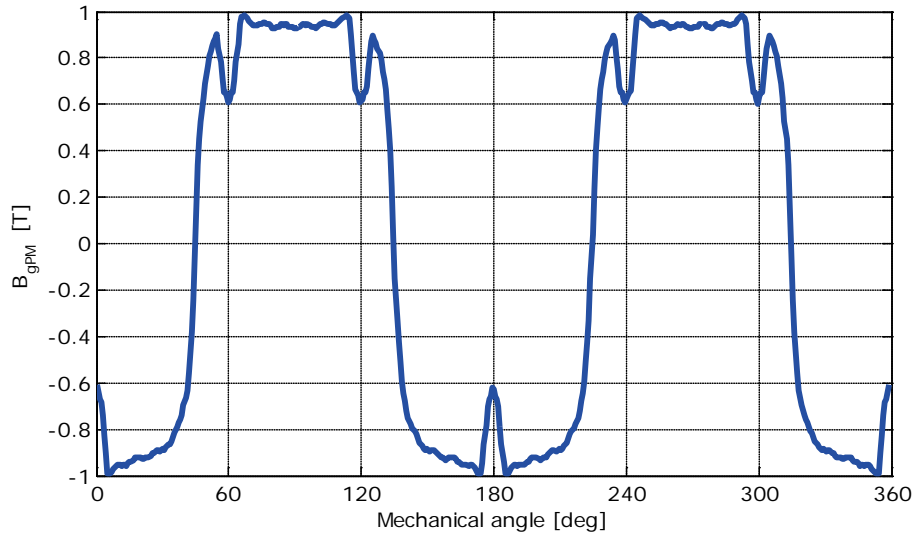


Fig. 3.9 Air gap flux density at no-load (d-axis aligned with the tooth corresponding to phase A) for HJ

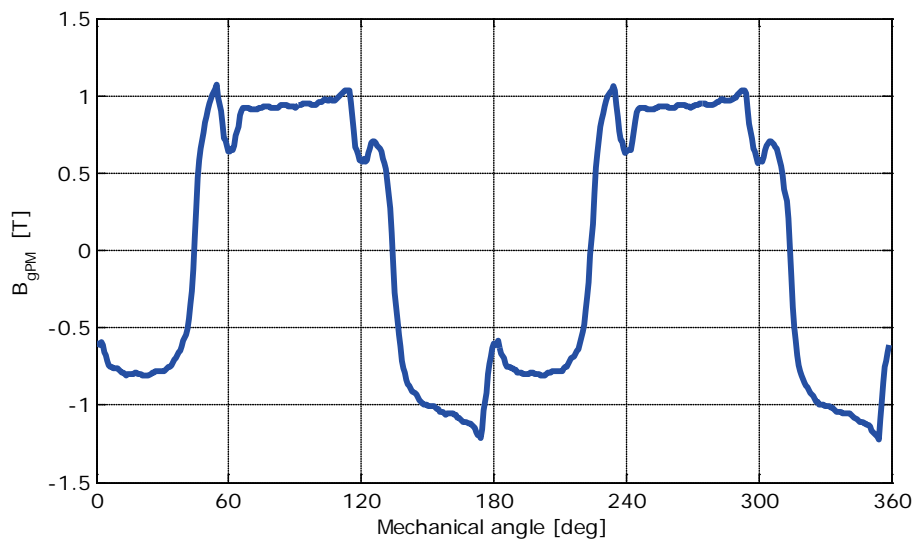


Fig. 3.10 Air gap flux density under load (d-axis aligned with the tooth of phase A) for HJ

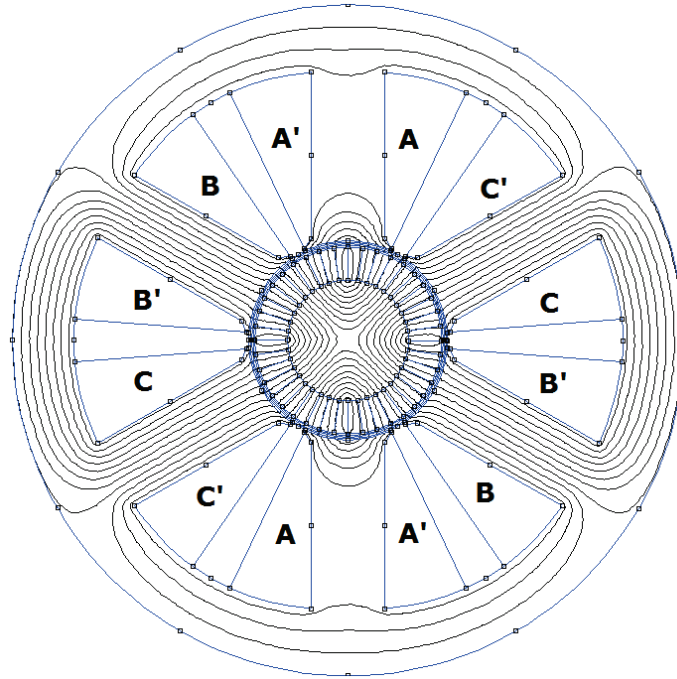


Fig. 3.11 Field distribution at no-load (q-axis aligned with the tooth of phase A) for HJ

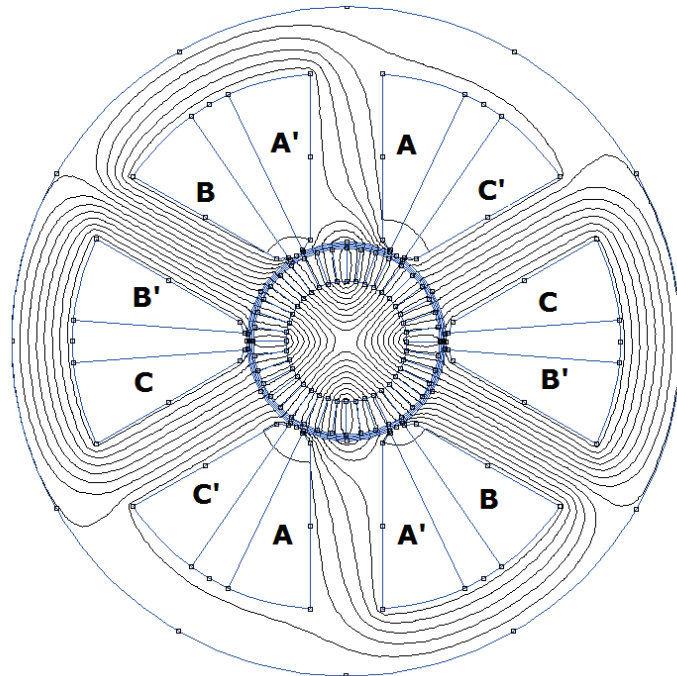


Fig. 3.12 Field distribution under load (q-axis aligned with the tooth of phase A) for HJ

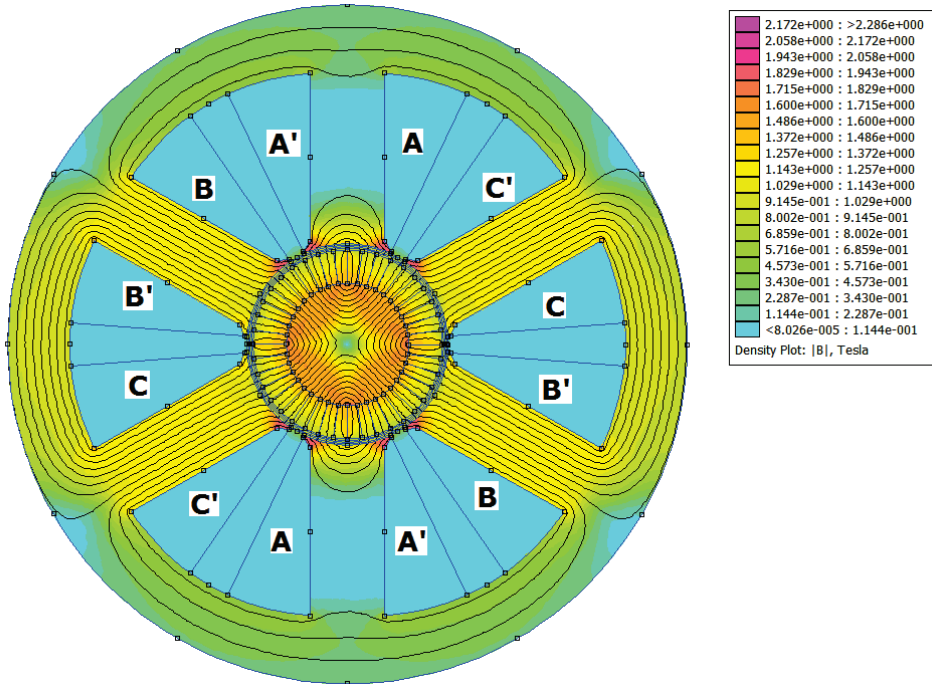


Fig. 3.13 Flux density distribution at no-load (q-axis aligned with tooth of A) for HJ

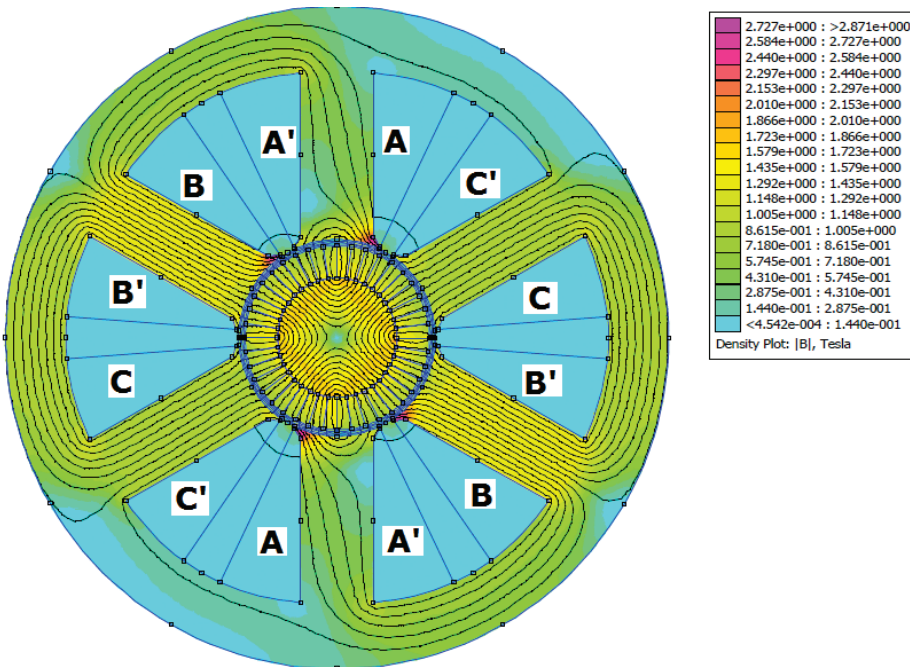


Fig. 3.14 Flux density distribution under load (q-axis aligned with tooth of A) for HJ

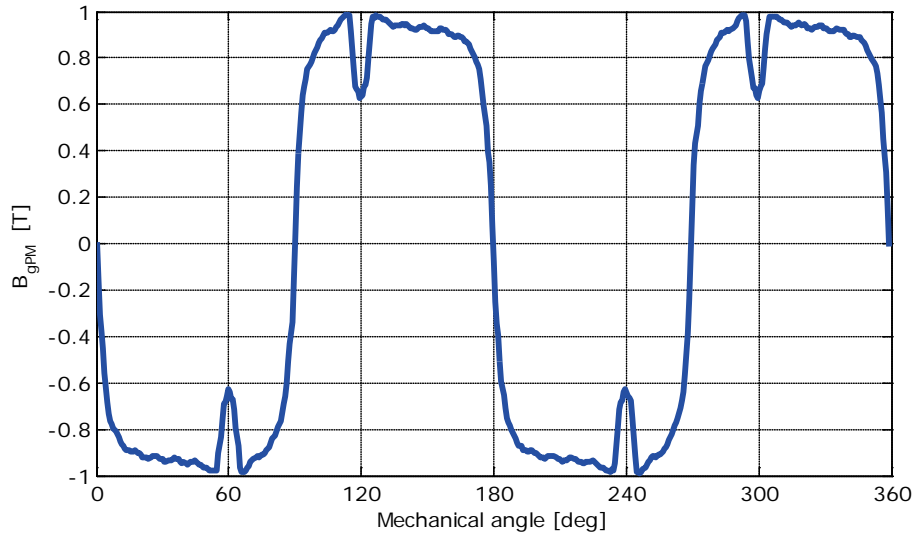


Fig. 3.15 Air gap flux density at no-load (q-axis aligned with the tooth of A) for HJ

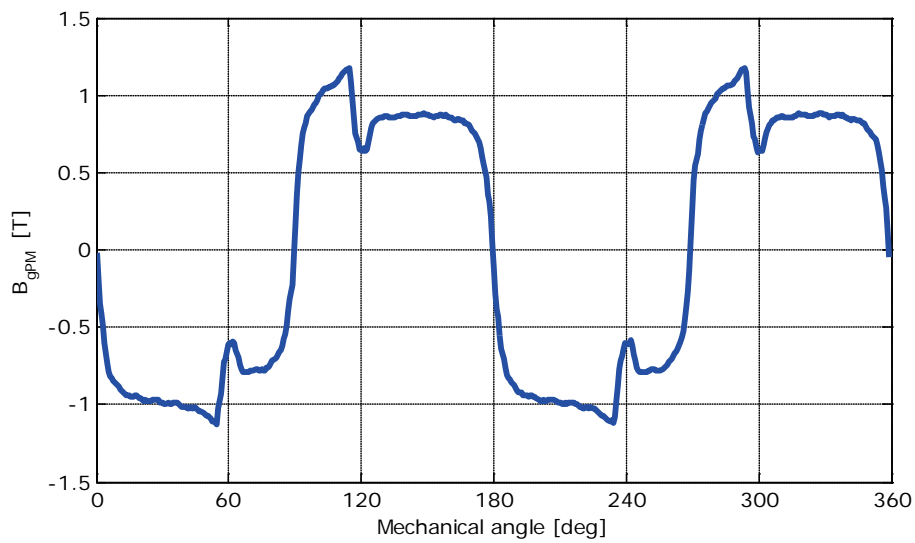


Fig. 3.16 Air gap flux density under load (q-axis aligned with the tooth of A) for HJ

As can be observed from figures above, no-load field distribution validates the geometrical dimensions obtained from hybrid Hooke-Jeeves optimization method. The peak value of the flux density provided by the permanent magnet, measured in the air gap, is slightly lower than 1 [T].

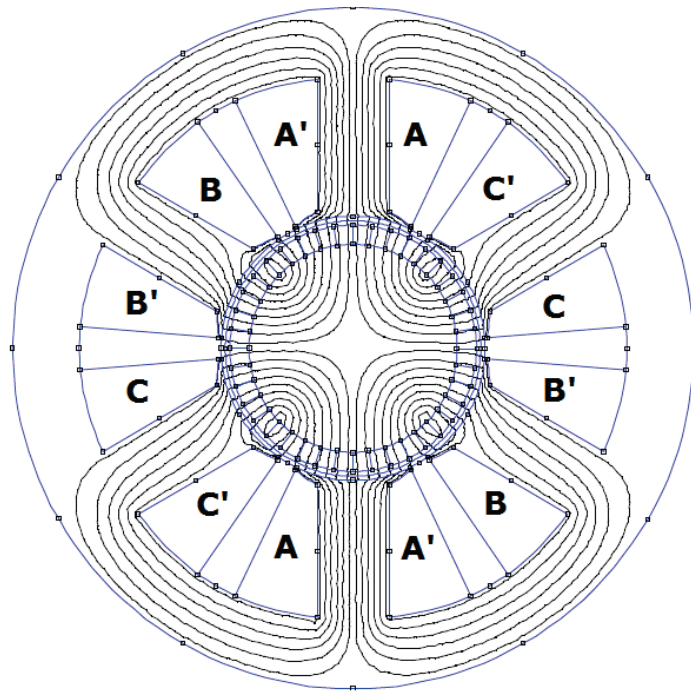


Fig. 3.17 Field distribution at no-load (d-axis aligned with the tooth of phase A) for ABC

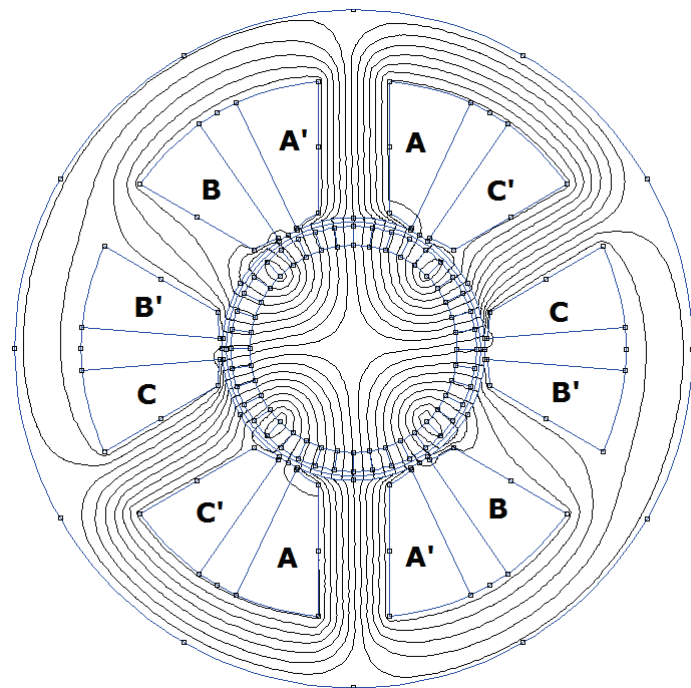


Fig. 3.18 Field distribution under load (d-axis aligned with the tooth of A) for ABC



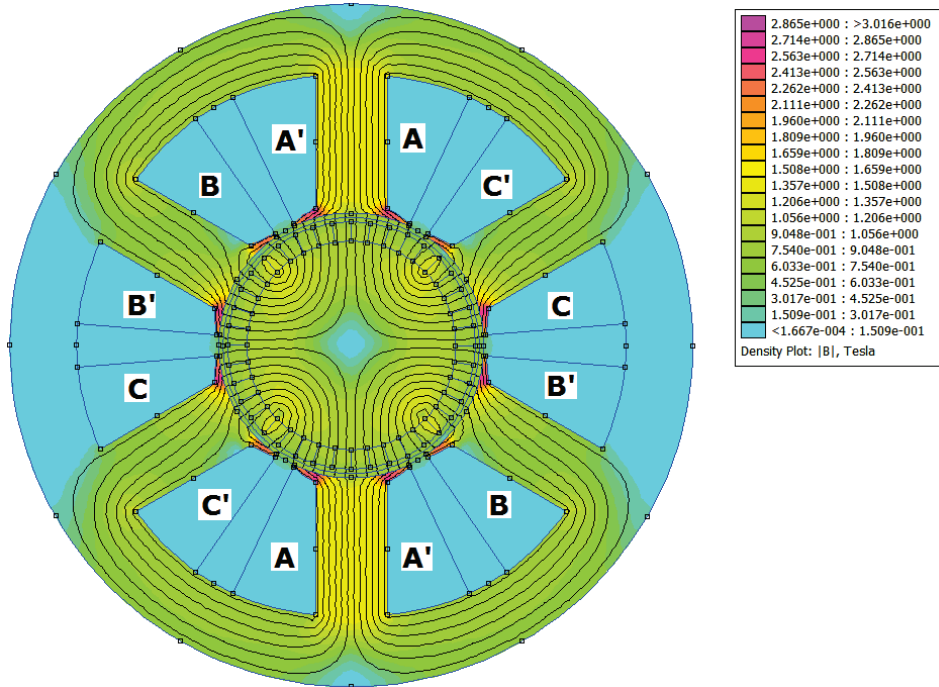


Fig. 3.19 Flux density distribution at no-load (d-axis aligned with tooth of A) for ABC

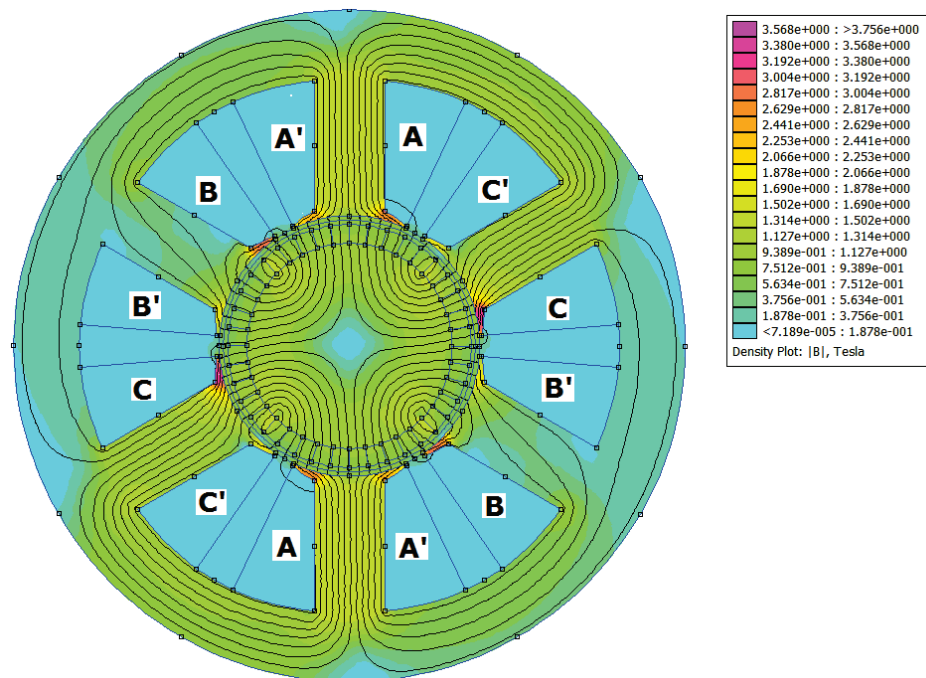


Fig. 3.20 Flux density distribution under load (d-axis aligned with tooth of A) for ABC

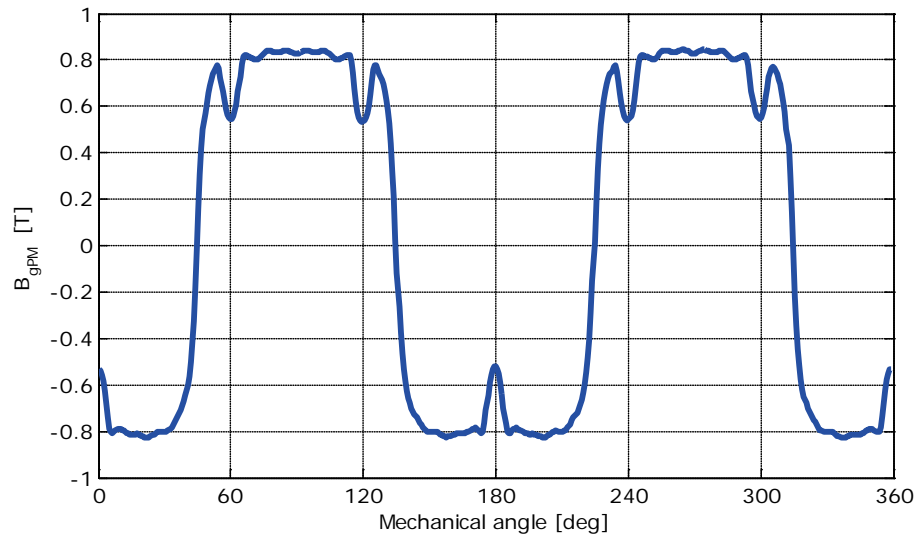


Fig. 3.21 Air gap flux density at no-load (d-axis aligned with tooth of A) for ABC

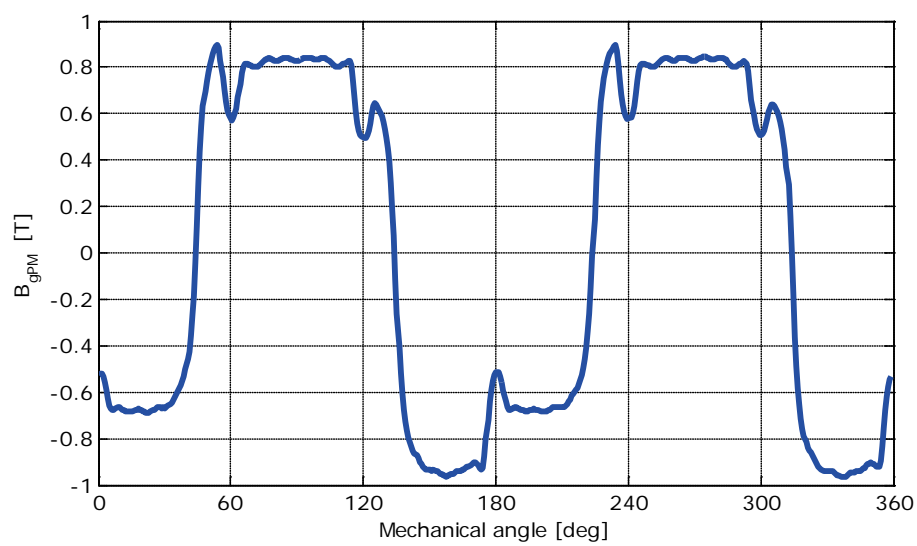


Fig. 3.22 Air gap flux density under load (d-axis aligned with tooth of A) for ABC

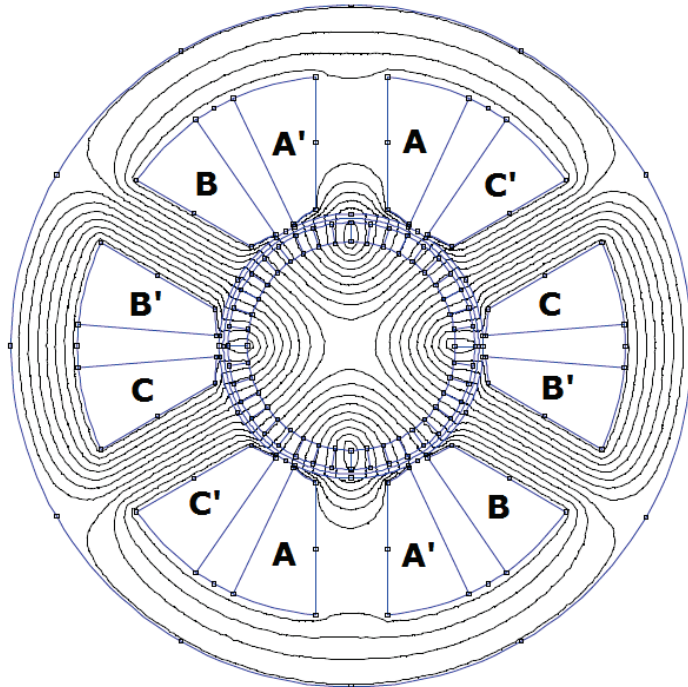


Fig. 3.23 Field distribution at no-load (q-axis aligned with the tooth of phase A) for ABC

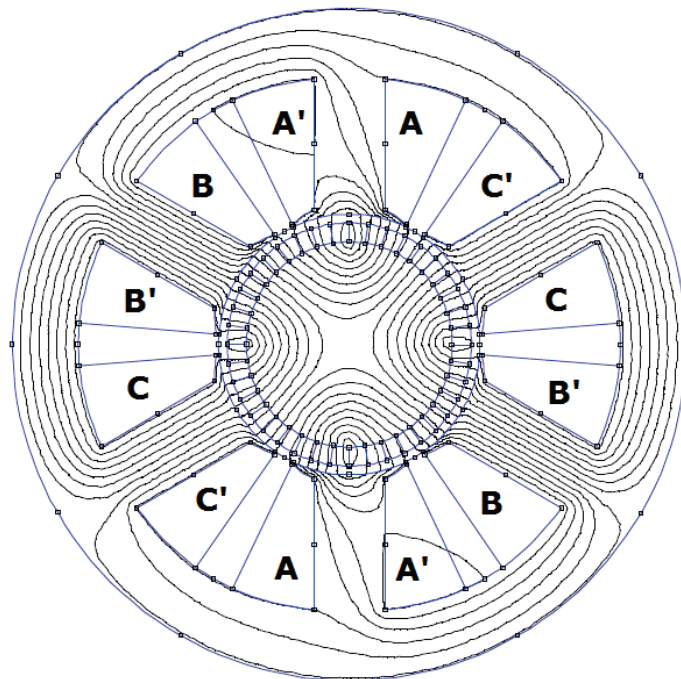


Fig. 3.24 Field distribution under load (q-axis aligned with the tooth of A) for ABC

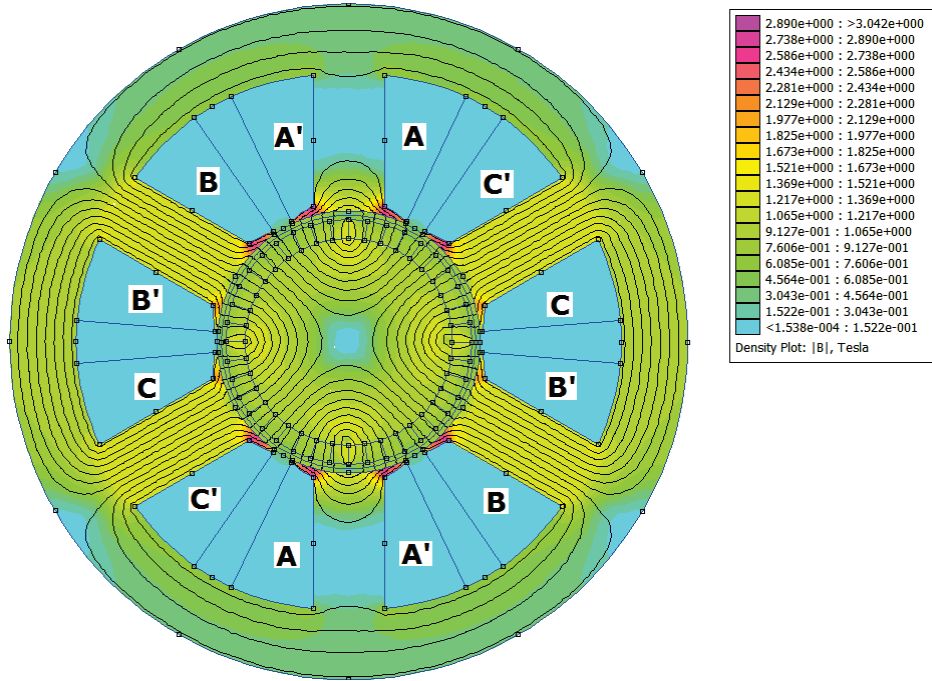


Fig. 3.25 Flux density distribution at no-load (q-axis aligned with tooth of A) for ABC

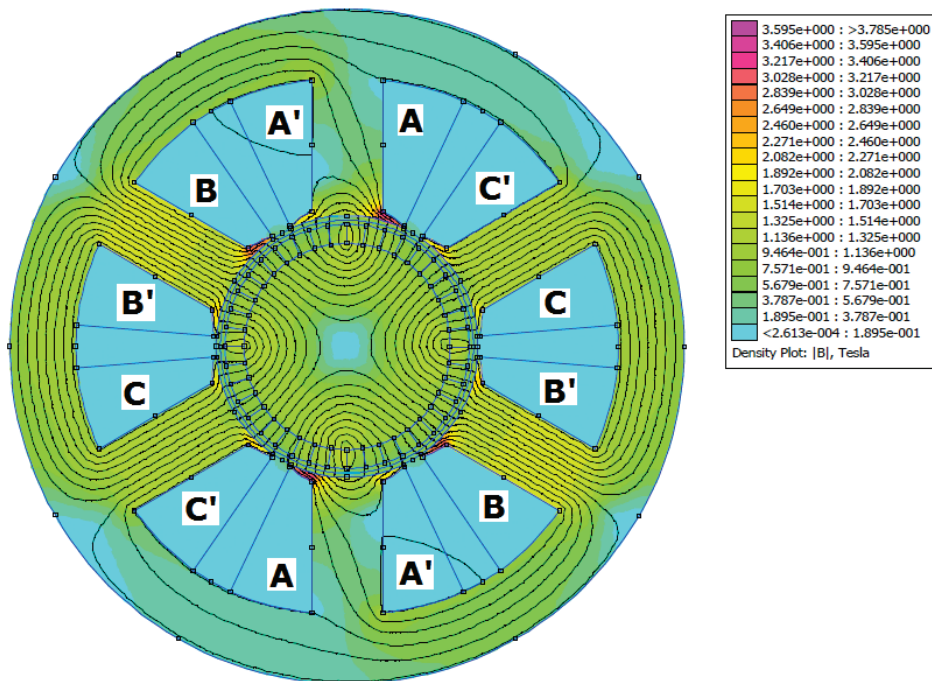


Fig. 3.26 Flux density distribution under load (q-axis aligned with tooth of A) for ABC

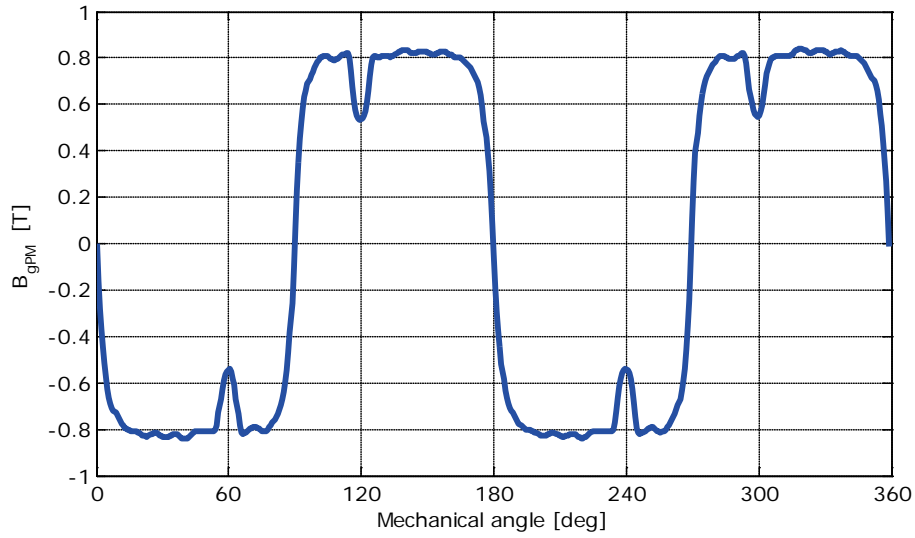


Fig. 3.27 Air gap flux density at no-load (q-axis aligned with the tooth of A) for ABC

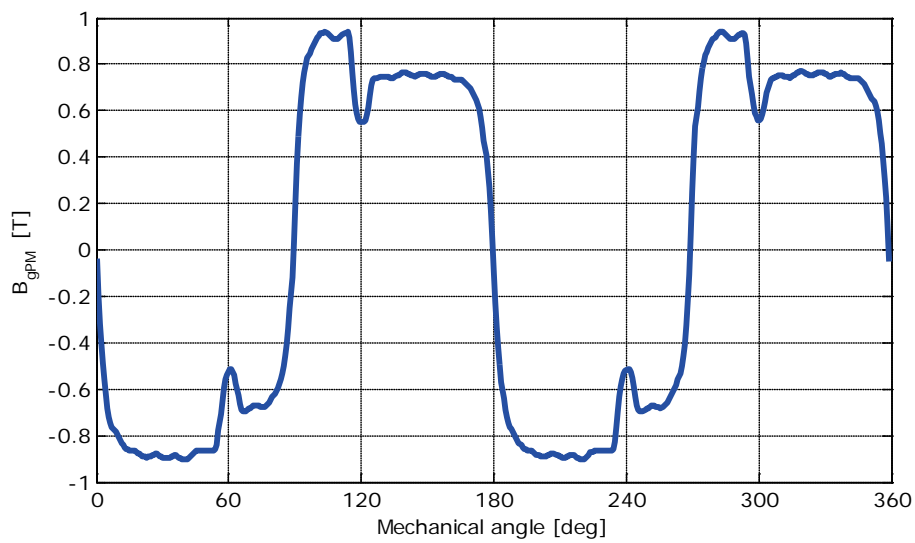


Fig. 3.28 Air gap flux density at load (q-axis aligned with the tooth of A) for ABC

As in the previous case, the field distribution validates the geometrical dimensions obtained through hybrid Artificial Bee Colony optimization method. However, the value of the flux density provided by the permanent magnet, calculated

in the air gap, is lower than in the previous case. From figures 3.21 and 3.27 it can be noticed that the peak value for  $B_{gPM}$  is less than 1 [T].

This is possible due to the reduced magnet height, as can be seen in Fig. 3.17. From Table 2.7 in Chapter 2, the value of  $h_{PM}$  for HJ case is 2.5 [mm], while for the ABC case  $h_{PM}$  is 1.4 [mm].

### 3.3.4 No-load flux linkages and back EMFs

The back EMF expression is given in (3.21) and its meaning is given by Faraday's law of induction, which states that the induced electromotive force (EMF) in any closed circuit is equal to the time rate of change of the magnetic flux through the circuit. Since the back EMF is dependent on the magnetic flux, first we need to determine how this is linked to the magnetic flux density.

Since the magnetic flux lines paths are through the teeth of the phases, the magnetic flux will go through stator teeth and yoke. The surface where the magnetic flux lines pass can be written as:

$$S = w_{sp} \cdot L_{stk} \quad (3.44)$$

Equivalent to the expression of electric flux, the magnetic flux can be written:

$$\lambda_{PM} = \int_S \bar{B} \cdot dS \quad (3.45)$$

Given the relation that describes the tooth's surface, (3.44), and knowing that the stack length is constant throughout the motor, the total flux in a flux bulk path can be determined using the line integral of the normal component of the flux density along a specified contour. Our contour is the tooth width, and the line integral evaluates a large number of points evenly spaced along the contour and integrating using a simple trapezoidal-type integration scheme [10]. This way, the equation of the magnetic flux becomes:

$$\lambda_{PM} = L_{stk} \cdot \int_{\Gamma} B_n \cdot dl \quad (3.46)$$

The curve  $\Gamma$  is equal to the tooth width. In our situation, we need to investigate the magnetic flux for three phases, thus three different curves must be defined. Once the value of the magnetic flux is evaluated for each rotor position, the back EMF for each phase can be calculated, taking into account Faraday's law expressed in (3.21).

$$e = -\frac{d\lambda_{PM}}{dt} = -\frac{d\lambda_{PM}}{d\theta} \cdot \frac{d\theta}{dt} = -\left( N_{ph} \cdot \frac{d\Phi_{PM}}{d\theta} \right) \cdot \omega_m = k_e \cdot \omega_m \quad (3.47)$$

As can be seen, the amplitude of the back EMF on each phase depends on the value of the mechanical speed. Once the mechanical speed reaches its nominal value, the value of the back EMF becomes equal to the amplitude of the input voltage. Beyond nominal speed the motor can be controlled only by flux weakening. Since in our case, the nominal speed is equal to the maximum speed, no flux weakening is required. The other term in back EMF's expression is the back EMF constant, which is dependent on the magnetic flux and the number of turns per phase.

$$k_e = -N_{ph} \cdot \frac{d\Phi_{PM}}{d\theta} \quad (3.48)$$

In what follows, the no-load flux linkages (figures 3.29 and 3.32), back EMF constant (figures 3.30 and 3.33) and no-load back-EMF (figures 3.31 and 3.34) will be shown for Hooke-Jeeves optimization case and ABC optimization case.

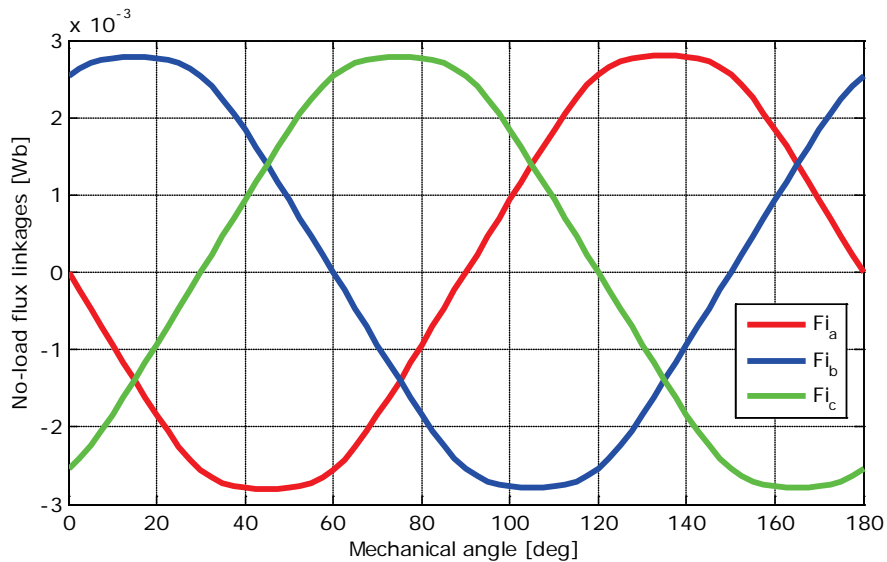


Fig. 3.29 No-load flux linkages for each phase for HJ case

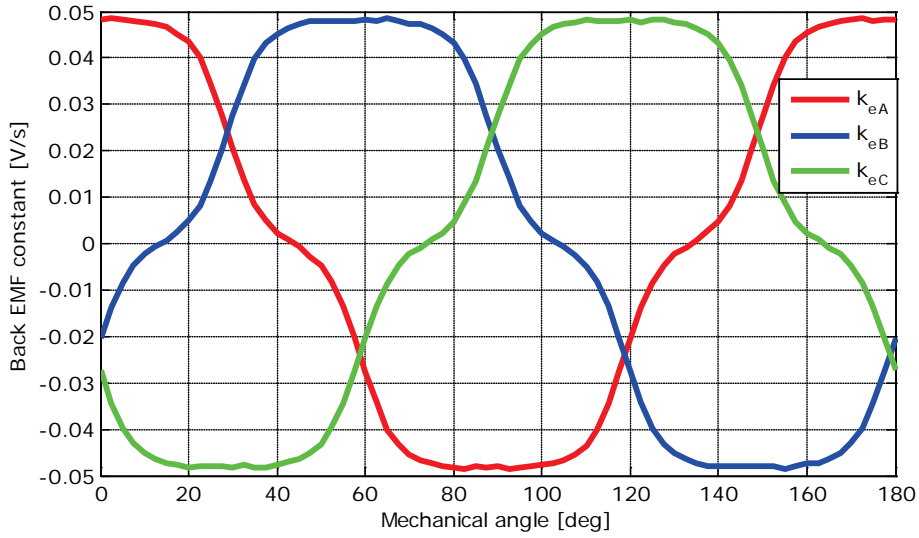


Fig. 3.30 Back EMF constant versus rotor position for HJ case

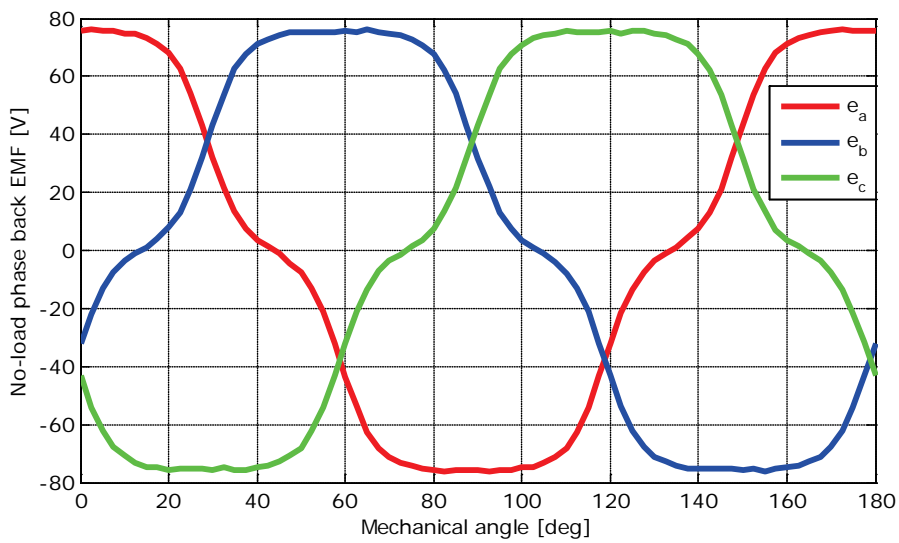


Fig. 3.31 No-load phase back EMF for HJ case at base speed ( $\omega_m = 1570$  [rpm])



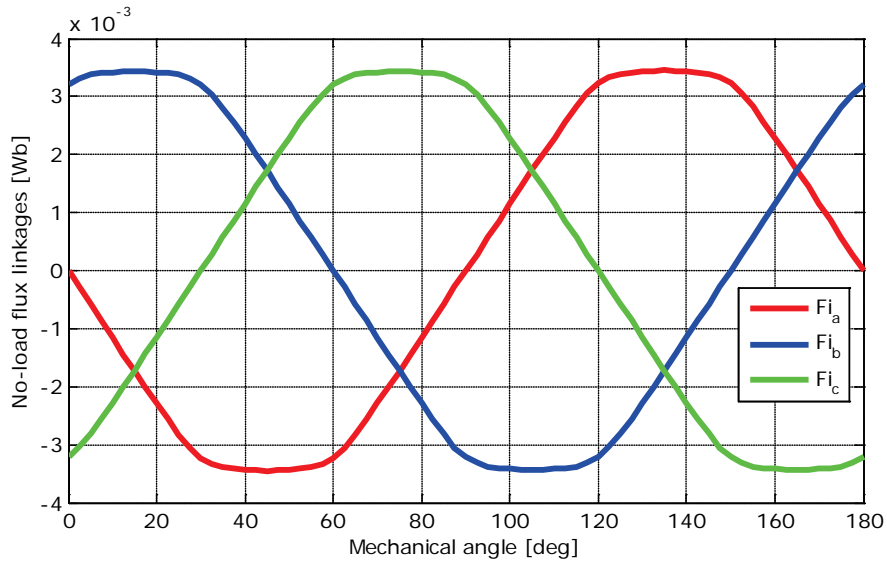


Fig. 3.32 No-load flux linkages for each phase for ABC case

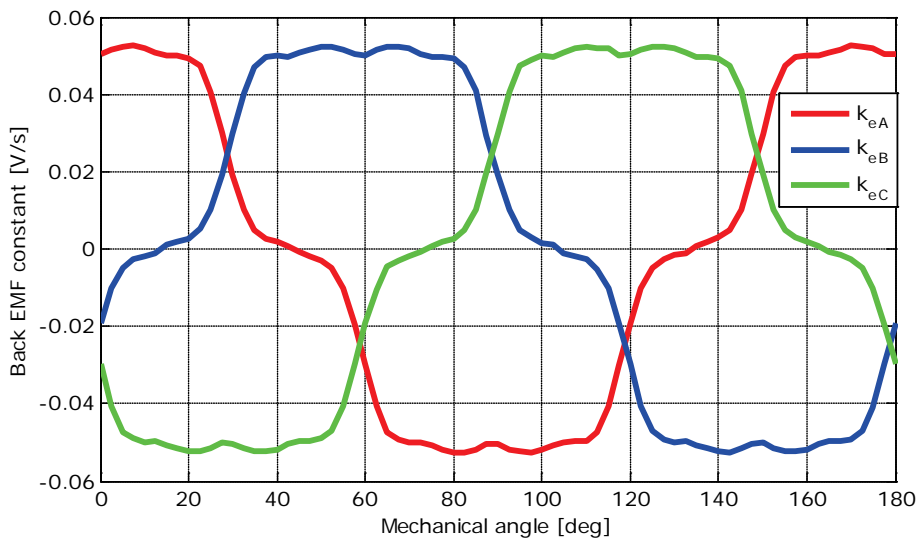


Fig. 3.33 Back EMF constant versus rotor position for ABC case

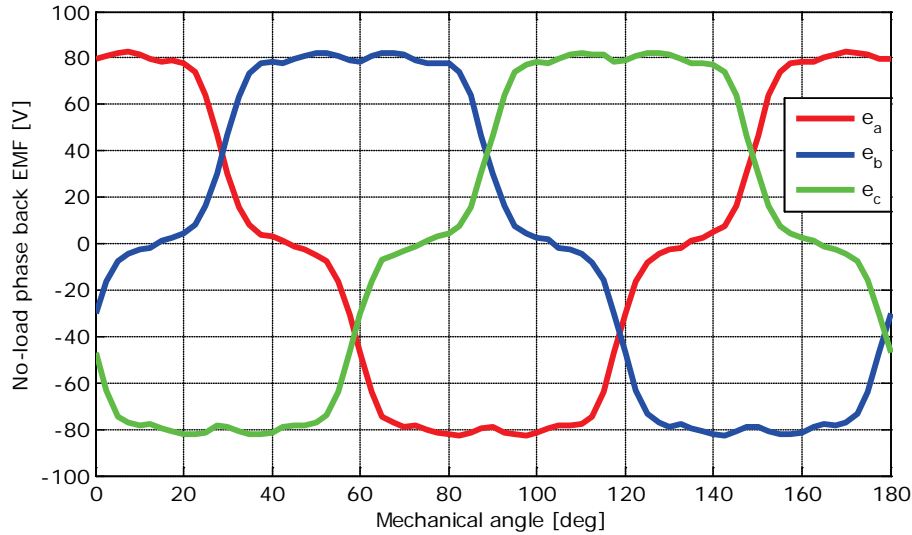


Fig. 3.34 No-load phase back EMF for ABC case at base speed ( $\omega_m = 1570$  [rpm])

From figures 3.31 and 3.34 one can notice that the shape of the back EMF is trapezoidal, thus confirming the necessity of controlling the BLDC with trapezoidal currents.

### 3.3.5 Forces in an electromagnetic field

One of the most important attributes of FEM is the possibility to calculate the forces and torques. To do this, there are four methods: the Maxwell stress tensor, the co-energy method, the Lorentz force equation and the rate of change of field energy method ( $B \partial B / \partial x$ ) [1]. The choice of the proper method to obtain forces and torques depends on the problem, but usually the first two methods are used to solve electrical machine problems.

The **Lorentz force equation method** is suitable to compute the force on a collection of currents in a region containing only materials with a unit relative permeability [10]. The formula for this method is [9]:

$$\bar{F} = \int_V \bar{J} \times \bar{B} dv \quad (3.49)$$

The **Maxwell stress tensor** prescribes a force per unit area produced by the magnetic field on a surface. Thus, a differential force is calculated, while by integration of it, the total force through that surface can be obtained [9].

$$\bar{F} = \oint_{\Sigma} d\bar{F} = \oint_{\Sigma} \left[ \frac{1}{\mu_0} B(B \cdot n) - \frac{1}{2\mu_0} B^2 n \right] dS \quad (3.50)$$

The electromagnetic force has two components, in the normal and tangential directions to the surface where is calculated, as can be seen in the figure below.

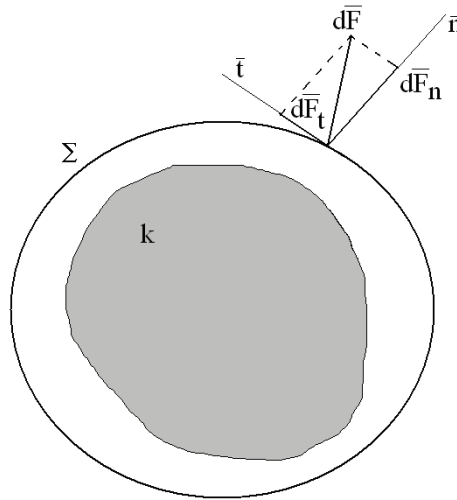


Fig. 3.35 Integration of Maxwell tensor with all components of the force shown [9]

The expressions for the normal and tangential components of the force are:

$$F_n = \frac{L_{stk}}{2\mu_0} \int (B_n^2 - B_t^2) dl \quad (3.51)$$

$$F_t = \frac{L_{stk}}{\mu_0} \int B_n B_t dl \quad (3.52)$$

In the equations above the terms are the stack length ( $L_{stk}$ ), the normal vector to the surface ( $n$ ), integration contour ( $dl$ ), radial (normal) component of the magnetic flux density ( $B_n$ ) and tangential component of the magnetic flux density ( $B_t$ ).

With the **co-energy method**, the force or torque is calculated as the derivative of the stored magnetic co-energy  $W'$  with respect to a small displacement.

$$F_s = \frac{dW'}{ds} \approx \frac{\Delta W'}{\Delta s} \quad (3.53)$$

In what follows, the total forces that stress the rotor are shown for both optimization cases, as in the previous sub-chapters. This is very important, since the surface magnets, especially at high speeds, are stressed. This way, we can see what are the centrifugal forces that act on the rotor at the base mechanical speed of 1570 [rpm] (equivalent to the electrical speed of 15000 [rpm]).

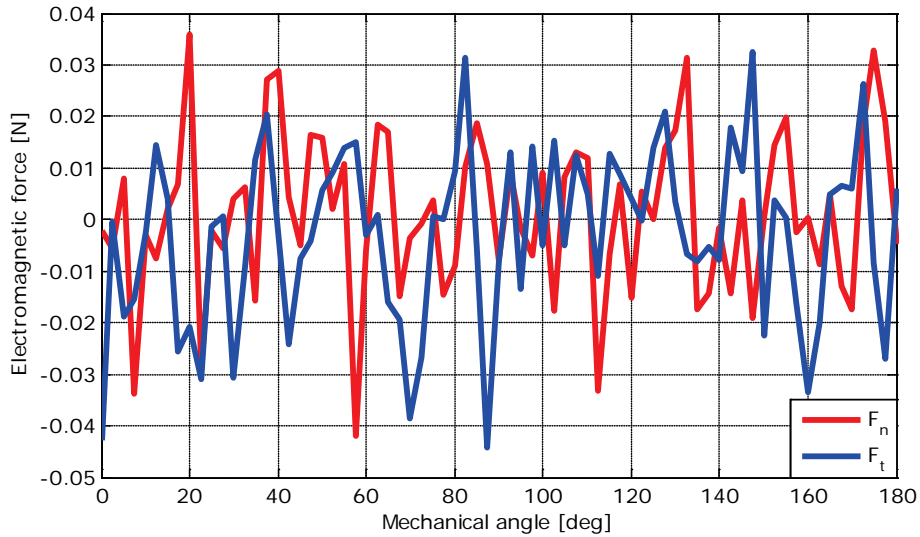


Fig. 3.36 No-load electromagnetic force for HJ case at base speed ( $\omega_m = 15000$  [rpm])

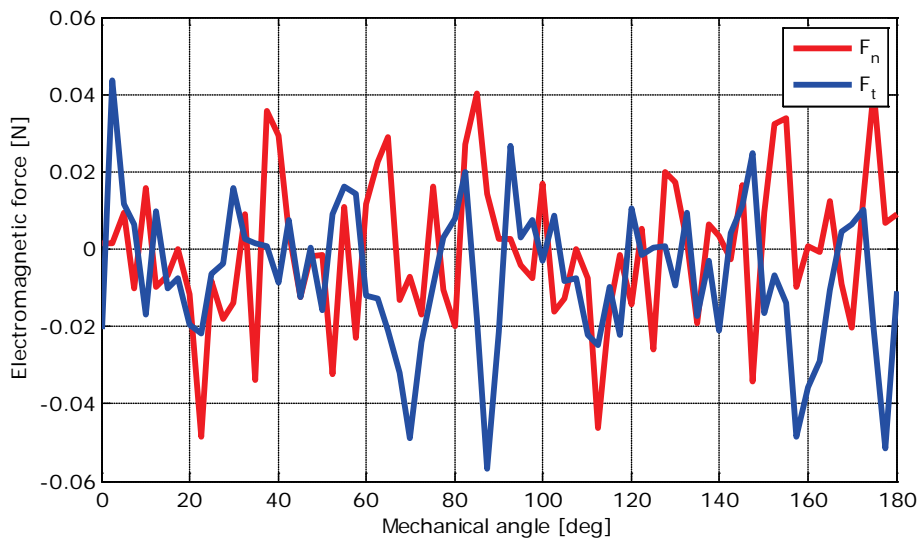


Fig. 3.37 Electromagnetic force under load for HJ case at base speed ( $\omega_m = 15000$  [rpm])

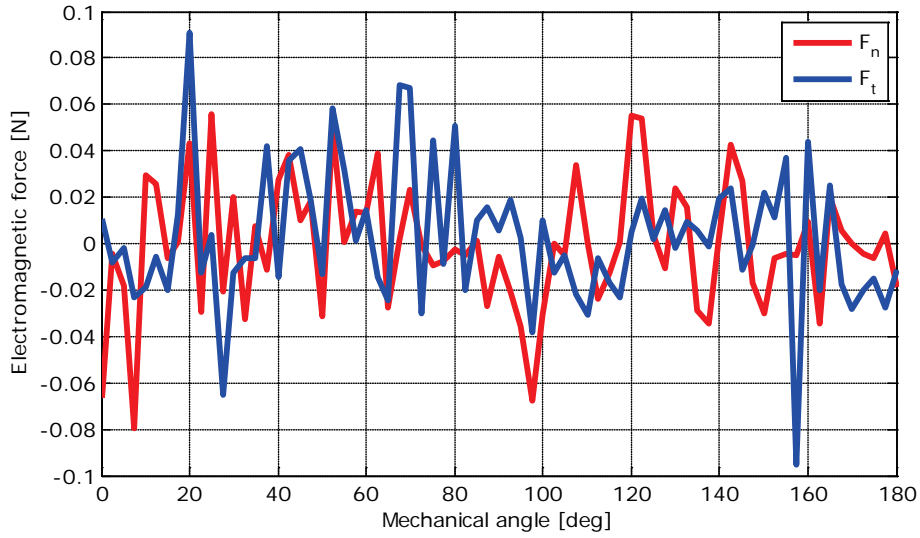


Fig. 3.38 No-load electromagnetic force for ABC case at base speed ( $\omega_m = 15000$  [rpm])

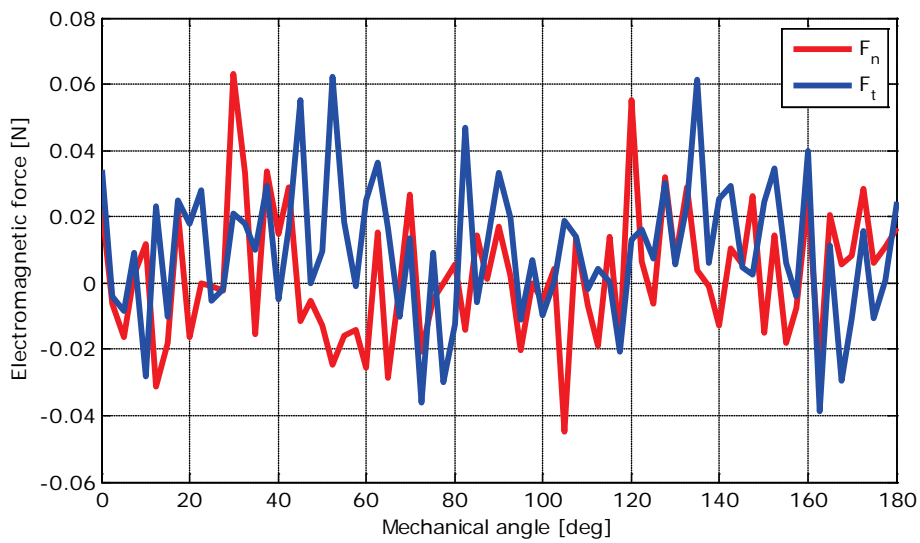


Fig. 3.39 Electromagnetic force under load for ABC case at base speed ( $\omega_m = 15000$  [rpm])

As can be observed, the forces for the ABC case are somewhat higher than for the HJ case, which will lead to increased noise, vibrations and added stress on the magnets.

### 3.3.6 Torques in an electromagnetic field

Like in the case of forces, the value of the torque can be calculated with one of the three methods presented above.

With the **Maxwell stress tensor**, the value of the torque can be obtained through the following expression:

$$T = r \times F_t = \frac{Lstk}{\mu_0} \oint_I r B_n B_t dl \quad (3.54)$$

In equation (3.54),  $r$  is the radius of the circumference which lies in the air gap. The accuracy of this method is markedly dependent on the model discretization and on the selection of the integration line or contour. The Maxwell stress tensor line integration necessitates a precise solution in the air gap, demanding a fine discretization of the model in the air gap since the flux density is discontinuous at the nodes and across boundaries of first order elements [1, 10].

With **co-energy method**, the instantaneous torque is:

$$T = \frac{dW'}{dt} \approx \frac{\Delta W'}{\Delta t} \quad (3.55)$$

The problem with the finite difference approach is that two finite element models have to be calculated, doubling the calculation time [1].

With **Lorentz force theorem**, the instantaneous torque expression becomes a function of phase EMFs and phase currents:

$$T = \sum_{l=A,B,C} i_l(t) \left[ 2pN_{ph} \int_{-\frac{\pi}{2mp}}^{\frac{\pi}{2mp}} r L_{stk} B(\theta, t) d\theta \right] \quad (3.56)$$

$$T = \frac{1}{2\pi n} [e_a(t)i_a(t) + e_b(t)i_b(t) + e_c(t)i_c(t)] \quad (3.57)$$

From the last equation, we can see that the instantaneous torque varies with the amplitude of the back EMF and phase currents and, implicitly, with the mechanical speed.

The output torque is the essential characteristic of an electric machine, which is designed to convert electrical power into mechanical power. In what follows, the load torque for both optimization cases and the one obtained from the analytical model will

be presented, as a comparison. Since in the previous chapter, one of the penalty functions was related to the value of the analytical electromagnetic torque, the evaluation for all three cases is necessary.

The load torque is composed of two parts, the excitation torque and the cogging torque. The first one depends on the value of the phase current, while the latter one is given by the interaction between permanent magnet edges and the slot opening and it will be discussed later on.

The electromagnetic torque's expression is:

$$T = T_{exc} + T_{cogg} \quad (3.58)$$

The excitation torque's expression is:

$$T_{exc} = k_e \cdot \frac{(i_a + i_b + i_c)}{3} \quad (3.59)$$

In the equation above the factor  $k_e$  is the same as for back EMF. The first thing to see is the dependence of the excitation torque on the phase currents. The ideal case is a rectangular shape for the current, but due to imperfections in motor design and control, the shape of the current is rather trapezoidal. In the figure below, we can observe the shape of the current applied in FEM evaluation. The current used has a waveform close to the rectangular shape, but still trapezoidal, which will inherently lead to load torque pulsations.

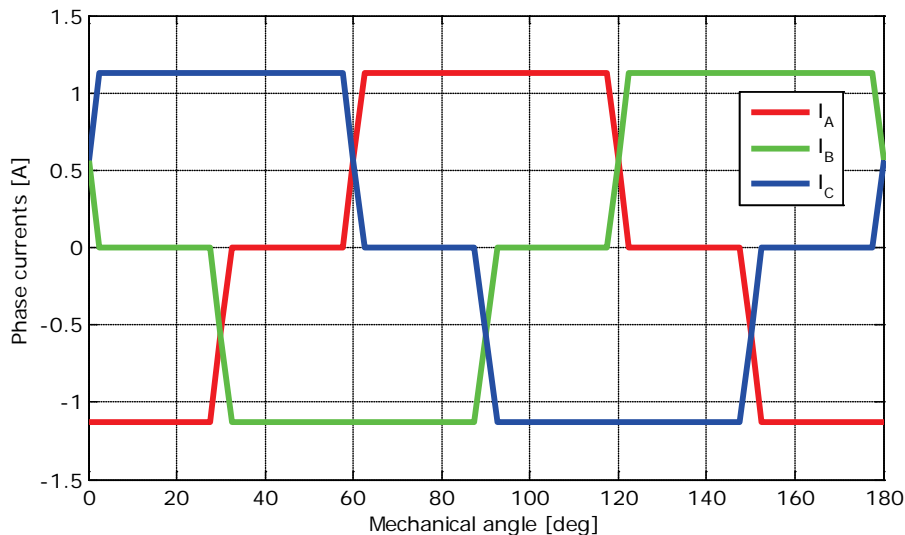


Fig. 3.40 Phase currents waveforms

The following figures will show the total torque, excitation torque and average torque for all three cases: analytical (Fig. 3.41), Hooke-Jeeves (Fig. 3.42) and ABC (Fig. 3.43).

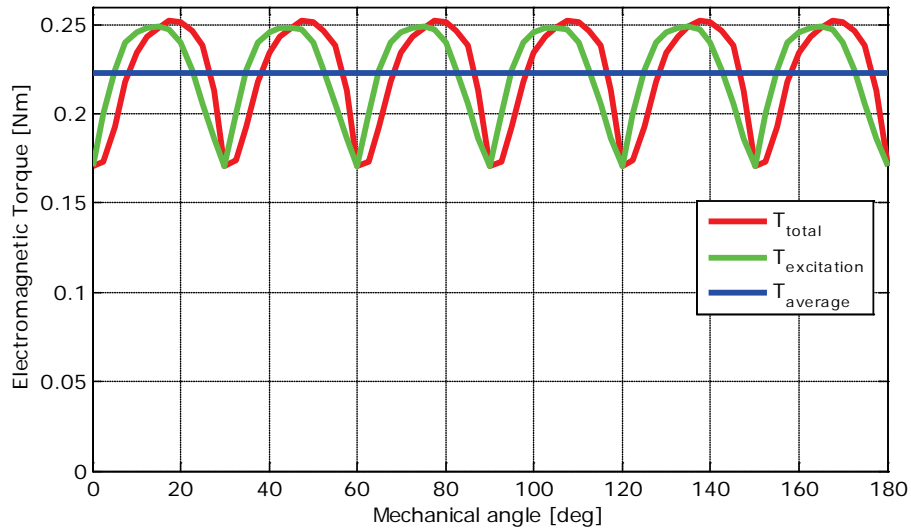


Fig. 3.41 Electromagnetic torque for analytical case (total, excitation and average)

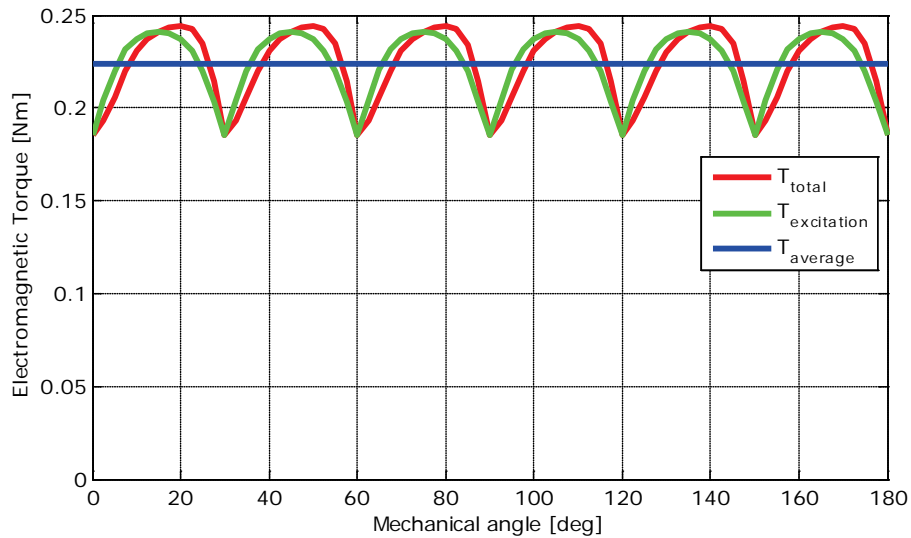


Fig. 3.42 Electromagnetic torque for HJ case (total, excitation and average)



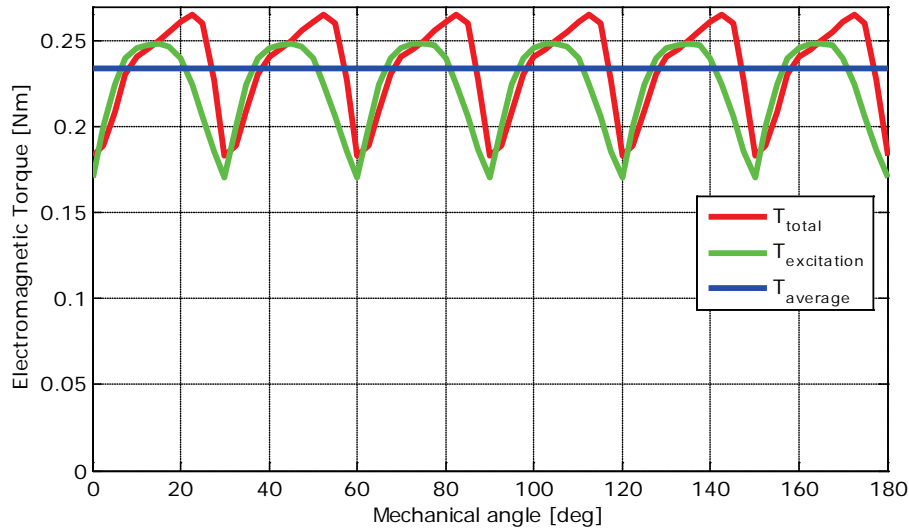


Fig. 3.43 Electromagnetic torque for ABC case (total, excitation and average)

From the figures above it can be noticed that the average value of the torque is higher for the ABC case (0.234 [Nm]), compared to the Hooke-Jeeves case (0.2237 [Nm]) and the analytical case (0.2228 [Nm]). In the previous chapter, the value of the electromagnetic torque for the penalty function was imposed to be at least 10% higher than analytical case to reduce the costs, which is not realized. The highest value was 5% higher than in analytical case.

However, it can be observed that for the Hooke-Jeeves case, the torque pulsations are smaller than in the other cases, while for the ABC case, the torque pulsations are the highest.

Next, the main reason for torque pulsations, the cogging torque, is analyzed.

### 3.3.7 Cogging torque

The most important parameter to find for an electrical machine is the output torque. As its main purpose is to transform electrical energy into mechanical energy (torque), it is only normal to consider the shape and amplitude of the latter one of greatest importance. As for any waveform, it is crucial to have a smooth shape, with no pulsations. As can be seen in figures 3.41 – 3.43, this is not the case, as the total electromagnetic torque has great pulsations.

Torque ripple can come from two sources, irregularities in the machine and the supply. From the supply, torque pulsations are induced by current ripple resulting from PWM or by phase current commutation. From equation (3.58) one can notice that the total torque is divided in two distinct components, the excitation torque (provided by the armature reaction) and the cogging torque (torque at zero current) [11 – 33].

Pulsations due to excitation current can be reduced by optimal shape of phase currents. The ideal case is when currents are supposed to be rectangular, thus an optimal current waveform can be obtained if the rising and falling slopes are steep enough so the variation of the current shape is closer to reality. Due to switching of the phases and since only two phases are working at a time, excitation torque pulsations are inherent. The only way that the waveform can be smoothed is by employing a sinusoidal current control with three phases working at a time.

From the machine, there are three possible sources of torque pulsations.

First source is the cogging (detent) effect, i.e. interaction between the rotor magnetic flux and variable permeance of the air gap due to stator slot geometry, which leads to cogging torque. Cogging torque is harmful for the motor because is the main source of both vibrations and noise, effects that can be amplified in variable speed drives when the torque frequency is equal with the mechanical resonant frequency of the stator or the rotor. Besides these known mechanical disadvantages, the cogging torque will also affect seriously the speed control performances at low speeds, which is an essential issue in systems that need very accurate position precision at all speeds, like robots [27].

The second source is the distortion of trapezoidal distribution of the magnetic flux density in the air gap, which leads to the apparition of field electromagnetic torque.

The last source of torque pulsation in the machine is the difference between permeances of the air gap in the d and q axis, which produces the reluctance torque [13].

However, the most prominent component of the electromagnetic torque that generates the pulsations in our motor is the cogging torque. The source of this parasitic torque and the best ways to reduce it will be treated in this sub-chapter. The issue is a main concern in PMSMs, as it is treated in numerous books [11 – 13] and articles [14 – 33].

Cogging torque, also known as detent torque, is defined as an outcome of the interaction between the rotor magnets and the slots and poles of the stator (stator saliency). All permanent magnet motors suffer from this annoying parasitic element in motor design, but it is more visible on motors with surface permanent magnets. Cogging torque doesn't affect slotless motors or motors with closed slots.

There are two ways to evaluate cogging torque in a motor, namely the analytical method and the numerical method, also known as finite element. Although more easy to implement and accurate for simpler geometries, the analytical method has limited performance in evaluating the cogging torque for more complex topologies, due to oversimplification. On the other hand, the numerical methods are more efficient, independent of geometry complexity, but take more computation time. This way, a compromise of using these two methods together must be found. Usually, the analytical way to predict cogging torque is used during the preliminary optimization design, while the finite element is used to verify the design parameters.

In the previous chapter, during the preliminary design stage, numerical method was employed because, as it turned out, the negative and positive peaks can be found with minimum computational effort. In case the magnet pitch covers the entire pole or,

to respect the reality, almost the entire pole, due to constructional imperfections, the instantaneous cogging torque is zero when the interpole axes align with the centers of teeth or with the centers of slots. In terms of magnetic interaction, the first case corresponds to a stable equilibrium position, because the leakage flux paths between the north and south poles are closing only through the air gap, while the second case corresponds to an unstable equilibrium position, because the leakage flux paths now cross the slot openings also [14].

However, one is interested during the design stage to know when cogging torque negative and positive peaks occur and what is their amplitude. From the definition, it is clear that those peaks appear whenever the interpole is aligned with stator slots edges.

There are three basic ways to analytically predict cogging torque, by integration of the lateral forces along the slot sides, derivation of the air gap co-energy and integration of the tangential component of Maxwell stress tensor along a circular contour inside the air gap [33]. Basically, there are five distinct factors that influence the amplitude and shape of the cogging torque, as presented in [12, 20].

**Magnet strength** is the first factor that affects the cogging torque, due to the remanent flux density, which is affected by the temperature (while the motor is moving) and initial charging of the magnets (a permanent condition). On the other hand, the surface PMs can be surface-parallel, surface-radial or bread-loaf type, while the magnetization can be parallel or radial; radial magnetization leads to an increase of 30% in the cogging torque peak-to-peak value compared to parallel magnetization.

**Slot width** is the second factor; in conventional design, the slot opening is equal with the tooth width; to reduce the interaction between slot openings and magnets, while maximizing the output torque, and still keeping space for windings to be introduced, a minimum opening must be chosen carefully; there are motor without slots (slotless, toothless, ironless), but they are only used for very low power applications (few Watts). A limit will be reached when windings can't be inserted anymore automatically, which is a huge drawback in case of mass production; this means that the slot opening should have a minimum width such as automated winding process is still feasible.

**Manufacturing irregularities** is the third factor; in this order, the accuracy of magnet placement in the rotor and the dimensional accuracy are important for the shape and amplitude of cogging torque.

**Manufacturing impact on materials** is the fourth and the last factor; this refers to the changes in the stator lamination isotropy due to punching, stamping, grain orientation, method of stacking and interlocking, but also to the eccentricity of the rotor due to imperfections in the bearings and design tolerances.

**Rotor eccentricity** – causes unwanted cogging torque frequency components and unbalanced forces.

Some of the factors that contribute to the cogging torque are considered in the analytical model [14]:

- a) Slot and pole number combination;
- b) Slot opening width, air gap length and magnet thickness;

- c) Magnet pole arc to pole-pitch ratio;
- d) Magnetization distribution (sinusoidal to rectangular);
- e) Skewing and stepped skewing equivalent;
- f) Disposition of magnets.

The period of cogging torque is equal with the slot pitch, is alternating and almost symmetric about its angular axis. In many commercially available machines, the nominal value of cogging torque is 5 to 10 % of the rated torque, while in high performance machines is 1 to 2% [12].

The formula for the cogging cycles per mechanical revolution, taking into account that the motor has 6 stator slots and 4 rotor poles, is:

$$N_{CG} = LCM(N_S, 2p_1) = LCM(6, 4) = 12 \quad (3.60)$$

With the above formula and knowing that the maximum frequency of the motor, at the maximum speed is equal to 500 [Hz], we can calculate the maximum cogging torque frequency:

$$f_{CG} = N_{CG} \cdot f = 12 \cdot 500 = 6000[\text{Hz}] \quad (3.61)$$

The fundamental frequency of the cogging torque, independent of stator current, is a function of the number of stator slots  $N_s$ , number of pole pairs  $2p_1$  and input frequency  $f$ . The cogging cycles are higher for concentrated windings than for distributed windings, which leads to higher cogging torque frequency, but diminished amplitude [13].

For cogging torque, two analytical formulas can be written, one based on the interaction between the rotor magnetic flux and variable permeance of the air gap due to stator slot geometry (3.62) [11] and the second one based on Fourier series (3.63) [12]:

$$T_{cog} = -\frac{1}{2} \phi_g^2 \frac{dR}{d\theta} \quad (3.62)$$

$$T_{cog} = \sum_{n=1}^{\infty} T_n \cdot \sin(n \cdot N_{CG} \cdot \theta + \varphi_n) \quad (3.63)$$

In this equation,  $n$  is the number of harmonic, thus  $T_1$  is the peak fundamental of the cogging torque, while  $\theta$  is the position.

All the expressions above are about analytical model. In our case, numerical methods were employed for calculation of the cogging torque. Thus its value is computed at each angular position by means of FE analysis, integrating the Maxwell stress tensor on a surface containing the rotor, with null stator currents. Neglecting the end effects, a two-dimensional (2-D) model can be adopted. Then, it is sufficient to

integrate the Maxwell stress tensor along a circumference located in the air gap and multiplying the result by the rotor length  $L_{stk}$  [18].

In what follows, the cogging torques for analytical model, Hooke-Jeeves optimal case and ABC optimal case are presented.

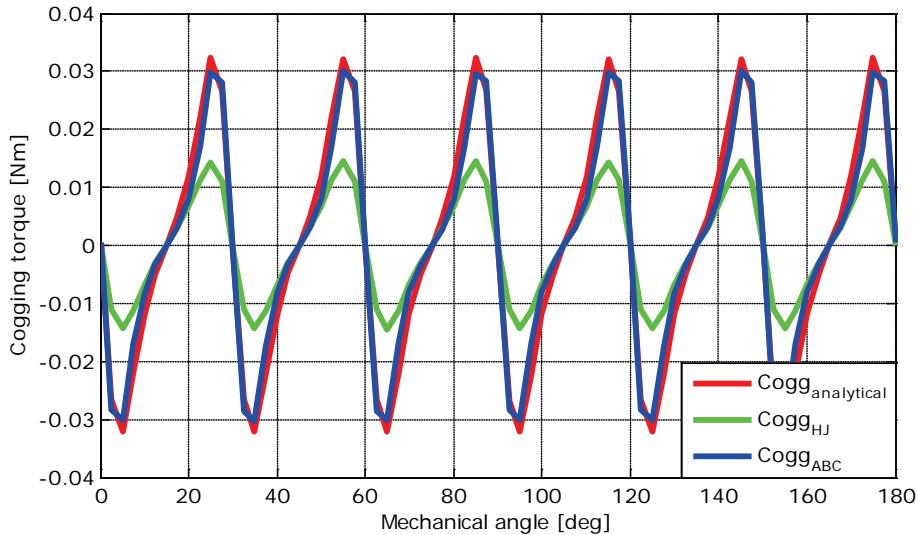


Fig. 3.44 Cogging torques for analytical model, HJ and ABC optimization cases

It can be seen that by far, the better topology in terms of cogging torque is the one obtained through hybrid Hooke-Jeeves optimization, while the worst topology is the one obtained from the analytical model. However, to have a clearer view of the topic, we must report the peak value of the cogging torque to the average value of the electromagnetic torque.

From this report, the most disadvantageous case remains the analytical model, with a percentage of 14.47. For the hybrid ABC optimization case, the percentage is 12.89, while for the hybrid Hooke-Jeeves optimization case, the percentage is 6.45. The statement above, that hybrid Hooke-Jeeves is the best topology in terms of reduced cogging torque still stands.

Though high enough, the detent torque peaks can be largely reduced by applying some design methods. In what follows, torque pulsation reduction techniques will be presented and applied for both cases of optimization. The analytical model is ruled out because it offers the worst topology in terms of price, output torque and cogging torque. The purpose is to find the method that qualifies for a clean implementation during the manufacturing process and that offer the best compromise between cogging torque reduction and average torque reduction.

### 3.3.8 Torque pulsations reduction techniques

One of the major issues concerning the proper motor functioning is the reduction of the parasitic components of the torque, since they induce vibration, noise and may affect even the motor control. As pointed previously, the torque components are due to the magnets, at zero current, and due to current excitation. Hence, the pulsations occur due to cogging torque and commutation. The latter one cannot be avoided, since two out of three phases work at a time. Current shaping can be done in such a manner that its waveform is closer as can be to the ideal rectangular shape, which was realized in the design process.

This being said, the main concern regarding torque pulsations is the cogging torque. During the last years, since permanent magnet motors began to be more and more used, various techniques were developed to reduce this parasitic component of the torque [11 – 33]. In order to reduce it, since its elimination is impossible, one must treat the causes. From definition, the cogging torque comes from the interaction between the rotor magnetic flux and variable permeance of the air gap due to stator slot geometry. This way, one of these two or both of them must be eliminated or their effect reduced as much as possible.

The most obvious thing to do is to go to the extremes, such as to take out the magnet edges from the equation or to eliminate the slot openings. To make the magnet edges disappear, the magnet must be built in one piece, but this will bring with itself problems with proper magnetization and construction.

Slot openings on the other hand can be eliminated. One way is to make the motor slotless, thus the interaction with magnet edges will not take place and cogging torque is eliminated. This particular topology was briefly presented in the previous chapter but it was rejected since it requires more windings and more magnet volume to produce the same torque-per-volume as with slots, leading to an increase in motor price, which is to be avoided.

The other way to eliminate cogging torque is to completely close the slot openings, but this will add complexity to the manufacturing process, since a minimum slot opening must be kept to introduce the stator windings. If slot openings are fully closed, other means to introduce the windings must be found, new inserting machines must be bought and money must be spent, which is undesirable.

Most of the methods to reduce the cogging torque, which are placed between the extreme points above, aim to reduce the amplitude and to increase the periodicity (frequency). Some of the methods that are not so widely used are [11 – 13]:

- Adding **shoes to the stator teeth** to reduce the air gap reactance, which has no direct effect on motor performance, but increases the winding inductance;
- **Fractional pitch winding**, which reduces the net cogging torque by de-phasing the reluctance variation for each magnet;
- **Air gap lengthening**, similar to slotless configuration, which assumes that the air gap length is increased to reduce the reactance, but the magnet must be increased by the same amount, to maintain the torque-producing air gap flux; this compromise leads to an increase in magnet length and cost;

- **Variation of the slot width** method says that a ratio of 0.5 between slot width and slot pitch is optimal;
- **Shaping the stator slots** is another method based on slots design in order to increase the frequency of the cogging torque and reduce its amplitude; this technique includes bifurcated slots, empty slots, closed slots and teeth with different width of the active surface; the main drawback of this method is the increased manufacturing complexity;
- **Selection of the number of stator slots** has the same purpose as the previous technique, respectively to increase the number of stator slots in order to increase the cogging torque frequency and to decrease its amplitude; for this, the  $\text{GCD}[N_s, 2p_1]$  or the  $\text{LCM}[N_s, 2p_1]$  has to increase;
- **Shaping the PMs** to be thinner at the edges than at the center can reduce both the cogging torque and commutation ripples; this shape of the magnets, combined with bifurcated slots has the same effect on reducing the cogging torque as the skewing technique, without affecting as much the EMF.

For motor design, several types of techniques are employed, like elimination of slots, skewed slots, special shape slots and stator laminations, selection of the number of stator slots with respect to the number of poles, decentered magnets, skewed magnets, shifted magnets segments, selection of magnet width, and direction-dependent magnetization of PMs. All cogging torque reduction techniques also reduce the back-EMF and resulting desired mutual torque.

In what follows, several methods are presented and their effects on the cogging and average electromagnetic torque of the designed BLDC motor are shown.

### 3.3.8.1 Skewing

One of the most popular and effective techniques in reducing the cogging torque is skewing, by which the air gap reactance is cancelled all over each magnet face. For this to happen, the total skew must be equal to one slot pitch. A particularity of this method, which places it on top of the others, is its versatility. The technique can be applied both to the stator slots and to the magnets. In each case, there is an increase in length and price and also reduces and smooth the EMF shape [11].

The skewing doesn't cancel the cogging torque, but reduces it greatly; this difference is due to fringing effects and unavoidable machining tolerances of magnets and stator laminations [12]. The disadvantages of skewing are: reduces back-EMF, the output power and torque, increases leakage inductance and stray losses and increases the manufacturing complexity. Another disadvantage of the skewing is that a normal force adds to the torque, somehow like the rotor is trying to advance like a screw to the stator; this extra component puts an extra load to the bearings [11].

Stator slots skewing is done with one slot pitch (sometimes even less). The drawbacks of this technique are high manufacturing complexity and the reduction of the EMF and of the motor performance. Skewing the magnets (Fig. 3.45) is complex and it's not worth implementing, but stepped skewing has the same efficiency in reducing the cogging torque and is easier to implement, without the change of the

magnetization of the PMs. Bread loaf magnets with edges cut aslant are equivalent to skewing [13].

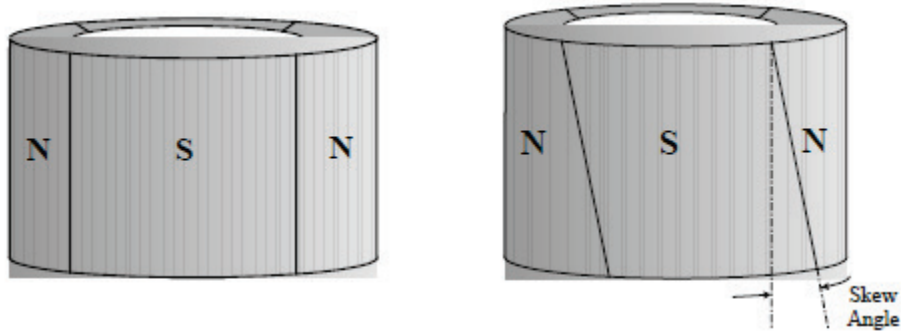


Fig. 3.45 Skewing of the rotor magnets [18]

While in [14] a more complex formula is given for the skew factor, the equation below is similar. Taking into account that  $\theta_{se}$  is the stator pole pitch in electrical radians, the skew factor for our motor is:

$$k_S = 1 - \frac{\theta_{se}}{2\pi} = 1 - \frac{\frac{2\pi}{3}}{2\pi} = 1 - \frac{1}{3} = \frac{2}{3} \approx 0.667 \quad (3.64)$$

The skewing angle can span half or full slot pitch, the formula for the angle being:

$$\theta_{cg} = \theta_{sk} = \frac{2\pi}{N_{cg}} = \frac{2\pi}{6} = \frac{\pi}{3} = 60^\circ \quad (3.65)$$

Skewing is usually done for one slot pitch, but it is not always essential since the fundamental and harmonic orders of the cogging torque are integers of  $N_c$ . The relation for the optimal skew which eliminates the cogging torque is given in:

$$\theta_{sk} = \frac{k \cdot N_s}{N_c}, \quad k = 1, 2, \dots, \frac{N_c}{N_s} \quad (3.66)$$

In our case, the maximum value for  $k$  is 2, thus  $\theta_{sk}$  can take only two values, i.e. 0.5 and 1. The optimal skew can be done either for half the slot pitch or for the entire slot pitch, the latter being valid for every combination of slots and magnet pole pairs [14].



Stepped skewing, a low cost approximation of regular skewing, is adopted in industry for mass production of motors, instead of skewing, and is realized by placing magnets axially skewed with a total angle equal to half the slot pitch.

The possibility of obtaining lower torque ripple in the skewed motor depends on where the minimum ripple point is located and on the magnitude of the ripple at this position. This minimum point should be close to the optimum skew angle for a good design [25].

The axial skewing angle  $\theta_{ss}$  between each PM piece depends on the number of skewing steps  $N_{ss}$ . The following formula is used to determine the skewing angle of each module:

$$\theta_{ss} = \frac{\theta_{sk}}{N_{ss}} \quad (3.67)$$

With magnets equally skewed, all cogging torque harmonics are eliminated, except harmonics of order multiple of  $N_{ss}$ .

By employing the step skew, the cogging torque expression might be written [20]:

$$T_{cg} = \sum_{n=1}^{N_{ss}} \sum_{k=1}^{\infty} T_{ck} \left[ \cos kQ \left( \theta - (n-1) \frac{2\pi}{N_s \cdot N_{ss}} \right) \right] \quad (3.68)$$

The cancellation takes place depending on the number of steps and the shift angle among the magnets along the stack length.

Stepped skewing can be done with many segments, but it is not recommended because it increases the manufacturing complexity and hence the costs; as normal skewing, the back-EMF top is reduced, thus being more sinusoidal than rectangular [12]. Usually, a three-step skew is a good compromise between performance and manufacturing complexity.

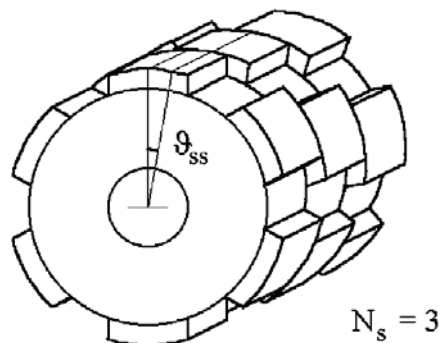


Fig. 3.46 Stepped rotor skewing with three modules [18]

In case of a three-step skewing only the multiple of third harmonics will remain. In most cases, the cancellation of the fundamental and the second harmonic will result in significantly lower cogging torque. From that perspective, a three-step skew may be considered better and appropriate for implementing the step skew [20].

For our case we choose an optimal skew angle of  $30^\circ$ . Two stepped skewing cases were chosen, one with three modules and one with four modules. Knowing that  $N_{ss}$  is either 3 or 4, the skewing angle of each module, based on (3.67), is:

$$\theta_{ss1} = \frac{30^\circ}{3} = 10^\circ \quad (3.69)$$

$$\theta_{ss2} = \frac{30^\circ}{4} = 7.5^\circ \quad (3.70)$$

For the hybrid Hooke-Jeeves optimal case, the results of stepped skewing compared to the normal configuration are shown in Fig. 3.47.

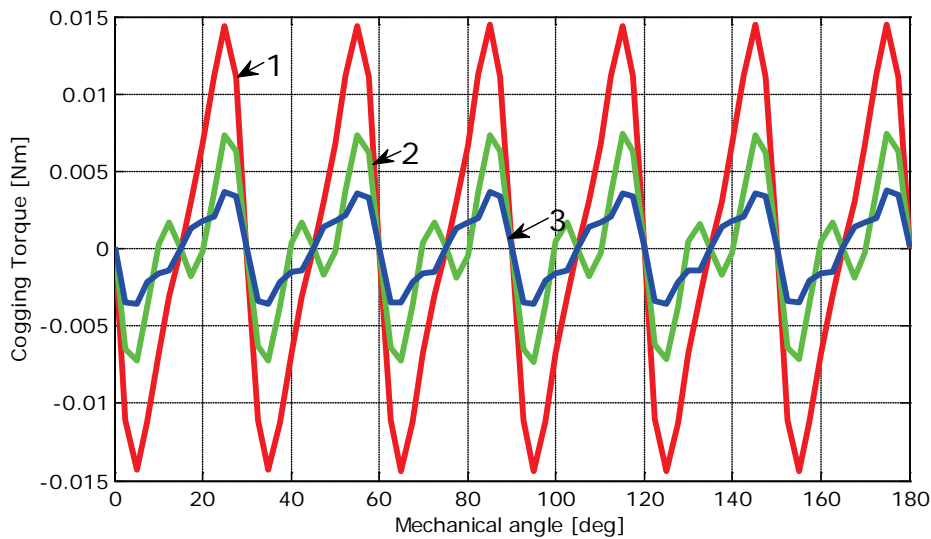


Fig. 3.47 Cogging torque for HJ case for: 1 – original configuration; 2 – stepped skew rotor with 3 modules; 3 – stepped skew rotor with 4 modules

As can be seen, the cogging torque is greatly reduced with stepped skewing, especially in the case with 4 modules. However, the total torque must be shown, as it is affected by skewing.

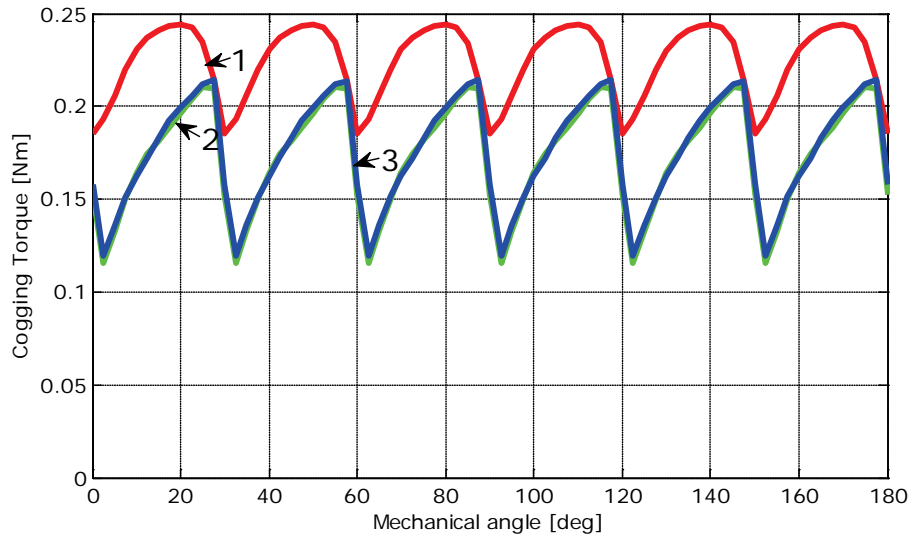


Fig. 3.48 Total torque for HJ case for: 1 – original configuration; 2 – stepped skew rotor with 3 modules; 3 – stepped skew rotor with 4 modules

Next, the results of stepped skewing compared to the normal configuration for the ABC optimization case are shown in Fig. 3.49.

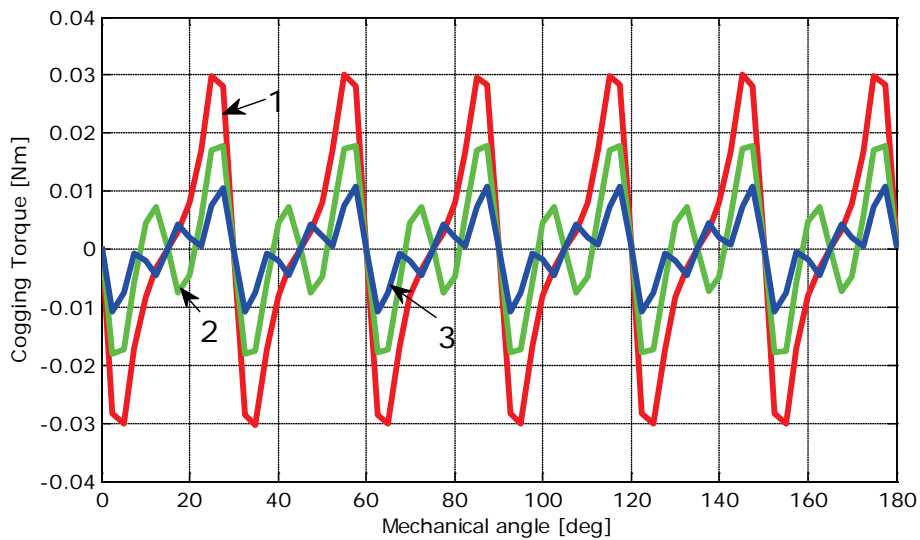


Fig. 3.49 Cogging torque for ABC case for: 1 – original configuration; 2 – stepped skew rotor with 3 modules; 3 – stepped skew rotor with 4 modules

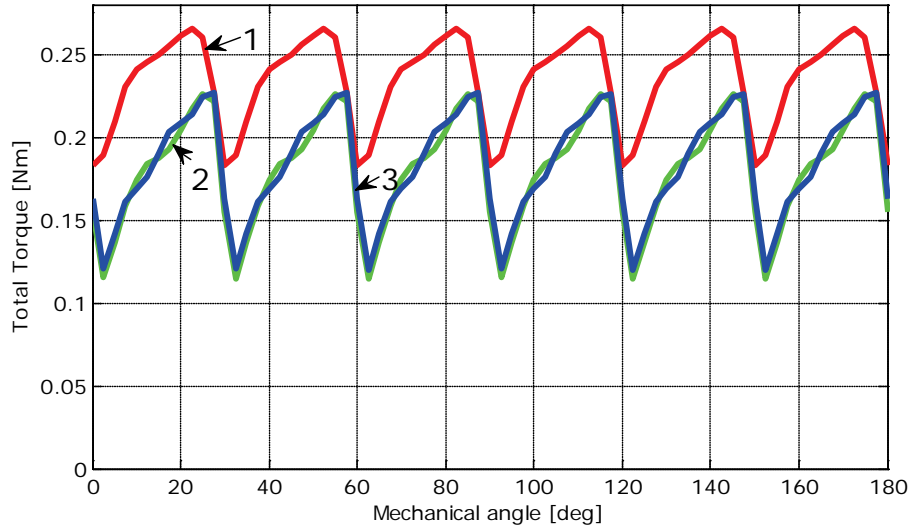


Fig. 3.50 Total torque for ABC case for: 1 – original configuration; 2 – stepped skew rotor with 3 modules; 3 – stepped skew rotor with 4 modules

Like in the previous case, for the motor obtained from hybrid ABC optimization the cogging torque is greatly reduced with stepped skewing, especially in the case with 4 modules. However, the total torque is also reduced and not only that, but the pulsations are still present.

The cogging torque is reduced greatly for both motor topologies. For HJ case and stepped skewing with 3 modules, the value of the parasitic torque dropped at 51% compared to the initial configuration. For stepped skewing with 4 modules, the reduction is even more efficient, now the cogging torque being only 25% from the original one.

For ABC case, the minimization is also significant. Stepped skewing with 3 modules reduces the value of the cogging torque at 59% from the original one, and with 4 modules reduces it at 36% compared to the original configuration.

In terms of values, the average torque is reduced at 77% for both optimization cases for stepped skewing with 3 modules, while for 4 modules the drop is at 78%. This is a clear disadvantage of the skewing technique, because it is very effective in cogging torque minimization, but greatly affects the value of the output torque, which is undesirable. Another drawback is the increase in torque pulsations, an effect that is exactly the opposite of what is intended in the first place.

Next, another popular technique in cogging torque minimization is presented and it addresses the width of the permanent magnets. Although in the ideal case the magnet occupies the full pole pitch (for 4 poles is  $90^\circ$ ), in real situation the pole pitch is slightly smaller. In what follows, an optimal pole pitch is calculated and its results on cogging torque are presented.

### 3.3.8.2 Magnet width variation

The disadvantages of skewing are the increase in the leakage inductance and stray losses, while also reducing the output torque, especially in the motors with a small ratio of teeth per pole [27], as in our case.

Magnet shaping is another technique for cogging torque minimization, because the shape of the magnet has a great influence on the cogging torque. Reducing the magnet pole or the magnet height as we approach the edge also reduces the magnet flux coupling with the stator windings [11].

The optimal magnet pole arc can be found with the following equation, taking into consideration the fringing of the magnet flux:

$$\alpha_p = \frac{N - k_1}{N} + k_2, \quad k_1 = 1, 2, \dots, N - 1 \quad (3.71)$$

In the equation above, the terms are:  $\alpha_p$  – optimum ratio (pole-arc to pole-pitch),  $N$  is the ratio between  $N_{cg}$  and  $2p$  and  $k_2$  has a value between 0.1 and 0.3, depending on the air gap length.

Since a higher value for the optimal ratio is preferred and while a pole arc equal with the pole pitch is harder to achieve, due to fabrication constraints and since this is not an optimum value for cogging torque,  $k_1 = 1$  is considered to be the best solution. In our case, the optimal pole-arc is calculated to be:

$$\alpha_p = \frac{\frac{12}{4} - 1}{\frac{12}{4}} = \frac{3 - 1}{3} = \frac{2}{3} = 0.667 \quad (3.72)$$

Taking into consideration that the pole span angle is  $90^\circ$ , the optimal magnet pole arc is:

$$\alpha_p = 0.667 \times 90^\circ \approx 60^\circ \quad (3.73)$$

In this case,  $k_2$  was not considered, so it can be noticed that the optimal value of the magnet arc is equal to the slot pitch.

However, the magnet width is calculated with Slemon's inequality [27], as he was the first one to study this method, where magnet pole pitch is  $(n+0.14)$  or  $(n+0.17)$  times the slot pitch. The exact number  $x$  from  $(n+x)$  times the stator slot pitch must be carefully chosen, depending on the magnetization or placement of the magnets.

Since it is clear that the optimal magnet width is higher than the slot pitch with 0.14 or 0.17, the value of the pole arc angle from (3.73) becomes:

$$\alpha'_{p1} = 60^\circ \cdot (1 + 0.14) = 68.4^\circ \quad (3.74)$$

$$\alpha'_{p2} = 60^\circ \cdot (1 + 0.17) = 70.2^\circ \quad (3.75)$$

The value of  $n$  in our case cannot be higher than 1, because for other integer values the optimal pole arc will be higher than  $90^\circ$ , which is not possible.

Next, the effect of the optimal pole arc width on the cogging torque is shown in Fig. 3.52 for HJ case and in Fig. 3.55 for ABC case and its effect on the total torque is shown in Fig. 3.53 for HJ case and in Fig. 3.56 for ABC case.

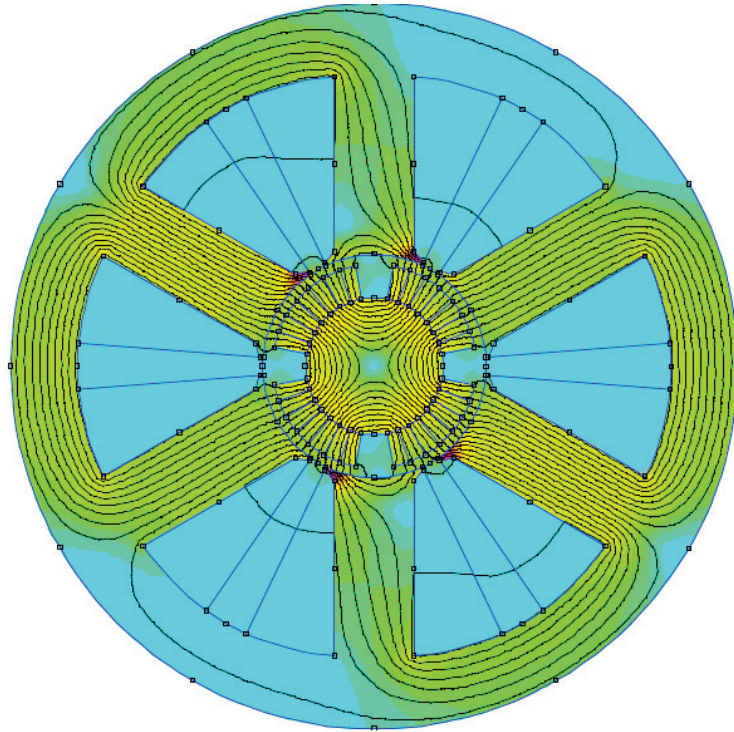


Fig. 3.51 Flux density distribution under load (q-axis aligned with tooth of A) for HJ with pole arc width of  $68.4^\circ$

From the figure below it can be seen that the minimization of the cogging torque is not that significant as with the stepped skewing. For an optimal pole arc angle of  $68.4^\circ$ , the cogging torque is 42% of the original one, while for a pole arc of  $70.2^\circ$ , the value is 55% of the original one. From that, it seems that the magnet arc that spans with only 0.14 more than the slot pitch is more effective in reducing the parasitic component of the torque.

In terms of total torque pulsations, as it is shown below, they are reduced, which means that this technique is effective. In terms of average torque, its value dropped at 90% in case of a magnet arc that spans on  $68.4^\circ$ , while for a pole arc of  $70.2^\circ$ , the average torque is down at 92%.

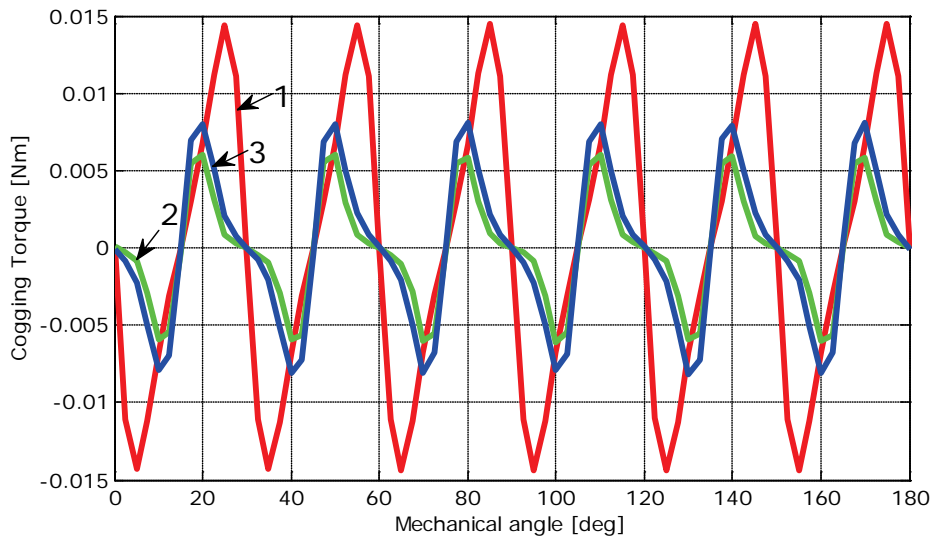


Fig. 3.52 Cogging torque for HJ case for: 1 – original configuration; 2 – magnet arc width of  $68.4^\circ$ ; 3 – magnet arc width of  $70.2^\circ$

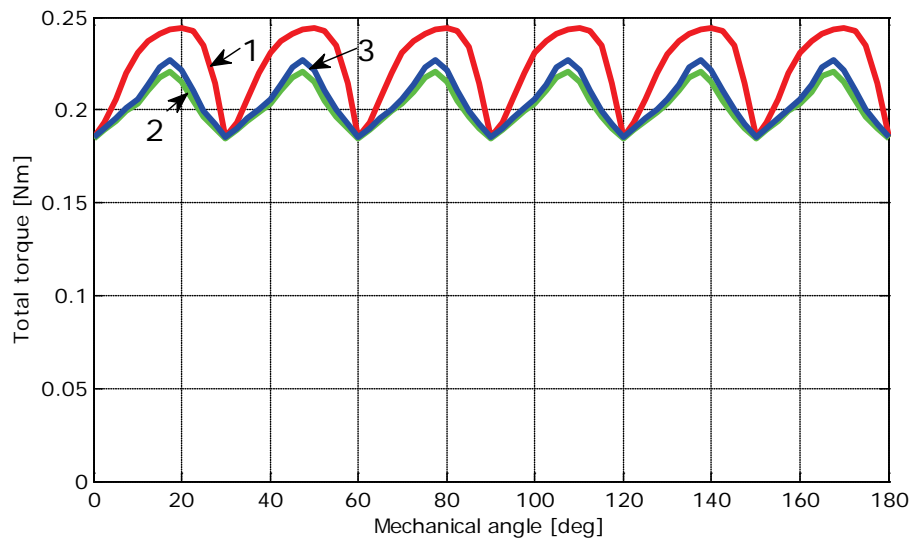


Fig. 3.53 Total torque for HJ case for: 1 – original configuration; 2 – magnet arc width of  $68.4^\circ$ ; 3 – magnet arc width of  $70.2^\circ$

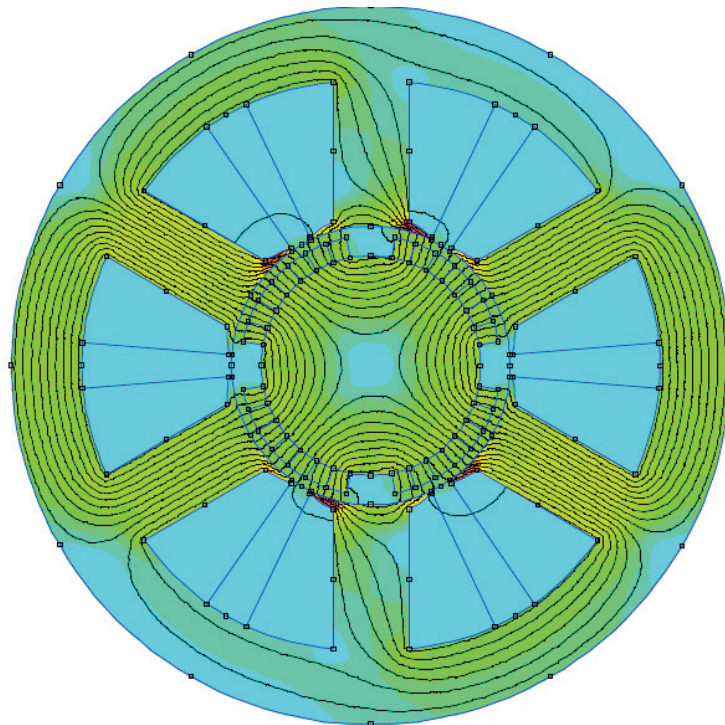


Fig. 3.54 Flux density distribution under load (q-axis aligned with tooth of A) for ABC with pole arc width of  $68.4^\circ$

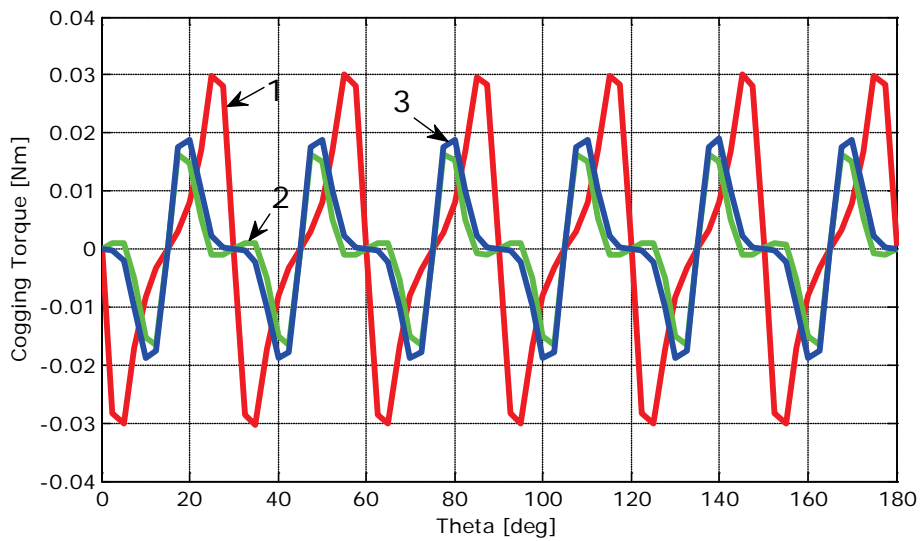


Fig. 3.55 Cogging torque for ABC case for: 1 – original configuration; 2 – magnet arc width of  $68.4^\circ$ ; 3 – magnet arc width of  $70.2^\circ$



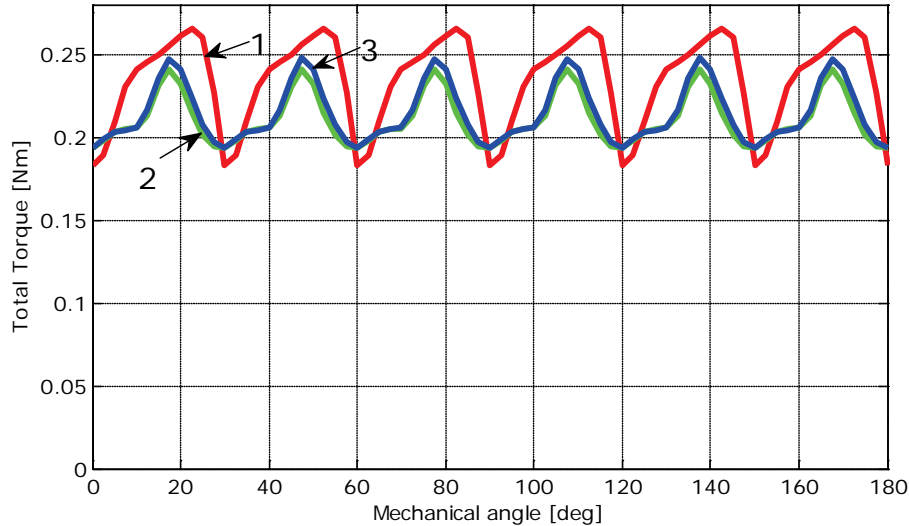


Fig. 3.56 Total torque for ABC case for: 1 – original configuration; 2 – magnet arc width of  $68.4^\circ$ ; 3 – magnet arc width of  $70.2^\circ$

For an optimal pole arc angle of  $68.4^\circ$ , the cogging torque is 55% of the original one, while for a pole arc of  $70.2^\circ$ , the value is 63% of the original one.

In terms of average torque, its value dropped at 90% in case of a magnet arc that spans on  $68.4^\circ$ , while for a pole arc of  $70.2^\circ$ , the average torque is down at 92%.

Overall, this seems to be a better technique for cogging torque minimization than skewing, taking into consideration the small drop of the average torque and the fact that torque pulsations are diminished.

To try to improve this technique a combination with pole shifting is chosen. In what follows, the method of magnet shifting with optimal pole arc width of  $68.4^\circ$  is realized and the results on the cogging and total torques for both optimization cases are shown.

### 3.3.8.3 Magnet shifting

Shifting alternate pair of poles reduces also the torque pulsations, but has a minor disadvantage – it introduces an asymmetry between adjacent poles. It is a combination of techniques meant to reduce not only the cogging torque, but also the torque ripples, without skewing the stator or the rotor, but with same effects. The method combines the adequate choosing of the magnet width with rotor pole pair shifting with a proper angle value [18, 28].

Odd-order harmonic components of the torque can be eliminated by shifting one pole pair. To eliminate the second-order components, which are independent of the stator current, an appropriate value of the magnet width must be chosen. Both cogging

and commutation torque can be reduced by shifting the pole pairs by half a slot pitch and by choosing the appropriate value of magnet width [28, 29].

Another technique derived from pole shifting is shifting PM segments. This technique is about dividing the pole magnet into 3 to 6 segments, shifted from each other with equal or unequal distances. Creating magnetic circuitry asymmetry can be done by shifting each magnet by a fraction of the pole pitch with respect to the symmetrical position or designing different sizes of N and S magnets of the same pole pair [13].

The method of magnet pole segmentation is proposed for high power machines, where building a large PM is problematic and segmentation is a viable solution. However, to reduce the cogging torque, the spacing between magnet segments must be calculated in order to find the proper values for cancelling the effects of the torque pulsations [32].

Magnet shifting is done in order to distribute more uniformly on the stator slot pitch the effects of the interaction between the magnet edges and slot openings. This way, it can be assimilated with a "circumferential skewing". The general formula used to calculate the shifting angle of each pole is given:

$$\theta_{sh,j} = \frac{360^\circ \cdot (j-1)}{2 \cdot p \cdot N_{cg} \cdot N_s}, \quad j = 1, 2, \dots, 2p \quad (3.76)$$

As this method is similar with skewing, it is only normal to emulate both cases presented, with 3 and 4 modules.

In our case, the shifting angles for each magnet, with the relation above will be:

$$\begin{aligned} \theta_{sh1} &= \frac{360^\circ \times 0}{4 \times 2 \times 6} = 0^\circ \\ \theta_{sh2} &= \frac{360^\circ \times 1}{4 \times 2 \times 6} = \frac{360^\circ}{48} = 7.5^\circ \\ \theta_{sh3} &= \frac{360^\circ \times 2}{4 \times 2 \times 6} = \frac{720^\circ}{48} = 15^\circ \\ \theta_{sh4} &= \frac{360^\circ \times 3}{4 \times 2 \times 6} = \frac{1080^\circ}{48} = 22.5^\circ \end{aligned} \quad (3.77)$$

This relation is similar with stepped skewing with 4 modules. To shift magnets equivalent to step skewing with 3 modules, the angles become 10°, 20° and 30°.

Next, the effects of pole shifting with magnet widths of 68.4° for HJ and ABC cases are shown.

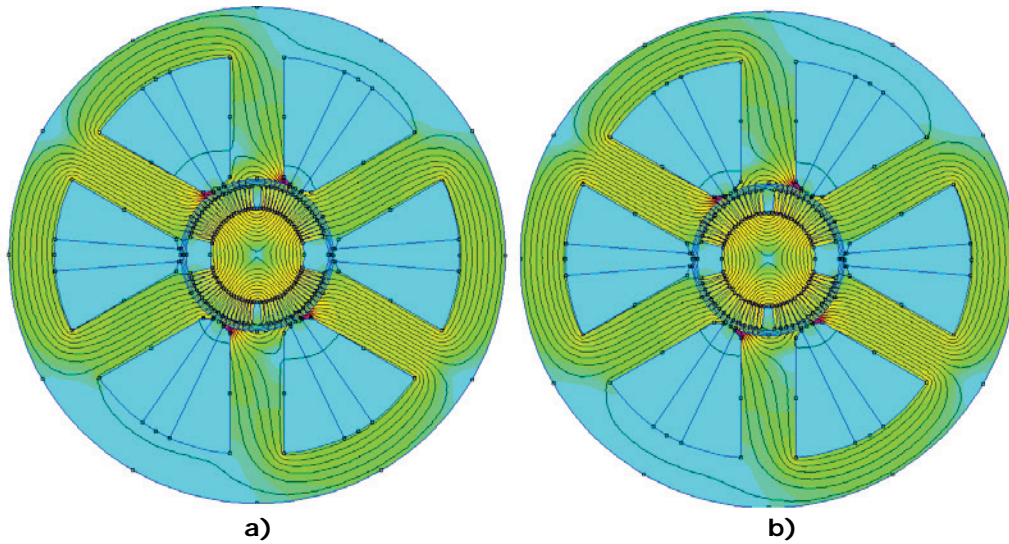


Fig. 3.57 Flux density distribution under load (q-axis aligned with tooth of A) for HJ with pole arc width of  $68.4^\circ$  and pole shifting of: a)  $7.5^\circ$  and b)  $10^\circ$

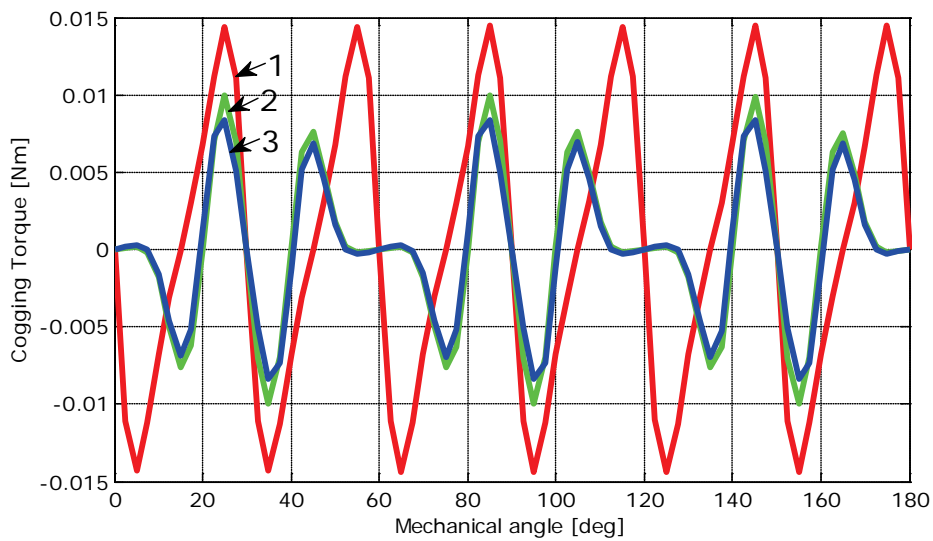


Fig. 3.58 Cogging torque for HJ case for: 1 – original configuration; 2 – magnet arc width of  $68.4^\circ$  and pole shifting of  $7.5^\circ$ ; 3 – magnet arc width of  $68.4^\circ$  and pole shifting of  $10^\circ$

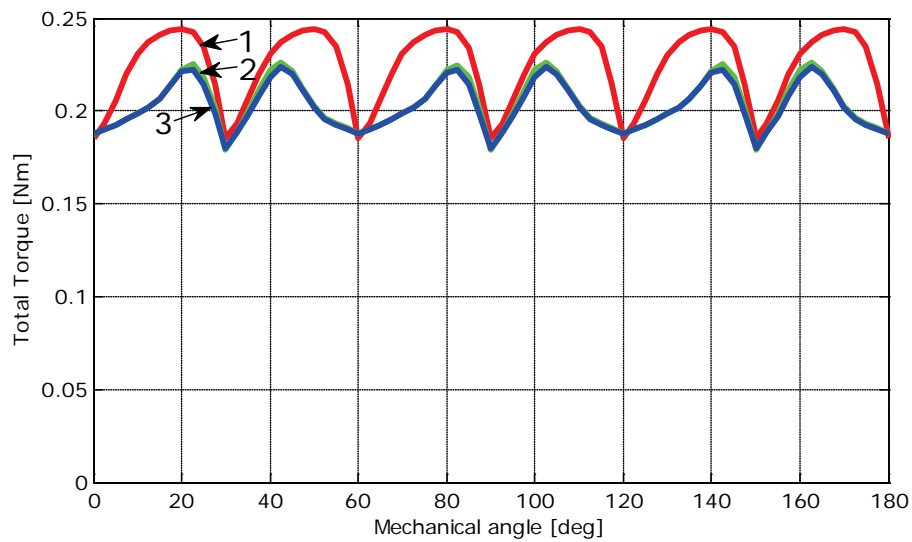


Fig. 3.59 Total torque for HJ case for: 1 – original configuration; 2 – magnet arc width of 68.4° and pole shifting of 7.5°; 3 – magnet arc width of 68.4° and pole shifting of 10°

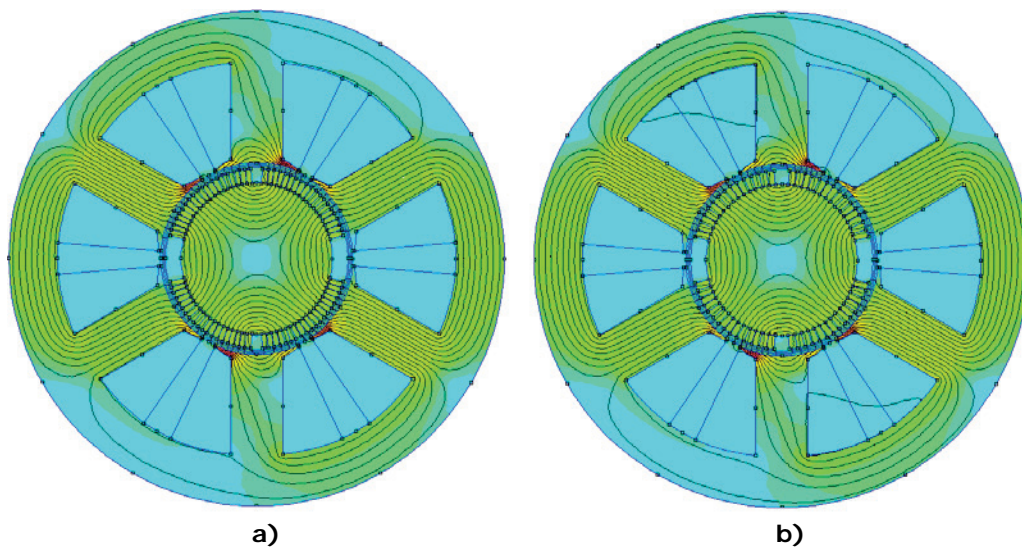


Fig. 3.60 Flux density distribution under load (q-axis aligned with tooth of A) for ABC with pole arc width of 68.4° and pole shifting of: a) 7.5° and b) 10°

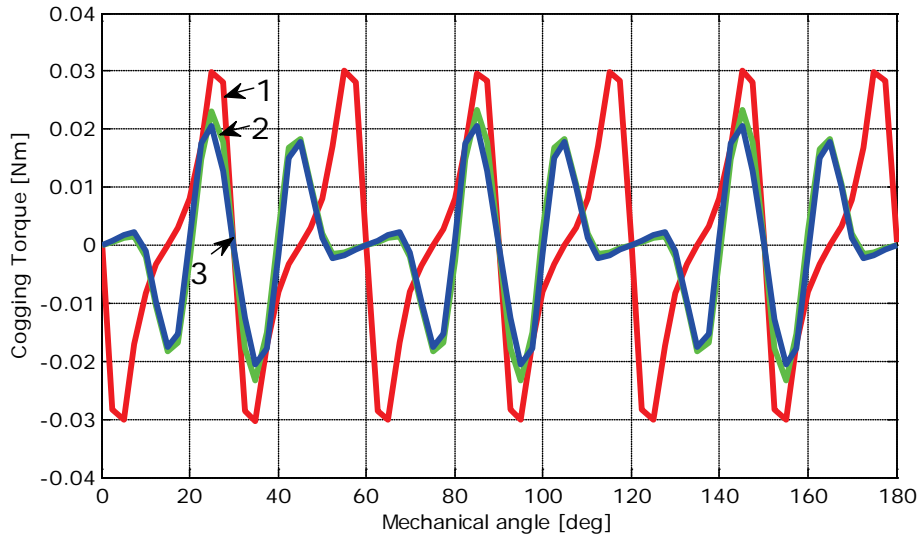


Fig. 3.61 Cogging torque for ABC case for: 1 – original configuration; 2 – magnet arc width of  $68.4^\circ$  and pole shifting of  $7.5^\circ$ ; 3 – magnet arc width of  $68.4^\circ$  and pole shifting of  $10^\circ$

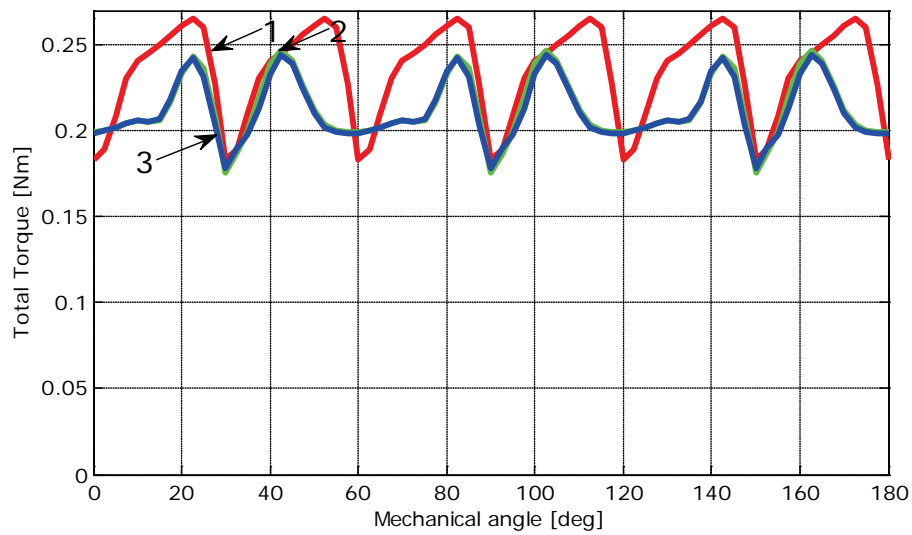


Fig. 3.62 Total torque for ABC case for: 1 – original configuration; 2 – magnet arc width of  $68.4^\circ$  and pole shifting of  $7.5^\circ$ ; 3 – magnet arc width of  $68.4^\circ$  and pole shifting of  $10^\circ$

From the figures above it can be seen that the minimization of the cogging torque is not that significant as with the stepped skewing or optimal pole arc width. For an optimal pole arc angle of  $68.4^\circ$  and pole shifting angles multiple of  $7.5^\circ$ , the cogging torque is 70% of the original one for HJ case and 77% for ABC case, while for shifting angles multiple of  $10^\circ$ , the value is 58% of the original one for HJ case and 68% for ABC case.

In terms of average torque, its value dropped at 91% in case of pole shifting angles multiple of  $7.5^\circ$  both for HJ and ABC cases, while for shifting angles multiple of  $10^\circ$ , the average torque is down at 90% for both optimization cases.

With this method the average torque didn't dropped much, which is ideal, but the cogging torque is still high, higher than in previous cases. This means that pole shifting is not efficient enough.

The last technique that is applied considers the introduction of tooth notches, also known as dummy slots.

#### 3.3.8.4 Tooth notches

All the techniques presented above considered only changes of the permanent magnets. Either it was stepped skewing of the rotor or optimal magnet width or magnet shifting, minimization of cogging torque was tried only on the rotor side. The last technique is the only one applied to the stator, namely introduction of tooth notches.

Tooth notches, also presented as dummy slots, are meant to emulate the slot openings (their width and height) in order to increase cogging torque's frequency and reduce its amplitude. To be an effective measure and to keep the manufacturing complexity at its minimum, only one or two notches are necessary. In figure 3.63, the way dummy slots look on stator teeth is shown, for the case of 1 and 2 notches per tooth.

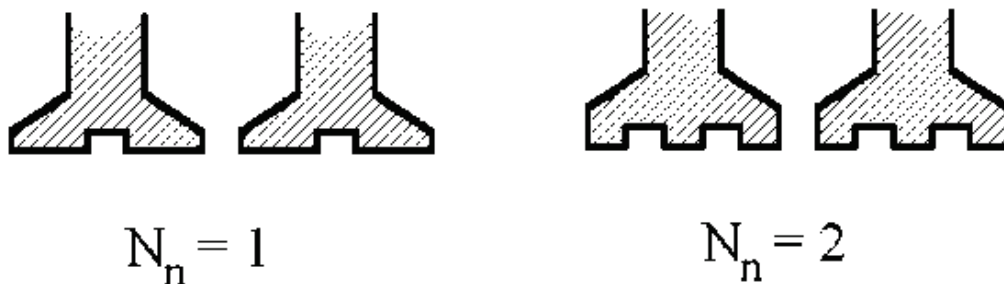


Fig. 3.63 Notches in the tooth [18]

The introduction of dummy slots in the stator teeth must be carefully done. There are several shapes of these slots, like semicircular, rectangular and U-shaped, as

can be seen in Fig. 3.64 [20]. In our case, the shape of the tooth notches was chosen to be rectangular.

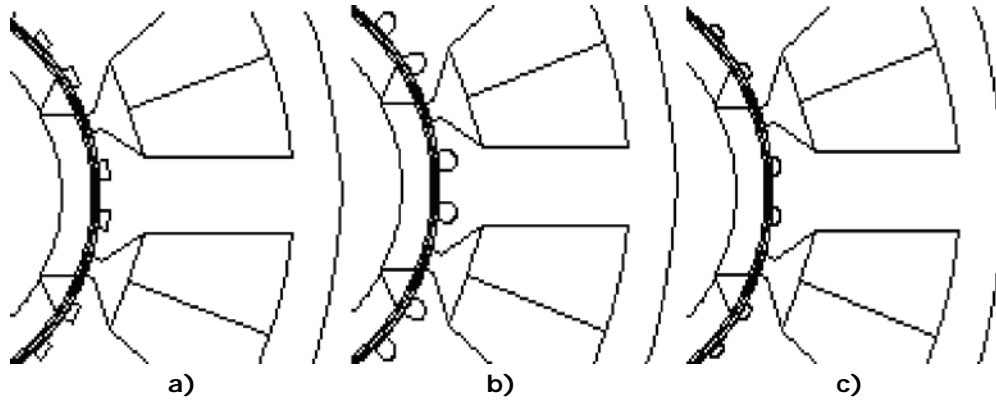


Fig. 3.64 Different types of stator tooth notches: a) rectangular, b) U-shaped and c) semicircular [20]

The  $N_n$  term above means number of notches. The decision of how many notches will be introduced is taken with the following formula:

$$GCF[(N_n + 1), N_p] = 1 \quad (3.78)$$

In the previous relation, the value of  $N_p$  is calculated with the equation:

$$N_p = \frac{2p}{GCF[N_s, 2p]} = \frac{4}{2} = 2 \quad (3.79)$$

Since the GCF in relation (3.78) needs to be one, than the sum  $(N_n + 1)$  must be an odd number, since the value of  $N_p$  is 2, an even number. Since the slot opening is  $9^\circ$  and the tooth spans on  $51^\circ$ , the number of notches cannot be higher than 5. Since only even values of  $N_n$  are accepted for the sum  $(N_n + 1)$  to be an odd number, there can be only 2 or 4 notches. Since 4 is a pretty high number for such a small motor, 2 notches per teeth seem to be the better option. Another rule that must be respected says that the notches must reduce the harmonics with highest amplitude, otherwise the goal is not achieved or it may get even worse, albeit it will increase the cogging torque [18]. Next, the effect of tooth notches on the cogging and total torques of the motors designed with HJ and ABC are presented. First of all, the case of magnets spanning on full pole pitch will be treated and afterwards, all the cases presented earlier will be combined with dummy slot configuration, as treated in [30].

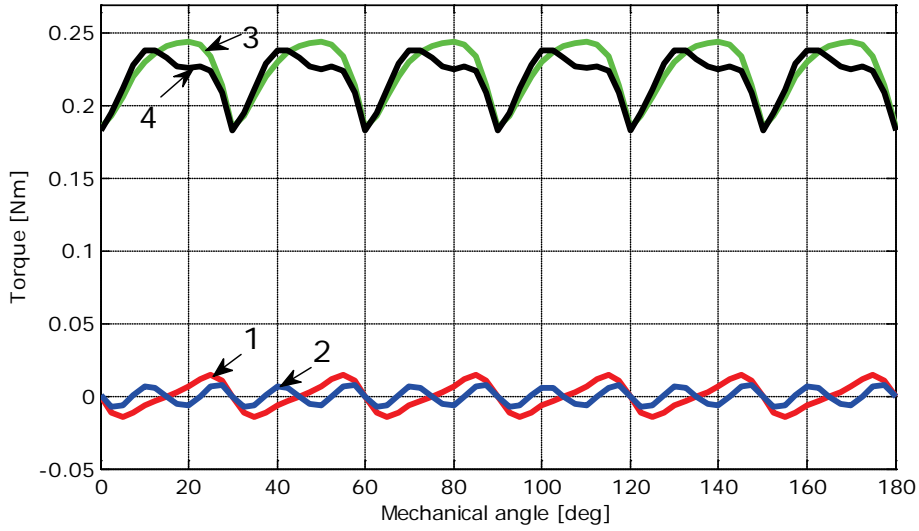


Fig. 3.65 HJ case: 1 – cogging torque for original configuration; 2 – cogging torque for motor with dummy slots; 3 – total torque for original configuration; 4 – total torque for motor with dummy slots

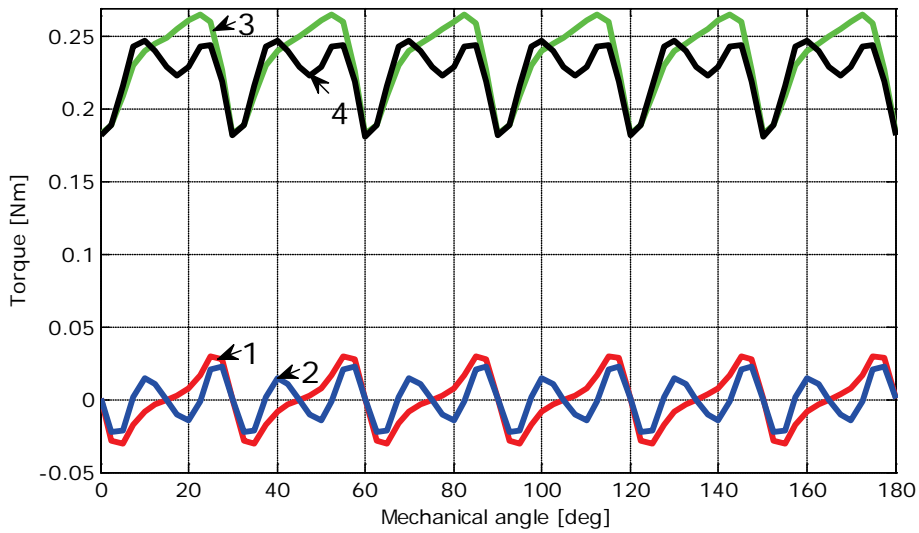


Fig. 3.66 ABC case: 1 – cogging torque for original configuration; 2 – cogging torque for motor with dummy slots; 3 – total torque for original configuration; 4 – total torque for motor with dummy slots



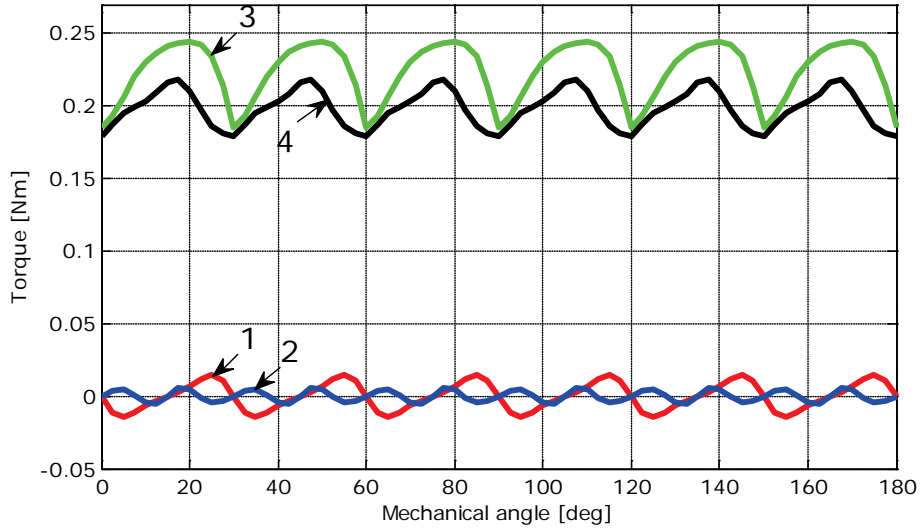


Fig. 3.67 HJ case, pole arc width of 68.4°: 1 – cogging torque for original configuration; 2 – cogging torque for motor with dummy slots; 3 – total torque for original configuration; 4 – total torque for motor with dummy slots

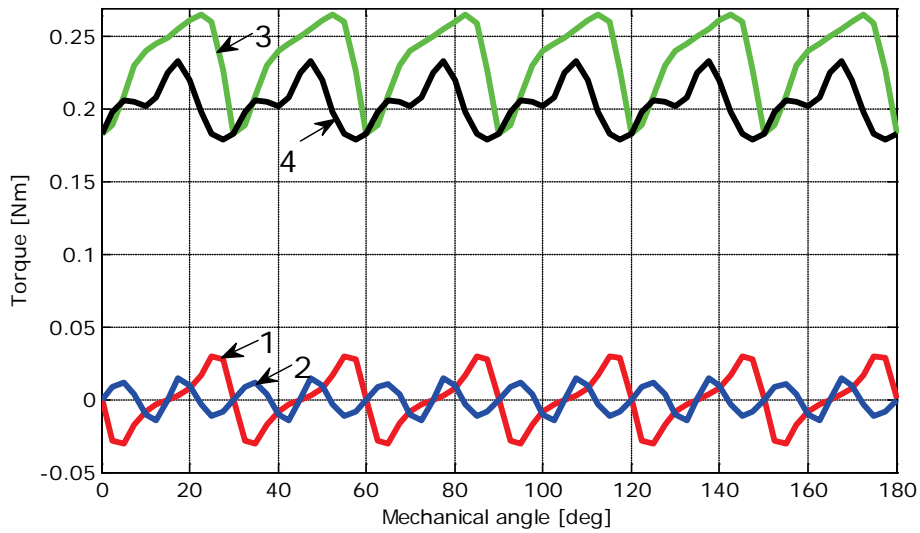


Fig. 3.68 ABC case, pole arc width of 68.4°: 1 – cogging torque for original configuration; 2 – cogging torque for motor with dummy slots; 3 – total torque for original configuration; 4 – total torque for motor with dummy slots

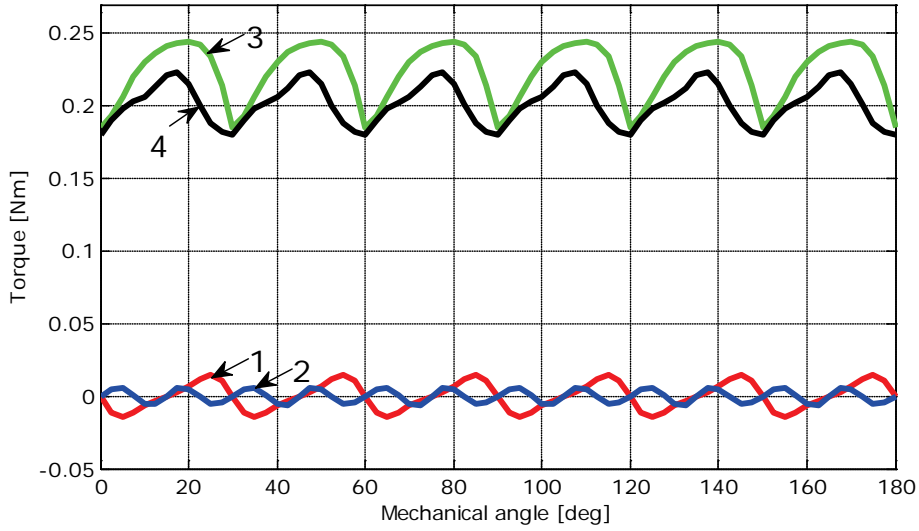


Fig. 3.69 HJ case, pole arc width of  $70.2^\circ$ : 1 – cogging torque for original configuration; 2 – cogging torque for motor with dummy slots; 3 – total torque for original configuration; 4 – total torque for motor with dummy slots

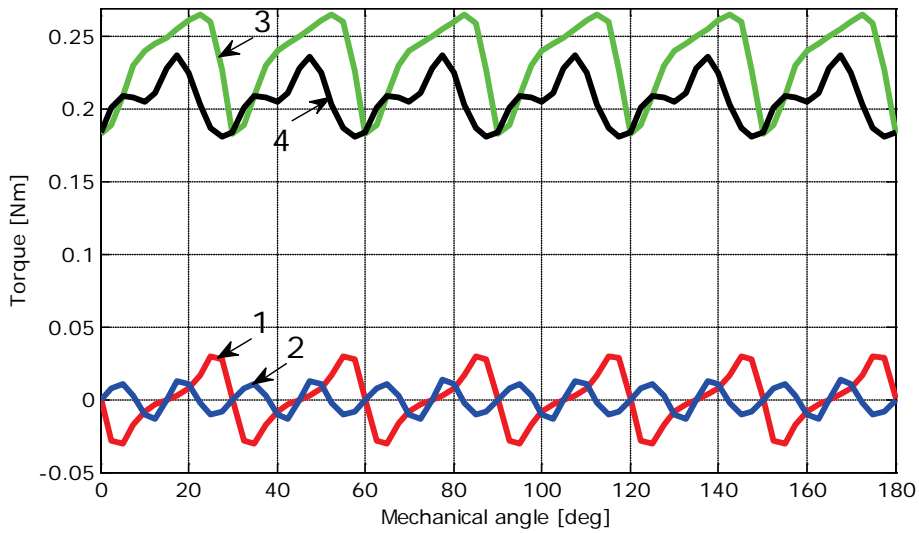


Fig. 3.70 ABC case, pole arc width of  $70.2^\circ$ : 1 – cogging torque for original configuration; 2 – cogging torque for motor with dummy slots; 3 – total torque for original configuration; 4 – total torque for motor with dummy slots

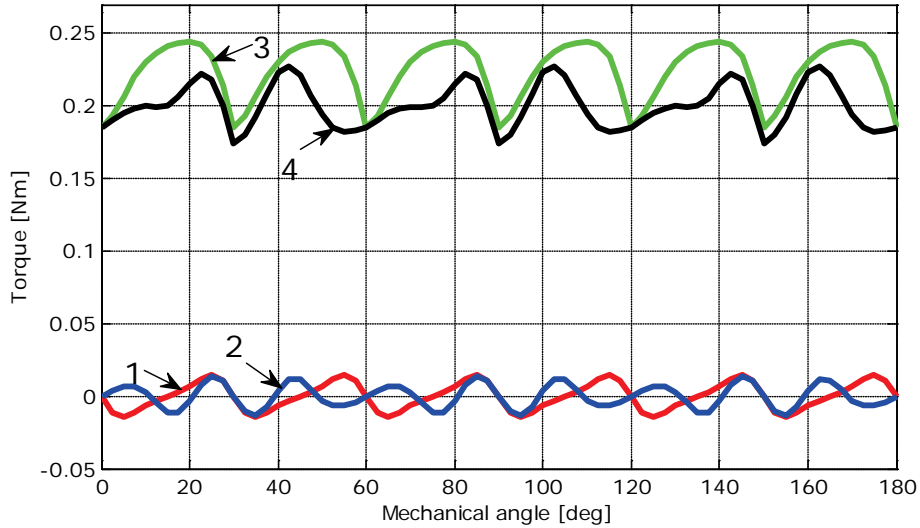


Fig. 3.71 HJ case, pole shifting multiple of  $7.5^\circ$ : 1 – cogging torque for original configuration; 2 – cogging torque for motor with dummy slots; 3 – total torque for original configuration; 4 – total torque for motor with dummy slots

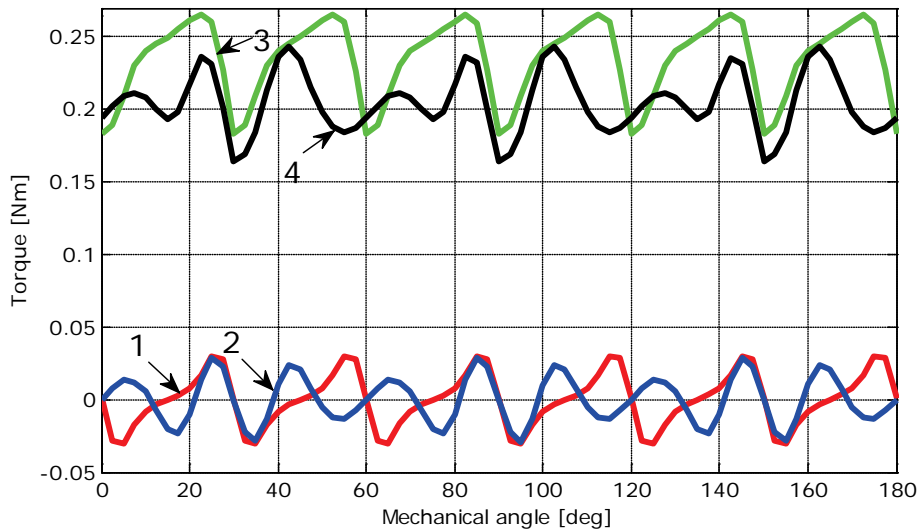


Fig. 3.72 ABC case, pole shifting multiple of  $7.5^\circ$ : 1 – cogging torque for original configuration; 2 – cogging torque for motor with dummy slots; 3 – total torque for original configuration; 4 – total torque for motor with dummy slots

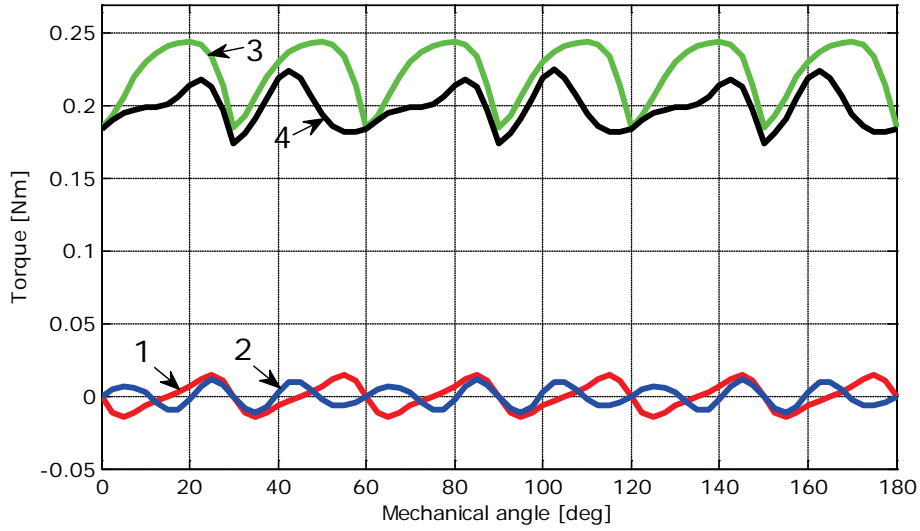


Fig. 3.73 HJ case, pole shifting multiple of  $10^\circ$ : 1 – cogging torque for original configuration; 2 – cogging torque for motor with dummy slots; 3 – total torque for original configuration; 4 – total torque for motor with dummy slots

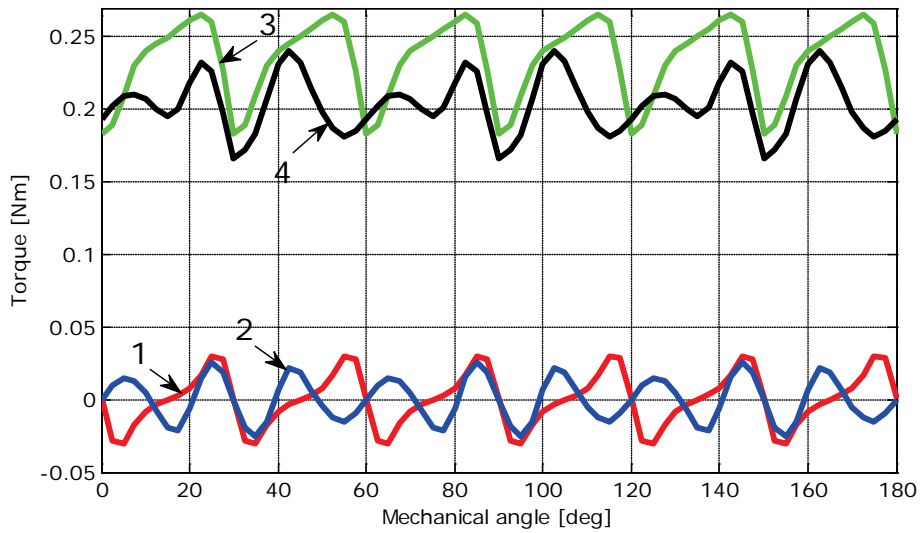


Fig. 3.74 ABC case, pole shifting multiple of  $10^\circ$ : 1 – cogging torque for original configuration; 2 – cogging torque for motor with dummy slots; 3 – total torque for original configuration; 4 – total torque for motor with dummy slots

From figures above it can be seen that introduction of tooth notches helps in reducing the torque pulsations without affecting very much the average torque. However, the situations that involve a combination between dummy slots and pole shifting doesn't seem to offer any cogging torque reduction and even more, the torque waveform looks very irregular.

In case of pole shifting by multiple of  $7.5^\circ$ , the cogging torque is 94% of the initial one for HJ designed motor, while the average torque dropped at 90% (Fig. 3.71). For ABC motor, the cogging torque is 96% of the initial one and the average torque is 88% of the initial average value (Fig. 3.72).

For pole shifting with multiple of  $10^\circ$ , the situation looks somehow better. The minimization of the cogging torque leads to a value that is 80% of the initial value, while the average torque drops to 89% for the HJ motor (Fig. 3.73). ABC motor's cogging torque is as low as 85% with this technique, while the average value of its torque is at 87% (Fig. 3.74). As it can be seen, pole shifting combined with dummy slots is not a very effective technique. More than that, for our motor it seems that is the worst possible method to minimize cogging torque.

If the pole arc width is kept at an optimal value without shifting and dummy slots are introduced, the situation improves considerably. Although the optimal arc width was calculated to be  $68.4^\circ$ , both values were tried once again, as the combination with dummy slots may prove that  $70.2^\circ$  is also an optimal arc width, depending on the situation.

For  $68.4^\circ$  arc width and HJ motor, the cogging torque is reduced at 39% and the average torque is down at 89% from their original values (Fig. 3.67). For the ABC motor, the cogging torque goes down to 48% of the initial value, while the average torque drops at 87% (Fig. 3.68).

With an arc width of  $70.2^\circ$ , the cogging torque is 42% and average torque is 90% for the HJ motor (Fig. 3.69). For the ABC motor, the cogging torque is 44% and the average torque is 88% of the initial values (Fig. 3.70).

Until now, tooth notches combined with other techniques were considered. In the end it is time to check what the effect of the dummy slots is without tampering with the magnets. For the HJ topology, the cogging torque dropped to 53% and the average torque to 98% (Fig. 3.65). For the ABC topology, the cogging torque is down at 76%, while the average torque drops only by 4 percent, at 96% (Fig. 3.66).

Though there are many methods to reduce the cogging torque, the most modern ones including the involvement of the optimization techniques [31] or FEM analysis in the design process [23, 26], the most popular methods remain the ones presented in this sub-chapter. What was sought of them was the ease of implementation in the manufacturing process, the effectiveness in reducing the torque ripples and cogging torque and the ability to keep the average output torque as close as possible to the original value.

In the table below all the results obtained from these techniques are shown, in terms of percentages: peak cogging torque per average torque, peak cogging torque after minimization versus initial peak cogging torque, average torque after minimization versus initial average torque value.

**Table 3.1 Torque ratios after torque pulsations reduction techniques were applied**

No.	Technique	$T_{cogg}$ [mNm]		$T_{avg}$ [mNm]		Peak $T_{cogg}$ per $T_{avg}$ [%]		$T_{cogg}$ vs. initial $T_{cogg}$ [%]		$T_{avg}$ vs. initial $T_{avg}$ [%]	
		HJ	ABC	HJ	ABC	HJ	ABC	HJ	ABC	HJ	ABC
1.	Initial	14.4	30.2	223.7	234	6.5	12.9	100	100	100	100
2.	Skewing with 3 segments	7.4	17.9	173.1	180.6	4.3	9.9	51.4	59.3	77.4	77.2
3.	Skewing with 4 segments	3.6	10.8	175.3	182.8	2.1	5.9	25	35.8	78.4	78.1
4.	Pole arc width 68.4°	6.1	16.5	201.9	210.8	3	7.8	42.4	54.6	90.3	90.1
5.	Pole arc width 70.2°	8.1	19	205.2	214.3	4	8.9	56.3	62.9	91.7	91.6
6.	Pole arc 68.4°, dummy slots	5.6	14.5	198.3	203.3	2.8	7.2	38.9	48	88.7	86.9
7.	Pole arc 70.2°, dummy slots	6.1	13.3	201.6	206.4	3	6.5	42.4	44	90.1	88.2
8.	Full pole and dummy slots	7.6	23	219.7	225	3.5	10.2	52.8	76.2	98.2	96.1
9.	Pole shifting multiple of 7.5°	10	23.2	203.8	212.8	4.9	10.9	69.4	76.8	91.1	91
10.	Pole shifting multiple of 10°	8.4	20.6	202.7	211.6	4.2	9.7	58.3	68.2	90.6	90.4
11.	Pole shifting multiple of 7.5° and dummy slots	13.5	29	200.2	204.9	6.7	14.2	93.8	96	89.5	87.6
12.	Pole shifting multiple of 10° and dummy slots	11.4	25.7	199.1	203.8	5.7	12.6	79.2	85.1	89	87.1

The skewing method offers the lowest cogging torque, but the average torque is reduced accordingly so this method doesn't comply with our requests. Pole shifting technique on the other hand reduces the average value of the torque with 13% in the worst case, but the cogging torque is still high, which makes this method also not suitable for our purposes.

Optimal pole arc width yields the best results, because the cogging torque is reduced at least to half its initial value, while the average torque is only 10% less than in the initial case. Taking into account that in real case the magnets doesn't span on full pole pitch because the need to be glued to the rotor and thus space is needed, and that magnets are built separately, an optimal arc width can be chosen before the assembly is done. Hence, this method doesn't require extra tools or machinery and it is quite efficient in reducing the torque pulsations.

However, the introduction of dummy slots in combination with the tooth notches reduces the cogging torque with 3 to 10 percents, but also reduces the average value of the torque in the same range. Tooth notches are not so hard to implement either, the stator lamination being stamped beforehand. So, it is designer's task to choose which technique should be implemented to further reduce the cogging torque.

From Table 3.1 it is visible that the best results for the HJ motor are obtained with optimal pole arc width of  $68.4^\circ$  with and without tooth notches and with full pole arc with tooth notches.

For the ABC motor, from the same table, it is clear that the techniques that comply with our requests are optimal pole arc width of  $68.4^\circ$  with and without tooth notches and optimal pole arc width of  $70.2^\circ$  with tooth notches.

Next, the effect of eccentricity due to misalignment during assembly on the total torque is shown.

### 3.3.9 Rotor eccentricity

One of the things that could affect the motor's performances and can happen during the assembling process is misalignment. The air gap should be uniform all across its circumference, but due to small imprecision during the introduction of the rotor inside the motor and imperfections of the rotor, the air gap could be not uniform along its circumference.

What we are interested on is the effect of the rotor eccentricity  $\varepsilon$  defined as dependent on the air gap length  $g$  in the radial direction:

$$\varepsilon = \frac{g_{\max} - g_{\min}}{g_{\max} + g_{\min}} \cdot 100 \quad (3.80)$$

In our case, the eccentricity in percents was increased in steps of 12.5%, to check if the severity of the eccentricity will strongly affect the total output torque. In the figures below, the total torque for HJ and ABC motors, for all eccentricity's values and the original cases are shown.

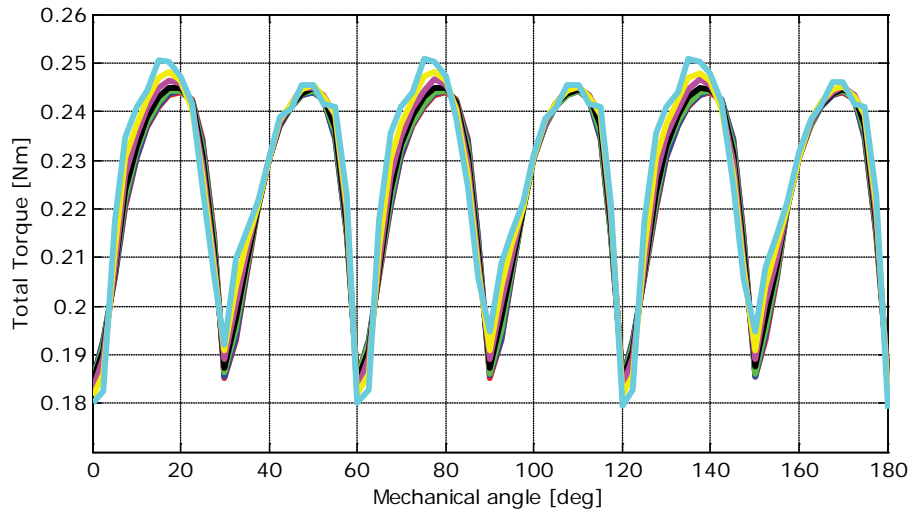


Fig. 3.75 Total torque for HJ case with no eccentricity and with 12.5%, 25%, 37.5%, 50%, 62.5%, 75% and 87.5% eccentricities

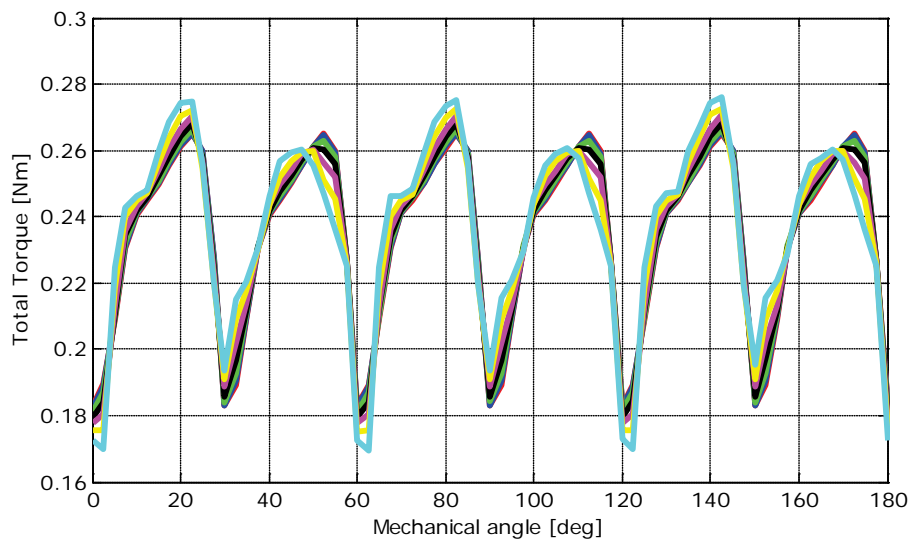


Fig. 3.76 Total torque for HJ case with no eccentricity and with 12.5%, 25%, 37.5%, 50%, 62.5%, 75% and 87.5% eccentricities

As can be seen, the output torque is not affected seriously by the rotor eccentricity. However, this doesn't mean that a precision tool to insert the rotor is not needed, because even small variations of the torque waveform can lead to noise, vibrations and fast degradation in time.



### 3.4 Conclusion

In this chapter, the motors obtained from optimal design in the previous chapter were analyzed with FEM. All the important characteristics in a BLDC were drawn from finite element analysis. A realistic image of the field distribution and flux linkages at no-load and at load, back-EMF at no-load, cogging torque (torque at zero current), load torque variation with rotor angular position, load torque pulsations and the variation of the radial forces with rotor angular position was obtained and FEM validated the designs.

Furthermore, to decide which topology is the best, an in-depth analysis of their output torques and torque pulsations was done. Since the electromagnetic torque is the most important characteristic of the motor, the smoothness of its shape is essential. Two factors play a key role in torque's waveform, current commutation and shape and torque at zero current. While the first one can be dealt with from control, the later one cannot be avoided in surface permanent magnet motors.

Although by now the two topologies went head-to-head, with a slight advantage for the one obtained from ABC optimization due to its higher value of the output torque, the HJ motor seems to be, by far, the better one in terms of cogging torque, as its value is half of the one of the ABC motor.

Since torque pulsations reduction is critical in motor design, as they are the cause for noise and vibrations and can lead to fast deterioration of the motor, minimization techniques were deployed. While the cogging torque was the culprit, the aim of these methods was to reduce its value without affecting too much the value of the average torque. Another essential criteria, since the purpose of the motor design was to offer something cheap and efficient, was the ease of implementation in the manufacturing process of each of the minimization techniques.

With a brief analysis of the existing minimization techniques, the most popular and viable solutions were chosen. Their effects on the cogging and average torques for each motor were studied and the results were presented in a table.

In terms of output torque, the ABC motor is the undisputed winner, but in terms of cogging torque, even after minimization, it is clear that the HJ motor is superior. Depending on each application, one of them is suited, but for a compressor the HJ motor is better fitted.

In the final part of the chapter, a brief view of the effects of the rotor eccentricity on the output torque's waveform is presented. The influence is not significant even for a serious displacement, but it may cause mechanical damages.

Once the design part is finished and the motor is validated by the finite element analysis, it is time to move on to the experimental part of the thesis, where how the motor works is analyzed.

## References

- [1] Jacek F. Gieras, "Permanent Magnet Motor Technology – Design and Applications", book, 3<sup>rd</sup> edition, CRC Press, Taylor & Francis Group LLC, Boca Raton, Florida, 2010
- [2] Michael J. Melfi, S. David Rogers, Steve Evon and Bill Martin, "Permanent-magnet motors for energy savings in industrial applications", *IEEE Trans. on Ind. Appl.*, vol.44, no.5, pp.1360-1366, September/October 2008
- [3] Nicola Bianchi, Silverio Bolognani and Fabio Luise, "Potentials and limits of high speed PM motors", *IEEE Trans. on Ind. Appl.*, vol.40, no.6, pp.1570-1578, November/December 2004
- [4] Nicola Bianchi, Silverio Bolognani and Fabio Luise, "Analysis and design of a PM brushless motor for high-speed operations", *IEEE Trans. on Energy Conv.*, vol.20, no.3, pp.629-637, September 2005
- [5] Z.Q. Zhu, David Howe, Ekkehard Bolte and Bernd Ackermann, "Instantaneous magnetic field distribution in brushless permanent magnet dc motors, Part I: Open-circuit field", *IEEE Trans. on Magn.*, vol.29, no.1, pp.124-135, January 1993
- [6] Z.Q. Zhu and David Howe, "Instantaneous magnetic field distribution in brushless permanent magnet dc motors, Part II: Armature-reaction field", *IEEE Trans. on Magn.*, vol.29, no.1, pp.136-142, January 1993
- [7] Z.Q. Zhu and David Howe, "Instantaneous magnetic field distribution in brushless permanent magnet dc motors, Part III: Effect of stator slotting", *IEEE Trans. on Magn.*, vol.29, no.1, pp.143-151, January 1993
- [8] Z.Q. Zhu and David Howe, "Instantaneous magnetic field distribution in brushless permanent magnet dc motors, Part IV: Field on load", *IEEE Trans. on Magn.*, vol.29, no.1, pp.152-158, January 1993
- [9] Ion Boldea and Lucian Tutelea, "Electric Machines – Steady State, Transients and Design with MATLAB®", book, CRC Press, Taylor & Francis Group LLC, Boca Raton, Florida, 2010
- [10] David Meeker, "Finite Element Method Magnetics – User's Manual, Version 4.2", manual, October 2010
- [11] Duane C. Hanselman, "Brushless Permanent-Magnet Motor Design", book, McGraw-Hill Inc., New York, 1994
- [12] Ramu Krishnan, "Permanent Magnet Synchronous and Brushless DC Motor Drives", book, CRC Press, Taylor & Francis Group LLC, Boca Raton, Florida, 2010
- [13] T.J.E. Miller, "SPEED's electric motors – An outline of some of the theory in the SPEED software for electric machine design with problems and solutions", book, University of Glasgow, 2002
- [14] Z.Q. Zhu and David Howe, "Influence of design parameters on cogging torque in permanent magnet machines", *IEEE Trans. on Energy Conversion*, vol.15, no.4, pp.407-412, December 2000
- [15] Jiang Xingtong et al., "Theoretical and simulation analysis of influences of stator tooth width on cogging torque of BLDC motors", *IEEE Trans. on Magn.*, vol.45, no.10, pp.4601-4604, October 2009

- 
- [16] Jacek F. Gieras, "Analytical approach to cogging torque calculation of PM brushless motors", *IEEE Trans. on Ind. Appl.*, vol.40, no.5, pp.1310-1316, September/October 2004
- [17] Kwang-Woon Lee et al., "Quality assurance testing for magnetization quality assessment of BLDC motors used in compressors", *IEEE Trans. on Ind. Appl.*, vol.46, no.6, pp.2452-2458, November/December 2010
- [18] Nicola Bianchi and Silverio Bolognani, "Design techniques for reducing the cogging torque in surface-mounted PM motors", *IEEE Trans. on Ind. Appl.*, vol.38, no.5, pp.1259-1265, September/October 2002
- [19] Seok-Myeong Jang, Han-Wook Cho and Dae-Joon You, "Cogging torque minimization in permanent magnet brushless DC motors for high speed application", *KIEEE Intl. Trans. on Elec. Machinery and Energy Conv.*, vol.5-B, no.2, pp.146-153, 2005
- [20] Mohammad S. Islam, Sayed Mir and Tomy Sebastian, "Issues in reducing the cogging torque of mass-produced permanent-magnet brushless motor", *IEEE Trans. on Ind. Appl.*, vol.40, no.3, pp.813-820, May/June 2004
- [21] Nicola Bianchi et al., "MMF harmonics effects on the embedded FE-analytical computation of PM motors", in *Proc. of 42<sup>nd</sup> IAS Annual Meeting*, pp.1544-1551, 2007
- [22] Vlad Grădinaru, Lucian Tutelea and Ion Boldea, "25 kW, 15 krpm, 6/4 PMSM: optimal design and torque pulsation reduction via FEM", in *Proc. of 11<sup>th</sup> Intl. Conf. on Optimization of Electric and Electronic Equipment (OPTIM'08)*, pp.249-256, 2008
- [23] Vlad Grădinaru, Lucian Tutelea and Ion Boldea, "Hybrid analytical/FEM optimization design of SPMSM for refrigerator compressor loads", in *Proc. of Intl. Aegean Conf. on Electrical Machines and Power Electronics (ACEMP)*, 2011
- [24] Mohammed Fazil and K.R. Rajagopal, "A novel air-gap profile of single-phase permanent-magnet brushless DC motor for starting torque improvement and cogging torque reduction", *IEEE Trans. on Magn.*, vol.46, no.11, pp.3928-3932, November 2010
- [25] Rakib Islam et al., "Permanent-magnet synchronous motor magnet design with skewing for torque ripple and cogging torque reduction", *IEEE Trans. on Ind. Appl.*, vol.45, no.1, pp.152-160, January/February 2009
- [26] Julio-César Urresty et al., "A simple 2-D finite-element geometry for analyzing surface-mounted synchronous machines with skewed rotor magnets", *IEEE Trans. on Magn.*, vol.46, no.11, pp.3948-3954, November 2010
- [27] Touzhu Li and Gordon Slemon, "Reduction of cogging torque in permanent magnet motors", *IEEE Trans. on Magn.*, vol.24, no.6, pp.2901-2903, November 1988
- [28] Takeo Ishikawa and Gordon Slemon, "A method of reducing ripple torque in permanent magnet motors without skewing", *IEEE Trans. on Magn.*, vol.29, no.2, pp.2028-2031, March 1993
- [29] Luke Dosiek and Pragasen Pillay, "Cogging torque reduction in permanent magnet machines", *IEEE Trans. on Ind. Appl.*, vol.43, no.6, pp.1565-1571, November/December 2007

- [30] C. Bréton et al., "Influence of machine symmetry on reduction of cogging torque in permanent-magnet brushless motors", *IEEE Trans. on Magn.*, vol.36, no.5, pp.3819-3823, September 2000
- [31] Ningning Chen, S.L. Ho and W.N. Fu, "Optimization of permanent magnet surface shapes of electric motors for minimization of cogging torque using FEM", *IEEE Trans. on Magn.*, vol.46, no.6, pp.2478-2481, June 2010
- [32] Mahdi Ashabani, and Yasser Abdel-Rady I. Mohamed, "Multi-objective shape optimization of segmented pole permanent-magnet synchronous machines with improved torque characteristics", *IEEE Trans. on Magn.*, vol.47, no.4, pp.795-804, April 2011
- [33] W. Fei and P.C.K. Luk, "A new technique of cogging torque suppression in direct-drive permanent magnet brushless machines", *IEEE Trans. on Ind. Appl.*, vol.46, no.4, pp.1332-1340, July/August 2010

## Chapter 4

### Dynamic model of BLDC

#### Abstract

The previous chapters are focused on motor design for a refrigerator compressor. Two optimization methods were used to find the proper motor configuration, in order to be low cost, high efficiency and to have a low cogging torque. Finite element analysis was used to obtain electrical and mechanical characteristics of the designed motor, which were in good agreement with calculated ones. However, the motor cannot work by itself, but as a part of a drive. The other essential parts of a drive are the converter, which supplies the necessary voltages and currents, and the controller, which takes the position information from the motor and transforms it in switching signals.

The purpose of this chapter is to present a complete model of the drive, with all its elements. For the motor, the back-EMF waveform obtained from the FEM analysis is considered, and the commutation phenomenon will be considered on the inverter side. The simulation of the drive is compared to experimental results, showing a similar behavior of both the simulation model and the real drive.

#### 4.1 Introduction

The rapid extending usage of the BLDC motors in a wide range of applications is a certainty nowadays. Many motor manufacturers produce this type of motor for low and mid-power drives, due to their high efficiency and torque-per-volume. While for electromechanical design various optimization methods were developed and finite element analysis became more and more accurate in predicting the motor characteristics, drive simulation is essential in evaluating the system's behavior.

A drive is usually composed of three parts: the motor and the load, the converter and the controller [1 – 6]. With the evolution of the simulation software, each part mentioned earlier could be modeled closer to the real behavior. Mathematical motor models were developed based on state-space equations or Fourier series. One of the main issues was the introduction of the back-EMF in the model. The ideal waveform can be used, but the results are remote from the real case. Fourier series are also used, with much better results, but the best method is to use the back-EMF obtained from the FEM analysis, as it is based on the motor geometry. Because the flux distribution is non-sinusoidal, the d-q model cannot be applied in the simulation, so the phase mathematical model is considered to be the best [1 – 8].

The converter is not usually modeled outside the drive simulation, although papers that focus strictly on this part exist in the literature [9 – 11]. Voltage drops on the switches, commutation losses are not considered in the drive simulation due to the increased complexity of the model, hence the switches are considered to be ideal.

The controller is an essential part of the simulation as it transforms the motor information in switching signals. The most common controllers used for BLDC motors are speed, torque and current ones. Input information may come from sensors (Hall, encoders or resolvers) or it can be estimated from voltage and currents for sensorless control [1 – 25].

Lately, complete simulation models were developed, taking into account the commutation phenomenon [12, 13, 16, 18, 19]. Real back-EMF waveform is considered in [17], while for large- and small-signal analysis of BLDC motor drive systems, the so-called average-value models are indispensable [14, 15].

In this chapter, a complete drive model is developed and analyzed. The motor model is based on state-space equations, with the back-EMF waveform integrated from the FEM analysis. The inverter model, although it is considered to have ideal switches, will be modeled to take into account the phase commutation phenomenon. Open-loop control, based on Hall sensor information, will be used in this simulation. The aim of this model is to be as close to reality as it can be, as it will be used in the following chapters for sensorless control simulation, where precision is needed.

## 4.2 BLDC motor

Before starting the simulation of the drive, each component part will be briefly analyzed. PM DC brushless motors use direct feedback of the rotor angular position so that the input armature current can be switched, among the motor phases, in exact synchronism with the rotor motion. This concept is known as self-controlled synchronization, or electronic commutation [5]. Between sinusoidal and trapezoidal PM machines with self-control, the latter gives performance closer to that of a DC motor. For this reason it is widely known as a brushless DC motor (BLDC). Basically, it is an electronic motor and requires a three-phase inverter in the front end [1].

The main reason for the popularity of these machines over its counterpart is because of its control simplicity. To initiate the onset and commutation of current in the phase of a machine, the beginning and end of the constant flat portion of the back-EMF have to be tracked. That amounts to only six discrete positions for a three-phase machine in each of the electrical cycle, resulting in a major cost saving in the feedback sensor. The flux distribution in PM brushless DC motor is trapezoidal and therefore the d-q rotor reference frames model developed for the PM synchronous motor is not applicable. Given the non-sinusoidal flux distribution, it is prudent to derive a model of the BLDC motor in phase variables [3]. The derivation of this model is based on the following assumptions:

1. The motor is not saturated.
2. The motor windings have a constant resistance, self inductance, and mutual inductance and the first two are identical for all phases.

3. All three phases have an identical back-EMF shape.
4. Power semiconductor devices in the inverter are ideal.
5. Iron losses are negligible.
6. Eddy currents and hysteresis effect are neglected.

The coupled circuit equation of the stator windings in terms of motor electrical constants is:

$$\begin{bmatrix} V_{a0} \\ V_{b0} \\ V_{c0} \end{bmatrix} = \begin{bmatrix} R_s & 0 & 0 \\ 0 & R_s & 0 \\ 0 & 0 & R_s \end{bmatrix} \cdot \begin{bmatrix} i_a \\ i_b \\ i_c \end{bmatrix} + \frac{d}{dt} \left( \begin{bmatrix} L_{aa} & L_{ab} & L_{ac} \\ L_{ba} & L_{bb} & L_{bc} \\ L_{ca} & L_{cb} & L_{cc} \end{bmatrix} \cdot \begin{bmatrix} i_a \\ i_b \\ i_c \end{bmatrix} \right) + \begin{bmatrix} e_a \\ e_b \\ e_c \end{bmatrix} + \begin{bmatrix} V_{n0} \\ V_{n0} \\ V_{n0} \end{bmatrix} \quad (4.1)$$

In the above equation,  $V_{a0}$ ,  $V_{b0}$  and  $V_{c0}$  are phase voltages,  $R_s$  is phase resistance,  $L_{aa}$ ,  $L_{bb}$  and  $L_{cc}$  are phase self inductances,  $L_{ab}$ ,  $L_{ac}$ ,  $L_{ba}$ ,  $L_{bc}$ ,  $L_{ca}$  and  $L_{cb}$  are mutual inductances,  $i_a$ ,  $i_b$  and  $i_c$  are phase currents,  $e_a$ ,  $e_b$  and  $e_c$  are phase back-EMFs and  $V_{n0}$  is the voltage between motor and inverter neutral points.

The BLDC motor that is analyzed has surface PM rotor and is non-salient. Under this assumption, the phase self inductances and mutual inductances are considered to have a constant value with rotor position, so the following simplifications can be made:

$$L_{aa} = L_{bb} = L_{cc} = L \quad (4.2)$$

$$L_{ab} = L_{ba} = L_{ac} = L_{ca} = L_{bc} = L_{cb} = M \quad (4.3)$$

For proper functioning of the BLDC, the phase currents are constrained to be balanced:

$$i_a + i_b + i_c = 0 \quad (4.4)$$

Using the simplifications from equations (4.2) – (4.4) in relation (4.1), we obtain the equation for the electromagnetic part of the motor:

$$\begin{bmatrix} V_{a0} \\ V_{b0} \\ V_{c0} \end{bmatrix} = \begin{bmatrix} R_s & 0 & 0 \\ 0 & R_s & 0 \\ 0 & 0 & R_s \end{bmatrix} \cdot \begin{bmatrix} i_a \\ i_b \\ i_c \end{bmatrix} + \begin{bmatrix} L-M & 0 & 0 \\ 0 & L-M & 0 \\ 0 & 0 & L-M \end{bmatrix} \cdot \frac{d}{dt} \begin{bmatrix} i_a \\ i_b \\ i_c \end{bmatrix} + \begin{bmatrix} e_a \\ e_b \\ e_c \end{bmatrix} + \begin{bmatrix} V_{n0} \\ V_{n0} \\ V_{n0} \end{bmatrix} \quad (4.5)$$

The back-EMF relation is given by Faraday's law:

$$e = -\frac{d\lambda_{PM}}{dt} = -\frac{d\lambda_{PM}}{d\theta_m} \cdot \frac{d\theta_m}{dt} = k_e \cdot \omega_m \quad (4.6)$$

In the above equations,  $\lambda_{PM}$  is the PM magnetic flux,  $\theta_m$  is the mechanical angle,  $\omega_m$  is the mechanical speed and  $k_e$  is the back-EMF constant.

In figure 4.1, the overall system configuration of the three-phase BLDC drive is shown. In figure 4.2, the ideal current and back-EMF waveforms and switching modes are presented.

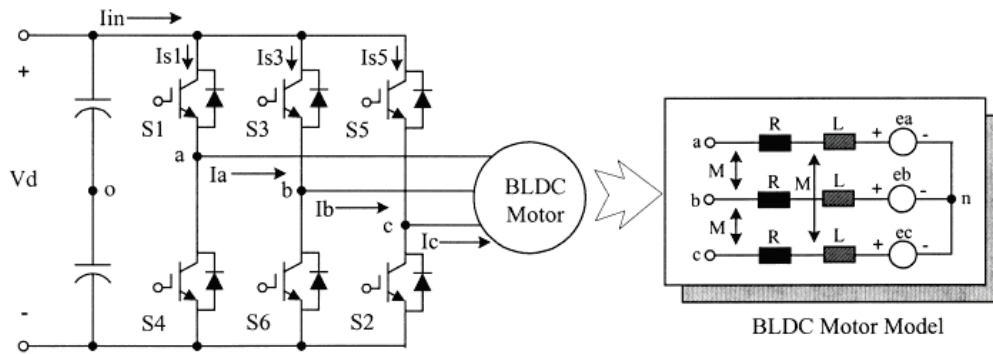


Fig. 4.1 Configuration of BLDC motor drive system [13]

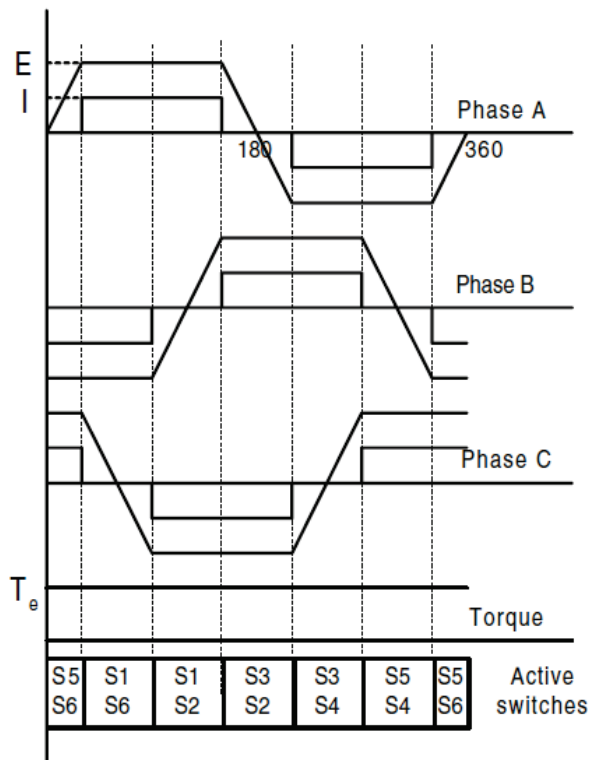


Fig. 4.2 Ideal currents, phase back-EMFs, and electromagnetic torque of a three phase BLDC Y-connected motor with 120° bipolar currents [20]



The output of the electromagnetic part of the motor is the torque:

$$T_e = \frac{e_a \cdot i_a + e_b \cdot i_b + e_c \cdot i_c}{\omega_m} \quad (4.7)$$

The equation of motion for a simple system with inertia  $J$ , friction coefficient  $B_m$ , and load torque  $T_l$  is:

$$J \cdot \frac{d\omega_m}{dt} + B_m \cdot \omega_m = T_e - T_l \quad (4.8)$$

The electrical speed (angle) is related to the mechanical speed (angle) with the following relationship, where  $p$  is the number of rotor pole pairs:

$$\omega_e = p \cdot \omega_m \quad , \quad \theta_e = p \cdot \theta_m \quad (4.9)$$

Based on equations (4.5) and (4.7) the electromagnetic part of the BLDC motor will be simulated, while the mechanical part is represented by equation (4.8). Although there are some analytical ways to introduce the back-EMF waveform in the model [1 – 8, 12 – 19], in this motor modeling the back-EMF shape obtained from motor FEM analysis will be used, as it will provide more accurate output waveforms.

### 4.3 Inverter

Up until now, only the motor was considered. However, the motor by itself cannot work, so he needs to be supplied with voltages and currents or excited, in order to produce electromagnetic torque. For a specified kVA rating of an inverter, a suitable power switching device is to be selected and then the voltage and current ratings of the devices are to be designed on a worst-case basis. The devices have to withstand the voltage  $V_{DC}$  in the forward direction, so a typical 50% margin is to be added to withstand the transient overshoot at turn-off switching. The diodes should be fast recovery type to reduce the switching loss. The peak and average current in the devices can be determined from the current waves. If the inverter is required to have a higher power rating on a short-term basis, the design should take this into consideration [1].

For BLDC motors only two possible operation modes are available, half-wave or unipolar excitation and full-wave or bipolar excitation. The first mode is used in low cost applications, being cheaper than its counterpart, as it contains at least one switch per phase, but less than two switches per phase. The full-wave mode (bipolar excitation) is used in most applications as it is more efficient. In this mode, two switching schemes are possible, namely soft and hard switching (chopping). Both modes, with their particularities, will be presented in this sub-chapter.

### 4.3.1 Half-wave mode (unipolar excitation)

This operation mode of an inverter is widely used for low cost applications, where losses are not that important, but the cost is a major constraint. The full-wave mode provides very limited opportunities for innovations in the inverter topology and six-switch full-bridge topology has stayed on as the most optimal topology so far. A number of converter topologies emerge if the BLDC motor is operated in the half-wave mode. Although the cost of the motor and controller with single chips has been optimized, the only other subsystem available for optimization is the power converter. The half-wave operation is a major asset in this aspect as many power converter topologies are possible with minimum number of switches [3]. A typical topology of such a converter is shown in figure 4.3, namely the C-dump inverter. Other types of half-wave inverters are variable DC link and variable voltage converter with buck-boost front-end [3].

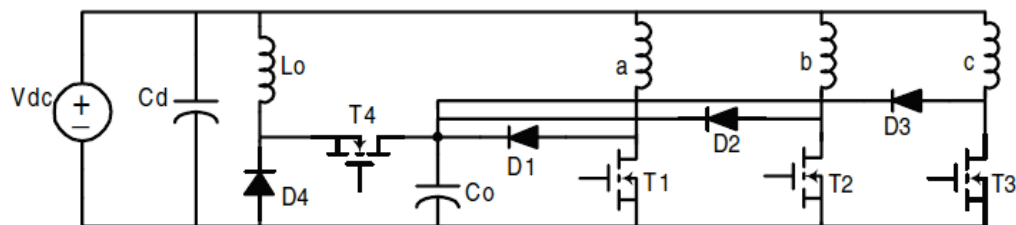


Fig.4.3 Schematic of C-dump topology for unipolar three-phase BLDC motor [4]

The DC voltage  $V_{DC}$  is switched across phase-to-neutral terminals with the aid of one solid state switch per phase. Each phase terminal receives positive voltage and the neutral wire is of negative polarity. For the current sequence  $i_a, i_b, i_c$ , the MMF phasors  $F_a, F_b, F_c$  rotate counterclockwise. If the switching sequence is reversed, the direction of rotation of MMF phasors will be clockwise. For a linear magnetic circuit the phase magnetic fluxes are proportional to MMFs. This type of commutation is called half-wave mode because conduction occurs only during the positive half of the EMF waveform [5]. The main advantages of this type of commutation is the reduction of the costs by using less than two switches per phase, the risk of shoot-through faults is eliminated and the isolation circuitry for switching of devices is not necessary anymore. However, the disadvantages are also of paramount importance. In this case, the motor neutral has to be available because motor currents are no longer balanced. The main drawback of this scheme is the increase of the torque ripple by almost 50% compared to the full-wave operation, so the proper choice of the inverter topology for each application should be weighted carefully.

### 4.3.2 Full-wave mode (bipolar excitation)

Although half-wave operation mode is very fit for low cost applications, full wave operation more is used in the majority of all BLDC applications because it does

not have the drawbacks of its counterpart. PM synchronous motors use three switches at a time, one for each phase, while for brushless DC motor, only two switches at a time are used, which reduces the switching losses. The typical inverter configuration for bipolar excitation is presented in fig.4.1, while the MMF phasors (voltage vectors) are shown in fig.4.4. This operation is called full wave operation because conduction occurs for both the positive and negative half of the back EMF waveform.

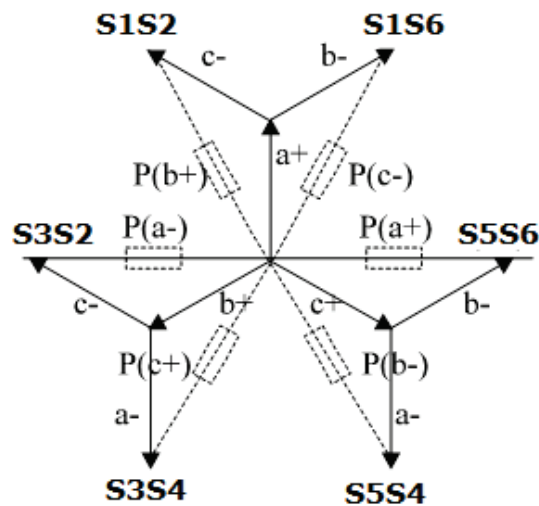


Fig.4.4 MMF phasors for three phase full wave operation of a Y-connected PM DC brushless motor [2]

The DC voltage is switched between phase terminals and two windings belonging to different phases are series connected during each conduction period. The current sequence is  $i_{AB}$ ,  $i_{AC}$ ,  $i_{BC}$ ,  $i_{BA}$ ,  $i_{CA}$  and  $i_{CB}$ . Two solid state switches per phase are required. For this current sequence, the MMFs  $F_{AB}$  (S1 – S6),  $F_{AC}$  (S1 – S2),  $F_{BC}$  (S3 – S2),  $F_{BA}$  (S3 – S4),  $F_{CA}$  (S5 – S4) and  $F_{CB}$  (S5 – S6) rotate counterclockwise.

The inverter is usually responsible for both the electronic commutation and current regulation. Electronic commutation is done opening and closing the six switches according to the position information obtained from the position sensor. The exact commutation points are needed in order to keep the current in phase with the back-EMF, which makes the motor to output a rather smooth torque. If the BLDC machine is operated as a motor, the polarity of the current must be the same as for the back-EMF. However, if the BLDC machine is operated as a generator, especially for regenerative braking, the polarity of the phase currents is reversed with respect to the back-EMFs.

To change the polarity of the current and its amplitude, current regulation is needed. There are two possible ways to control the voltage and current continuously at the machine terminals, soft PWM chopping (freewheeling mode) (fig.4.5.a) and hard PWM chopping (feedback mode) (fig.4.5.b). The first one has the advantage of lower switching losses, while the later one has the advantage of using only one DC link current sensor, because machine current is always flowing in the line.

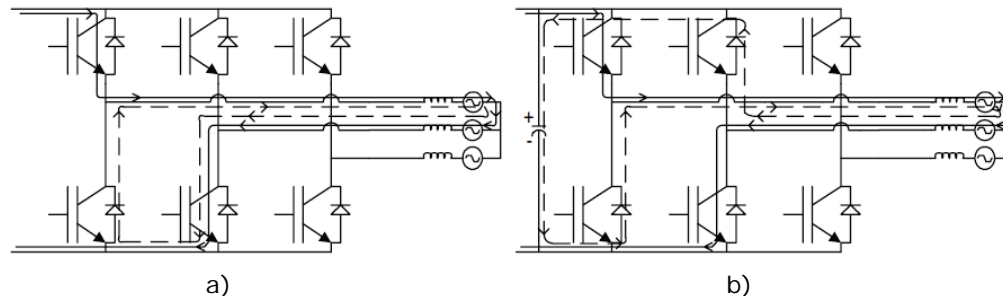


Fig.4.5 Illustration of: a) soft chopping and b) hard chopping for current regulation [4]

Let's consider the  $60^\circ$  interval where S1 and S6 are conducting. For soft chopping mode, S6 is kept on during the whole interval, while S1 is chopping. When S1 is on,  $V_{DC}$  is applied across phases A and B, because both S1 and S6 are on. When S1 is turned off, decaying freewheeling current flows through S6 and D4, short-circuiting the motor terminals, as can be seen on the dashed lines. Alternatively, S6 could be turned off and then the current would flow through S1 and D3.

In hard chopping mode, both S1 and S6 are chopping together. When S1 and S6 are on, phase A and phase B currents will increase and  $V_{DC}$  is larger than  $e_{ab}$ . However, when the devices are turned off, the current will decrease because of feedback through diodes D3 and D4.

In six step operation mode only one upper and one lower solid state switch are turned on at a time. With more than two switches on at a time, a  $180^\circ$  current conduction can be achieved. If the full current flows, say, through one upper leg, two lower legs conduct half of the current [5].

#### 4.4 Controllers

The need for controllers is given by the fact that the stator excitation for BLDC motors needs to be synchronized with rotor speed and position to produce constant torque. The controller has to keep track of the rotor angular position and switch the excitation among the motor phases appropriately. The rotor position needs to be detected at six discrete points in each electrical cycle, i.e. at  $60^\circ$  electrical intervals for the commutation. The most common method of sensing the rotor position is by means of a Hall effect position sensor [20 – 27]. A Hall effect position sensor consists of a set of Hall switches and a set of trigger magnets. The Hall switch is a semiconductor switch based on the Hall effect that opens or closes when the magnetic field is higher or lower than a certain threshold value. A signal conditioning circuit integrated with the Hall switch provides a TTL-compatible pulse with sharp edges and high noise immunity for connection to the controller. For a three phase BLDC motor, three hall switches spaced  $120^\circ$  electrical apart are mounted on the stator frame. The trigger magnets can be a separate set of magnets aligned with the rotor magnets and mounted on the shaft in close proximity to the hall switches.

The rotor magnets can also be used as the trigger magnets, with the hall switches mounted close enough to be energized by the leakage flux at the appropriate rotor positions. The digital signals from the Hall sensors are then decoded to obtain the three-phase switching sequence for the inverter. In the block diagram of a BLDC motor drive shown in fig.4.6, this function is performed by the controller, which also processes the signal from the DC link current sensor. Based on these two inputs, gating signals are provided to the six inverter switches. High-resolution encoders or resolvers can also be used to provide position feedback for applications in which their cost is justified by the improved performance [4].

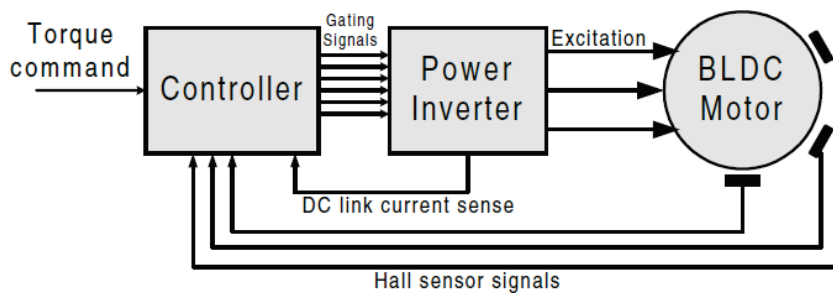


Fig.4.6 BLDC motor drive schematic [4]

For applications requiring speed or position control, the speed and position control loops can be built around the inner current control loop as shown in figure 4.7. The ability to operate with just three Hall sensors gives the trapezoidal brushless permanent magnet motor an edge over its sinusoidal counterpart in low cost applications. It should be mentioned that PMSM motors are also sometimes operated with rectangular currents to minimize the cost of the position sensor, although the output torque waveform is far from ideal because of the mismatch between the motor and the inverter [4].

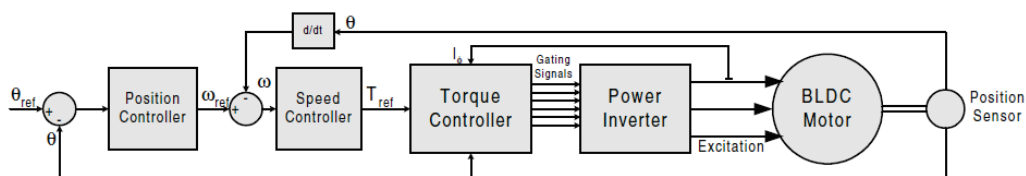


Fig.4.7 Position servo using the BLDC motor [4]

## 4.5 Dynamic model implementation

Until now, a general overview of the ensemble of a BLDC drive was presented. Before any experiment can be done, especially if new types of controls are employed, a precise simulation of the drive is necessary. The aim of this subchapter is to present in detail how this particular BLDC drive was simulated in Matlab®/Simulink® and how reliable it is for the future introduction of sensorless control techniques.

### 4.5.1 BLDC Motor block

The first building block of the simulation is the motor itself. Starting from motor's equations, the motor can be divided in two blocks, electrical and mechanical. The output of the electrical part is considered to be the phase current, input to the mechanical part, while the later one outputs position and speed.

The electrical part of the motor is characterized by equations (4.5) and (4.6), as can be seen in figure 4.8.

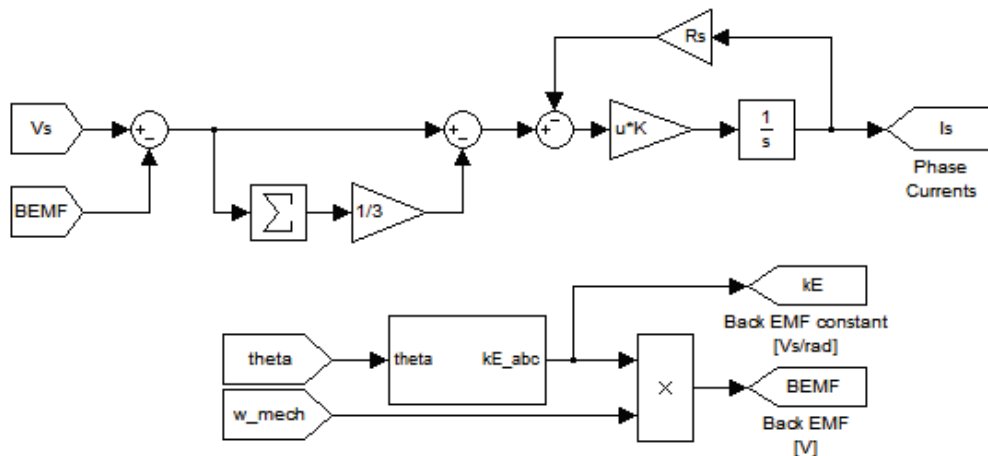


Fig.4.8 Electromagnetic part of the BLDC motor

The permanent magnet flux variation with rotor position is taken from FE analysis and implemented as look-up table to obtain the back-EMF constant  $k_e$ .

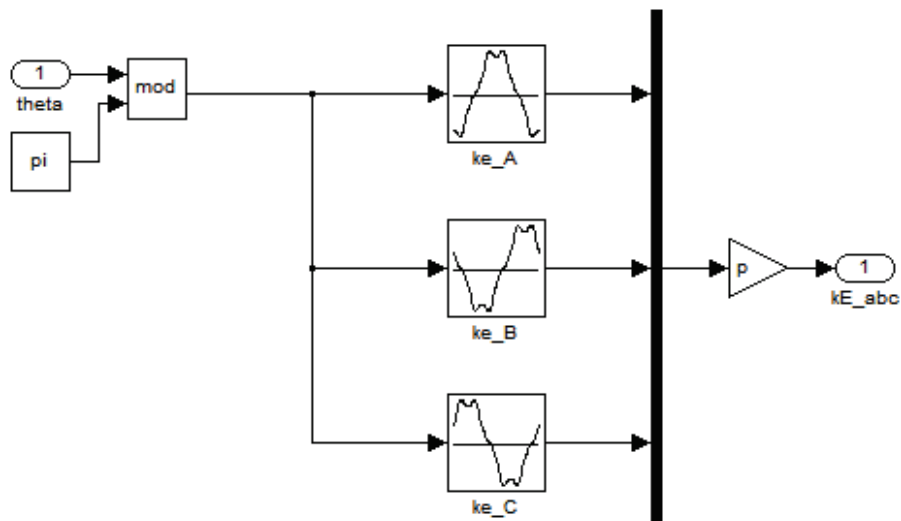


Fig.4.9 Permanent magnet flux versus rotor position look-up tables

The mechanical part of the motor is characterized by equations (4.7) and (4.8). as can be seen in figure 4.10.

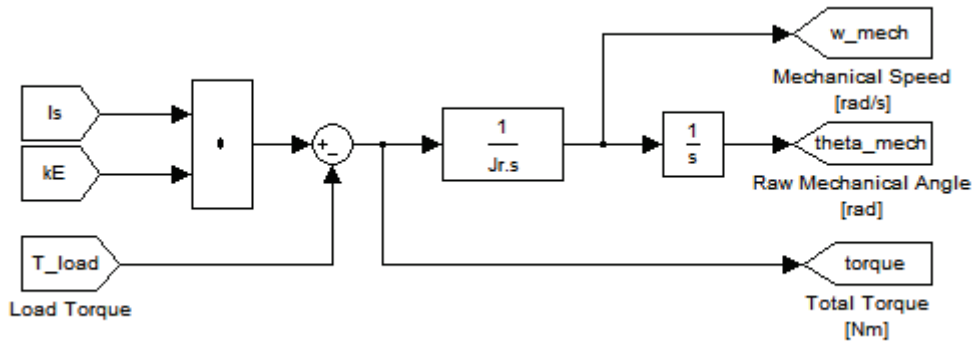


Fig.4.10 Mechanical part of the BLDC motor

#### 4.5.2 Voltage source inverter block

The inverter is used to transform the request from controllers into voltage to be fed to the motor. This is done through power switches that are turned on and off with a rate given by the PWM. In simulation, there are some ways to implement an inverter. One can use typical power electronics devices from Simulink® library or to interface the Matlab® with other software dedicated for power electronics like PSIM. However, there are ways for BLDC to be modeled through equations in such ways as to consider the commutation case [12 – 17].

For each  $60^\circ$ , only two phases are on at a time. In each sector the voltage expression, taking into account equations (4.2) – (4.6), can be expressed as:

$$V_{+0} = \frac{V_{dc}}{2} = R_s \cdot i_+ + (L - M) \cdot \frac{di_+}{dt} + e_+ + V_{n0}$$

$$V_{-0} = -\frac{V_{dc}}{2} = R_s \cdot i_- + (L - M) \cdot \frac{di_-}{dt} + e_- + V_{n0} \quad (4.10)$$

$$V_n = e_n + V_{n0}$$

$$V_{n0} = \frac{1}{2} \cdot (-e_+ - e_-) \quad (4.11)$$

The equations above are generic and they apply to each normal interval. In the table below, the conducting (+ and -) and non-conducting (n) phases are shown for each sector.

If equations (4.10) and (4.11) describe the voltages for normal interval, from the table below the voltage expressions for commutation interval can be deduced.

**Table 4.1 Conducting and non-conducting phases for each sector for normal and commutation intervals**

Sector	Phase A	Phase B	Phase C
1	$-0.5 \cdot V_{DC}$	0	$+0.5 \cdot V_{DC}$
1 -> 2	$+0.5 \cdot V_{DC}$ (- to 0)	$-0.5 \cdot V_{DC}$ (0 to -)	$+0.5 \cdot V_{DC}$
2	0	$-0.5 \cdot V_{DC}$	$+0.5 \cdot V_{DC}$
2 -> 3	$+0.5 \cdot V_{DC}$ (0 to +)	$-0.5 \cdot V_{DC}$	$-0.5 \cdot V_{DC}$ (+ to 0)
3	$+0.5 \cdot V_{DC}$	$-0.5 \cdot V_{DC}$	0
3 -> 4	$+0.5 \cdot V_{DC}$	$+0.5 \cdot V_{DC}$ (- to 0)	$-0.5 \cdot V_{DC}$ (0 to -)
4	$+0.5 \cdot V_{DC}$	0	$-0.5 \cdot V_{DC}$
4 -> 5	$-0.5 \cdot V_{DC}$ (+ to 0)	$+0.5 \cdot V_{DC}$ (0 to +)	$-0.5 \cdot V_{DC}$
5	0	$+0.5 \cdot V_{DC}$	$-0.5 \cdot V_{DC}$
5 -> 6	$-0.5 \cdot V_{DC}$ (0 to -)	$+0.5 \cdot V_{DC}$	$+0.5 \cdot V_{DC}$ (- to 0)
6	$-0.5 \cdot V_{DC}$	$+0.5 \cdot V_{DC}$	0
6 -> 1	$-0.5 \cdot V_{DC}$	$-0.5 \cdot V_{DC}$ (+ to 0)	$+0.5 \cdot V_{DC}$ (0 to +)

Equation (4.12) is for commutation intervals where the non-conducting phase starts to build negative current (1 to 2, 3 to 4 and 5 to 6) while the current in negative phase goes up to 0.

$$\begin{aligned}
 V_{+0} &= \frac{V_{dc}}{2} = R_s \cdot i_+ + (L - M) \cdot \frac{di_+}{dt} + e_+ + V_{n0} \\
 V_{-0} &= \frac{V_{dc}}{2} = R_s \cdot i_- + (L - M) \cdot \frac{di_-}{dt} + e_- + V_{n0} \\
 V_n &= -\frac{V_{dc}}{2} = R_s \cdot i_n + (L - M) \cdot \frac{di_n}{dt} + e_n + V_{n0} \\
 V_{n0} &= \frac{1}{2} \cdot \left( \frac{V_{dc}}{2} - e_+ - e_- - e_n \right)
 \end{aligned} \tag{4.12}$$

Equation (4.13) is for commutation intervals where the non-conducting phase starts to build positive current (2 to 3, 4 to 5 and 6 to 1) while the current in positive phase goes down to 0.

$$\begin{aligned}
 V_{+0} &= -\frac{V_{dc}}{2} = R_s \cdot i_+ + (L - M) \cdot \frac{di_+}{dt} + e_+ + V_{n0} \\
 V_{-0} &= -\frac{V_{dc}}{2} = R_s \cdot i_- + (L - M) \cdot \frac{di_-}{dt} + e_- + V_{n0} \\
 V_n &= \frac{V_{dc}}{2} = R_s \cdot i_n + (L - M) \cdot \frac{di_n}{dt} + e_n + V_{n0} \\
 V_{n0} &= \frac{1}{2} \cdot \left( \frac{V_{dc}}{2} - e_+ - e_- - e_n \right)
 \end{aligned} \tag{4.13}$$



The sectors are obtained from the position sensor based on Hall effect, as can be seen in the figure below.



Fig.4.11 Transition from electrical angle to sector number via Hall sensors

In order to avoid increased complexity in transformation of the electrical angle in Hall signals and in sector, the correspondence between them is implemented through S-functions, according to the table 4.2 in sub-chapter 4.5.3.

The sector information or Hall signals can be used to obtain the commutation and normal intervals. To distinguish between them the commutation points and their period must be determined thoroughly as it influences the output torque.

The commutation is presented in figure 4.12, while in figure 4.13 its implementation in Simulink® is shown.

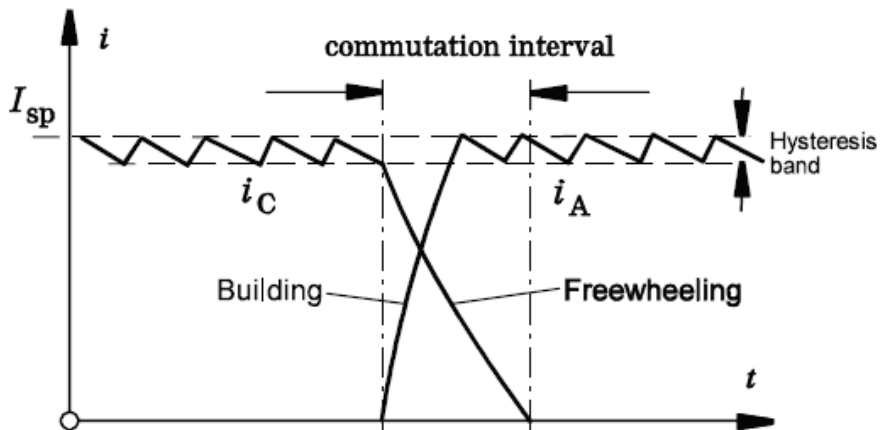


Fig. 4.12 Commutation interval between phases C and A [28]

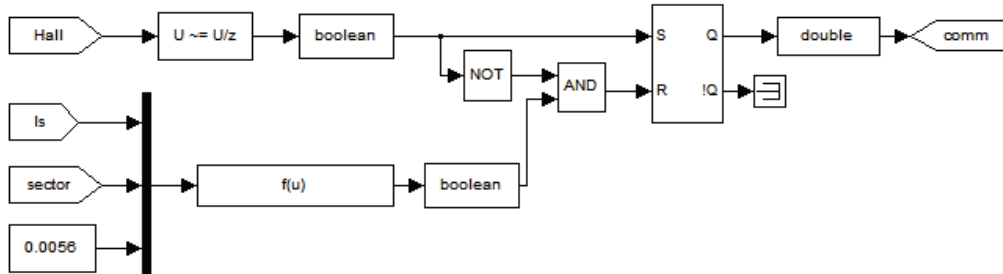


Fig.4.13 Commutation interval signal determination

The value of  $V_{n0}$  from the equations (4.11) for normal interval and (4.12) and (4.13) for commutation interval is determined from the implementation below.

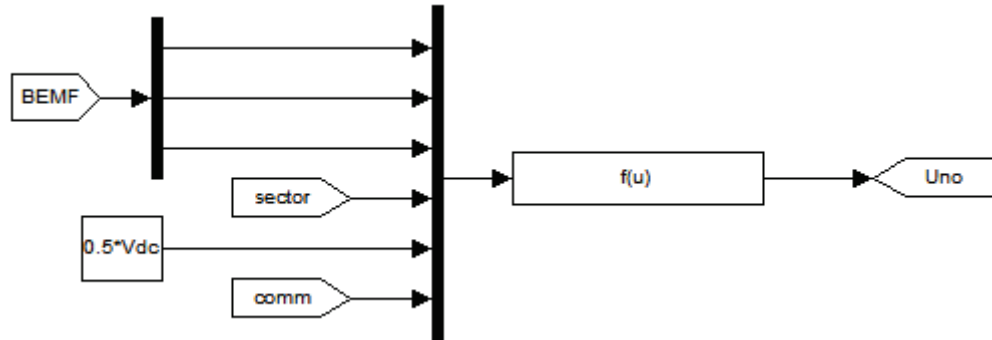


Fig.4.14 Voltage  $V_{n0}$  between motor and inverter neutral points

### 4.5.3 Hall sensor feedback

Usually, for sensed control of BLDC motors, three Hall sensors are used. The Hall effect sensors give three  $180^\circ$  overlapping signals, thus providing the six mandatory commutation points. The rising and the falling edges of the sensor output are detected and the corresponding flags are generated (1 for rising and 0 for falling). The system first determines which edge has been detected, then computes the time elapsed since the last detected edge and commutates the supplied phases.

The speed feedback is derived from the position sensor output signals. As it is already known, there are six commutation signals per electrical revolution. In other words, between two commutation signals there are  $60^\circ$  electrical. As the speed can be written as the report between the variation of the angle and the time variation, it is possible to get the speed from the computed elapsed time between two captures [20].

For the mounting of the Hall sensors there are two possible ways: embedded on the stator or on the rotor. Embedding the Hall sensors into the stator is a complex process because any misalignment in these Hall sensors, with respect to the rotor magnets, will generate an error in determination of the rotor position. Since this might become a problem in motor control, Hall sensor unbalancing and misalignment is treated in literature and solution are proposed in [22–26] with very good results.

The motor for our application also suffers from Hall misalignment, information provided by comparison of the Hall signals versus the back-EMF shape [27]. After repeated measurements were done, a deviation of  $10^\circ$  was discovered. Having the Hall signals as sampled inputs in the system, the following equation was used to compensate for misalignment in terms of samples:

$$N = \frac{\pi}{18 \cdot \omega \cdot p \cdot T_s} \quad (4.14)$$

In the equation above,  $N$  is the number of samples for Hall misalignment correction,  $\omega$  is the mechanical speed in [rad/s],  $p$  is the number of pole pairs and  $T_s$  is the sample time in [s].

In the table below the Hall signals combination versus phase excitation for both positive (counterclockwise) and negative (clockwise) rotation direction is presented.

**Table 5.2 Hall signals versus phase excitation and sector**

Hall A	Hall B	Hall C	Sector	Counterclockwise (positive direction)			Clockwise (negative direction)		
				A	B	C	A	B	C
0	0	1	0	0	+	-	+	-	0
0	1	1	1	+	0	-	0	-	+
0	1	0	2	+	-	0	-	0	+
1	1	0	3	0	-	+	-	+	0
1	0	0	4	-	0	+	0	+	-
1	0	1	5	-	+	0	+	0	-

Hall sensors are used to obtain commutation information, from which we can derive the mechanical angle and speed. However, to properly control the motor, speed and/or current control are needed.

#### 4.5.4 Current and speed controllers

Proportional-integral (PI) control with hysteresis or Pulse Width Modulation (PWM) switching is the most widely used speed control technique for BLDC motors with trapezoidal back-EMF [28–30]. In fig.4.7 such closed loop control for BLDC motor it is shown, containing three PI controllers – position, speed and torque (current). For our application only two of the aforementioned are needed, namely the speed and current controller.

In fig.4.16 the simulation control block is shown.

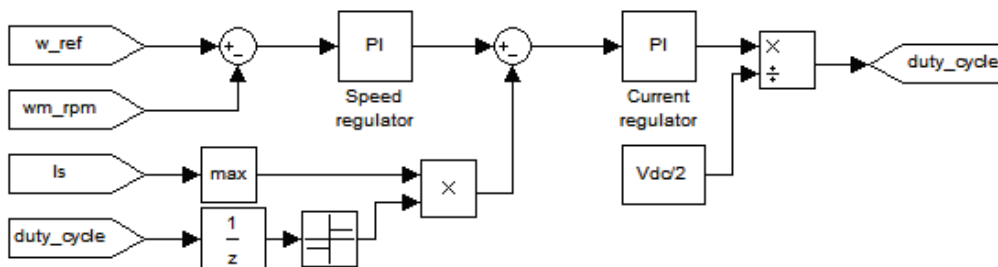


Fig.4.16 Speed and torque (current) control blocks

In fig.4.17 the detailed implementation of speed PI controller is shown. To tune the PI gains, Ziegler-Nichols method was used. From this method, the gain values obtained are:  $K_{pw}=0.0002$  [A/rpm] and  $K_{iw}=0.003$  [1/s]. The output of the speed controller is limited between  $-I_{max}$  and  $+I_{max}$ , where  $I_{max}$  is chosen as twice the value of  $I_n$ .

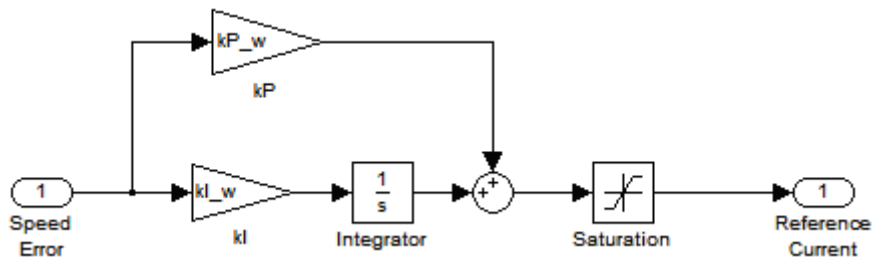


Fig.4.17 PI speed controller

The detailed implementation of the current PI controller is presented in fig.4.18. The controller gains were also calculated using Ziegler-Nichols method, and the results are:  $K_{pi}=15$  [V/A] and  $K_{ii}=4000$  [1/s]. The output of the current controller is limited between  $-0.5 \cdot V_{DC}$  and  $+0.5 \cdot V_{DC}$ .

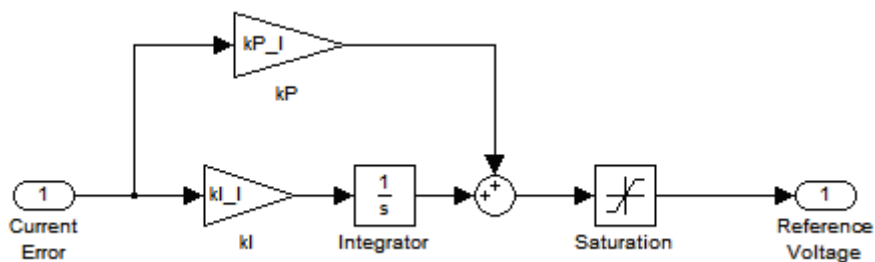


Fig.4.18 PI current controller

## 4.6 Simulation results and discussions

The dynamic simulation of the drive needs to be validated. In what follows, the most significant regimes of motor functioning will be tested i.e. motor acceleration up to different speeds (speed step), constant speed operation and load torque step.

In fig.4.19 the phase currents, back-EMF, torque, speed, position and Hall signals are shown for the motor accelerating to 7500 [rpm] and then running at constant speed. The load torque varies with speed and reaches 0.0475 [Nm] at prescribed speed.

In fig.4.20 the phase currents, back-EMF, torque, speed, position and Hall signals are shown for the motor accelerating to 15000 [rpm] and then running at constant speed. The load torque varies with speed and reaches 0.095 [Nm] at nominal speed.

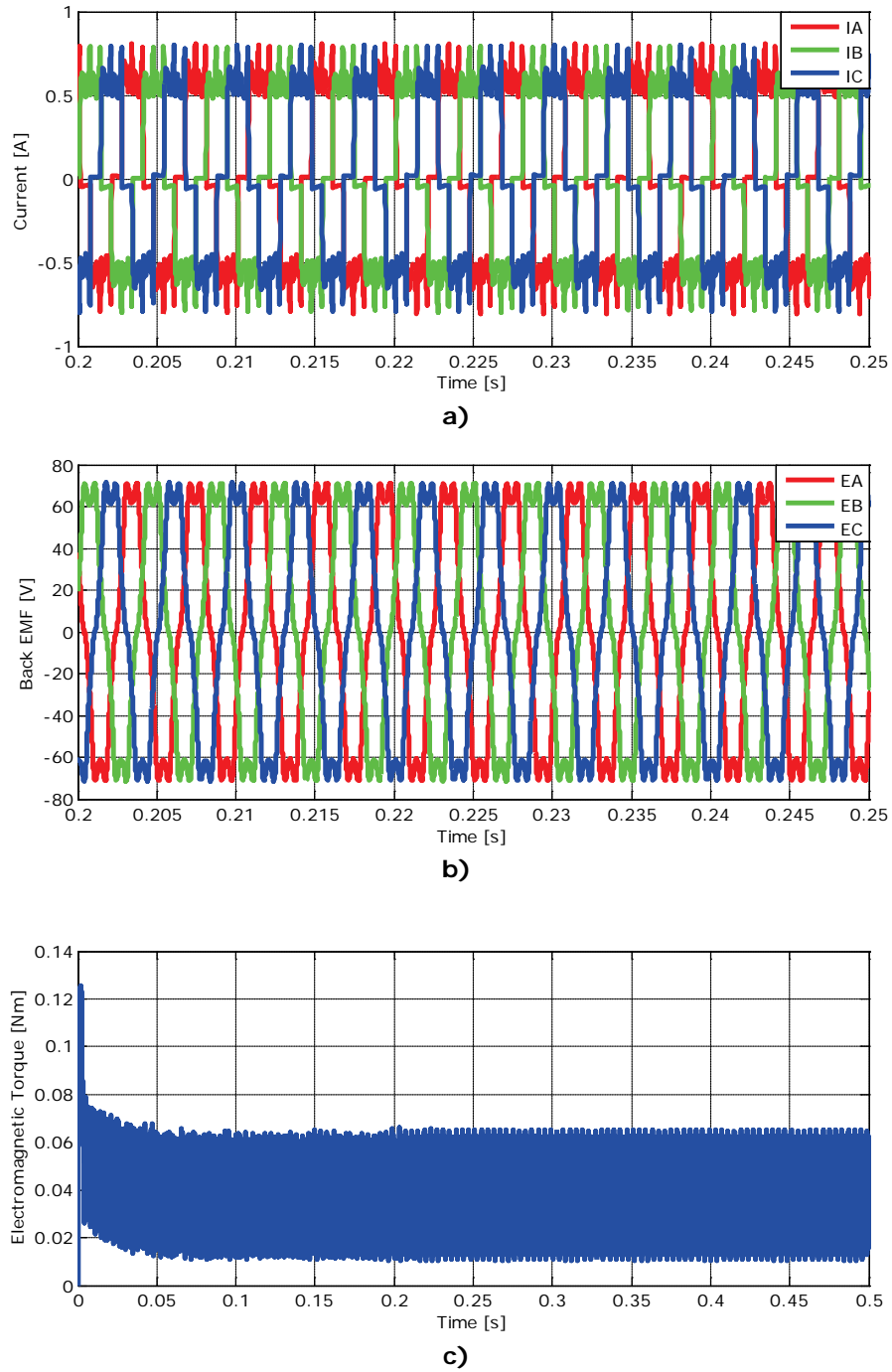
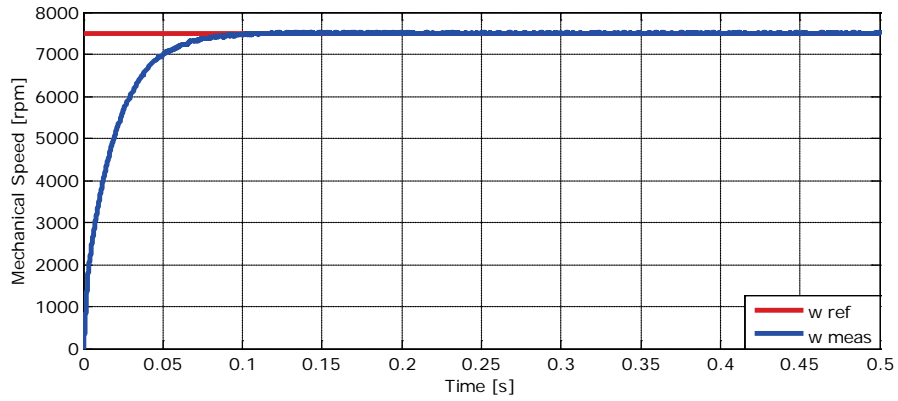
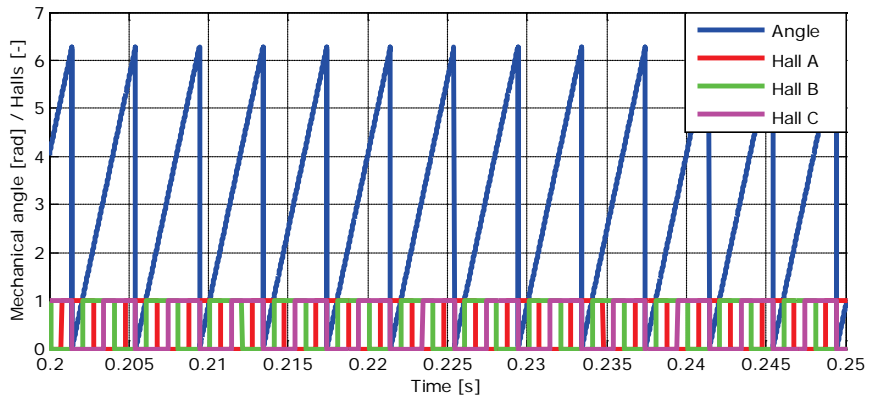


Fig.4.19 (continued)

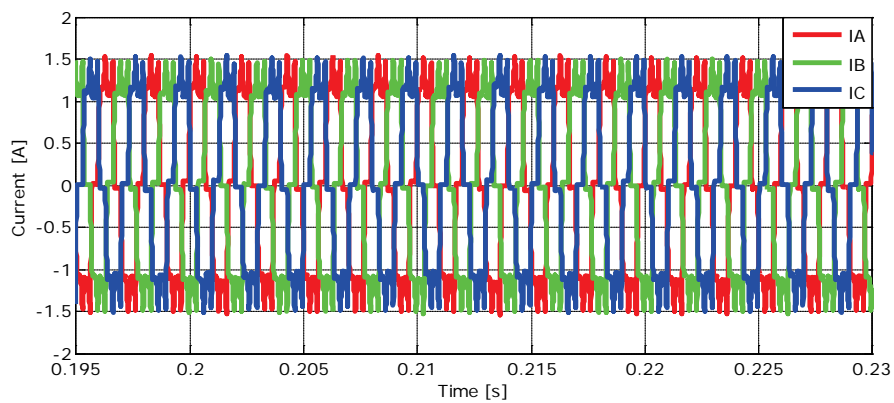


d)



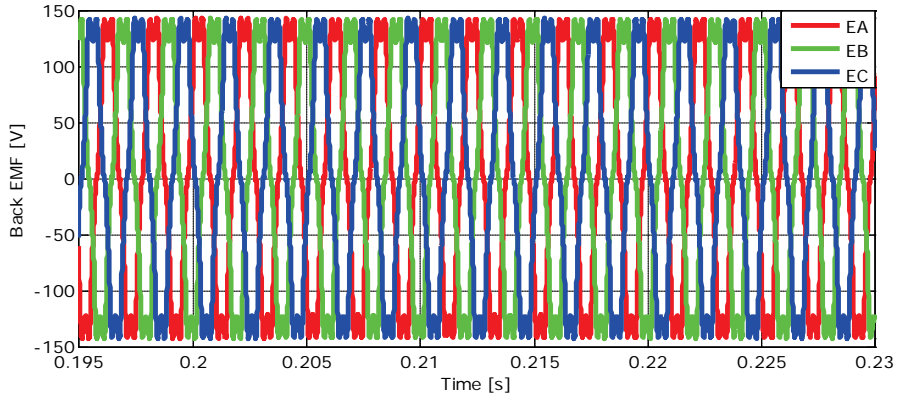
e)

Fig.4.19 7500 [rpm] and 0.0475 [Nm] with closed-loop control: a) phase currents, b) phase back-EMFs, c) torque, d) speed and e) rotor position versus Hall signals

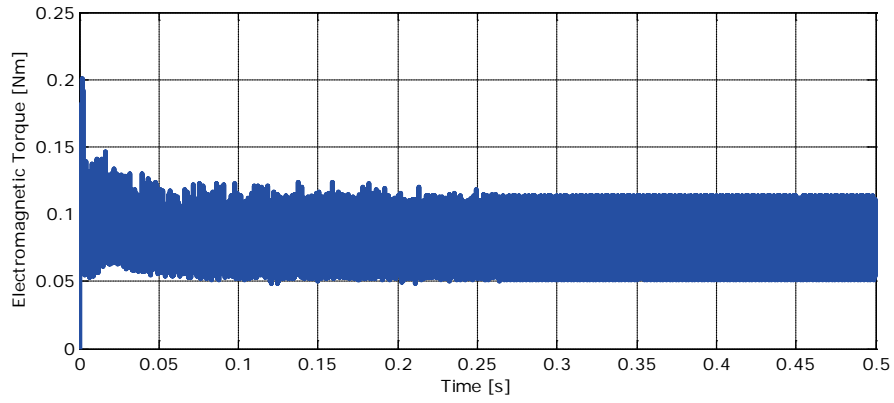


a)

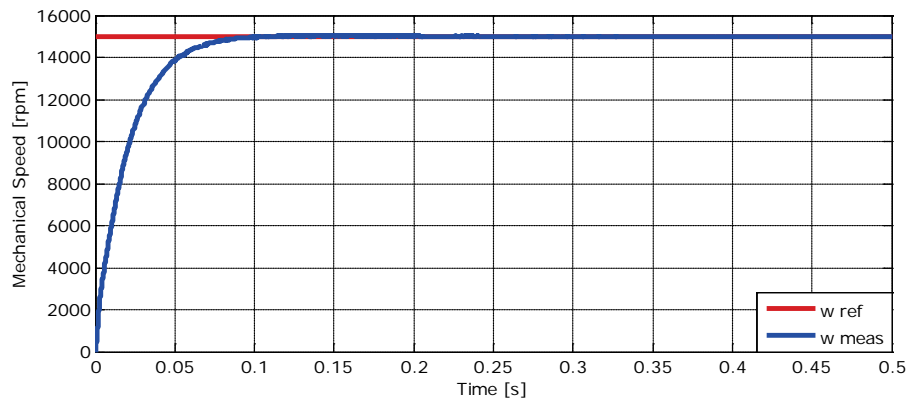
Fig.4.20 (continued)



**b)**



**c)**



**d)**

Fig.4.20 (continued)

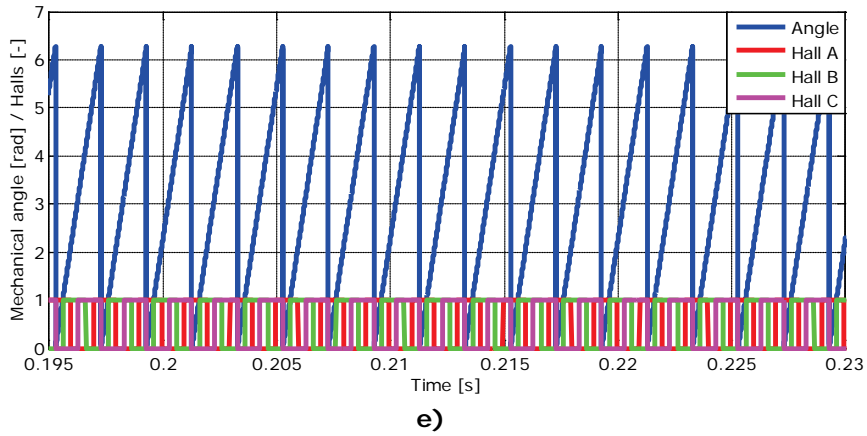


Fig.4.20 15000 [rpm] and 0.095 [Nm] with closed-loop control: a) phase currents, b) phase back-EMFs, c) torque, d) speed and e) rotor position versus Hall signals

In fig.4.21 the phase A current, torque and speed are shown for the motor running at 15000 [rpm]. The load torque will step from 0.095[Nm] to 0.0475[Nm] at 0.2[s] and back to 0.095[Nm] at 0.3[s].

In fig.4.22 the phase A current, phase A back-EMF and motor speed will be shown for motor acceleration from 7500 [rpm] to 15000 [rpm].

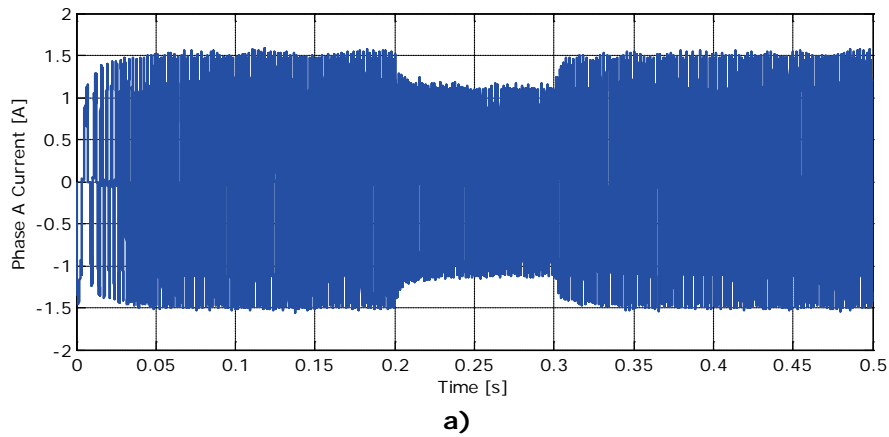
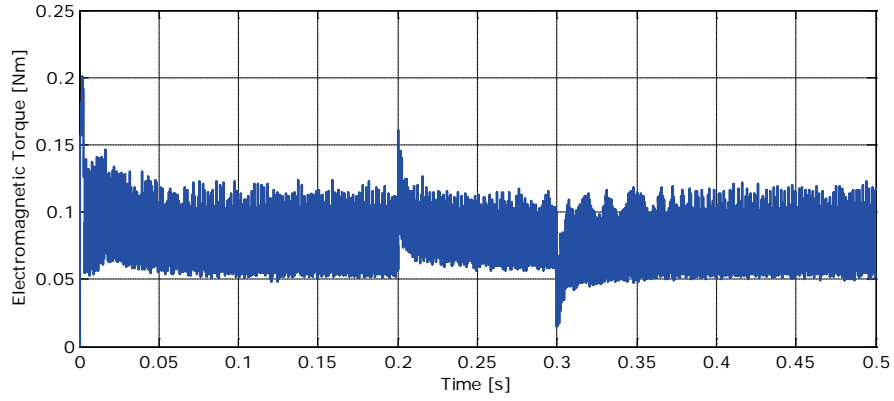
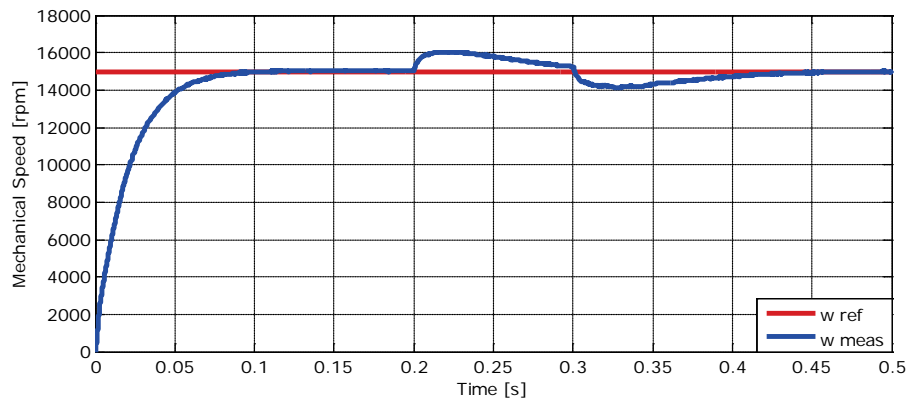


Fig.4.21 (continued)



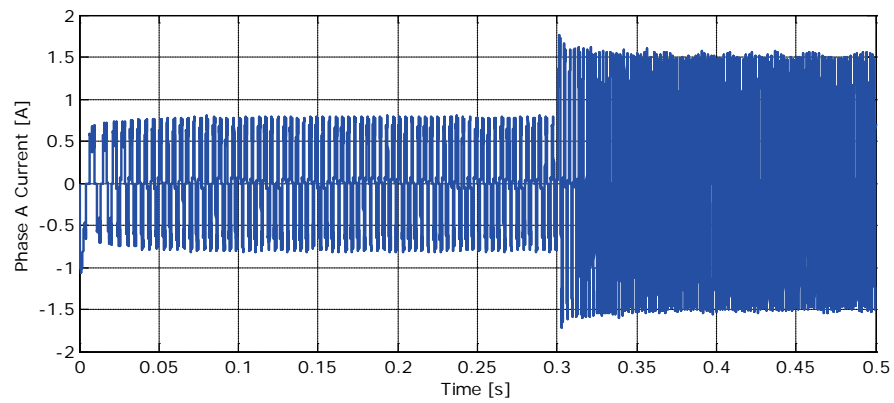


**b)**



**c)**

Fig.4.21 Load changes from 0.095[Nm] to 0.0475[Nm] at 0.2[s] and back to 0.095[Nm] at 0.3[s]: a) phase A current, b) electromagnetic torque and c) speed



**a)**

Fig.4.22 (continued)

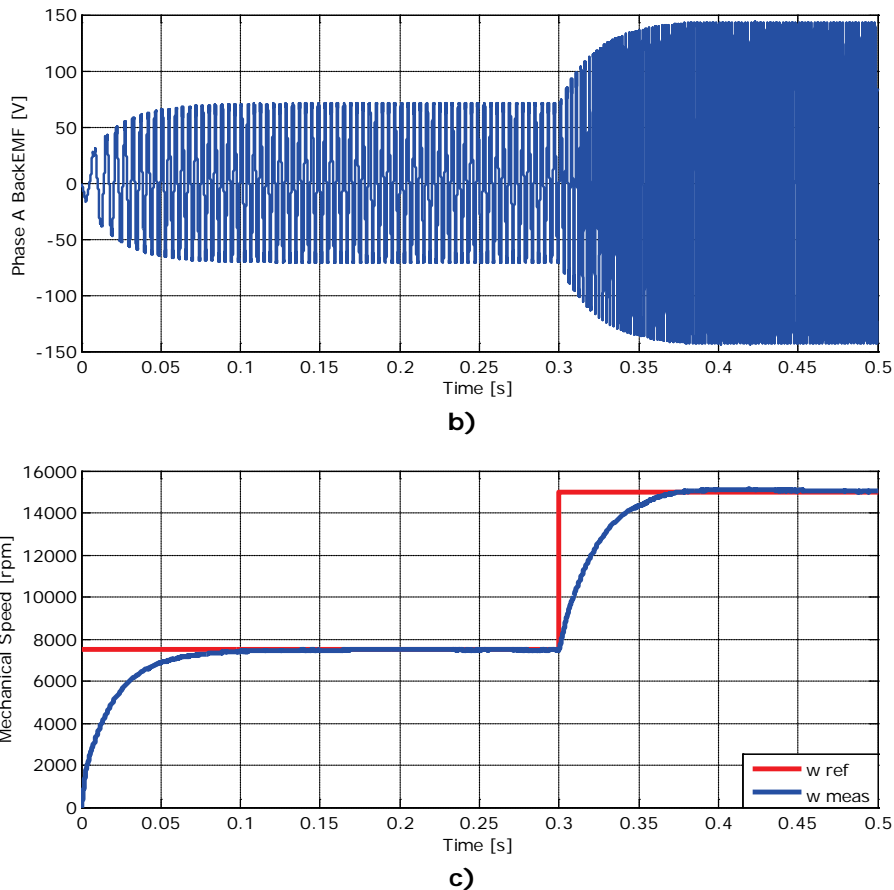


Fig.4.22 Acceleration from 7500[rpm] to 10000[rpm]: a) phase A current, b) phase A back-EMF, c) mechanical speed

## 4.7 Conclusion

The purpose of this chapter was to develop a simulation model for BLDC taking into account the commutation phenomenon. The advanced simulation model was created to emulate as real as possible the actual drive, inverter and motor. It offers the possibility to anticipate control issues and motor limitations, especially for worst case scenarios without the need of using the actual motor. This opportunity helps preventing motor damage by improper control or forcing it beyond its limits. To have a closer-to-reality simulation, back-EMFs were implemented from finite element analysis in previous chapter as look-up tables. Whole drive was simulated in Matlab®/Simulink®, as it is easier to transfer the control, after its development, to dSpace platform for experimental tests. The advanced model presented above will be used in the following chapter for the implementation of sensorless control techniques.

---

## References

- [1] Bimal K. Bose, "Modern power electronics and AC drives", book, Prentice Hall PTR, Prentice Hall Inc., Upper Saddle River, New Jersey, 2002
- [2] Ion Boldea and Syed A. Nassar, "Electric Drives", book, 2<sup>nd</sup> edition, CRC Press, Taylor & Francis Group LLC, Boca Raton, Florida, 2005
- [3] Ramu Krishnan, "Permanent Magnet Synchronous and Brushless DC Motor Drives", book, CRC Press, Taylor & Francis Group LLC, Boca Raton, Florida, 2010
- [4] Hamid A. Toliyat and T. Gopalarathnam, "AC machines controlled as DC machines (Brushless DC machines/Electronics)", Chapter 10 in "The power electronics handbook", J.D. Irwin, CRC Press LLC, Boca Raton, Florida, 2002
- [5] Jacek F. Gieras, "Permanent Magnet Motor Technology – Design and Applications", book, 3<sup>rd</sup> edition, CRC Press, Taylor & Francis Group LLC, Boca Raton, Florida, 2010
- [6] S. Baris Ozturk, "Modelling, simulation and analysis of low-cost direct torque control of PMSM using Hall-effect sensors", Master Thesis, Texas A&M University, 2005
- [7] Stefån Baldursson, "BLDC motor modeling and control – A Matlab®/Simulink® implementation", Master Thesis, Chalmers Tekniska Högskola, May 2005
- [8] Pragasen Pillay and Ramu Krishnan, "Modeling, simulation, and analysis of permanent-magnet motor drives, part II: the brushless DC motor drive", *IEEE Trans. on Ind. Appl.*, vol.25, no.2, pp.274–279, March/April 1989
- [9] E.P. Weichmann, P.D. Ziogas and V.R. Stefanović, "Generalized functional model for three-phase PWM inverter/rectifier converters", *IEEE Trans. on Ind. Appl.*, vol.IA-23, no.2, pp.236–246, March/April 1987
- [10] P.D. Ziogas, E.P. Weichmann and V.R. Stefanović, "A computer-aided analysis and design approach for static voltage source inverters", *IEEE Trans. on Ind. Appl.*, vol.IA-21, no.5, pp.1234–1241, March/April 1985
- [11] L. Salazar and G. Joós, "PSPICE simulation of three-phase inverters by means of switching functions", *IEEE Trans. on Power Electronics*, vol.9, no.1, pp.35–42, January 1994
- [12] Byoung-Kuk Lee and Mehrdad Ehsani, "A simplified functional simulation model for three-phase voltage-source inverter using switching function concept", *IEEE Trans. on Ind. Electronics*, vol.48, no.2, pp.309–321, April 2001
- [13] Byoung-Kuk Lee and Mehrdad Ehsani, "Advanced simulation model for brushless DC motor drive", *Electric Power Components and Systems*, vol.31, no.9, pp.841–868, September 2003
- [14] Q. Han, N. Samoylenko and J. Jatskevich, "Average-value modeling of brushless DC motors with 120° voltage source inverter", *IEEE Trans. on En. Conversion*, vol.23, no.2, pp.423–432, June 2008
- [15] K. Tabarraee, J. Iyer and J. Jatskevich, "Average-value modeling of brushless DC motors with trapezoidal back-EMF", *Proc. of 20<sup>th</sup> IEEE Intl. Symposium on Ind. Electronics (ISIE '11)*, pp.531–537, June 2011
- [16] W. Hong, W. Lee and B.-K. Lee, "Dynamic simulation of brushless DC motor drives considering phase commutation for automotive applications", *Proc. of Intl. Conf. on Electric Motors and Drives (IEMDC 2007)*, vol.2, pp.1377–1383, May 2007

- [17] Y.S. Jeon et al., "A new simulation model of BLDC motor with real back EMF waveform", *The 7<sup>th</sup> Workshop on Computers in Power Electronics (COMPEL 2000)*, pp.217–220, July 2000
- [18] Tingna Shi et al., "A new approach of minimizing commutation torque ripple for brushless DC motor based on DC–DC converter", *IEEE Trans. on Ind. Electronics*, vol.57, no.10, pp.3483–3490, October 2010
- [19] Todd D. Batzel and Kwang Y. Lee, "Commutation torque ripple minimization for permanent magnet synchronous machines with Hall effect position feedback", *IEEE Trans. on En. Conversion*, vol.13, no.3, pp.257–262, September 1998
- [20] Bilal Akin and Manish Bhardwaj, "Trapezoidal Control of BLDC Motors Using Hall Effect Sensors", Application Note, Texas Instruments, Ver. 1.0, February 2010
- [21] F. Giulii Capponi et al., "AC brushless drive with low resolution Hall-effect sensors for an axial flux PM machine", *Conf. Rec. of the 2004 IEEE 39<sup>th</sup> Ind. Appl. Conf. (IAS 2004)*, vol.4, pp.2382–2389, October 2004
- [22] C. Zwysig, S.D. Round and J.W. Kolar, "Power electronics interface for a 100W, 500000 rpm gas turbine portable power unit", *Proc. of 21<sup>th</sup> Annual Applied Power Electronics Conf. (APEC 2006)*, pp.283–289, March 2006
- [23] P.B. Beccue et al., "Compensation for asymmetries and misalignment in a Hall-effect position observer used in PMSM torque-ripple control", *IEEE Trans. on Ind. Appl.*, vol.43, no.2, pp.560–570, March/April 2007
- [24] N. Samoylenko, Q. Han and J. Jatskevich, "Balancing hall-effect signals in low-precision brushless DC motors", *Proc. of 22<sup>nd</sup> Annual Applied Power Electronics Conf. (APEC 2007)*, pp.606–611, February/March 2007
- [25] N. Samoylenko, Q. Han and J. Jatskevich, "Dynamic performance of brushless DC motors with unbalanced Hall sensors", *IEEE Trans. on En. Conversion*, vol.23, no.3, pp.752–763, September 2008
- [26] P. Alaeinovin and J. Jatskevich, "Hall-Sensor signals filtering for improved operation of brushless DC motors", *Proc. of 20<sup>th</sup> IEEE Intl. Symposium on Ind. Electronics (ISIE '11)*, pp.613–618, June 2011
- [27] -, "Brushless DC Hall effect sensor configuration", Chapter 7 in "PMD motion processors" App. Notes, rev.1.0, Performance Motion Devices Inc., pp.69–79, June 2005
- [28] Piyush C. Desai and Ali Emadi, "A novel digital control technique for brushless DC motor drives: current control", *2005 IEEE Intl. Conf. on Electric Machines and Drives*, pp.326–331, May 2005
- [29] H. Lu, L. Zhang and W. Qu, "A new torque control method for torque ripple minimization of BLDC motors with un-ideal back-EMF", *IEEE Trans. on Power Electronics*, vol.23, no.2, pp.950–958, March 2008
- [30] Anand Sathyan et al, "An FPGA-based novel digital PWM control scheme for BLDC motor drives", *IEEE Trans. on Ind. Electronics*, vol.56, no.8, pp.3040–3049, August 2009

## Chapter 5

# Sensorless control of BLDC with instantaneous active power observer and I-f starting method, with experiments

### Abstract

Previous chapter presented the design of the closed loop control, validated with position sensor feedback. This chapter proposes a new sensorless technique based on instantaneous active power, which is calculated from the measured phase currents and voltages. From the mechanical equation of the motor and knowing that load torque is proportional to speed in refrigerator compressors, an equation that estimates motor mechanical speed from the instantaneous active power is derived.

For motor starting a robust method is used, i.e. I-f technique. Simulation model is developed to integrate both the starting method and the sensorless technique and experimental results are shown in order to validate their robustness.

### 5.1 Introduction

Hall sensors provide reliable information and are extensively used in numerous applications that are BLDC based. However, alternatives were sought since BLDC motors started to become popular, mainly in low cost applications and the ones that perform in harsh environments.

In Chapter 2 optimal design of the motor was performed. Since the aim of the application was to develop a low cost motor, the best price obtained in respect to the constraints was around 19\$. The average price for 3 Hall sensors varies from 1\$ to 3\$ so their cost becomes a problem. A sensorless method makes use of the electrical parameters of the motor, mainly, but not limited to, phase currents and phase voltages. The first ones can be measured using simple shunts, while the latter ones can be calculated by measuring only the DC voltage and knowing the switching states. In order to implement a simple sensorless technique, one can use the microcontroller that is inherent in the drive to control the inverter MOSFET or IGBT gates. Thus the extra costs are reduced.

Extensive reviews of known and well established sensorless techniques are presented in [1 – 4]. The majority of these techniques rely on estimating rotor position from voltage and current measurements in different configurations. Although many

combinations were tried, for a wide range of applications or for particular situations, state of the art in sensorless methods can be split into three distinct categories: back-EMF based, inductance based or flux linkage based.

In order to replace the position sensors, one thing is certain: for this type of motor, with trapezoidal current control, the rotor position information is needed only at the commutation points, every  $60^\circ$  electrical in the three phase machine [3]. The motion of the rotor causes back-EMF, making it dependent on rotor position. Also, inductance is dependent on rotor position in salient motors and the combination of both strongly influence the machine current and voltage waveforms. This fact lies at the base of sensorless techniques, using the aforementioned signals to extract the back-EMF, the inductance or a combination of these two and estimate the position.

The first sensorless category is based on back-EMF detection, namely back-EMF zero crossing (similar to Hall sensor commutation detection) and third harmonic sensing [5 – 12]. The first method relies on zero crossing of the back-EMF, although they not correspond to the rotor position where commutation between phases should take place. As a consequence, the signals must be shifted by  $90^\circ$  electrical before they can be used for commutation. Also, the sensorless mode can start only from a certain speed threshold [12], as back-EMF is speed dependent and thus useless at low speeds. For that open-loop starting is used from standstill and then switch to back-EMF zero crossing when the speed threshold is attained. Third harmonic sensing technique reduces the phase shifting problem by providing an additional star connection of three identical resistors connected between phase ends and neutral point.

Second category is based on inductance variation by monitoring rates of change of winding current. Since the rate of current change depends on the inductance of the winding, and this inductance is a function of rotor position and winding current, then rotor position can be deduced from winding current and its rate of change [3]. However this method is quite complicated and problematic, mainly due to position ambiguity.

The third category is based on flux linkage variation, with and without a mechanical model [3, 13 – 18]. The flux linkage is obtained by subtracting the resistive voltage drop from the phase voltage and integrating. Since integrating is prone to errors caused by drift, the pure integrator is usually replaced by a low pass filter or by closed-loop flux linkage estimation.

Alternate methods were developed, observer-based [19 – 22] or adaptation of sinusoidal sensorless techniques, like Direct Torque Control [23], Direct Torque and Indirect Flux Control [24] or Model Reference Adaptive Systems [25, 26]. With latest increase in microcontroller's processing power, FEM based flux linkage position observers with stored look-up tables [27, 28] were developed.

In what follows, a novel sensorless method with instantaneous active power estimation is designed and analyzed. A robust starting method, I-f technique, is used together with the above mentioned observer as an ensemble of sensorless control for BLDC refrigerator compressors. Simulation results together with experimental results validate the novel method.

## 5.2 Instantaneous active power observer

In this sub-chapter, a new speed and position observer is presented and its functionality analyzed. Starting from the mechanical equation of the motor, a dependency of motor power to the speed is obtained. Using only the measured phase currents and voltages and knowing machine parameters like phase resistance, inertia and viscous friction factor, a formula for mechanical speed is derived.

The first one who used instantaneous active and reactive powers for power compensators in three phase systems was Hirofumi Akagi in 1984 [30] and perfected [31 – 34] for n-phase systems. Reactive power based control loops have been used in PMSM and BLDC control in [35 – 38], while active and reactive power PLLs have been developed for three phase systems [39 – 41].

To use instantaneous active power in control, transformation from a-b-c coordinates to stator reference frame is needed.

$$\begin{bmatrix} X_\alpha \\ X_\beta \end{bmatrix} = \sqrt{\frac{2}{3}} \cdot \begin{bmatrix} 1 & -\frac{1}{2} & -\frac{1}{2} \\ 0 & \frac{\sqrt{3}}{2} & -\frac{\sqrt{3}}{2} \end{bmatrix} \cdot \begin{bmatrix} X_a \\ X_b \\ X_c \end{bmatrix} \quad (5.1)$$

In the formula above X represents any electrical parameter of the motor, current, voltage or back-EMF.

The instantaneous active power in a BLDC can be expressed in stator reference frame as:

$$P = \frac{3}{2} \cdot p \cdot (V_\alpha \cdot I_\alpha + V_\beta \cdot I_\beta) \quad (5.2)$$

where  $p$  denotes the number of machine's pole pairs.

Copper losses due to passing of the current in the coils in the reference frame are written as:

$$P_{loss} = \frac{3}{2} \cdot p \cdot R_s \cdot I^2 \quad (5.3)$$

The electromagnetic torque's expression in stator reference frame is:

$$T_e = \frac{3}{2} \cdot p \cdot \frac{(E_\alpha \cdot I_\alpha + E_\beta \cdot I_\beta)}{\omega_r} \quad (5.4)$$

Introducing expressions (5.2) and (5.3) in equation (5.4), the electromagnetic torque as function of power and mechanical speed is written as:

$$T_e \approx \frac{P - P_{loss}}{\omega_r} \quad (5.5)$$

The load torque can be represented also as a function of power and speed:

$$T_L = \frac{P_L}{\omega_r} \quad (5.6)$$

The mechanical equation of the motor is:

$$T_e - T_L = J_r \cdot \frac{d\omega_r}{dt} + B \cdot \omega_r \quad (5.7)$$

Introducing (5.5) and (5.6) in (5.7) we get the following expression:

$$\frac{P - P_{loss}}{\omega_r} - \frac{P_L}{\omega_r} = J_r \cdot \frac{d\omega_r}{dt} + B \cdot \omega_r \quad (5.8)$$

If we separate the powers and mechanical speed, we obtain a second degree equation of the speed:

$$\frac{P - P_{loss} - P_L}{\omega_r} = J_r \cdot s \cdot \omega_r + B \cdot \omega_r \quad (5.9)$$

$$P - P_{loss} - P_L = J_r \cdot s \cdot \omega_r^2 + B \cdot \omega_r^2 \quad (5.10)$$

Below, a general expression of the mechanical speed as a function of power is obtained:

$$\omega_r = \sqrt{(P - P_{loss} - P_L) \cdot \frac{1}{J_r \cdot s + B}} \quad (5.11)$$

If we consider the load torque proportional to the speed with a load factor  $k_L$ , equation (5.6) becomes:

$$P_L = k_L \cdot \omega_r \quad (5.12)$$

Introducing (5.12) in (5.11) the mechanical speed's expression becomes:



$$\omega_r = \sqrt{(P - P_{loss}) \cdot \frac{1}{J_r \cdot s + (B + k_L)}} \quad (5.13)$$

Once the mechanical speed is obtained, the mechanical angle is found by integrating the speed.

$$\theta_r = \int \omega_r \cdot dt \quad (5.14)$$

The block diagram of the proposed speed and position observer is shown below in Fig.5.1.

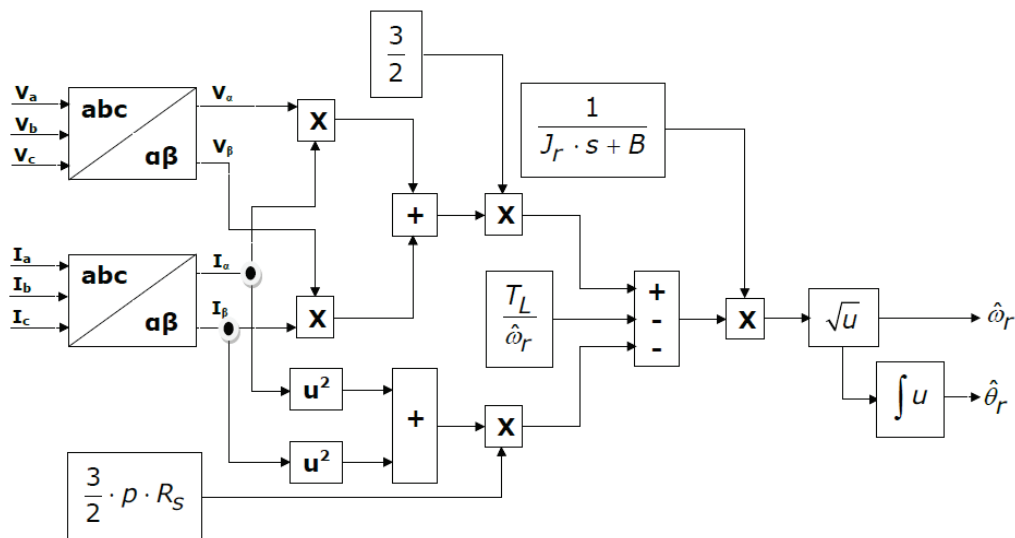


Fig.5.1 Block diagram of the proposed power based position and speed observer

The sensorless method makes use of the measured signals like phase currents and voltages and known motor parameters like phase resistance, inertia and viscous friction. Thus, its complexity is reduced and can be easily implemented in a cheap microcontroller.

### 5.3 I-f starting method

The need for a starting method appeared since the majority of the sensorless methods for BLDCs are not reliable at low speeds. The most known starting methods are inductance variation and "align and go". Since starting under heavy load conditions is mandatory in this case, a robust starting method without initial position detection is used, i.e. I-f starting technique.

Previously used with success in both BLDC [27, 28] and BLAC [29] sensorless controls, I-f start-up strategy is to ramp-up the stator current frequency to a pre-defined level, while keeping the amplitude of the current constant by the current controller [27].

The ramp-up period of the current frequency must be finite so a time variation ramp function of the frequency must be chosen.

$$f^* = \begin{cases} f_{\max}^* \cdot \sin^2(\omega_f \cdot t_f), & \omega_f \cdot t_f \leq \frac{\pi}{2} \\ f_{\max}^*, & \omega_f \cdot t_f > \frac{\pi}{2} \end{cases} \quad (5.15)$$

$$\omega_f \cdot t_f = \frac{\pi}{2} \Rightarrow 2 \cdot \pi \cdot f_f \cdot t_f = \frac{\pi}{2} \Rightarrow f_f = \frac{1}{4 \cdot t_f} \quad (5.16)$$

In equation above,  $t_f$  is the time period of the reference frequency ramp. From the current frequency, a current reference angle is calculated with the following formula:

$$\theta_{I-f} = \int 2 \cdot \pi \cdot f^* dt \quad (5.17)$$

## 5.4 Transition strategies

### 5.4.1 I-f to sensorless smooth transition

As I-f control is meant to be used only at low speeds, two speed thresholds must be defined – one at start-up, going from I-f to sensorless, and another one when motor is decelerated, going from sensorless to I-f. Since the estimated value of the angle and the reference angle from I-f technique will not be equal the sudden transition might lead in motor vibrations and loss of control. To avoid this, a smooth transition must be implemented. Subsequently, there will be three distinct regions of operation.

First region uses the angle calculated with relation (5.18) up to a certain frequency value denoted with  $f_{min}$ . Once this threshold is reached, a transition period will start and the angle will be calculated with the following formula until  $f^* > f_{max}$ :

$$\theta = (1 - k) \cdot \theta_{I-f} + k \cdot \hat{\theta} \quad (5.18)$$

In the above equation, factor  $k$  is determined with equation (5.19). Equation (5.18) can be a general form if we consider  $k$  equal to 0 when  $f^* < f_{min}$  and  $k$  equal to 1 when  $f^* > f_{max}$ .

$$k = \frac{\left| f^* \right| - f_{\min}}{f_{\max} - f_{\min}} \quad (5.19)$$

Below, the value of the control angle throughout all three regions is summarized.

$$\theta = \begin{cases} \theta_{I-f}, & \left| f^* \right| < f_{\min} \\ \theta_{I-f} + k \cdot \sin(\hat{\theta} - \theta_{I-f}), & f_{\min} \leq \left| f^* \right| \leq f_{\max} \\ \hat{\theta}, & \left| f^* \right| > f_{\max} \end{cases} \quad (5.20)$$

#### 5.4.2 Sensorless to I-f transition

The inverse transition, from sensorless control to I-f takes place once a threshold is reached, denoted as  $f_{\min I-f}$ . This value is usually different than previous thresholds. The angle value is calculated with equation (5.17) with initial condition of the integrator set to be equal with the last value of the estimated angle value, leading to the following relation:

$$\theta_{I-f1} = \int 2 \cdot \pi \cdot f^* dt + \hat{\theta} \quad (5.17)$$

Below, a graphical representation of both transition cases is presented with different control areas highlighted.

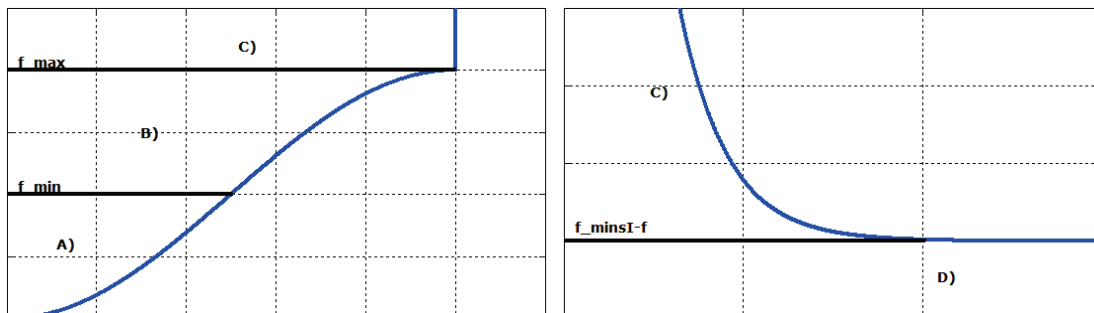


Fig.5.2 Control strategy separation: A) pure I-f control; B) I-f transition to sensorless; C) sensorless control and D) sensorless transition to I-f

## 5.5 Simulation results

The power based observer was first implemented in Matlab®/Simulink® to check its robustness.

In fig.5.3, the motor runs in sensorless mode at 7500 [rpm]. The phase A current,  $\alpha$ - $\beta$  currents,  $\alpha$ - $\beta$  voltages, calculated electrical and mechanical powers, mechanical speeds (reference, measured and estimated), speed error between measured and estimated values, estimated and measured angles and their error are shown. Load torque is 0.0475 [Nm].

Fig.5.4 presents the same waveforms as above but for motor running at nominal speed of 15000 [rpm] and loaded with 0.095 [Nm].

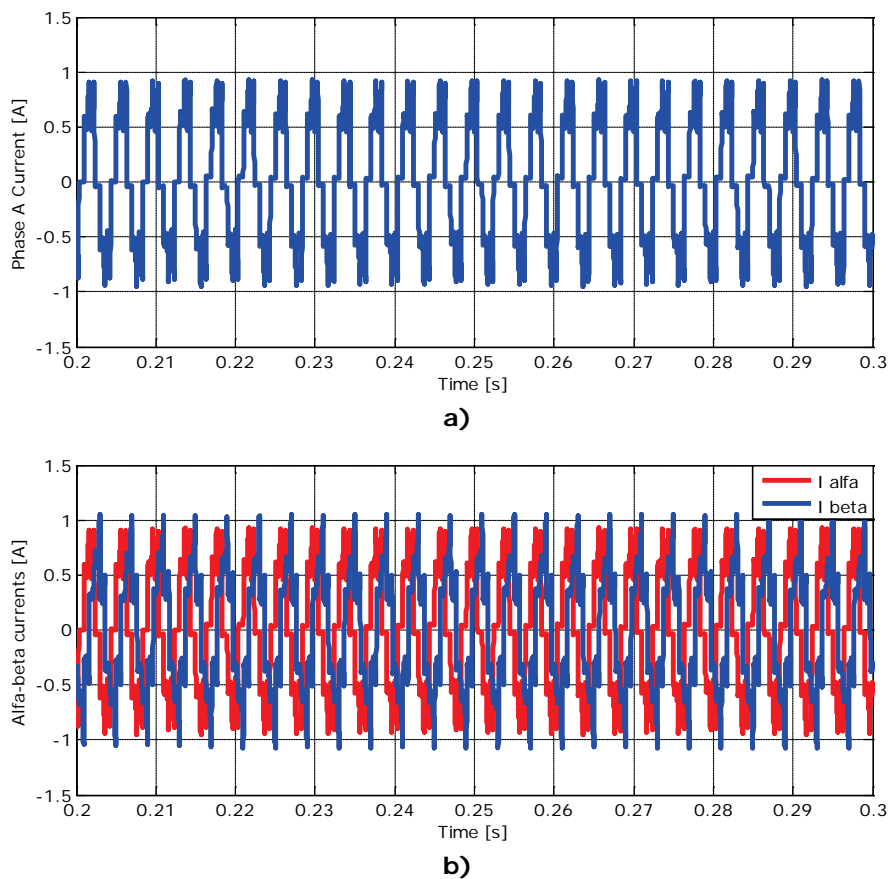
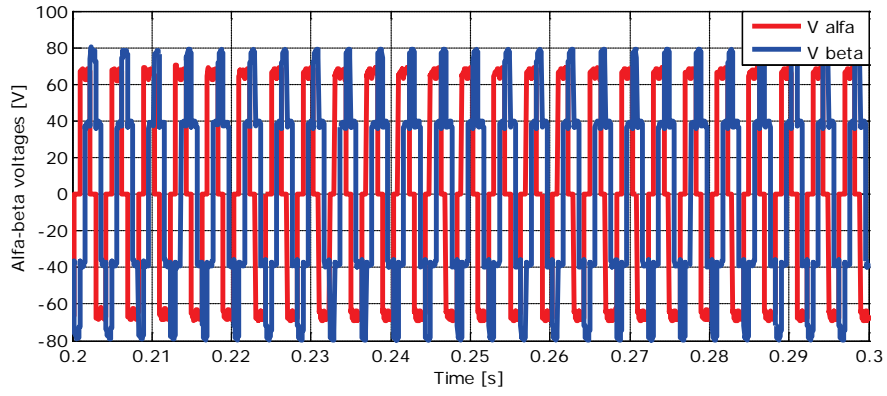
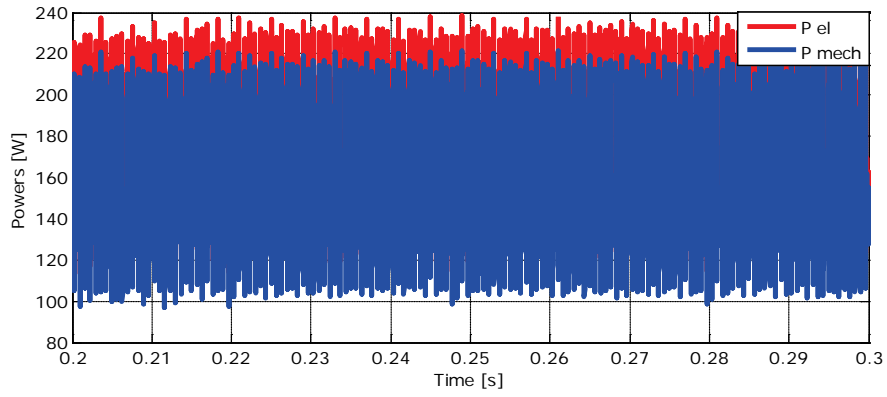


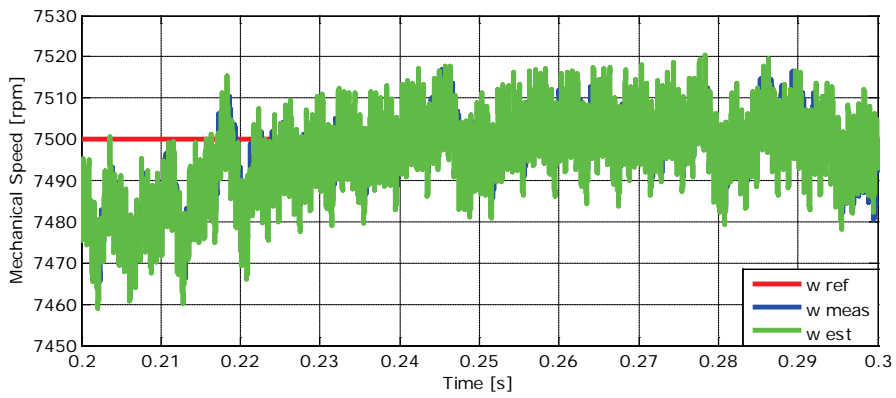
Fig.5.3 (continued)



c)



d)



e)

Fig.5.3 (continued)

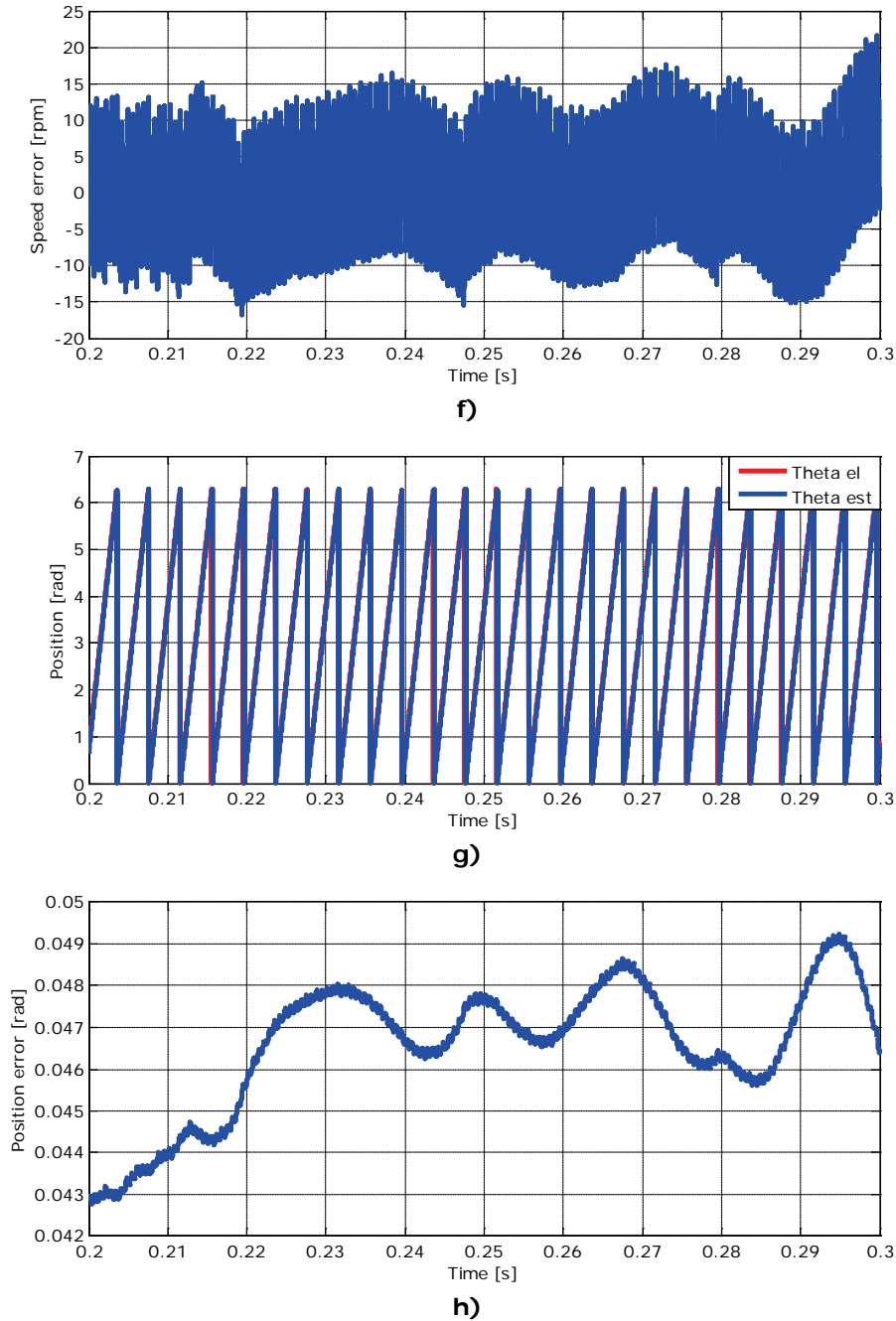


Fig.5.3 Simulation results of the proposed power based speed and position observer at 7500 [rpm] and 0.0475 [Nm] load: a) phase A current, b)  $\alpha$ - $\beta$  currents, c)  $\alpha$ - $\beta$  voltages, d) calculated electrical and mechanical powers, e) mechanical speeds, f) speed error, g) estimated and measured positions and h) position error

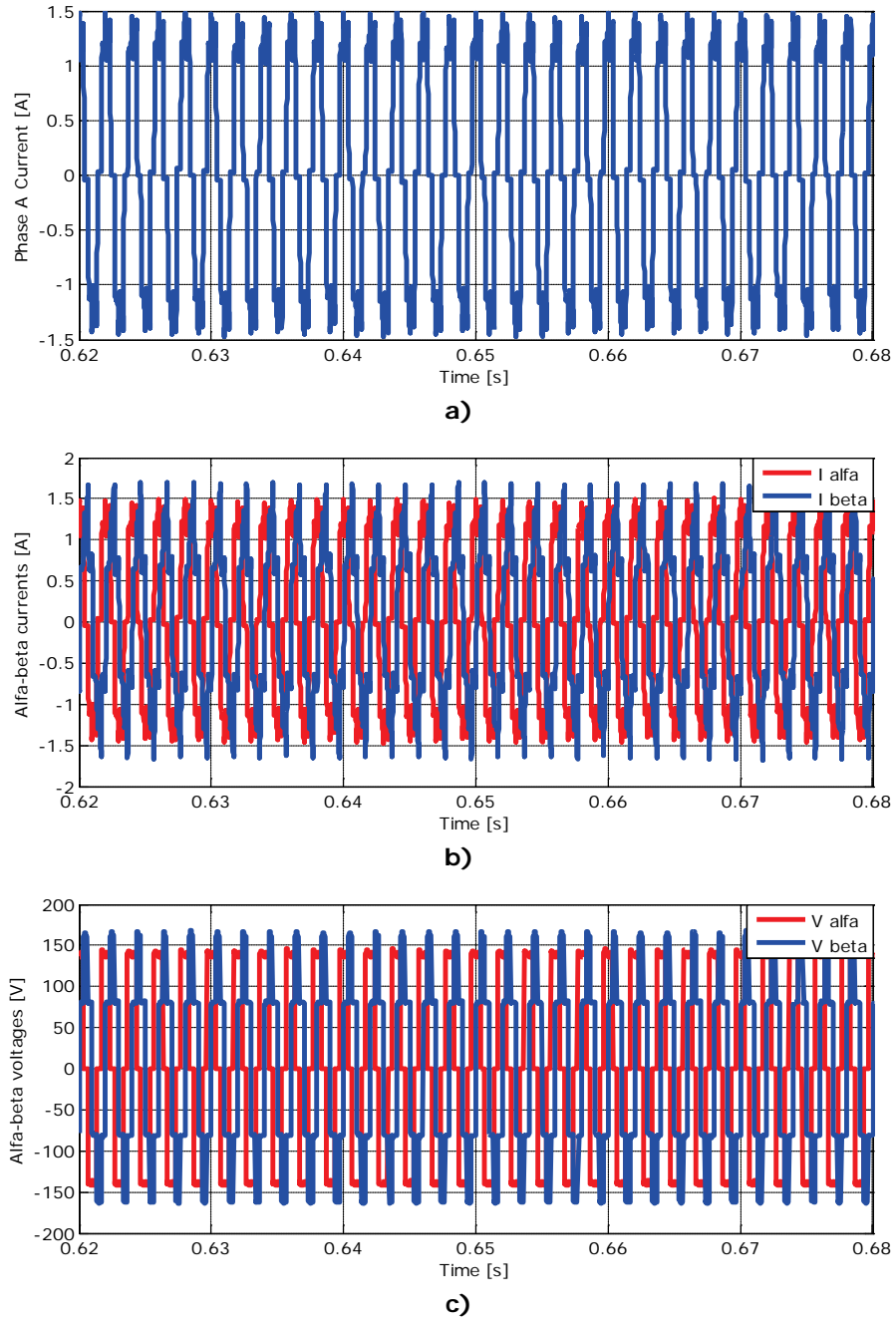


Fig.5.4 (continued)

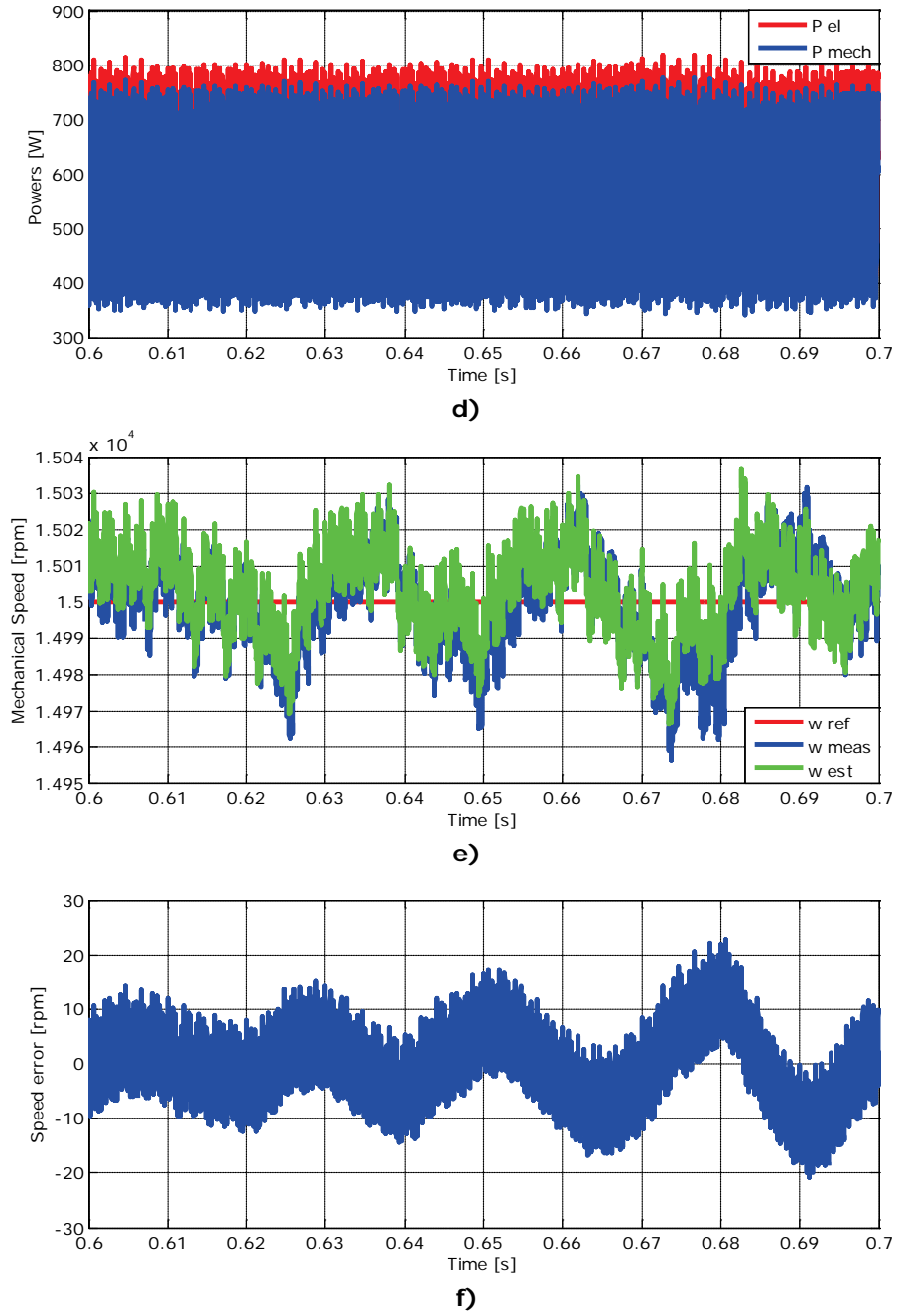


Fig.5.4 (continued)



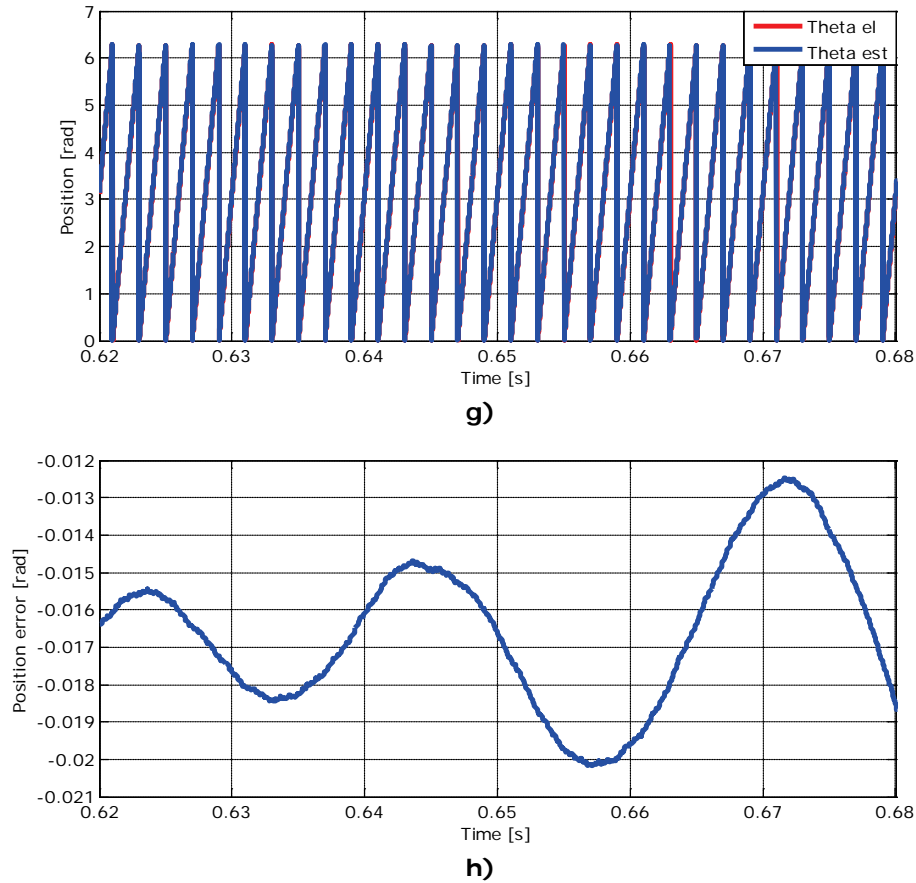


Fig.5.4 Simulation results of the proposed power based speed and position observer at 15000 [rpm] and 0.095 [Nm] load: a) phase A current, b)  $\alpha$ - $\beta$  currents, c)  $\alpha$ - $\beta$  voltages, d) calculated electrical and mechanical powers, e) mechanical speeds, f) speed error, g) estimated and measured angles and h) position error

Simulation results show satisfactory results. The speed and angle errors have acceptable values, thus proving the robustness and reliability of the proposed speed and position observer. Further, experimental results are presented to validate the observer in a drive.

## 5.6 Experimental results

Experiments were performed to validate the power based observer functionality and to prove that the sensorless algorithm is reliable during operation. The tests took place on a test bench, whose setup contains a surface PM BLDC motor loaded with a twin generator. To control the drive, a dSpace type platform was used and sensor

signals (currents and voltage) were acquired by means of a sensor board. Hall signals were used to calculate the motor speed for comparison purposes.

Fig.5.5 presents the overall system block diagram of the proposed sensorless drive. Two phase current signals are measured and the third one is calculated. Although phase voltages can be measured, due to cost and isolation issues only DC voltage is acquired and phase voltages are calculated from it and the known switching status. Speed and current controllers use the same values for their proportional and integral coefficients as calculated in the previous chapter.

Experiments include constant speed operation at 6000 [rpm] and 10000 [rpm] due to inverter limitations, acceleration from 6000 [rpm] to 10000 [rpm] and deceleration from 10000 [rpm] to 6000 [rpm]. In all tests the load torque is proportional to the speed.

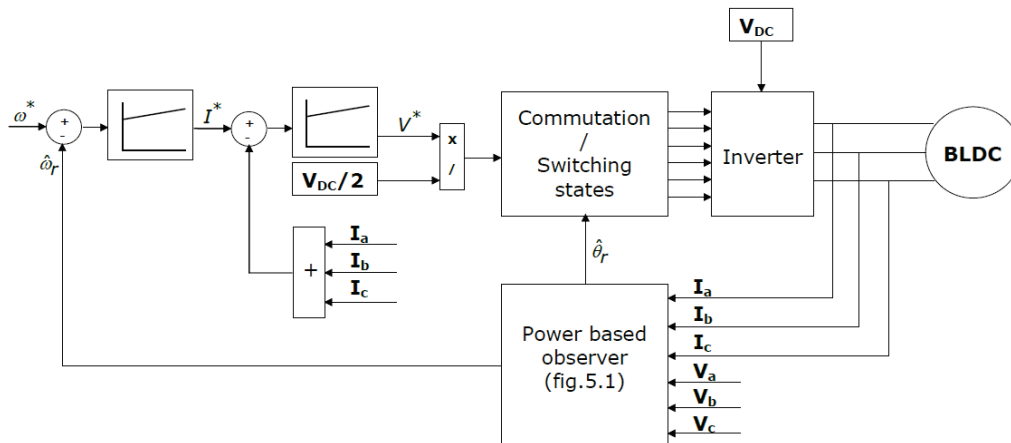


Fig.5.5 Overall system block diagram for experimental tests of the power based speed and position observer

### 5.6.1 Constant speed operation

In figures 5.6 and 5.7 operation of motor with sensorless control with power based observer at constant speeds is shown. In the first figure, operation at 6000 [rpm] at a load torque of 0.038 [Nm] is presented, while in the latter one, operation at 10000 [rpm] and 0.064 [Nm] is presented.

As can be seen, the drive performs more than satisfactory with the proposed observer, although some pulsations in speed exist due to mechanical connection with the twin BLDC that works as generator.

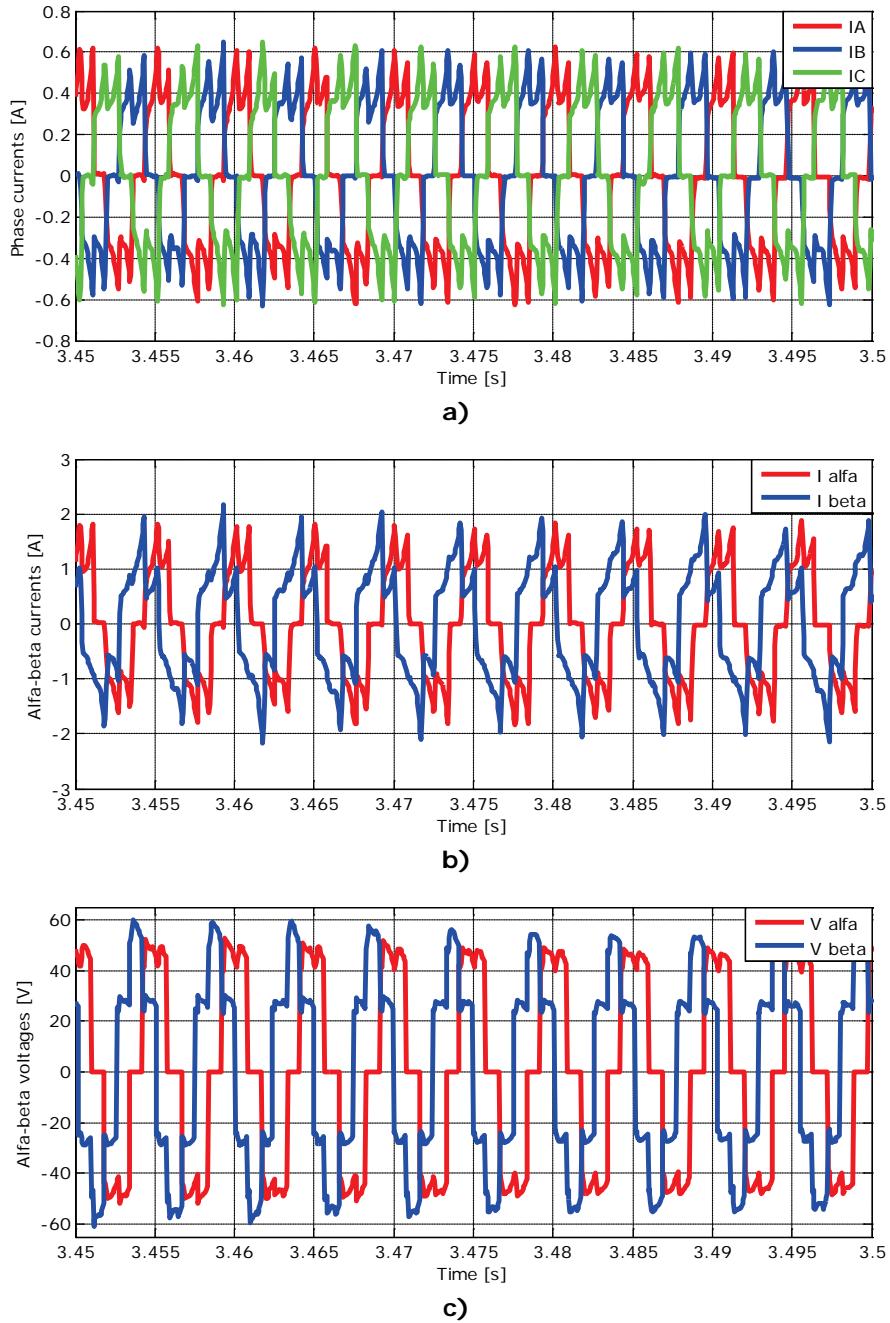
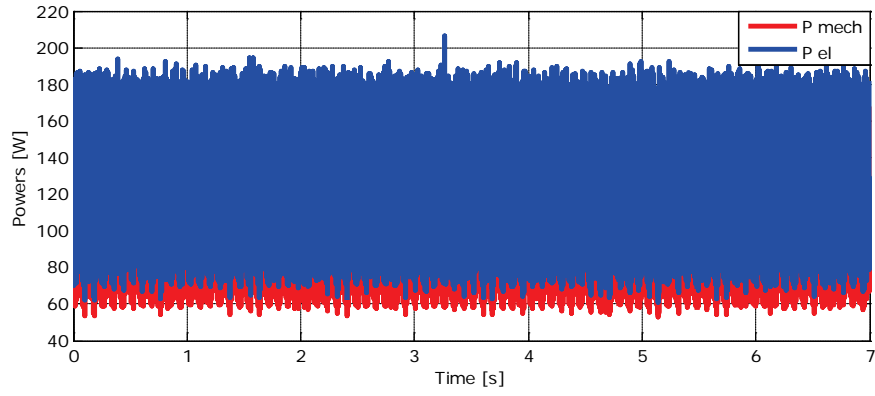
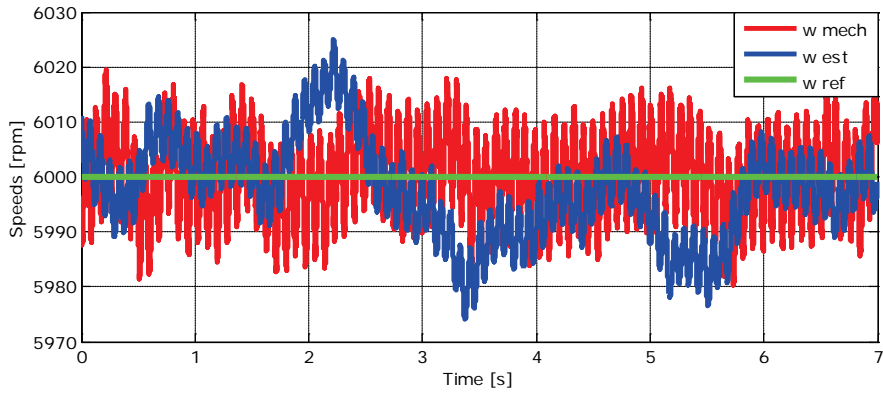


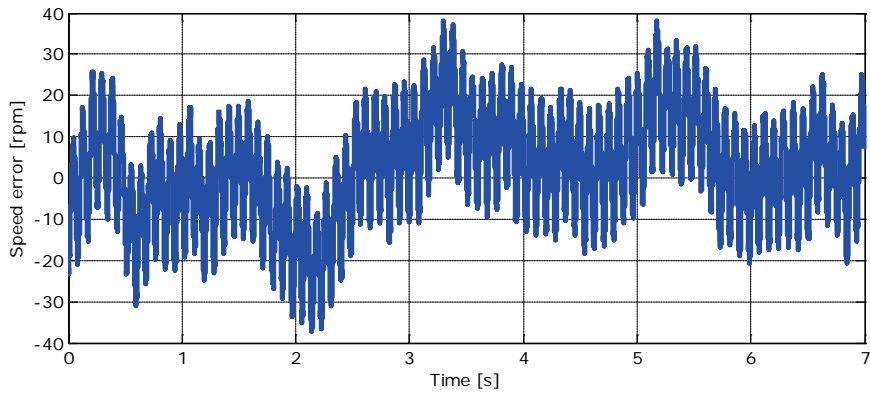
Fig.5.6 (continued)



d)

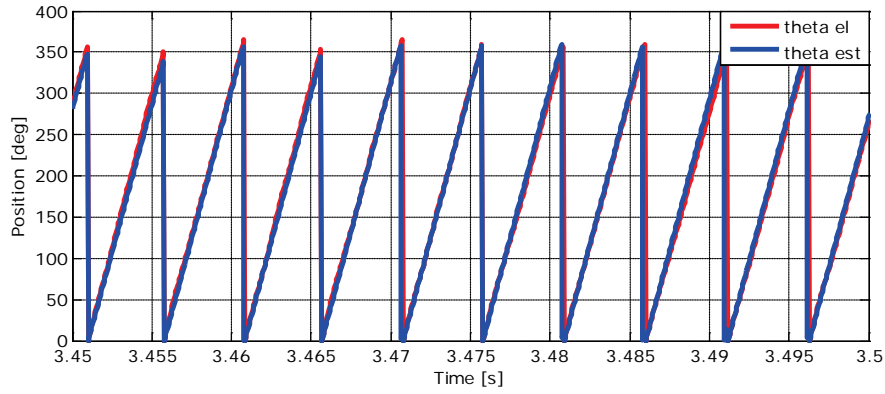


e)

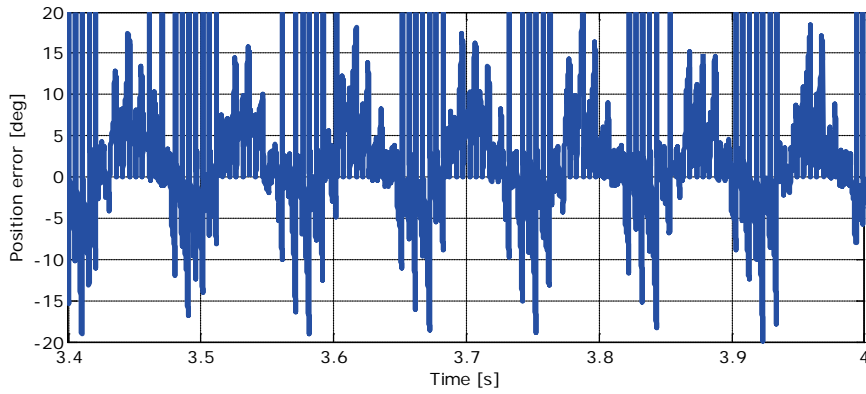


f)

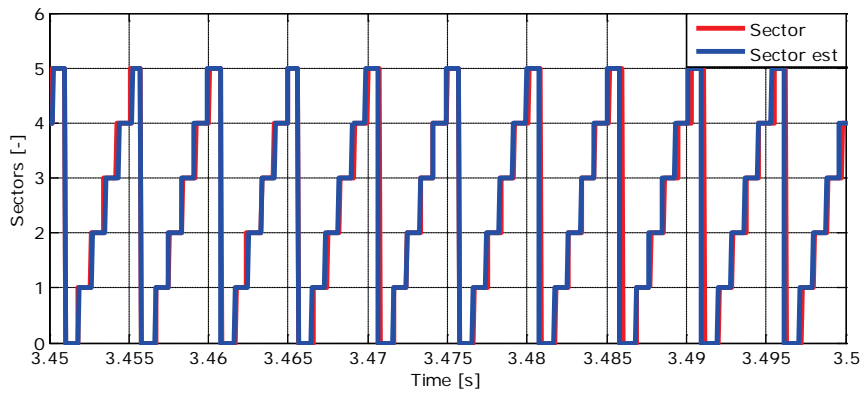
Fig.5.6 (continued)



g)



h)



i)

Fig.5.6 Experimental results of the proposed power based speed and position observer at 6000 [rpm] and 0.038 [Nm] load: a) phase A current, b)  $\alpha$ - $\beta$  currents, c)  $\alpha$ - $\beta$  voltages, d) calculated electrical and mechanical powers, e) mechanical speeds, f) speed error, g) estimated and measured angles, h) position error and i) sectors

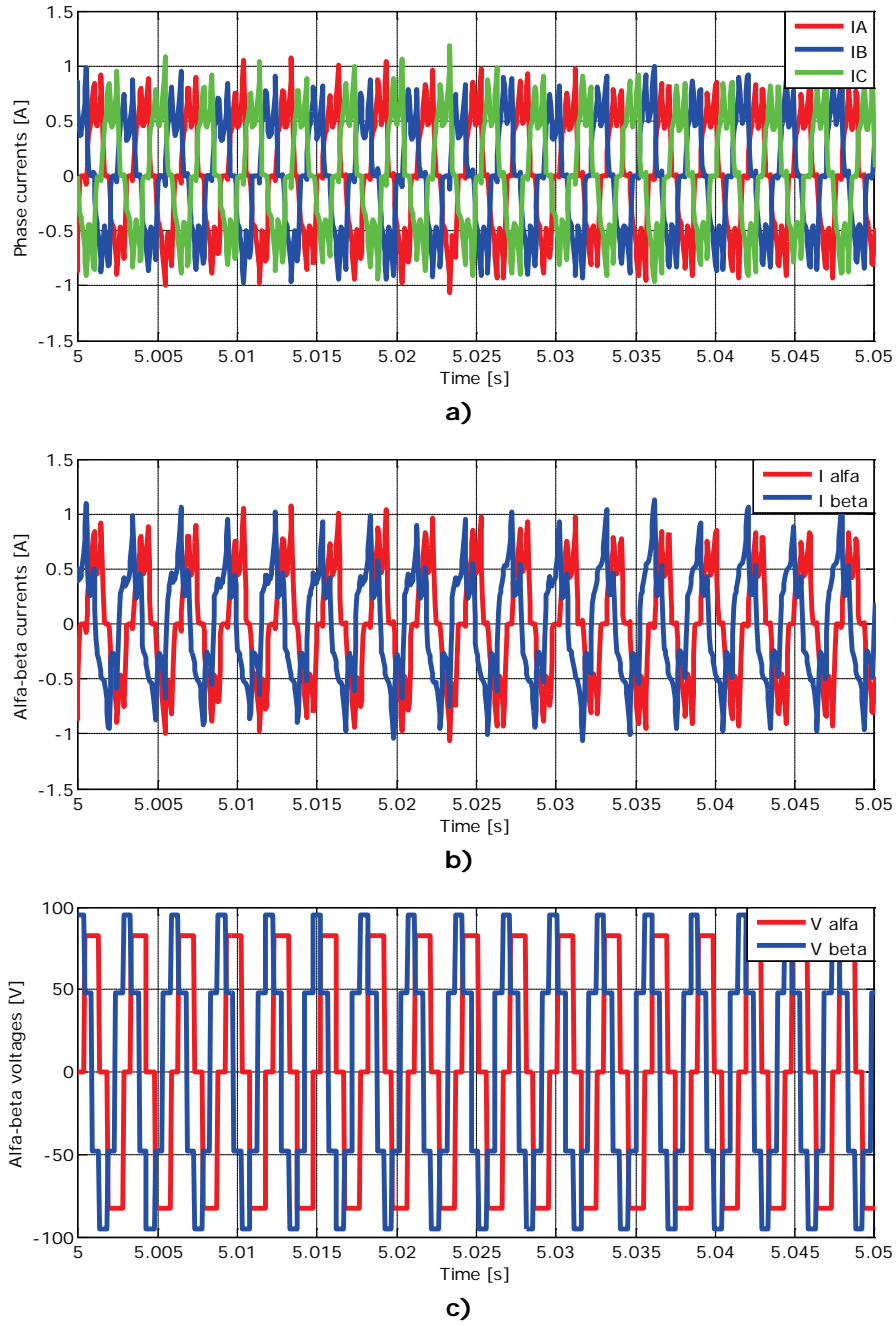
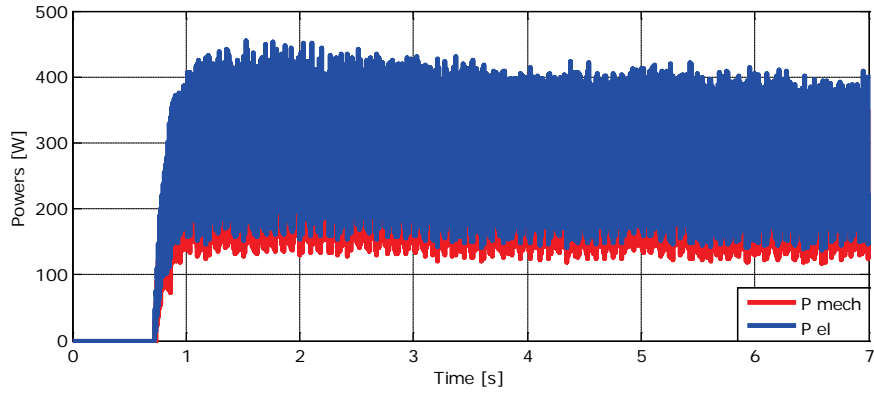
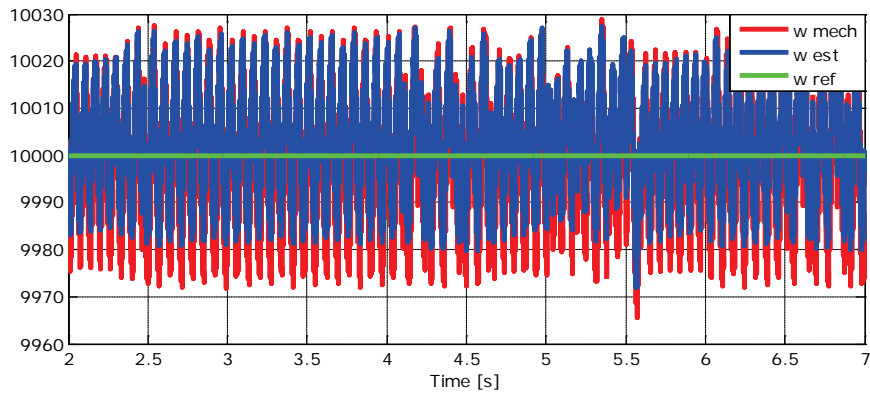


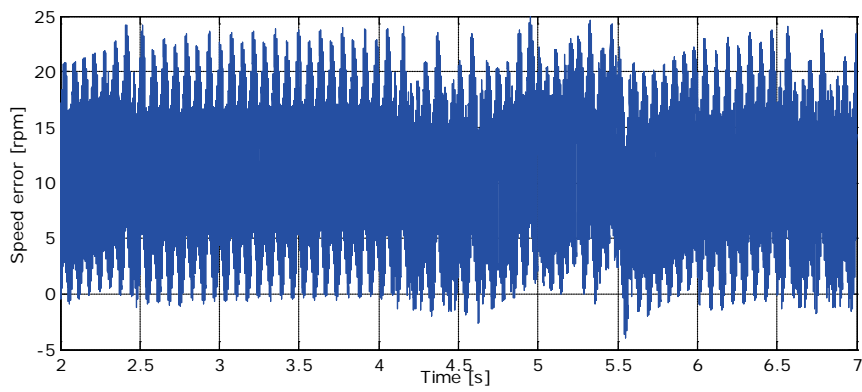
Fig.5.7 (continued)



d)

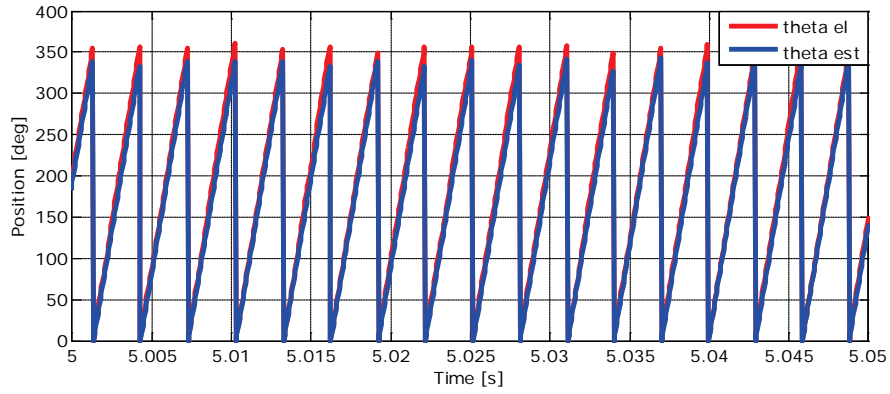


e)

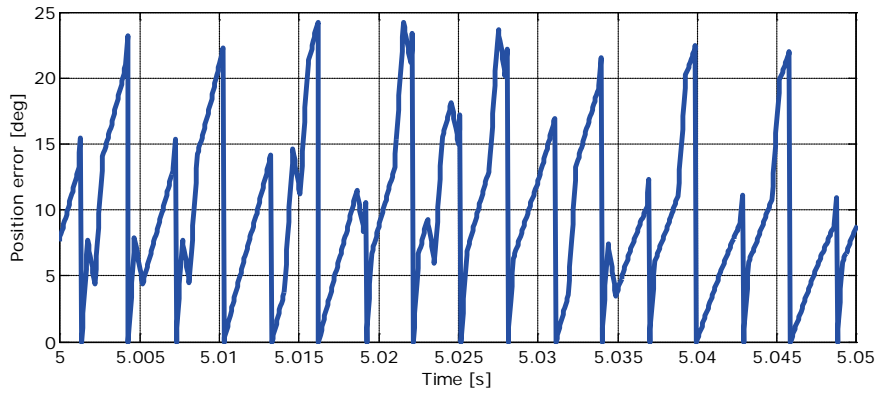


f)

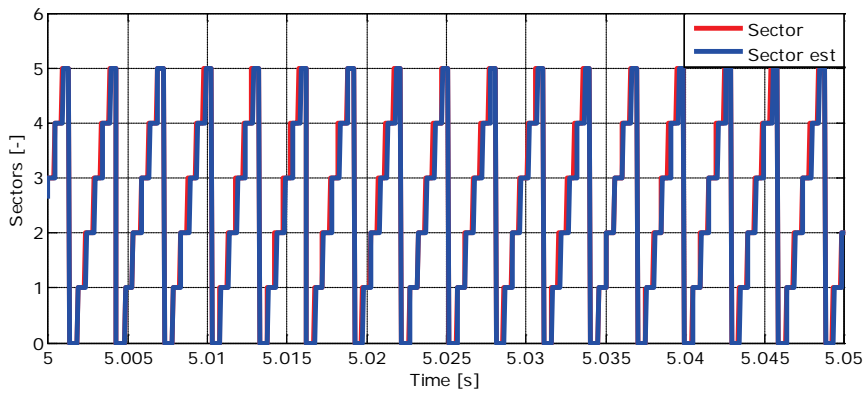
Fig.5.7 (continued)



g)



h)



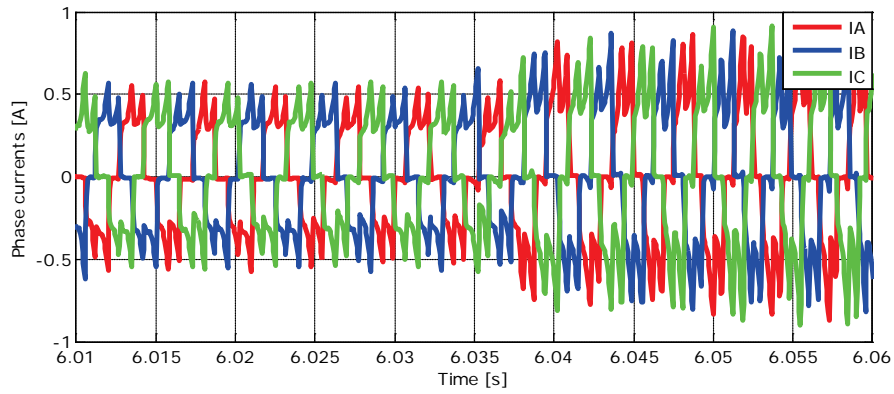
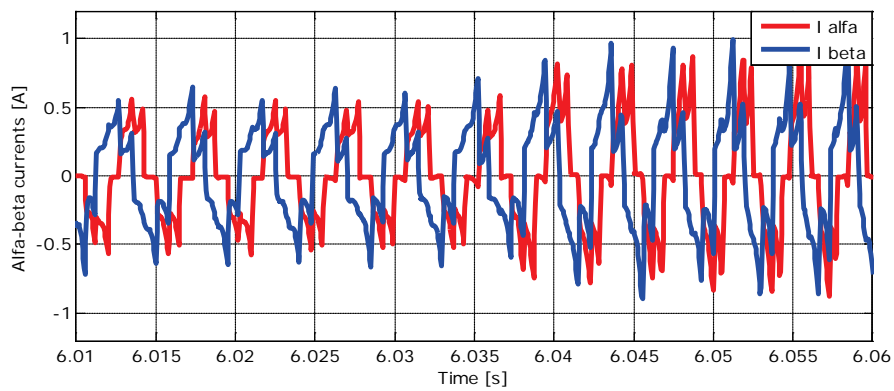
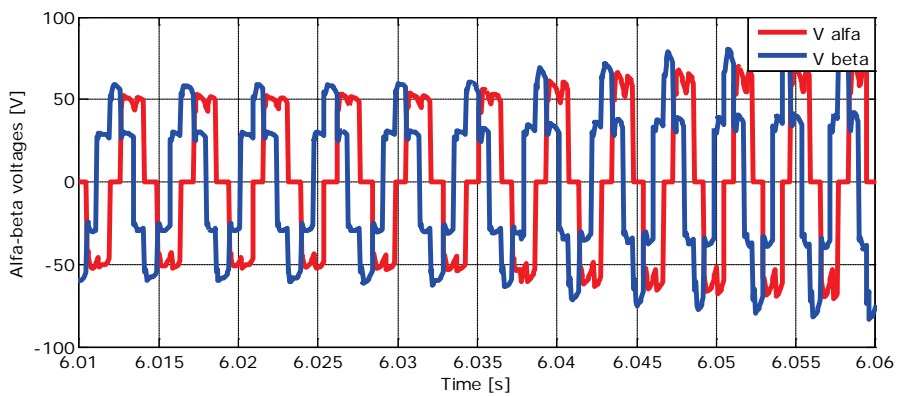
i)

Fig.5.7 Experimental results of the proposed power based speed and position observer at 10000 [rpm] and 0.064 [Nm] load: a) phase A current, b)  $\alpha$ - $\beta$  currents, c)  $\alpha$ - $\beta$  voltages, d) calculated electrical and mechanical powers, e) mechanical speeds, f) speed error, g) estimated and measured angles, h) position error and i) sectors



### 5.6.2 Dynamics

Below, acceleration from 6000 [rpm] to 10000 [rpm] (fig.5.8) and deceleration from 10000 [rpm] to 6000 [rpm] (fig.5.9) are shown.

**a)****b)****c)**

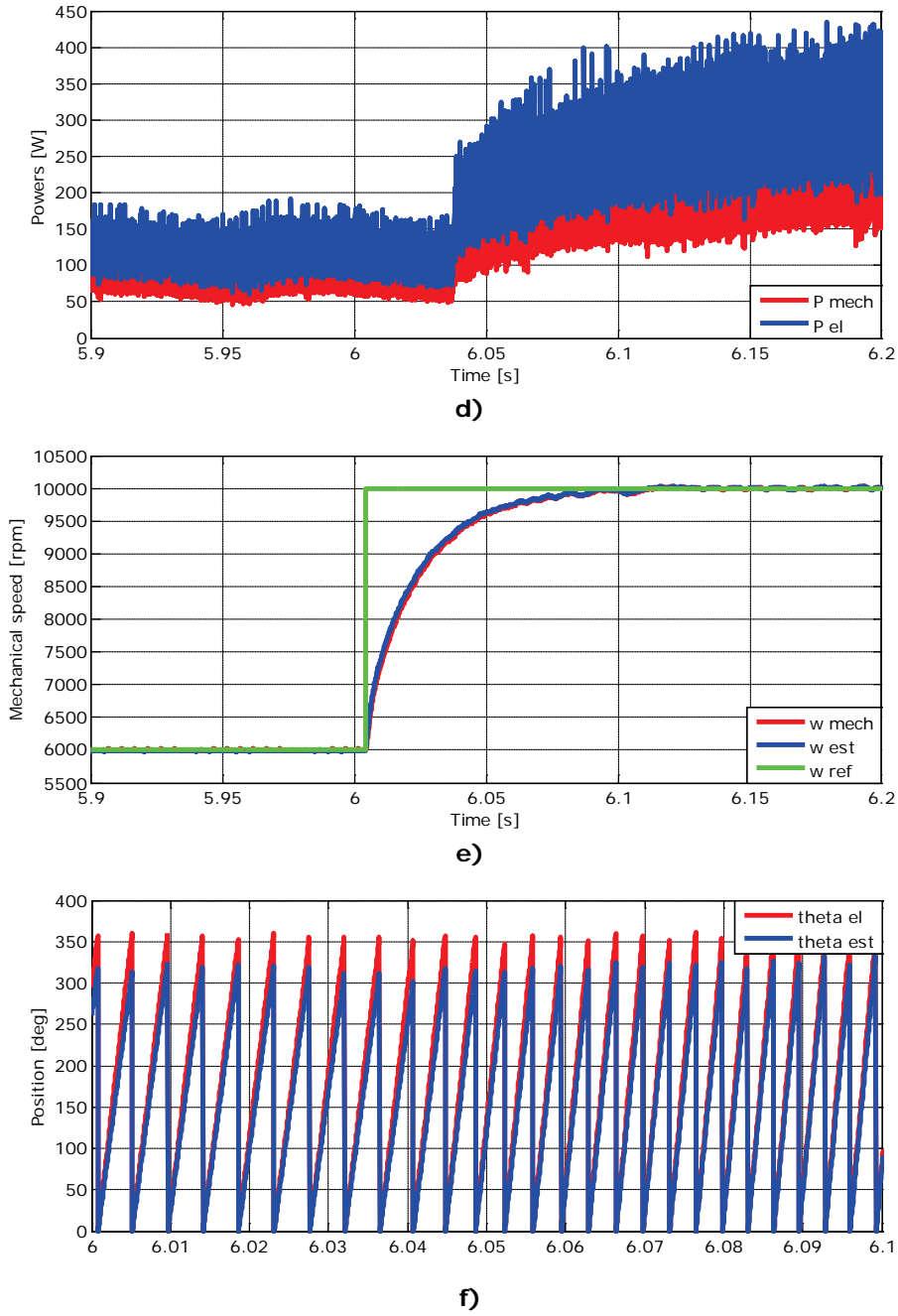
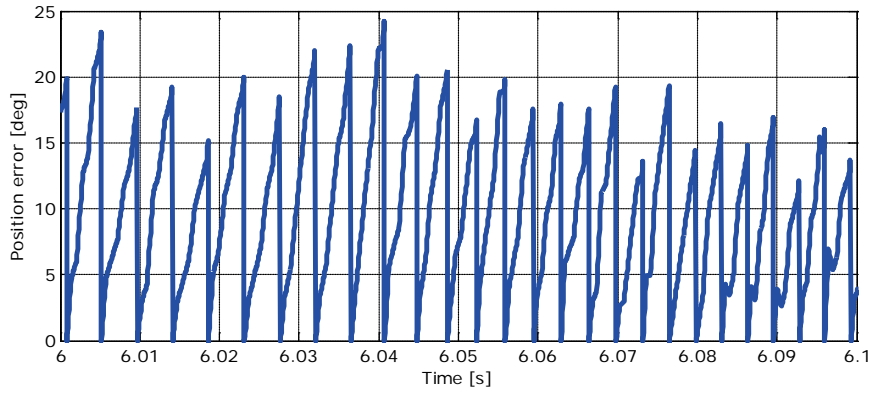
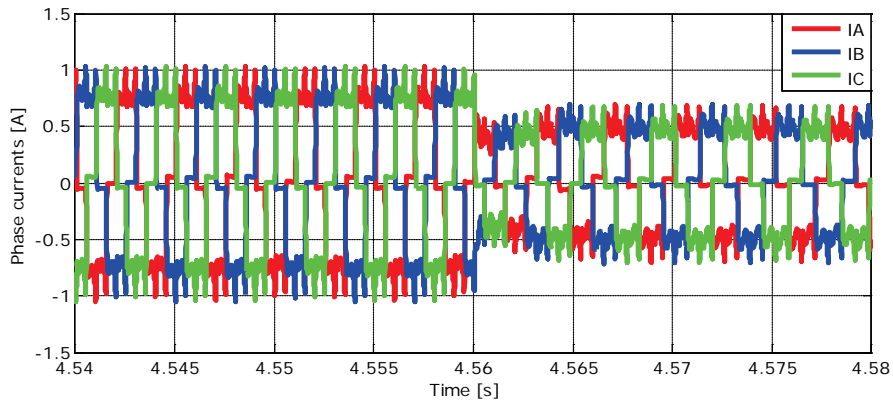


Fig.5.8 (continued)

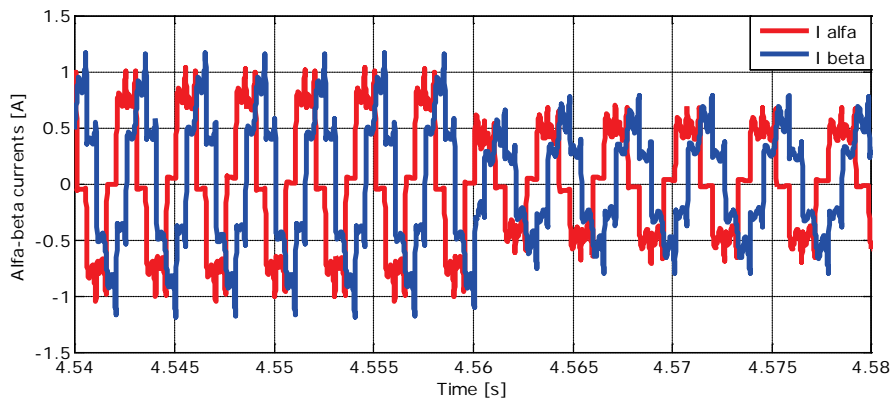


g)

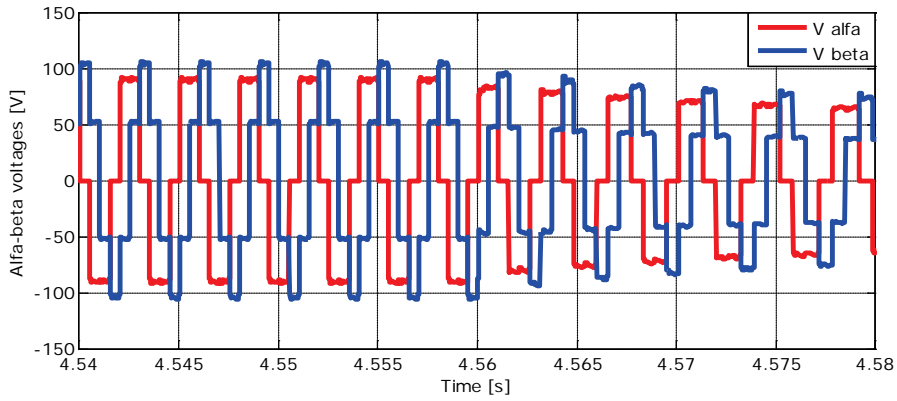
Fig.5.8 Experimental results of the proposed power based speed and position observer with acceleration from 6000 [rpm] to 10000 [rpm]: a) phase A current, b)  $\alpha$ - $\beta$  currents, c)  $\alpha$ - $\beta$  voltages, d) calculated electrical and mechanical powers, e) mechanical speeds, f) estimated and measured positions and g) position error



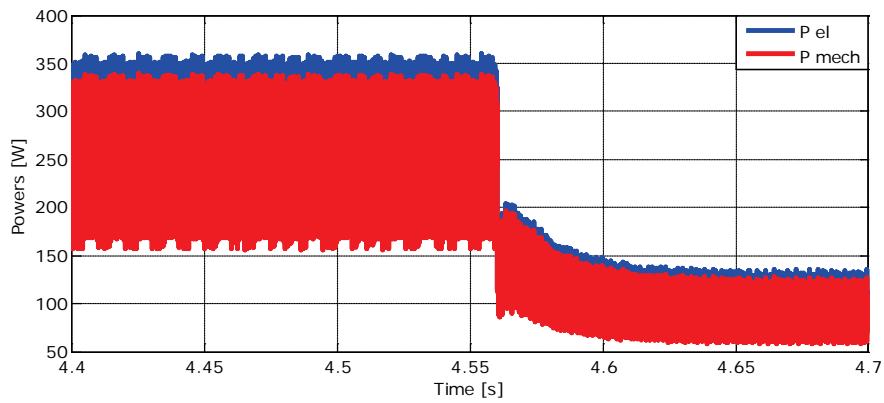
a)



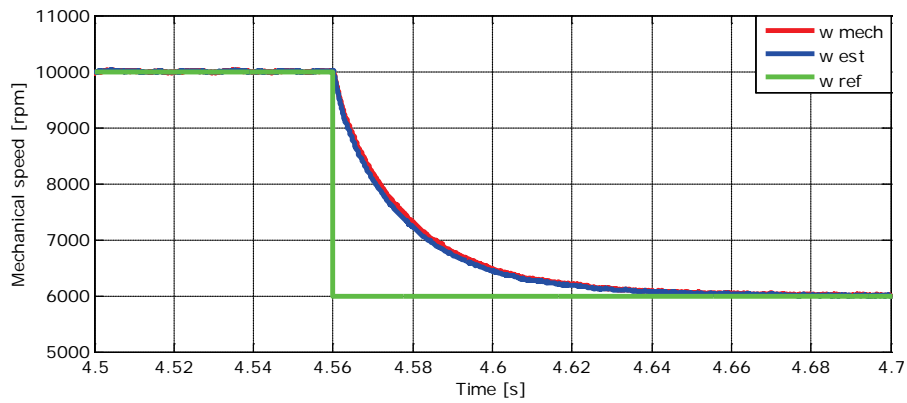
b)



c)

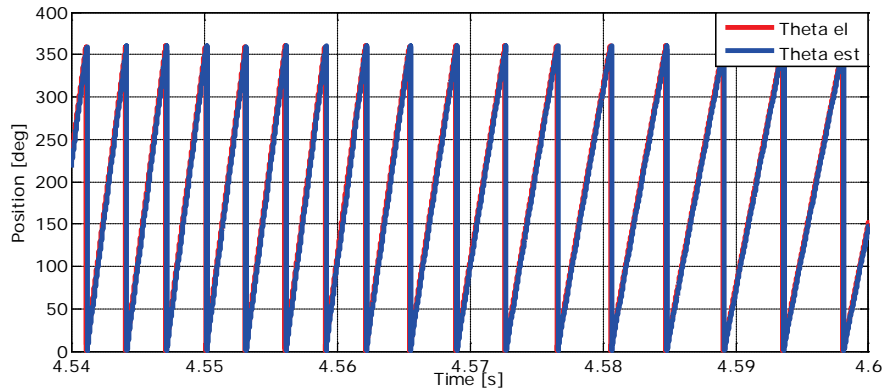


d)

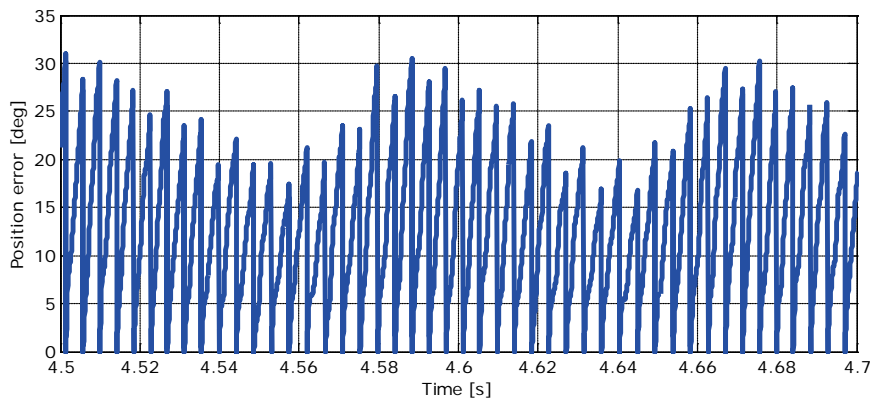


e)

Fig.5.9 (continued)



f)



g)

Fig.5.9 Experimental results of the proposed power based speed and position observer with deceleration from 10000 [rpm] to 6000 [rpm]: a) phase A current, b)  $\alpha$ - $\beta$  currents, c)  $\alpha$ - $\beta$  voltages, d) calculated electrical and mechanical powers, e) mechanical speeds, f) estimated and measured positions and g) position error

### 5.6.3 I-f to sensorless transition

In order to have a smooth start-up I-f control is applied. The transition is similar to the one in the left side of fig.5.2, up to 3000 [rpm]. Smooth transition is ensured in a frequency range between 10 [Hz] and 20 [Hz], while above 20 [Hz] sensorless control runs by itself. The start-up and transition are visible in figures 5.9 and 5.10.

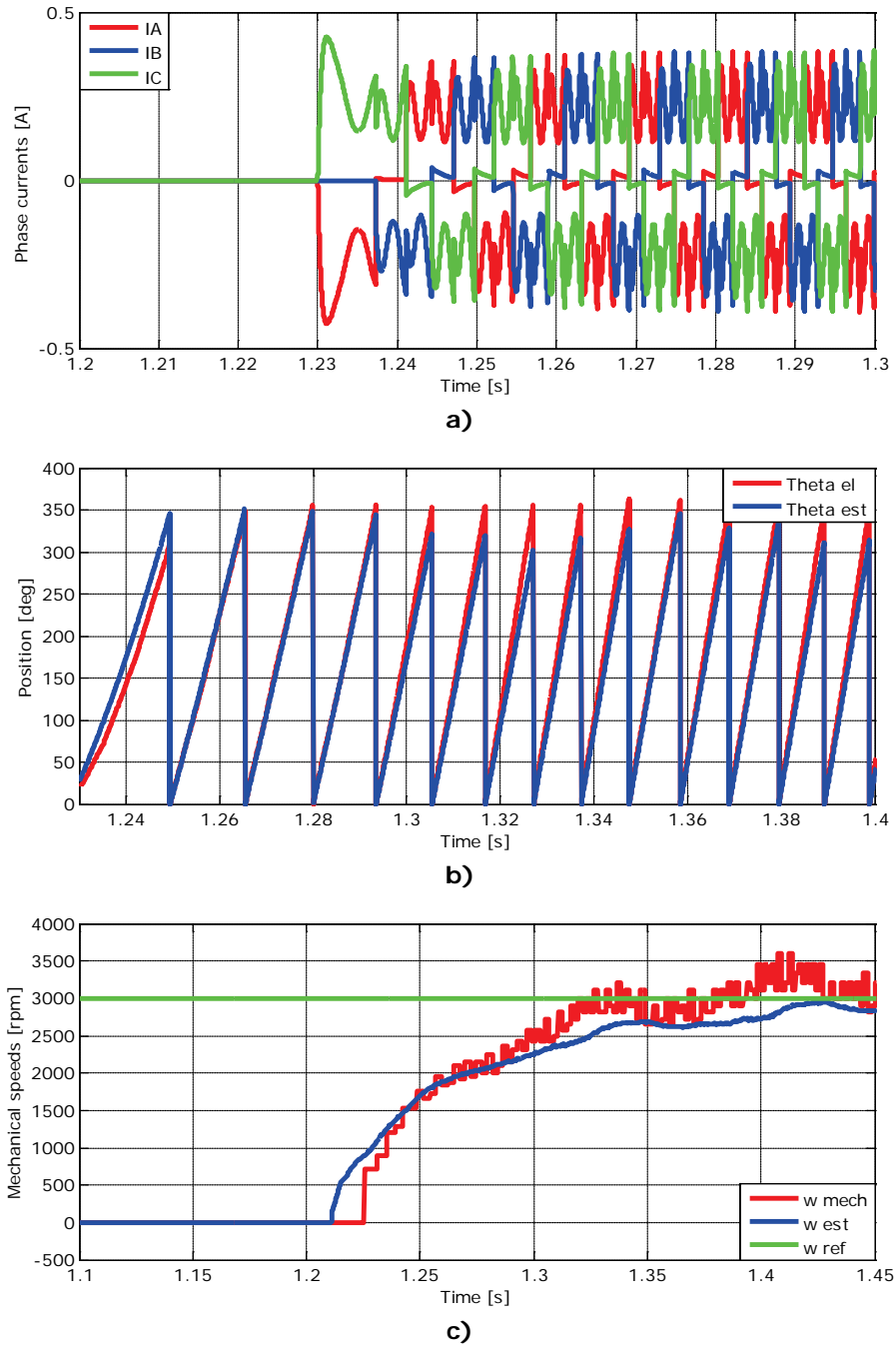


Fig.5.9 Transition from sensorless to I-f control: a) phase current, b) position and c) mechanical speeds (reference, measured and estimated)

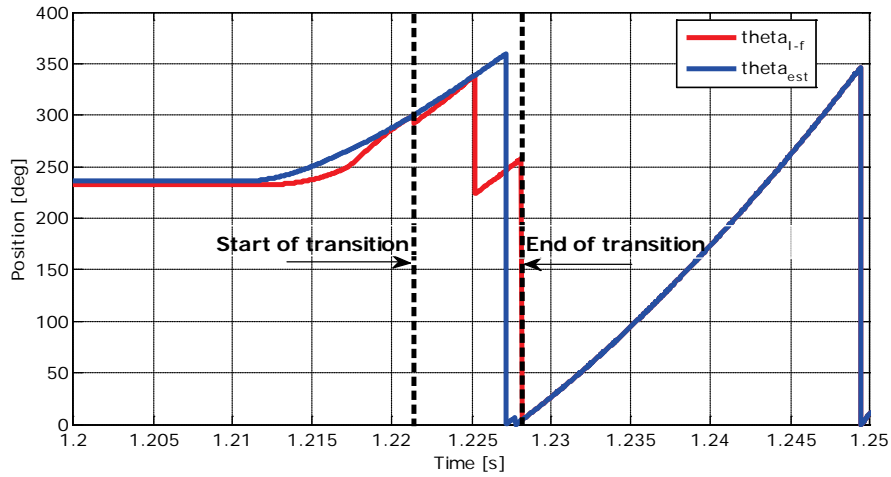


Fig. 5.10 I-f and estimated angle values in transition from I-f to sensorless control

#### 5.6.4 Sensorless to I-f transition

The transition back from sensorless control to I-f control takes place when the reference frequency values goes below a certain level, in our case 35 [Hz]. In fig.5.11 and 5.12 the seamless transition between the two control modes is visible.

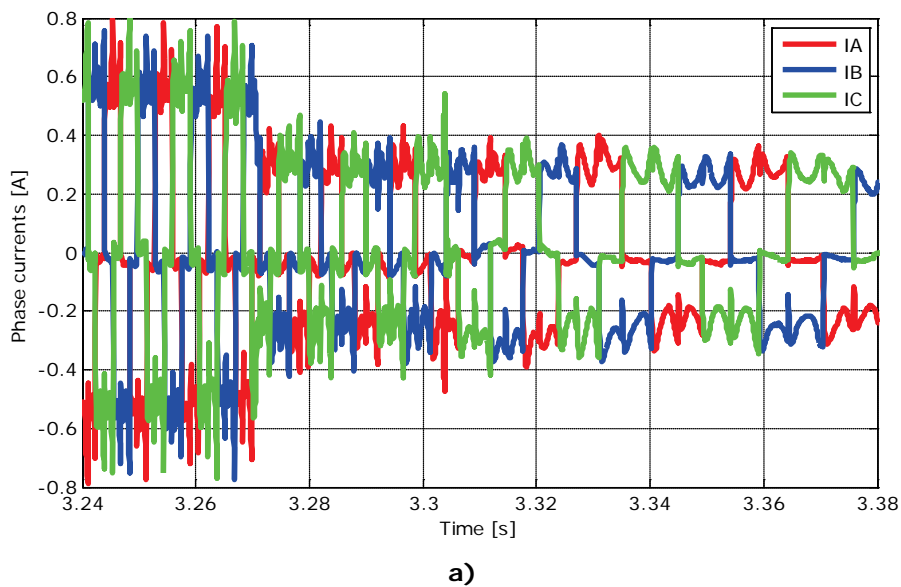
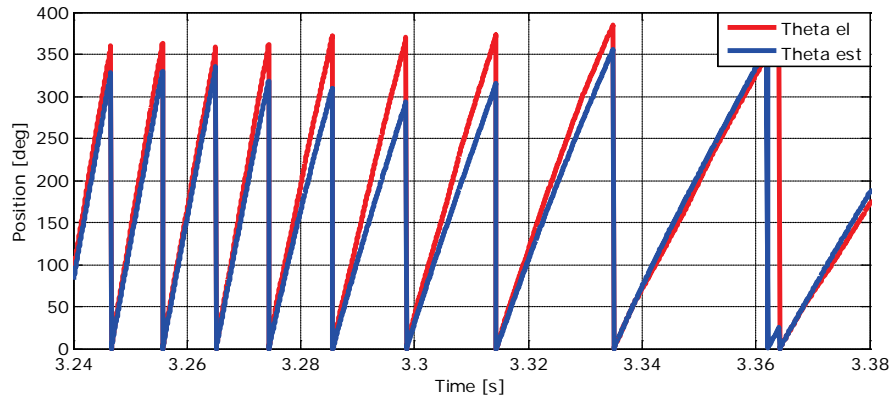
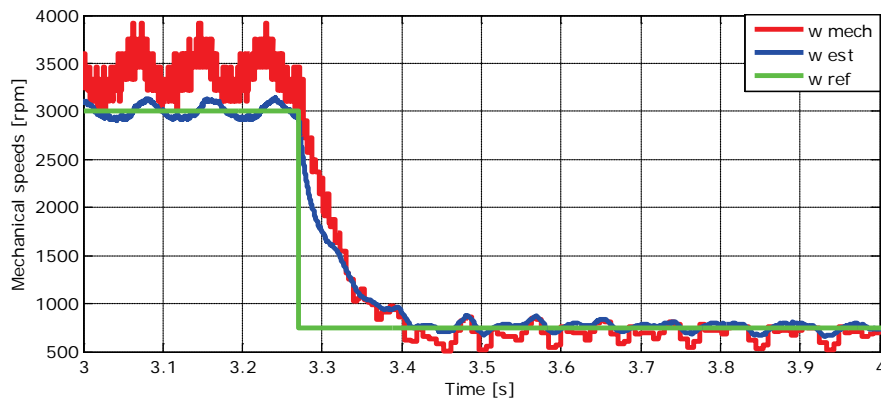


Fig.5.11 (continued)



b)



c)

Fig.5.11 Transition to I-f control: a) current, b) position and c) mechanical speeds

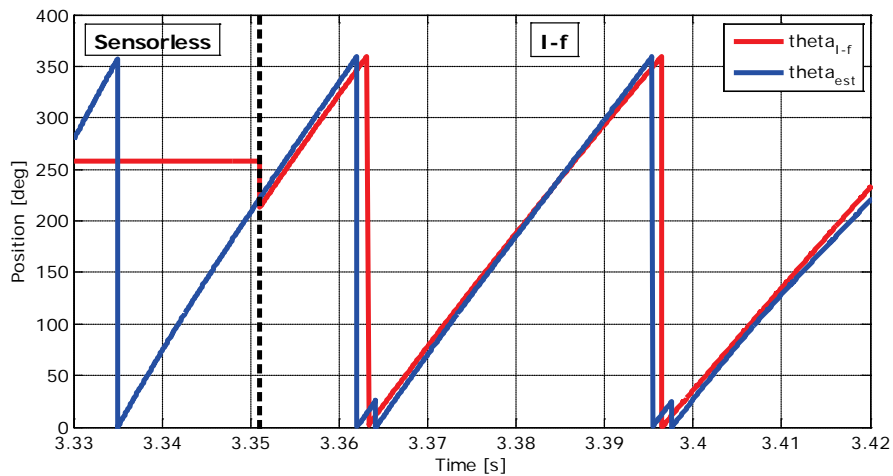


Fig.5.12 I-f and estimated angle values in transition from sensorless to I-f control



## 5.7 Conclusion

In this chapter a new sensorless control was proposed, analyzed, simulated and experimented. Two different formulas were given, one for load torque independent of speed and the other one for load torque dependent of speed. The power based observer with later formula was implemented and simulated showing good performance in constant speed region, at half and full base speed.

The performance of the control, combined with I-f starting method for start-up and low speeds regions, is experimented on the drive on a laboratory test bench. Experimental results show good agreement with simulation results, thus proving the reliability of this control method for compressor applications where the load is proportional to the speed.

Considering the ease of its implementation the control falls in the category of cheap control strategies, which makes it feasible for integration in a possible drive configuration. Thus, this control is complying to the thesis direction on development of a low cost high efficiency compressor drive.

## References

- [1] R. Dubey, P. Agarwal and M.K. Vasantha, "Programmable logic devices for motion control – a review", *IEEE Trans. on Ind. Electronics*, vol.54, no.1, pp.559–566, February 2007
- [2] J.P. Johnson, M. Ehsani and Y. Güzelgünler, "Review of sensorless methods for brushless DC", *Conf. Rec. of the 1999 IEEE 34<sup>th</sup> Ind. Appl. Conf. (IAS 1999)*, vol.1, pp.143–150, October 1999
- [3] Paul P. Acarnley and John F. Watson, "Review of position-sensorless operation of brushless permanent-magnet machines", *IEEE Trans. on Ind. Electronics*, vol.53, no.2, pp.352–362, April 2006
- [4] J.C. Gamazo-Real, E. Vázquez-Sánchez and J. Gómez-Gil, "Position and speed control of brushless DC motors using sensorless techniques and application trends", *Sensors Magazine*, no.10, pp.6901-6947, July 2010
- [5] Yen-Shin Lai and Yong-Kai Lin, "Back-EMF detection technique of brushless DC motor drives for wide range control", *32<sup>nd</sup> Annual Conf. on IEEE Ind. Electronics (IECON 2006)*, pp.1006-1011, November 2006
- [6] Yen-Shin Lai and Yong-Kai Lin, "A unified approach to back-EMF detection for brushless DC motor drives without current and Hall sensors", *32<sup>nd</sup> Annual Conf. on IEEE Ind. Electronics (IECON 2006)*, pp.1293-1298, November 2006
- [7] Yen-Shin Lai and Yong-Kai Lin, "Novel back-EMF detection technique of brushless DC motor drives for wide range control without using current and position sensors", *IEEE Trans. on Ind. Electronics*, vol.23, no.2, pp.934-940, March 2008
- [8] B. Nahid-Mobarakeh, F. Meibody-Tabar and F.-M. Sargos, "Back-EMF estimation-based sensorless control of PMSM: robustness with respect to measurements errors and inverter irregularities", *IEEE Trans. on Ind. Appl.*, vol.43, no.2, pp.485-494, March/April 2007

- [9] J. Shao, D. Nolan and T. Hopkins, "A novel direct back-EMF detection for sensorless brushless DC (BLDC) motor drives", *17<sup>th</sup> Annual IEEE Applied Power Electronics Conference and Exposition (APEC 2002)*, vol.1, pp.33-37, 2002
- [10] Jianwen Shao et al., "A novel microcontroller-based sensorless brushless DC (BLDC) motor drive for automotive fuel pumps", *IEEE Trans. on Ind. Appl.*, vol.39, no.6, pp.1734-1740, November/December 2003
- [11] Jianwen Shao, "An improved microcontroller-based sensorless brushless DC (BLDC) motor drive for automotive applications", *IEEE Trans. on Ind. Appl.*, vol.42, no.5, pp.1216-1221, September/October 2006
- [12] Robert W. Hejny and Robert D. Lorenz, "Evaluating the practical low-speeds limit for back-EMF tracking-based sensorless speed control using drive stiffness as a key metric", *IEEE Trans. on Ind. Appl.*, vol.47, no.3, pp.1337-1343, May/June 2011
- [13] Dongsheng Li et al., "Sensorless control and PMSM drive system for compressor applications", *CES/IEEE 5<sup>th</sup> Intl. Conf. IPEMC 2006*, vol.2, pp.1-5, August 2006
- [14] Jun Hu and Bin Wu, "New integration algorithms for estimating motor flux over a wide speed range", *IEEE Trans. on Power Electronics*, vol.13, no.5, pp.969-977, September 1998
- [15] Lennart Harnefors and Hans-Peter Nee, "A general algorithm for speed and position estimation of AC motors", *IEEE Trans. on Ind. Electronics*, vol.47, no.1, pp.77-83, February 2000
- [16] Nesimi Ertugrul and Paul Acarnley, "A new algorithm for sensorless operation of permanent magnet motors", *IEEE Trans. on Ind. Appl.*, vol.30, no.1, pp.126-133, January/February 1994
- [17] Chris French and Paul Acarnley, "Control of permanent magnet motor drives using a new position estimation technique", *IEEE Trans. on Ind. Appl.*, vol.32, no.5, pp.1089-1097, September/October 1996
- [18] Li Ying and Nesimi Ertugrul, "A novel, robust DSP-based indirect rotor position estimation for permanent magnet AC motors without rotor saliency", *IEEE Trans. on Power Electronics*, vol.18, no.2, pp.539-546, March 2003
- [19] J.S. Ko, S.K. Youn and B.K. Bose, "A study on adaptive load torque observer for robust precision position control of BLDC motor", *Proc. of 25<sup>th</sup> Annual Conf. of the IEEE Ind. Electronics Soc. (IECON 1999)*, vol.3, pp.1091-1096, 1999
- [20] Cristian De Angelo et al., "A rotor position and speed observer for permanent-magnet motors with nonsinusoidal EMF waveform", *IEEE Trans. on Ind. Electronics*, vol.52, no.3, pp.807-813, June 2005
- [21] Zhiqian Chen et al., "New adaptive sliding observers for position- and velocity-sensorless controls of brushless DC motors", *IEEE Trans. on Ind. Electronics*, vol.47, no.3, pp.582-591, June 2000
- [22] T.-S. Kim, J.-S. Ryu and D.-S. Hyun, "Sensorless drive of brushless DC motors using an unknown input observer", *31<sup>st</sup> Annual Conf. of IEEE Ind. Electronics Soc. (IECON 2005)*, November 2005
- [23] Seog-Joo Kang and Seung-Ki Sul, "Direct torque control of brushless DC motor with nonideal trapezoidal back EMF", *IEEE Trans. on Power Electronics*, vol.10, no.6, pp.796-802, November 1995

- [24] Salih B. Ozturk and Hamid A. Toliyat, "Sensorless direct torque and indirect flux control of brushless DC motor with non-sinusoidal back-EMF", *34<sup>th</sup> Annual Conf. of IEEE Ind. Electronics (IECON 2008)*, November 2008
- [25] J. Bernat and S. Stepień, "The adaptive speed controller for the BLDC motor using MRAC technique", *18<sup>th</sup> IFAC World Congress*, pp.4143-4148, September 2011
- [26] P. Crnošija, R. Krishnan and T. Bjažić, "Performance optimization of PM brushless DC motor drive with reference model and signal adaptation controller", *EDPE 2005*, September 2005
- [27] Alin Ştirban et al., "Motion sensorless control of BLDC PM motor with FEM assisted position and speed observer", *14<sup>th</sup> Intl. Power Electronics and Motion Control Conf. (EPE/PEMC 2010)*, vol.T4, pp.34-40, September 2010
- [28] L.I. Iepure, I. Boldea and F. Blaabjerg, "Hybrid I-f starting and observer-based sensorless control of single-phase BLDC-PM motor drives", *IEEE Trans. on Ind. Electronics*, vol.59, no.9, pp.3436-3444, September 2012
- [29] Marius Fătu et al., "I-f starting method with smooth transition to EMF based motion-sensorless vector control of PM synchronous motor/generator", *IEEE Power Electronics Specialists Conf. (PESC 2008)*, pp.1481-1487, June 2008
- [30] H. Akagi, Y. Kanazawa and A. Nabae, "Instantaneous reactive power compensators comprising switching devices without energy storage components", *IEEE Trans. on Ind. Appl.*, vol.1A-20, no.3, pp.625-630, May/June 1984
- [31] F.Z. Peng, G.W. Ott Jr. and D.J. Adams, "Harmonic and reactive power compensation based on the generalized instantaneous reactive power theory for three-phase four-wire systems", *IEEE Trans. on Power Electronics*, vol.13, no.6, pp.1174-1181, November 1998
- [32] H. Akagi, S. Ogasawara and H. Kim, "The theory of instantaneous power in three-phase four-wire systems: a comprehensive approach", *Conf. Record of the 34<sup>th</sup> IEEE IAS Annual Meeting Ind. Appl. Conf.*, vol.1, pp.431-439, October 1999
- [33] Moinuddin K. Syed and Dr. B.V. Sanker Ram, "Instantaneous power theory based active power filter: a Matlab/Simulink approach", *Journal of Theoretical and Applied Information Technology*, vol.4, no.6, pp.536-541, June 2008
- [34] R.S. Herrera et al., "Instantaneous reactive power theory: a new approach applied to n wire systems", *Intl. Conf. on Renewable Energies and Power Quality (ICREPO 2007)*, March 2007
- [35] R. Ancuţi, I. Boldea and G.-D. Andreescu, "Sensorless V/f control of surface PM-SM with two novel stabilizing loops for high speed dynamics", *IET Electric Power Application*, vol.4, no.3, pp.149-157, March 2010
- [36] M. Janaszek, "New method of direct reactive energy and torque control for permanent magnet synchronous motor", *Bull. of the Polish Academy of Sciences – Technical Sciences*, vo.54, no.3, pp.299-305, 2006
- [37] Jinsong Kang et al., "Research on field-weakening based on reactive power with BLDC motor for electric vehicle application", *Proc. of the 2007 IEEE Intl. Conf. on Integration Technology*, pp.437-441, March 2007
- [38] Chu Jianbo et al., "Direct active and reactive power control of PMSM", *IEEE 6<sup>th</sup> IPENC 2009*, pp.1808-1812, May 2009

- [39] F. Liccardo et al., "A new robust phase tracking system for asymmetrical and distorted three phase networks", *11<sup>th</sup> Intl. Conf. on Harmonics and Quality of Power*, pp.525-530, 2004
- [40] L.G.B. Rolim, D.R. da Costa jr. and M. Aredes, "Analysis and software implementation of a robust synchronizing PLL circuit based on the pq theory", *IEEE Trans. on Ind. Electronics*, vol.53, no.6, pp.1919-1926, December 2006
- [41] F. Liccardo, P. Marino and G. Raimondo, "Robust and fast three-phase PLL tracking system", *IEEE Trans. on Ind. Electronics*, vol.58, no.1, pp.221-231, January 2011

## **Chapter 6**

# **Pulse Amplitude Modulation (PAM) converter control of BLDC motor with and without Hall sensors – digital simulations**

### **Abstract**

Up until now the main focus was on motor optimal design and motor control with Hall sensors and with sensorless control. In this chapter an improved topology of BLDC motor drive with a DC-DC converter in the DC link and a combined Pulse Amplitude Modulation (PAM) and Pulse Width Modulation (PWM) technique is presented. The goal is to separate the speed control and inverter commutation, in order to reduce switching losses and the inverter size and cost. Digital simulations of the proposed drive are performed with position sensors and with sensorless strategy and a comparison with the typical 3-phase inverter is realized.

### **6.1 Introduction**

The main advantage of BLDC motors over conventional DC motors is the replacement of the mechanical commutator and brushes with power electronics, leading to better performances, elimination of sparks during the commutation and the extension of motor life. The replacement brought along the inherent problems of electronic commutation, like switching and power losses, a higher price per component but most of all, the need for position information in order to properly commutate the currents. From the beginning, Hall sensors were used to obtain precise position information [1 – 3, 22] but, due to their cost, volume and degrading accuracy with the increase in temperature, alternatives were sought. For more than two decades, sensorless techniques were proposed, improved, adapted for certain types of applications [4 – 9] to replace the position sensor. Due to its simplicity and short computation time, back-EMF sensing technique [4, 23 – 26] is, for now, the most used sensorless strategy. Other methods are back-EMF integration technique [5], flux-linkage technique [6] and freewheeling diode conduction technique [7]. They have the main advantage of easy implementation, but also drawbacks like instability at low speeds, the need for extra hardware circuit or position error during transients. For wide speed range, a speed-independent position function sensorless technique [8] with improvements [9] was proposed with good results.

In the sensorless methods presented above, the PWM technique is generally used as speed control, characterized by fixed DC voltage and inverter duty controlled by speed and load conditions. Another approach on BLDC control is to separate speed control and inverter commutation [10 – 13, 20, 21], especially in the high speed area. This is called Pulse Amplitude Modulation (PAM), when the inverter is operated with the squarewave of 120° conduction and the speed control is achieved by regulating the DC link input voltage of the inverter [10, 16 – 19]. An efficiency comparison between PWM control and PAM control for refrigerator applications was realized in [11] and the idea of a quasi-current source inverter was presented in [12]. The results were near unit power factor operation, thus improving the system overall efficiency, reducing the dc current ripples and reducing the size of the electrolytic DC filter capacitor. Further improvements can be brought by using a film capacitor in the DC link instead of the classic electrolytic capacitor [12, 13].

The idea of using a typology of buck-boost converter, namely a Cuk converter, ideal for household appliances, energized with a fixed AC voltage is presented in [14], taking into consideration mainly the economical aspects. Further, the cost is reduced by using SCRs in the inverter instead of IGBTs. However, the control strategy presented in [14] requires speed information from the motor, thus the usage of an encoder is inevitable.

In this chapter, an improved PAM control strategy is used, with a robust speed control loop, suitable for compressor applications. The inverter is used only to switch the energized motor phase and a buck-boost converter is used to adjust the DC voltage. Only the DC-DC converter is working at high frequency (20 kHz) while the inverter switches are working at low frequency (500Hz). Moreover the buck-boost transistor can also control the current shape of the AC supply source. Furthermore, a comparison of the proposed topology with PWM control with position information from Hall sensors versus back-EMF zero crossing detection technique will be presented.

## 6.2 Overview of the proposed drive

The structure of the BLDC motor drive is detailed in this part of the chapter. Every commercial BLDC drive has an AC supply source, an AC-DC converter, namely a rectifier, a DC link, usually a capacitor filter, and on the motor supply side an inverter (DC-AC converter). Since a BLDC is, in fact, a three-phase PMSM fed with trapezoidal currents, the inverter will be also a three-phase one. The rectifier can have three phases or only one phase, depending on the AC supply source. In most of the applications the drive is energized from an ordinary single phase AC power supply, so the rectifier is also single phase. A buck-boost converter is inserted in the DC link to control the DC voltage. The overall system is presented in Fig.6.1.

Since the BLDC motor characteristics and equations were already discussed in the previous chapters, in what follows a brief description of the other elements of the drive is presented.

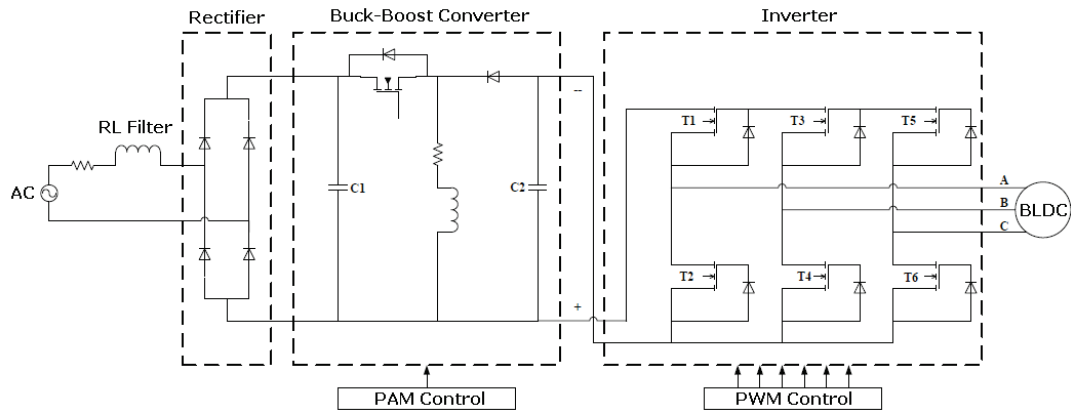


Fig.6.1 Proposed BLDC drive structure

### 6.2.1 Inverter

As mentioned before, a three-phase inverter driven with six-step commutation strategy is used to switch the energized stator phases. For a specified kVA rating of an inverter, a suitable power switching device is to be selected and then the voltage and current ratings of the devices are to be designed on a worst-case basis. The devices have to withstand the voltage  $V_{dc}$  in the forward direction, so a typical 50% margin is to be added to withstand the transient overshoot at turn-off switching. The switching devices typically used are MOSFETs, due to their high switching frequency and the ability to properly work at reasonable voltage levels. An enable/disable signal should be available for each inverter leg in order to disable the inverter leg during the zero current in the phase. This way only two from three inverter legs are working at a certain time, so the switching inverter losses compared with sinusoidal current control are drastically reduced. If monopolar modulation is applied, the switching losses could be reduced further because only one transistor is working at high frequency for  $120^\circ$  electrical. In this case, since only in the DC-DC converter high switching frequency is required, IGBTs can be used in the inverter instead. Since the maximum working frequency is 500 [Hz] tops, the switching losses will decrease even more and the PWM control strategy simplifies.

### 6.2.2 Rectifier

In commercial drives, the DC voltage is usually obtained from a single phase AC power supply. This is possible with the use of a simple diode rectifier. The network current is far from an ideal sinusoidal waveform, due to electric loads that introduce harmonics and perturbation, so the presence of a filter on the voltage supply source is needed. An RL filter, properly dimensioned is used. To reduce the voltage ripples in the DC link, a capacitor is used at the output of the rectifier.

### 6.2.3 Buck-boost converter

A buck-boost converter is a DC-DC converter used mainly in applications where the voltage needs to be adjusted. Due to its topology, as can be seen in Fig.6.2, the converter can output a larger or a smaller voltage than at the input.

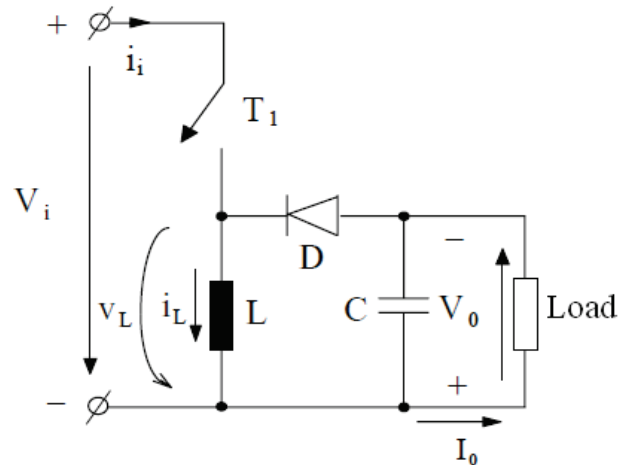


Fig.6.2 Buck-boost converter topology [27]

Depending on the application, the BLDC needs to speed up or slow down. Usually, this is realized by varying the PWM signal in the inverter which, especially at high speeds and transients, can cause commutation delay and high switching losses.

Instead of modifying six PWM signals, the speed adjustment is realized through PAM control, by altering the duty cycle of the buck-boost converter's switching device, leaving the PWM signal to deal only with the phase commutation sequence.

In theory, the value of the passive elements of the circuit used for current (RL branch) and voltage (output capacitor C2) waveform smoothing is considered high enough, so the waveforms are maintained at constant values at steady state. For economic and size considerations, the value of passive elements is limited, so the voltage and current ripples are kept to a decent level.

The duty cycle of the buck-boost converter is given in equation (6.1):

$$\frac{V_o}{V_i} = \frac{t_{on}}{t_{off}} = \frac{D}{1-D} \quad (6.1)$$

where  $V_i$  is the input voltage (rectifier output voltage),  $V_o$  is the DC link voltage (buck-boost converter output voltage),  $t_{on}$  is the period when the MOSFET is closed,  $t_{off}$  is the period when the MOSFET is open and  $D$  is the duty cycle.

Now that the system used for the BLDC drive was presented, the control developed for this application will be detailed next.



## 6.3 Control theory

The purpose of the control strategy implemented in this paper is to adjust the input voltage of the inverter whenever necessary, while providing 120° squarewave conduction on the inverter side.

### 6.3.1 Speed and current control (PAM control)

As mentioned before, voltage adjustment is realized by modifying the duty cycle of the buck-boost converter through a speed control loop (Fig. 6.3).

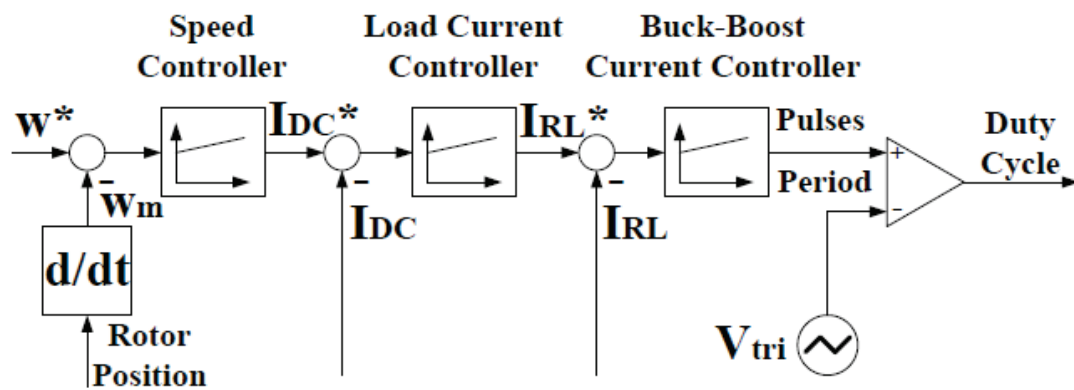


Fig.6.3 Speed and current control loop

First, the speed information is obtained from the motor. In practice is not desirable to have an encoder or, for that matter, any kind of position sensor, to save space and money. However, in some applications, where position information is very important for drive dynamics, Hall sensors are still used. In sensorless strategies, position and speed are calculated from other BLDC parameters, such as back-EMF voltages or flux linkages.

Speed error, between measured and prescribed speed, is fed to a PI speed controller to obtain the prescribed value of the DC current. A limiter is used to ensure overcurrent protection in the DC link.

DC current or reference current error is used as an input to the load current controller, another PI block. This is an optional block, but it is added for more accurate duty cycle. The amplitude of the current in the inductance depends on the "on" period of the switch and, consequently, on the amplitude of the DC current. For better performance, meaning less current ripple in the DC-DC converter, the implementation of this extra block is needed, at the cost of one more current sensor. Typically, for current measurements shunts are used, which is economically feasible.

Last, the inductance current error is fed to a PI block to obtain the conduction period of the MOSFET. The output of this block needs also to be limited, since a value

of 1 means that the switch is always on, leading the current in the inductance to raise to its short circuit value, while the load current will drop to zero. Limitation to a value of 0.9 is just right. Since the only disadvantages when the switch is always open is the absence of the current in the circuit, a maximum negative value of -1 is chosen for the lower limit.

The output of this block is then compared with a triangular voltage to impose the switching frequency of the MOSFET. In this case, the frequency was chosen to be 20 [kHz].

### 6.3.2 PWM control with Hall sensors

Many BLDC motor manufacturers supply motors with a three-element Hall effect position sensor. Each sensor element outputs a digital high level for 180° electrical of electrical rotation, and a low level for the other 180° electrical. The three sensors are offset from each other by 60° electrical so that each sensor output is in alignment with one of the electromagnetic circuits. A timing diagram showing the relationship between the sensor outputs and the required motor drive voltages is shown in Fig.6.4.

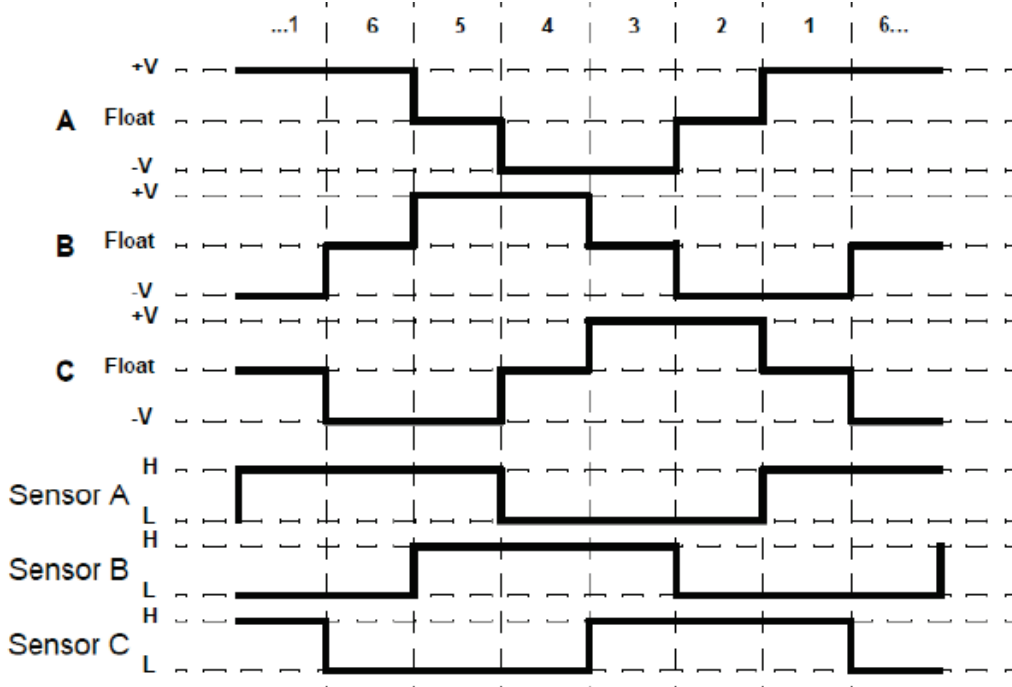


Fig.6.4 Sensor versus drive timing [1]

### 6.3.3 PWM control with back-EMF sensing technique

The most used sensorless control strategy for BLDCs is the back-EMF zero crossing detection. Since at any time, except for the commutation moments, only two phases are energized, the floating one can provide information about the phase induced voltage, namely the back-EMF.

Direct or indirect back-EMF sensing strategies exist and for this case the first one was chosen, due to speed limitations in the latter. Zero crossing detection in direct sensing is obtained from the difference between the motor terminal voltage and a voltage reference of 0 V during the freewheeling period.

At low speeds, since the back-EMF is proportional to speed, the control strategy doesn't work. Up to a speed threshold, where the back-EMF value is lower than the noise, a "blind" start-up of the motor is realized by energizing two phases for rotor alignment and after, a commutation sequence is used. When the speed is above the threshold value, the control is switched to back-EMF zero crossing detection.

## 6.4 Simulation results and discussions

The proposed drive topology was simulated. Hall sensor control and sensorless control were simulated with good results.

First simulation is done with a typical BLDC drive topology, when the motor is fed by a 3-phase IGBT inverter supplied by a DC source at 158 [Vdc] and a switching frequency of 500 [Hz]. Motor variables are shown in Fig.6.6.

Next, the proposed drive topology is simulated at rated speed with Hall sensors and with sensorless control. DC output voltage and current are depicted in Fig.6.5 and Fig.6.7, while BLDC variables and speed error are shown in Fig.6.8 and Fig.6.9.

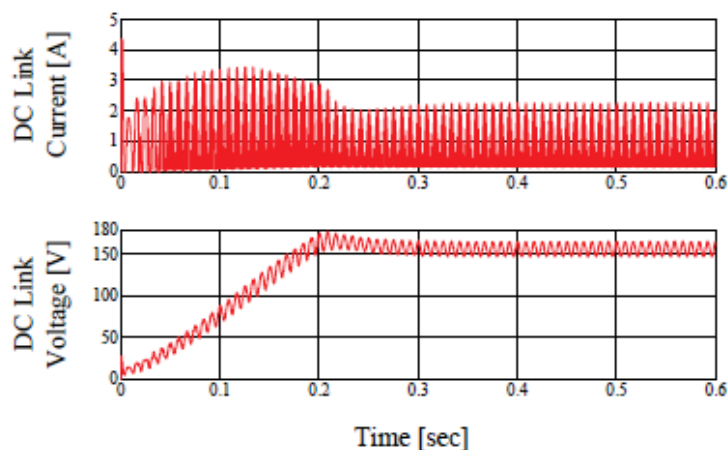


Fig.6.6 Simulation results for BLDC PAM/PWM control drive at rated speed (15000 rpm) and with Hall sensors (top to bottom): DC current and DC voltage

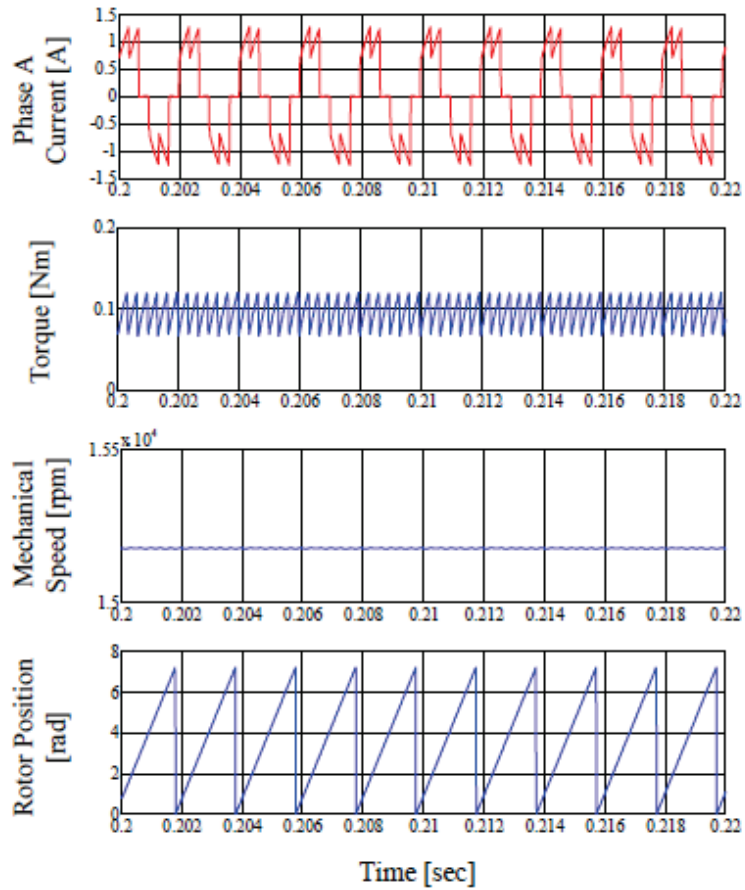


Fig.6.7. Simulation results for BLDC with PWM control at steady state at 15000 rpm (top to bottom): phase A current, torque, mechanical speed and rotor position

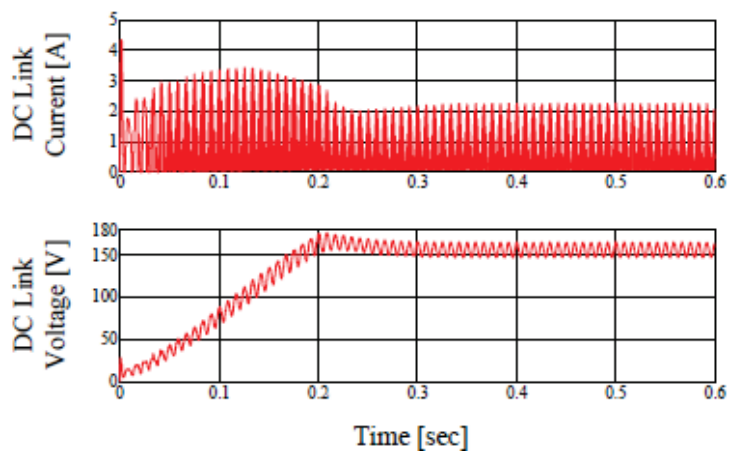


Fig.6.8 Simulation results for BLDC PAM/PWM sensorless control drive at 15000 rpm (top to bottom): DC current and DC voltage

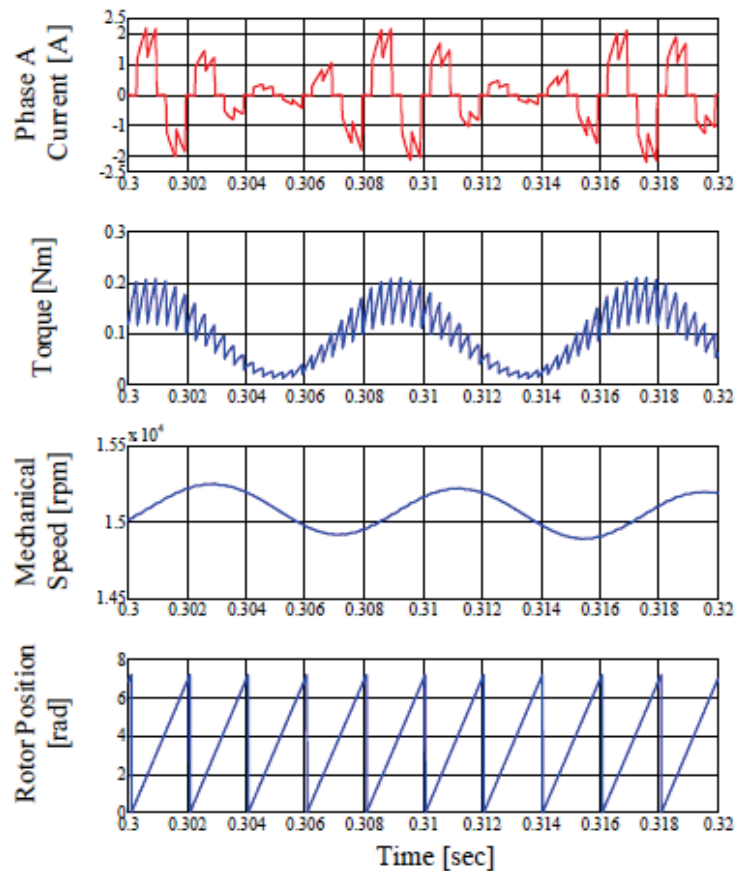


Fig.6.9 Simulation results for BLDC PAM/PWM control drive at rated speed with Hall sensors (top to bottom): phase currents, torque, mechanical speed and rotor position

The DC link voltage is increasing when the machine speed is increasing. The power delivered from a single phase sinusoidal source voltage has ripples with a frequency twice the value of voltage frequency, which causes ripples also in the DC voltage, this being the main drawback of this topology. The DC voltage ripple could be reduced only by increasing the DC capacitor  $C_2$  (Fig.6.1).

The motor start up time to the rated speed (15000 rpm) is around 0.2s with acceptable overload current. The main problem is phase currents and electromagnetic torque modulation with grid frequency (twice the value of grid frequency). These produce extra copper losses.

Next, a step variation of the speed is introduced (Fig.6.10 – Fig.6.17). At 0.4s, the speed command will drop to half the rated value. Total simulation time is 0.6 s. Variation of the DC current and voltage for both sensor and sensorless control is depicted in Fig.6.10 and Fig.6.12, while the variation of the BLDC variables is shown in Fig.6.11 and Fig.6.13.

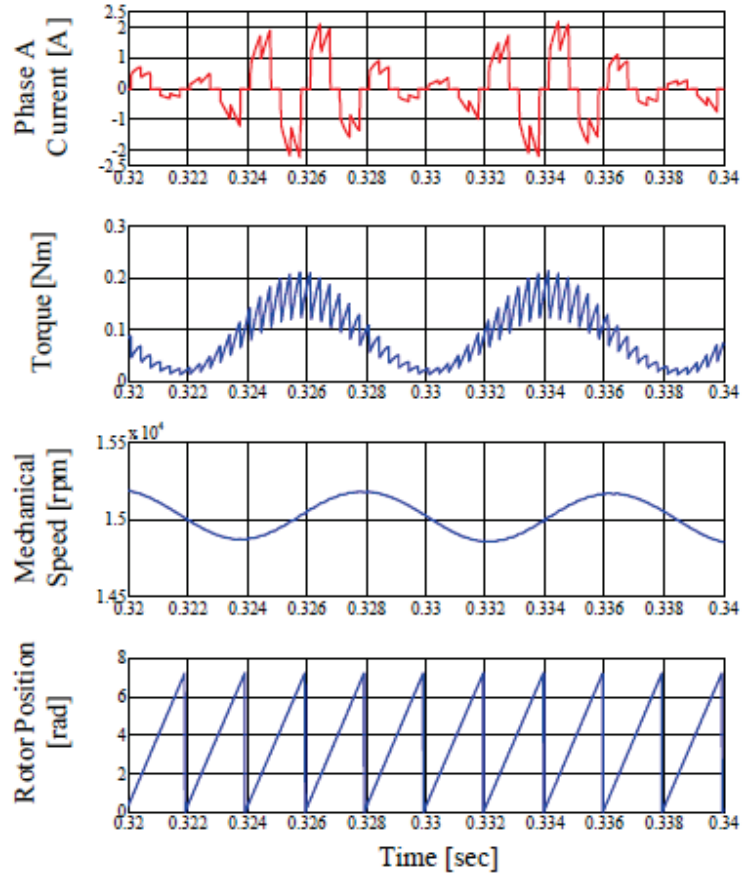


Fig.6.9 Simulation results for BLDC PAM/PWM sensorless control drive at 15000 rpm (top to bottom): phase currents, torque, mechanical speed and rotor position

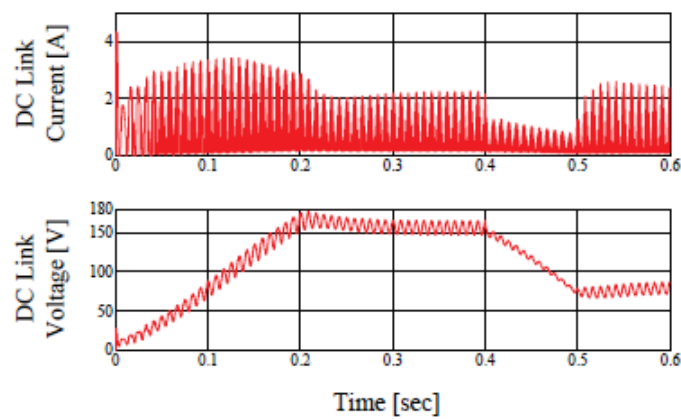


Fig.6.10 Simulation results for BLDC PAM/PWM control drive with Hall sensors for a step variation of the speed command, from 15000 rpm to 7500 rpm (top to bottom): DC current and DC voltage

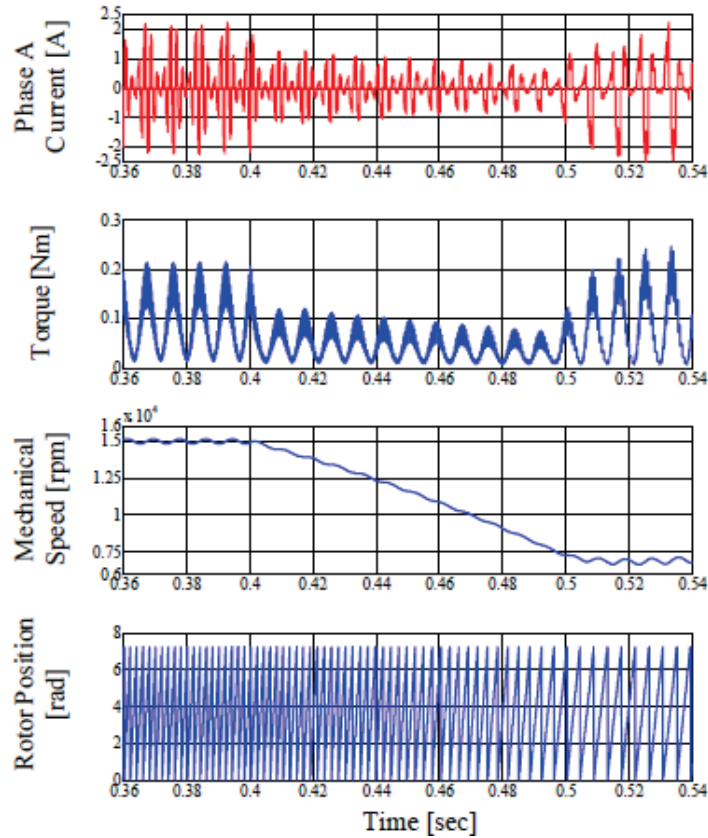


Fig.6.11 Simulation results for BLDC PAM/PWM control drive with Hall sensors for a step variation of the speed command, from 15000 rpm to 7500 rpm (top to bottom): phase currents, torque, mechanical speed and rotor position

The motor current ripple could be reduced using passive or active low pass filter. Already there is a passive filter made by C2 capacitor. This filter is more effective if the capacitor C2 is increasing. The C2 capacitor value does not influence the high frequency harmonic (6<sup>th</sup> harmonic, 3000Hz) in the electromagnetic torque. The high frequency (6<sup>th</sup> harmonic) is also reduced in this case by forcing a fast current commutation in the motor phase, but the price is the high overvoltage (600V or more) occurred in the inverter and BLDC motor. Designing a converter capable to handle that voltage leads to an increase of the switches cost.

Simulation results with a large C2 capacitor (500 [ $\mu$ F] instead 100 [ $\mu$ F]) and a step variation of the speed are presented in Fig.6.14 and Fig.6.16 for DC current and DC voltage (position sensor and sensorless control) and in Fig.6.15 and Fig.6.17 for the BLDC motor variables.

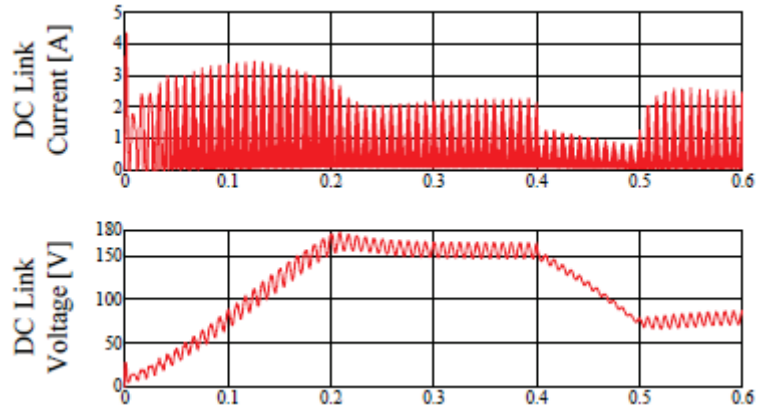


Fig.6.12 Simulation results for BLDC PAM/PWM sensorless control drive for a step variation of the speed command, from 15000 rpm to 7500 rpm (top to bottom): DC current and DC voltage

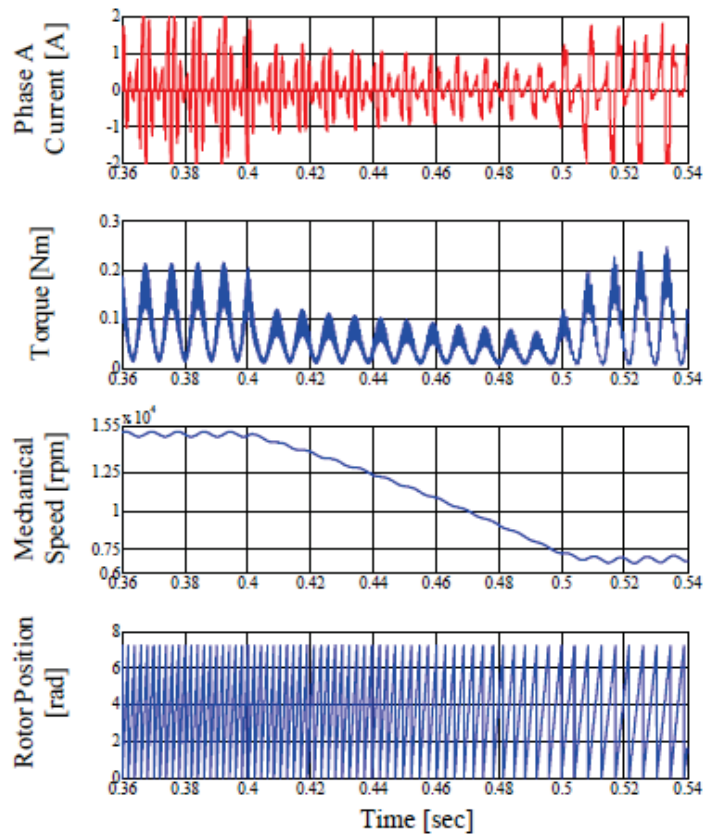


Fig.6.13 Simulation results for BLDC PAM/PWM sensorless control drive for a step variation of the speed command, from 15000 rpm to 7500 rpm (top to bottom): phase currents, torque, mechanical speed and rotor position



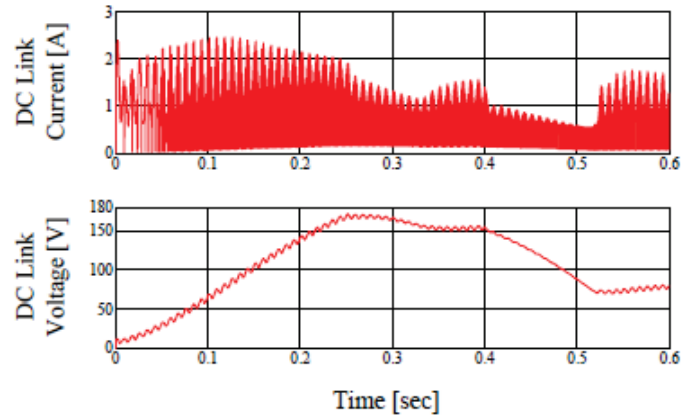


Fig.6.14 Simulation results for BLDC PAM/PWM control drive with Hall sensors for a step variation of the speed command, from 15000 rpm to 7500 rpm and a DC capacitor of 500  $\mu\text{F}$  (top to bottom): DC current and DC voltage

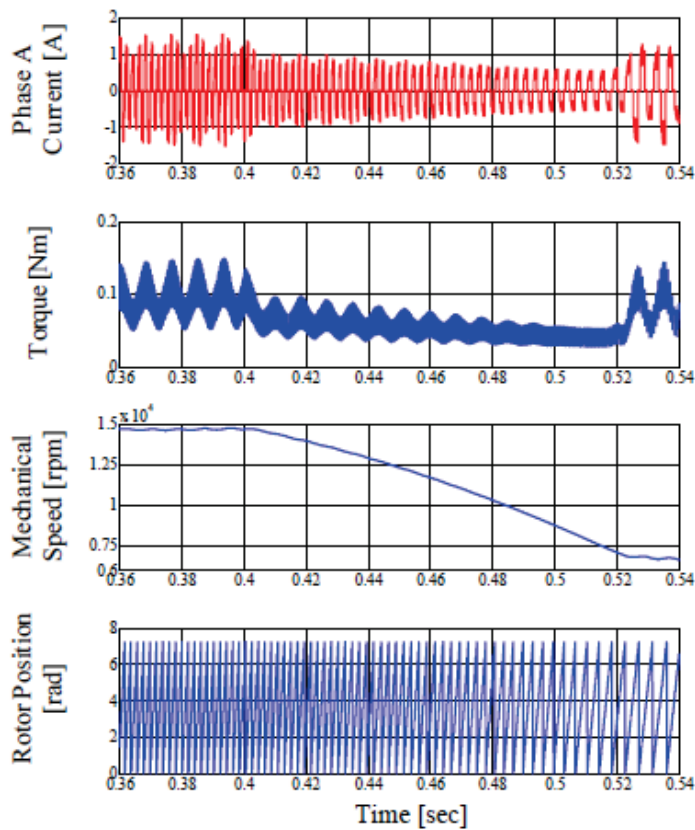


Fig.6.15 Simulation results for BLDC PAM/PWM control drive with Hall sensors for a step variation of the speed command, from 15000 rpm to 7500 rpm and a DC capacitor of 500  $\mu\text{F}$  (top to bottom): phase currents, torque, mechanical speed and rotor position

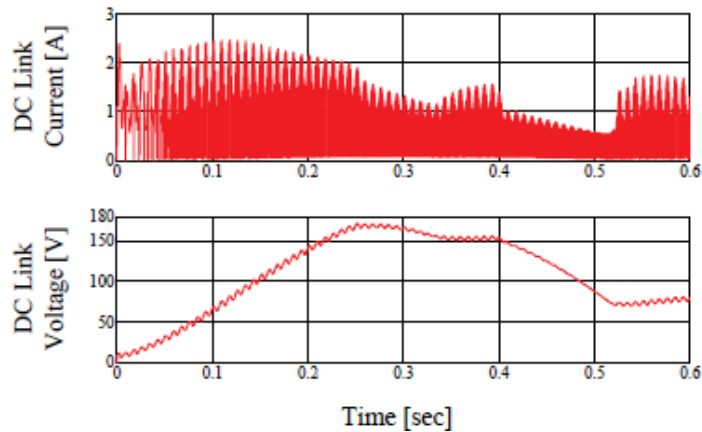


Fig.6.16 Simulation results for BLDC PAM/PWM sensorless control drive for a step variation of the speed command, from 15000 rpm to 7500 rpm and a DC capacitor of 500  $\mu$ F (top to bottom): DC current and DC voltage

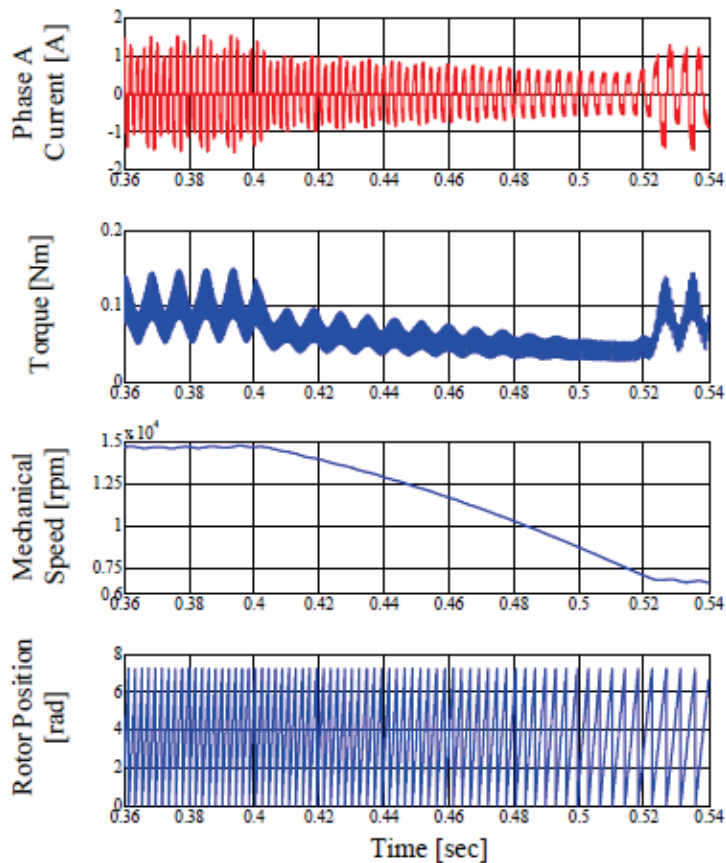


Fig.6.17 Simulation results for BLDC PAM/PWM sensorless control drive for a step variation of the speed command, from 15000 rpm to 7500 rpm and a DC capacitor of 500  $\mu$ F (top to bottom): phase currents, torque, mechanical speed, rotor position

In all the cases presented above the inductance  $L$  in the buck-boost converter has a value of 5 [mH], while the one used on the AC side is 0.5 [mH]. As can be observed, the start-up time and the speed overshoot are increasing but they are within acceptable range. A larger  $C_2$  capacitor, probably, is not economically feasible.

The active filter (rejection of the grid harmonic) can be implemented if the motor currents are controlled by switching the upper switches from the inverter. The MOSFET is used in this case to control the input current in phase with the grid voltage, thus the DC voltage can be controlled rather proportionally with the motor speed. This way, the commutation frequency of inverter switches could be reduced compared with the classical three phase inverter.

## 6.5 Conclusion

In this chapter, a new sensorless BLDC drive topology based on a combination of PAM/PWM control was introduced. The goal was to separate the speed control from inverter commutation, introducing a buck-boost converter in the DC link.

By doing so, the inverter switches will work at a lower frequency and can be downsized, which is economically efficient. Also, inverter switching losses are reduced, since only the DC-DC converter transistor is chopping at a high frequency.

Another advantage is the reduced value for starting currents and torque (5 times lower), at the expense of an increased start-up time (0.05 s to 0.2 s).

The main drawback of the topology is the propagation of voltage ripples from the AC source and, even with an increased DC capacitor the filtering is not that good. Further improvements would probably lead to an increase in drive cost.

## References

- [1] Ward Brown, "Brushless DC Control Made Easy", *Application Note AN857*, Microchip Technology Inc., 2002
- [2] L.N. Elevich, "3-Phase BLDC Motor Control with Hall Sensors Using 56800/E Digital Signal Controllers", *Application Note AN1916*, Rev. 2.0, Freescale Semiconductor, November 2005
- [3] N. Samoylenko, Q. Han, and J. Jatskevich, "Dynamic Performance of Brushless DC Motors With Unbalanced Hall Sensors", *IEEE Transactions on Energy Conversion*, vol.23, no.3, pp.752–763, September 2008
- [4] J. Shao, D. Nolan and T. Hopkins, "A Novel Direct Back EMF Detection for Sensorless Brushless DC (BLDC) Motor Drives", *Proceedings of IEEE APEC'02 Conference*, pp.33–37, 2002
- [5] R.C. Becerra, T.M. Jahns, and M. Ehsani, "Integrated Current Regulation for a Brushless ECM Drive", *Proceedings of IEEE APEC'91 Conference*, pp.202–209, 1991
- [6] N. Ertugrul and P. Acarnley, "A New Algorithm for Sensorless Operation of Permanent Magnet Motors", *IEEE Trans. on Ind. App.*, vol.30, pp.126–133, January/February 1994

- [7] S. Osagawara and H. Akagi, "An Approach to Position Sensorless Drive for Brushless DC Motor Drives", *IEEE Transactions on Industry Applications*, vol.27, pp.928–933, September/October 1991
- [8] T.-H. Kim and M. Ehsani "Sensorless Control of the BLDC Motors From Near-Zero to High Speeds", *IEEE Transactions on Power Electronics*, vol.19, no.6, pp.1635 – 1644, November 2004
- [9] T.-S. Kim, B.-G. Park, D.-M. Lee, J.-S. Ryu, and D.-S. Hyun, "A New Approach to Sensorless Control Method for Brushless DC Motors", *International Journal of Control, Automation, and Systems*, vol. 6, no. 4, pp.477–487, August 2008
- [10] K.-H. Kim, M.-J. Youn, "DSP-Based High-Speed Sensorless Control for a Brushless DC Motor Using a DC Link Voltage Control", *Electric Power Components and Systems, Taylor & Francis*, vol.30, issue 9, pp.889–906, September 2002
- [11] Y.-S. Lai, K.-Y. Lee, J.-H. Tseng, Y.-C. Chen, and T.-L. Hsiao, "Efficiency Comparison of PWM-Controlled and PAM-Controlled Sensorless BLDCM Drives for Refrigerator Applications", *Conference Record of the 42<sup>nd</sup> IEEE IAS Annual Meeting*, pp.268–273, September 2007
- [12] I. Takahashi, T. Koganezawa, G. Su, and K. Ohyama, "A Super High Speed PM Motor Drive System by a Quasi-Current Source Inverter", *IEEE Transactions on Industry Applications*, vol.30, no.3, pp.683–690, May/June 1994
- [13] H. Yoo, S.-K. Sul, H. Jang, and Y. Hong, "Design of a Variable Speed Compressor Drive System for Air-Conditioner without Electrolytic Capacitor", *Conference Record of the 42<sup>nd</sup> IEEE IAS Annual Meeting*, pp.305–310, September 2007
- [14] R. Khopkar, S.M. Madani, M. Hajiaghajani, and H.A. Toliyat, "A Low-Cost BLDC Motor Drive using Buck-Boost Converter for Residential and Commercial Applications", *IEEE International Electric Machines and Drives Conference*, vol.2, pp.1251–1257, June 2003
- [15] V. Gradinaru, L. Tutelea, and I. Boldea, "25 kW, 15 krpm, 6/4 PMSM: Optimal design and torque pulsation reduction via FEM", *OPTIM 2008*, pp.249–256, May 2008
- [16] Gui-Jia Su and Donald J. Adams, "Multilevel DC Link inverter for brushless permanent magnet motors with very low inductance", *IEEE Transactions on Industry Applications*, vol.41, no.3, pp.848-854, May/June 2005
- [17] K. Yamamoto, K. Shinohara and T. Nagahama, "Characteristic of permanent-magnet synchronous motor driven by PWM inverter with voltage booster", *IEEE Trans. on Ind. Appl.*, vol.40, no.4, pp.1145-1152, July/August 2004
- [18] Fang Lin Luo and Hock Guan Yeo, "Advanced PM brushless DC motor control & system for electric vehicles", *Conf. Record of the 2000 IEEE IAS Conf.*, vol.2, pp.1336-1343, October 2000
- [19] Primož Bajec et al, "Novel AC-DC converter control principle for automotive BLDC generator in low-speed range", *The 8<sup>th</sup> IEEE Intl. Workshop on Advanced Motion Control*, pp.105-110, March 2004
- [20] F.D. Kieferndorf, M. Förster and T.A. Lipo, "Reduction of DC-bus capacitor ripple current with PAM/PWM converter", *IEEE Trans. on Ind. Appl.*, vol. 40, no.2, pp.607-614, March/April 2004

- 
- [21] V. Grădinaru, L. Tutelea, and I. Boldea, "BLDC-SPM motor drive with DC-DC converter in the DC link: Hall sensor versus sensorless speed control", *OPTIM 2010*, pp.422-429, May 2010
- [22] F. Giulii Capponi et al, "AC brushless drive with low-resolution Hall effect sensors for an axial flux PM machine", *Conf. Record of the 2004 IEEE IAS Conf.*, vol.4, pp.2382-2389, October 2004
- [23] J. Shao, D. Nolan and T. Hopkins, "Improved direct back-EMF detection for sensorless brushless DC (BLDC) motor drives", *18<sup>th</sup> Annual IEEE APEC 2003*, vol.1, pp.300-305, February 2003
- [24] Yen-Shin Lai and Yong-Kai Lin, "Back-EMF detection technique of brushless DC motor drives for wide range control", *32<sup>nd</sup> Annual Conf. on IEEE IECON 2006*, pp.1006-1011, November 2006
- [25] Yen-Shin Lai and Yong-Kai Lin, "A unified approach to Back-EMF detection for brushless DC motor drives without current and Hall sensors", *32<sup>nd</sup> Annual Conf. on IEEE IECON 2006*, pp.1293-1298, November 2006
- [26] Yen-Shin Lai and Yong-Kai Lin, "Novel Back-EMF detection technique of brushless DC motor drives for wide range control without using current and position sensors", *IEEE Trans. on Power Electronics*, vol.23, no.2, pp.934-940, March 2008
- [27] Nicolae Muntean, "Convertoare statice", book, Ed. Politehnica, Timișoara, 1998

## Chapter 7

### The experimental test bench

#### Abstract

This chapter presents the laboratory setup used for the measurements in Chapter 5. The scope of it is to present both the hardware and software components used to acquire motor signals and to interface the closed loop control implemented in Matlab®/Simulink® with the electric drive.

Motor control, with Hall sensors and sensorless, outputs gate signals for the inverter MOSFETs, based on the duty cycle calculated in the closed loop. To have flexibility in sending those signals to the inverter a dSpace platform is needed. dSpace platform is also used to acquire motor signals via a measurement board, like phase currents, DC voltage and Hall signals.

The inverter MOSFET driver and the measurement board are briefly presented, while the motor's physical configuration is shown in detail.

#### 7.1 Brushless DC motor

The centerpiece of any electrical drive is the motor. Throughout the entire thesis the brushless DC motor was used for the refrigerator compressor application. Motivation for choosing this type of motor is given in Chapters 1 and 2. Below, the motor specific data is given.

**Table 7.1 Brushless DC motor parameters**

Parameter	Symbol	Value	Unit
Nominal power	$P_n$	150	W
Rated current	$I_n$	0.56	A
DC voltage	$V_{DC}$	305	V
Rated speed	$n_n$	15000	rpm
Rated torque	$T_{en}$	0.095	Nm
Number of pole pairs	$p$	2	-
Stator phase resistance	$R_s$	4.9372	$\Omega$
Stator phase inductance	$L_s$	0.0088	H
Moment of inertia	$J_r$	$1.691 \cdot 10^{-6}$	$\text{kg} \cdot \text{m}^2$
Viscous friction coefficient	$B$	$5 \cdot 10^{-5}$	Nms/rad

Fig. 7.1 shows the brushless DC motor used in this thesis.

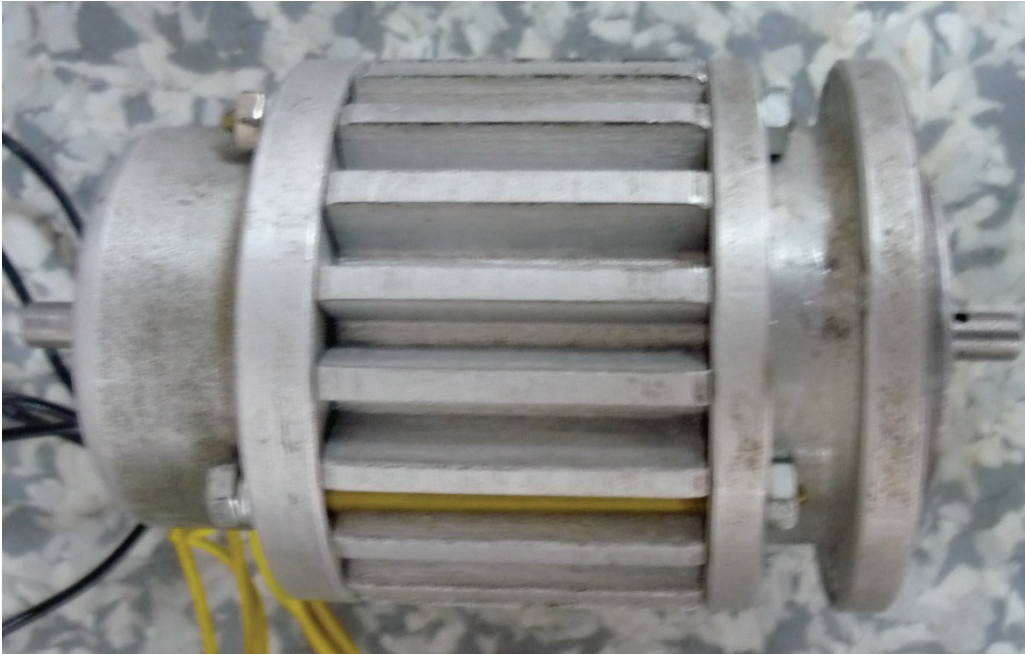


Fig.7.1 Brushless DC motor used for refrigerator compressor

## 7.2 Test bench equipment

The experimental platform is composed of two back-to-back twin three phase brushless DC machines, one of them working as a motor and the other one working as a generator (fig.7.2). The generator is loaded on each phase with load resistance. Since the three phases are unbalanced, the load resistances have different values:  $R_a = 156$  [ $\Omega$ ],  $R_b = 172$  [ $\Omega$ ] and  $R_c = 185$  [ $\Omega$ ] in order to obtain a balanced load torque.

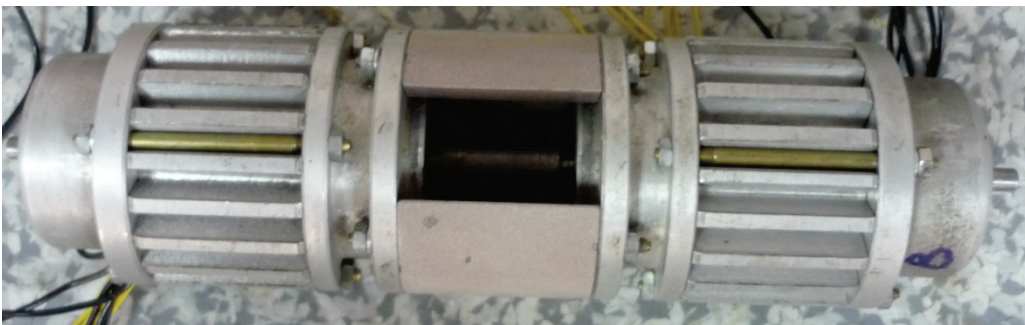


Fig.7.2 Back-to-back twin three-phase brushless DC machines for experiments

### 7.2.1 Inverter

Another component of the platform is the inverter. Originally a Danfoss commercial inverter, its command board was replaced with an interface and protection card. This card, developed at Aalborg University, has the purpose of providing external control over the IGBT's gate drivers. It also contains usual protection, against short-circuit overcurrent, DC overvoltage, inverter leg shoot-through and overtemperature [1]. Inverter and board are shown below, in fig.7.3.

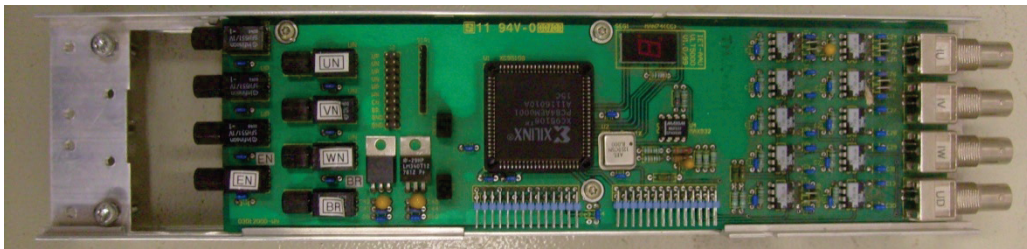


Fig.7.3 Inverter with interface card

The gate and enable signals are connected to the inverter card via optic fiber link, having provided eight receivers on-board. An adaptation board that connects to the dSpace on one end, through a 37 pins Sub-D male connector, and to the inverter card is needed. An octal buffer, type 74HCT540/541, is needed for the 6 PWM signals and Enable signal is mandatory. Optical transmitters, type SFH756V, are used to send the command signals through fiber optics.

In fig.7.4, the printed circuit board (PCB) of the PWM board is shown, while in fig. 7.5 the PWM board itself is presented.

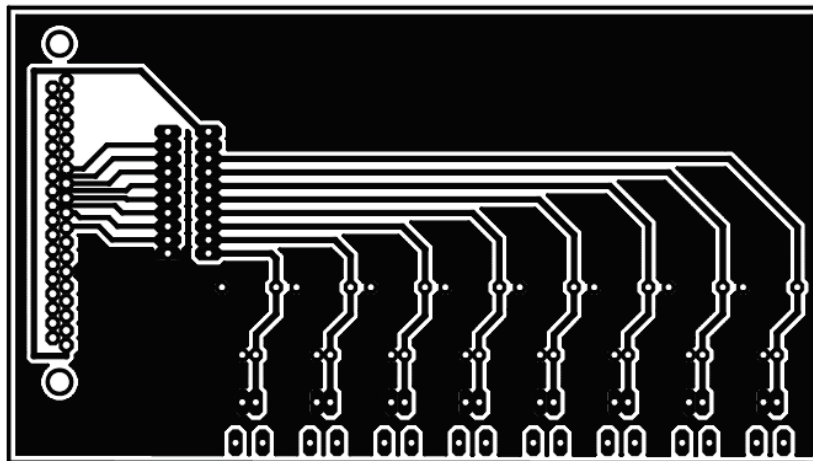


Fig.7.4 PCB of the PWM adaptation board



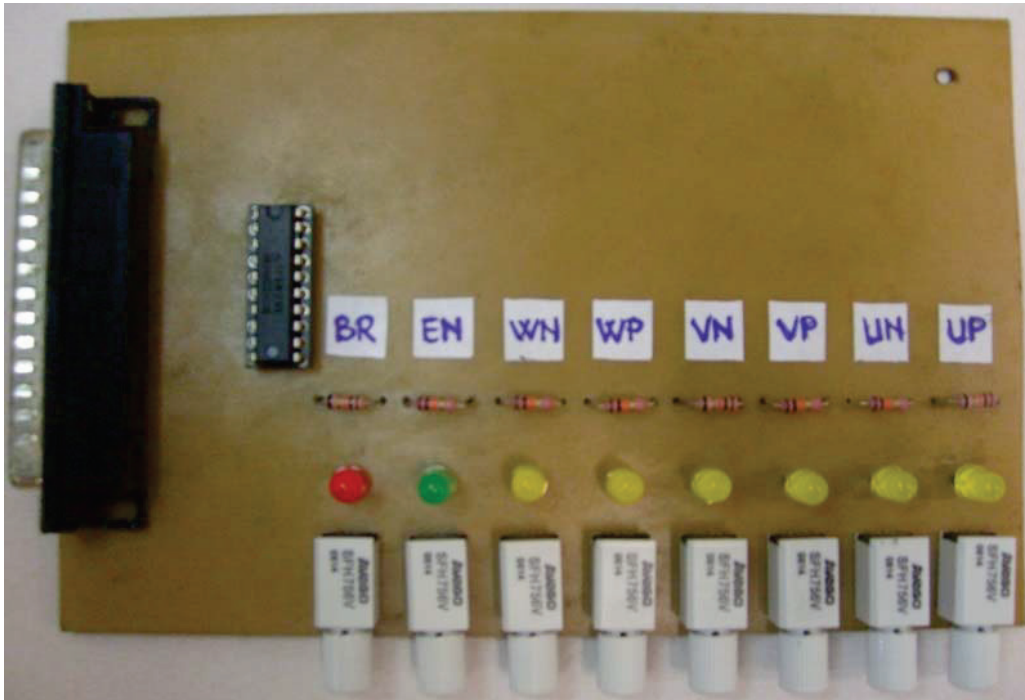


Fig.7.5 Component side of the PWM adaptation board

### 7.2.2 Measurement board

The previous sub-chapter, the interface between dSpace and inverter was detailed. However, to design and implement motor control, with or without position sensors, information from the motor must be taken. In chapter 4, Hall sensors based control was implemented, thus Hall signals need to be acquired.

Sensorless control, as seen in chapter 5, needs on-line information about DC voltage and at least two phase currents.

In order to obtain this information, a measurement board was designed and realized. It is supplied from 230 [V] AC plug and uses a transformer and rectifier to provide 5 [V] DC to supply the sensors. Although a regular DC supply or a battery could be used, we have the flexibility to power the board anywhere.

A voltage transducer, type LV25-P [2], capable of measuring both AC and DC voltages up to 500 [V] is used, taking into account that DC voltage for this application is around 305 [V].

Two current transducers, type LA55-P [3], capable of measuring AC and DC currents up to 50 [A] are used to acquire two phase currents.

Also, the board provides supply from the dSpace for the Hall sensors and takes position information from them. The PCB of the board is shown in fig.7.6, while the board itself is presented in fig.7.7.

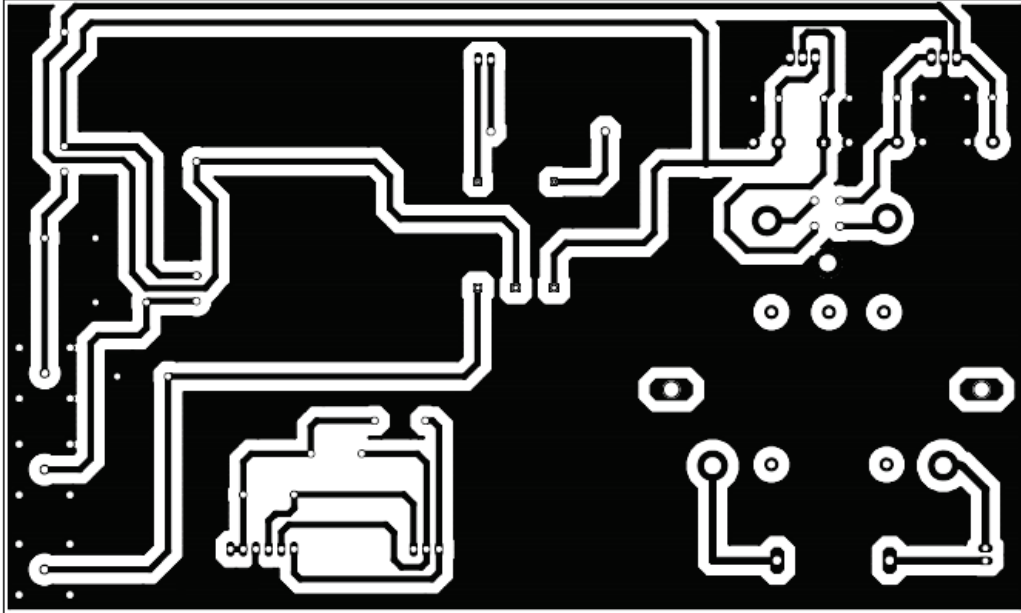


Fig.7.6 PCB of the measurement board

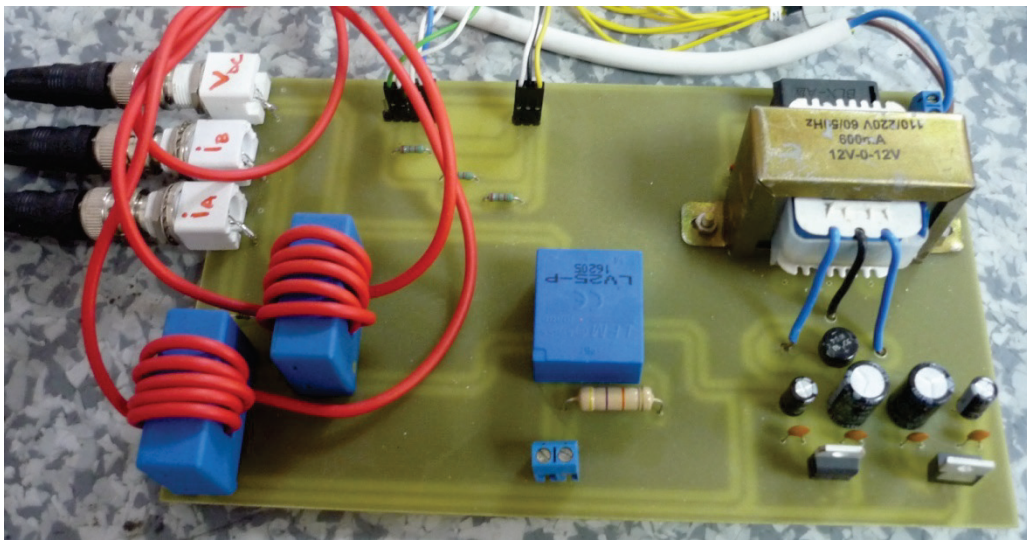


Fig.7.7 Component side of the measurement board

### 7.2.3 Hall signal sensors

The most common control of trapezoidal brushless DC motors is to switch commutation of two phases based on Hall sensors information. For our application,

three such Hall sensors were used, type A1201 from Allegro (fig.7.8).

These sensors have the following features and benefits [4]:

- Continuous time operation (fast power-on time and low noise)
- Stable operation over full operating temperature range
- Reverse battery protection
- Robust EMC performance

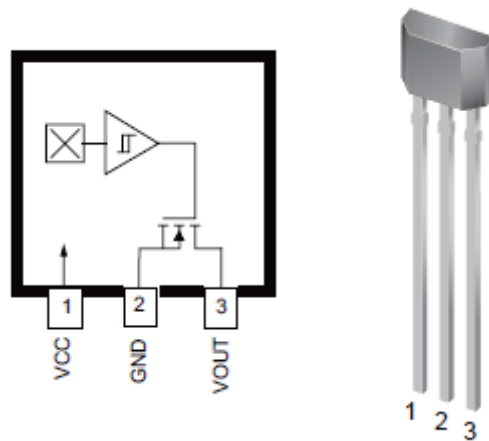


Fig.7.8 Hall sensor type A1201, package UA, 3-pin SIP [4]

#### 7.2.4 dSpace DS1103 platform

To interface the control developed in Matlab®/Simulink® with the inverter and to check on-line the behavior of the system, a DS1103 PPC Controller board is needed. From the manufacturer site [5], one can see that DS1103 is an all-rounder in rapid control prototyping. It has processing power and fast I/O in order to acquire all the necessary information from the sensors. In connection to Real-Time Interface (RTI), the controller board is fully programmable from the Simulink® block diagram environment. This allows configuration of I/O graphically by using RTI.

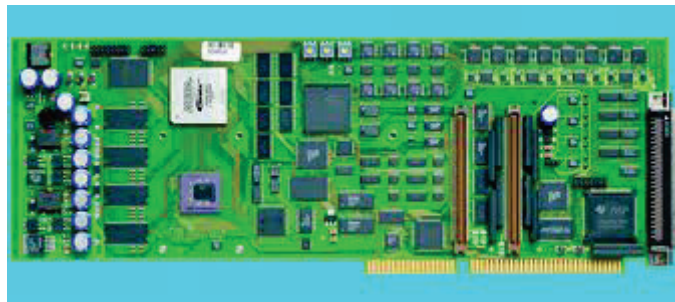


Fig. 7.9 Single board control system dSpace DS1103 [5]

### 7.3 Software implementation

So far, hardware equipment used in the experimental setup was presented. In previous chapters, simulation was also detailed. However, for practical implementation, the control tested in simulations suffers small adaptations in order to be successfully compiled using Microtec C compiler from Motorola Power PC and Texas Instruments C compiler and sent to dSpace platform.

In fig.7.10 the acquisition of Hall sensor information is shown. Both sensed and sensorless controls have same outputs, the PWM signals which are calculated from the duty cycle and sent to the inverter. This command is detailed in fig.7.11.

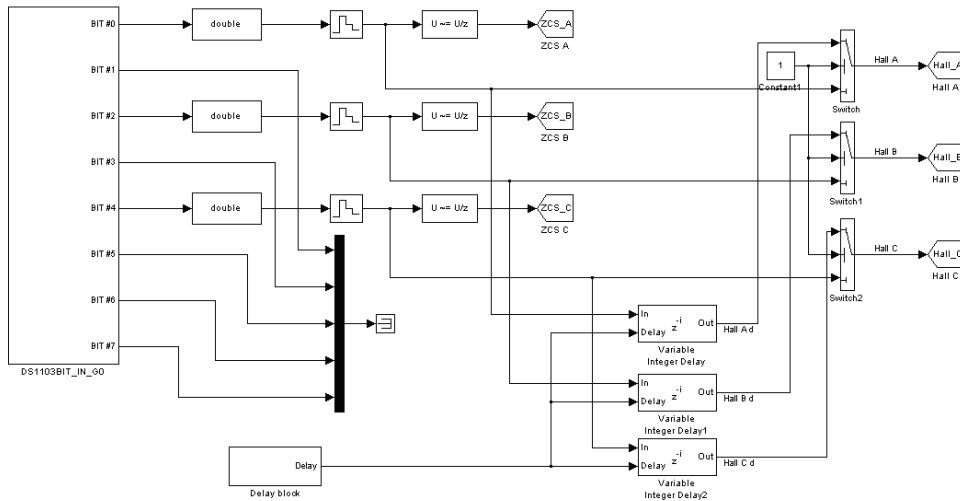


Fig. 7.10 Blocks for Hall sensor signal acquisition and correction

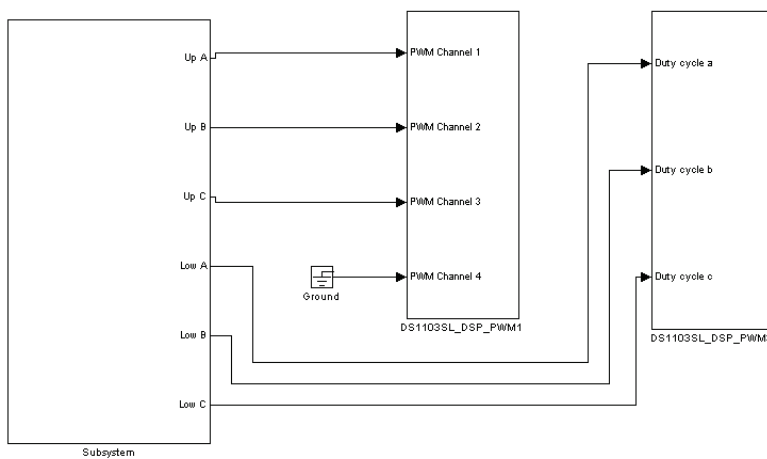


Fig.7.11 Inverter command

Figures 7.12 and 7.13 show how current and voltage sensor signals are received from dSpace I/Os and corrected before using them in the sensorless control algorithm.

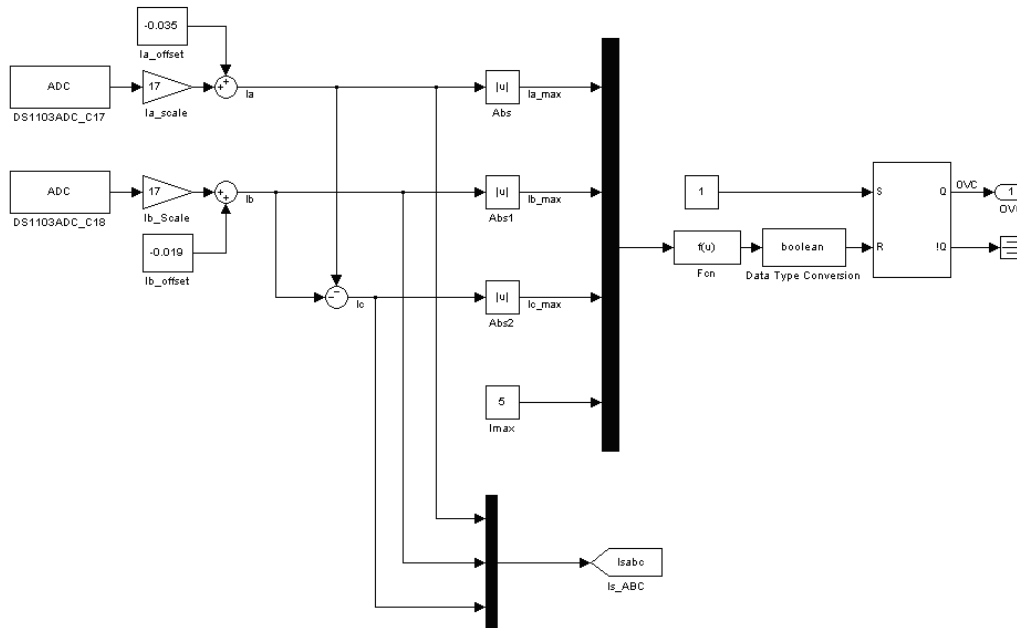


Fig.7.12 Blocks for phase current signals acquisition

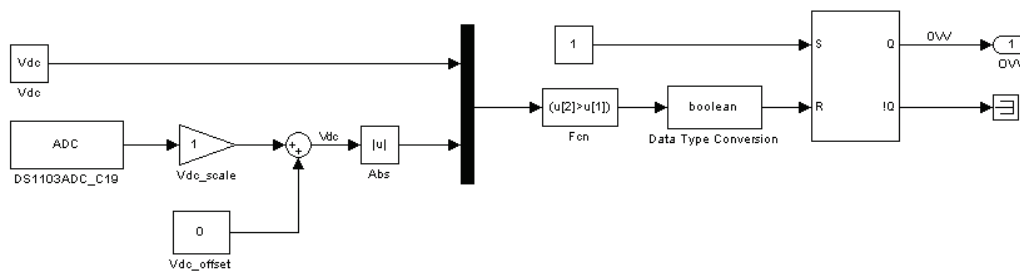


Fig.7.13 Blocks for voltage signals acquisition

After the soft is compiled and error free, it is downloaded in dSpace. A visual interface is provided to the user to see, change or acquire all the parameters from the software, either taken from sensors or calculated. Another advantage of this Control Desk interface is the possibility to change on-line any variable in order to have response from the system. A snapshot of the Control Desk can be seen in Fig.7.14.

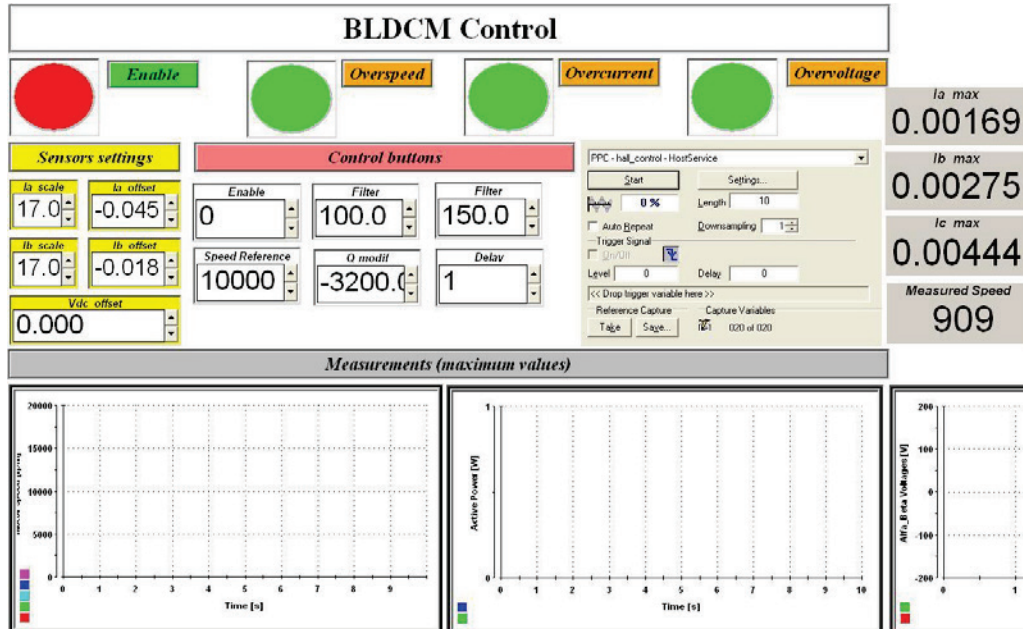


Fig.7.14 Control Desk environment snapshot

## 7.4 Conclusion

While previous chapters were dedicated to control description and to show simulation and experimental results, this chapter was dedicated entirely to the experimental test bench.

Hardware components, like motor, inverter, sensors and adaptation boards were presented and analyzed. The software component, so necessary to interface signal acquisition to proper command was also shown.

dSpace platform with its many advantages and Control Desk Developer interface were also displayed with details.

## References

- [1] R. Teodorescu, "IPC-VLT5000 interface and protection card", *User's Guide*, ver.1.3, Aalborg University, March 2000
- [2] - , "Voltage Transducer LV 25-P", *Application Note*, LEM, [www.lem.com](http://www.lem.com)
- [3] - , "Current Transducer LA 55-P", *Application Note*, LEM, [www.lem.com](http://www.lem.com)
- [4] - , "A1201, A1202, A1203 and A1204 – Continuous-time bipolar switch family", *Application Note*, Rev.1, ALLEGRO, [www.allegromicro.com](http://www.allegromicro.com)
- [5] [www.dspace.com](http://www.dspace.com)

## Chapter 8

### Conclusion and Contributions

#### 8.1 Conclusion

This thesis is dedicated to optimal design, dynamic modeling and control of a three phase brushless DC motor used in refrigerator compressors.

The major topics treated throughout the chapters can be summed to:

- overview of brushless DC motors topologies;
- operation principle of brushless DC motors;
- overview of principal control strategies of brushless DC motors;
- analytical and optimal design of a brushless DC motor used for refrigerator compressor application
- classification of cogging torque and torque ripple reduction techniques in order to reduce the inherent cogging torque with little effect in the value of the output torque
- simulation model for brushless DC motor drive
- development of a new sensorless strategy for trapezoidal brushless DC motors
- introduction of a buck-boost converter in the DC link to reduce the size, cost and commutation losses in the inverter and increase the DC link capacitor to reduce the DC voltage ripples

After treating in detail each of the above subjects the conclusions are:

- The advantages of PM motors over other categories, especially over induction motors, are highlighted to emphasize their popularity and the wide spread of their use in the latest drives.
- Since the fields mentioned above reached their peaks and only small steps are taken, the area of interest shifted to commutation techniques, in order to eliminate the usage of position sensors and development of reliable, robust and easy-to-implement sensorless methods.
- Two different optimization strategies are used to improve the analytical design. A direct search method, modified Hooke-Jeeves algorithm, and a stochastic one, artificial bee colony algorithm, are studied and compared in terms of results and optimization time. Finite element analysis is introduced in the optimization process, in order to obtain accurate values of the cogging and average torques.
- With a brief analysis of the existing minimization techniques, the most popular and viable solutions were chosen. Their effects on the cogging and

average torques for each motor were studied and the results were presented in a table. In terms of output torque, the ABC motor is the undisputed winner, but in terms of cogging torque, even after minimization, it is clear that the HJ motor is superior. Depending on each application, one of them is suited, but for a compressor the HJ motor is better fitted.

- A brief view of the effects of the rotor eccentricity on the output torque's waveform is presented. The influence is not significant even for a serious displacement but may cause mechanical damages.
- The advanced simulation model was created to emulate as real as possible the actual drive, inverter and motor. It offers the possibility to anticipate control issues and motor limitations, especially for worst case scenarios without the need of using the actual motor. This opportunity helps preventing motor damage by improper control or forcing it beyond its limits.
- A new sensorless control was proposed, analyzed, simulated and experimented. Two different formulas were given, one for load torque independent of speed and the other one for load torque dependent of speed. The power based observer with later formula was implemented and simulated showing good performance in constant speed region, at half and full base speed.
- The performance of the control, combined with I-f starting method for start-up and low speeds regions, is experimented on the drive on a laboratory test bench. Experimental results show good agreement with simulation results, thus proving the reliability of this control method for compressor applications where the load is proportional to the speed.
- A combination of PAM/PWM control was introduced. The goal is to separate the speed control from inverter commutation, introducing a buck-boost converter in the DC link. By doing so, the inverter switches will work at a lower frequency and can be downsized, which is economically efficient. Also, inverter switching losses are reduced, since only the DC-DC converter transistor is chopping at a high frequency.

## 8.2 Original contributions

From author's point of view, this thesis contains the following original contributions:

- A synthesis of topologies, control techniques and applications of brushless DC motors;
- Analytical electromagnetic design of a 6 slots/4 poles surface permanent magnet brushless DC motor, as a starting point for hybrid optimal/FEM design;
- Implementation of two new optimal design techniques with embedded FEM for cogging and output torque calculation;



- 
- Validation of brushless DC topologies obtained from optimal design using 2D-FEM, by determining all the relevant machine characteristics: field distribution at no-load and at load, flux linkages at no-load and at load, no-load back EMF, radial forces that affect the rotor, cogging torque, total torque and torque pulsations;
  - Analysis of the cogging torque and torque pulsations reduction techniques and finding what combination of them greatly reduces torque pulsations while little affecting the value of the output torque;
  - Implementation and simulation of a dynamic model of the brushless DC drive considering the commutation phenomenon and correction of Hall sensor delay for proper selection of the conducting phases;
  - Usage of back EMF waveforms obtained from FEM validation, which leads to a more realistic approximation of drive functioning;
  - Design and implementation of a new sensorless technique based on active power calculated from phase currents and voltages without copper losses, knowing that load torque is proportional to speed in compressors and knowing motor inertia and friction coefficient;
  - Usage of the above mentioned technique together with I-f starting method for low speeds region with smooth seamless transition between them;
  - Design and simulation of a converter topology that uses a buck-boost PAM converter in the DC link to reduce the size and commutation losses in the inverter, with and without Hall sensor control
  - Realization of a test bench, design and practical realization of PWM and measurement boards

### 8.3 Future work

Although all the topics were treated in detail, some points related to them can provide interesting research results in the future:

- Experimental results obtained from the topology with the PAM converter in the DC link and calculation of the threshold value of the DC link capacitor where DC voltage ripples are reduced but size and cost become important
- Expanding the simulation model by taking into account mechanical effects (bearings) and cogging torque on the brushless DC
- Improving the sensorless control also including the value of the iron losses which can surpass the copper losses at high speeds
- Include the best cogging torque reduction technique, found in Chapter 3, in the hybrid optimal/FEM design method to enhance the possibility of finding the optimal brushless DC motor topology

## **Author's papers related to the Ph.D. thesis**

[1] Grădinaru Vlad, Tutelea Lucian, Boldea Ion, "25 kW, 15 krpm, 6/4 PMSM: Optimal design and torque pulsation reduction via FEM", Proceedings of the 11<sup>th</sup> International Conference on Optimization of Electrical and Electronic Equipment, vol. I, pp. 249 – 256, Mai 2008 (ISI Proceedings, IEEE Xplore, Inspec, Compendex)

[2] Grădinaru Vlad, Tutelea Lucian, Boldea Ion, "BLDC-SPM Motor Drive with DC-DC Converter in the DC Link: Hall Sensor versus Sensorless Speed Control", Proceedings of the 12<sup>th</sup> International Conference on Optimization of Electrical and Electronic Equipment, PTS I-IV, pp. 422 – 429, Mai 2010 (ISI Proceedings, IEEE Xplore, Inspec, Compendex)

[3] Grădinaru Vlad, Tutelea Lucian, Boldea Ion, "Hybrid Analytical/FEM Optimization Design for SPMSM for Refrigerator Compressor Loads", Proceedings of the 6<sup>th</sup> Aegean Conference on Electrical Machines and Power Electronics (ACEMP), Septembrie 2011 (IEEE Xplore)

## Author's CV

### Vlad-Nicolae Grădinaru

**Office:** University Politehnica of Timișoara, România  
2, Vasile Pârvan Blvd., Building D, Room D108  
Tel.: +40 256403463  
e-mail: [Vlad.Gradinaru@continental-corporation.com](mailto:Vlad.Gradinaru@continental-corporation.com)

**Home address:** 3, Teodor Mihaly Str.  
Timișoara, Timiș, România  
Mobile: +40 721406007

#### EDUCATION

2006 – 2012 Ph.D. student at University "Politehnica" Timișoara,  
Faculty of Electrical and Power Engineering  
Department of Electrical Machines and Drives, Timișoara, România  
2006 Diploma degree in Electrical Engineering  
2001 – 2006 Student at University "Politehnica" Timișoara,  
Faculty of Electrical Engineering  
1997 – 2001 "Grigore Moisil" High School, Timișoara, România

#### PROFESSIONAL EXPERIENCE

Aug.2010 – Present Software Developer at Continental Automotive Romania  
S.R.L., Timișoara, România  
Nov.2006 – Mar.2011 Electrical Engineer at BeeSpeed Automatizari S.R.L.,  
Timișoara, România  
Mar.-Aug. 2008 Guest Researcher at EMBRACO S.A., Joinville, Brazil  
Jul.2004 – Aug.2006 Electronist at S.C. AEM S.A., Timișoara, România

#### PERSONAL INFORMATION

Born: April 3rd, 1982  
Family: Unmarried